ADVANCES IN NATURAL GAS ENGINEERING

Sour Gas and Related Technologies

Edited by Ying Wu, John J. Carroll and Weiyao Zhu

WILEY

Scrivener

Sour Gas and Related Technologies

Scrivener Publishing
100 Cummings Center, Suite 541J
Beverly, MA 01915-6106

Publishers at Scrivener
Martin Scrivener (martin@scrivenerpublishing.com)
Phillip Carmical (pcarmical@scrivenerpublishing.com)

Sour Gas and Related Technologies

Edited by

Ying (Alice) Wu

Sphere Technology Connection, Canada

John J. Carroll

Gas Liquids Engineering, Canada

and

Weiyao Zhu

University of Science & Technology
Beijing, China

Scrivener

WILEY

Co-published by John Wiley & Sons, Inc. Hoboken, New Jersey, and Scrivener Publishing LLC, Salem, Massachusetts.
Published simultaneously in Canada.

Illustration on front cover depicts interaction of stem cells into the nanobiomaterials for tissue engineering.

Cover design by Kris Hackerott

Library of Congress Cataloging-in-Publication Data:

ISBN-10: 0-470-94814-0

ISBN-13: 978-0-470-94814-9

Printed in the United States of America

10 9 8 7 6 5 4 3 2 1

Contents

Preface

The Third International Acid Gas Injection Symposium (AGIS) was held in Banff, Canada in mid-2012. Papers covering many aspects of sour gas in general, and the injection of acid gas in particular, were presented. Sour gas, as described in the Introduction, is natural gas that contains significant amounts of hydrogen sulfide, whereas acid gas is a mixture of hydrogen sulfide and carbon dioxide.

Closely related to the field of sour gas are carbon capture and storage and the use of carbon dioxide for enhanced oil recovery. These are also topics discussed at AGIS.

This new volume is a collection of the papers from the third AGIS covering the topics of sour gas and acid gas, including carbon dioxide. We are grateful to all of the authors whose papers appear in this volume. We would also like to thank all who participated in AGIS, as presenters, attendees, and sponsors.

Ying (Alice) Wu
John J. Carroll
Calgary, Canada

Introduction: Sour Gas

Ying Wu[1] and John J. Carroll[2]
[1]*Sphere Technology Connection, Calgary, AB, Canada*
[2]*Gas Liquids Engineering, Calgary, AB, Canada*

Sweet, easily accessible natural gas is becoming less plentiful, while the world's demand for energy continues to increase. This need will have to be filled with unconventional gas resources, including sour gas.

In the natural gas business, sour gas refers to gas with high concentrations of sulfur compounds. The most common of these compounds is hydrogen sulfide. There are several other sulfur compounds found in natural gas. These include mercaptans (also known as thiols), sulfides, disulfides, carbon disulfide (CS_2), and carbonyl sulfide (COS).

Another important sulfur compound is sulfur dioxide, SO_2. Although not found in natural gas, it is formed from the combustion of sulfur compounds.

Hydrogen sulfide is notorious for being poisonous at relatively low concentrations, and for its foul odor at even lower concentrations. The mercaptans also have a fetid odor, which is detectable by the human olfactory at relatively low concentrations. Perhaps the most famous of these is the oil sprayed from a skunk, which has a horrible odor.

The definition of sour gas varies from jurisdiction to jurisdiction, and from application to application. For example, what for raw gas to be considered sweet is very different from sales gas (the product delivered to the customer). For raw gas, the main interest is the emergency planning. Thus, gas that requires no emergency exclusions zones would be considered sweet.

According to the Energy Resources Conservation Board (RCB) in the province of Alberta, "sour gas is natural gas that contains measurable amounts of hydrogen sulfide."[1] Although not specified by

the ERCB, in oilfield terms, "measurable" typically means about 100 parts per million (ppm) or 0.01 mol%.

With this in mind, we present the following simple definitions for raw gas:

Sweet, Raw Gas	less than 100 ppm H_2S
Low Sour Gas	less than 1% H_2S, but greater than 100 ppm
Moderate Sour Gas	between 1 and 10% H_2S
High Sour	between 10 and 25% H_2S
Ultra High Sour Gas	greater than 25%

Please note, humans and animals subjected to an environment of breathing air of 100 ppm H_2S would be in a very dangerous situation. However, the raw gas containing 100 ppm would be diluted with air if released to the environment, and thus the concentration inhaled by those in the vicinity would be much less. Therefore, exclusion zones for the production of gas containing 100 ppm H_2S would be limited to the immediate area around the well, pipeline, and processing facilities.

Carbon dioxide is commonly associated with sour gas. However, strictly speaking, gas that contains CO_2 but is free of sulfur compounds is not sour. Carbon dioxide has similar properties to H_2S, and similar technologies are used to remove it from the raw natural gas. There is a paper in this volume that discusses the modeling of the processes for removing H_2S and CO_2 from natural gas[2].

The World

There are many regions in the world with important sour and high CO_2 fields. These include:

1. In the Canadian province of Alberta, there are several high sour fields. In the extreme is Bearberry, which is more than 90% H_2S, but is currently not a commercial field. However, there is production from high sour fields (35% H_2S) in Caroline and Zama, for example. According to the Canadian Association of Petroleum Producers (CAPP), approximately 1/3 of the production in Alberta is sour[3].
2. In the United States, there are several fields that are both high-CO_2 and sour. For example, the LeBarge

Field in Wyoming is 5% H_2S and 65% CO_2, and is currently produced commercially[4]. Much of the CO_2 produced in Wyoming and New Mexico is used for enhanced oil recovery in Texas.

3. Much of the associated gas produced in Kazakhstan is sour; much of this is produced offshore in the Caspian Sea. The raw gas contains more than 10% H_2S and about 5% CO_2. One of the papers in this volume addresses the problems with the sour gas at a Kazakhstani field[5].
4. The North Field/South Pars shared by Qatar and Iran in the Gulf region in the Middle East is probably the largest gas field in the world, and it is sour. However, the H_2S concentration is typically less than 1% throughout the field.
5. Many of the gas fields in Abu Dhabi are sour. One of these in the early stages of development is the Shah Field[6], which contains 25% H_2S and 10% CO_2.
6. The Sichuan Basin in southwest China has several sour fields[7]. SINOPEC's Puguang Field, one of the largest gas fields in China, is about 15% H_2S and 10% CO_2. The Luojiazhai field is about 10% H_2S, and is infamous for a blowout in 2003, which killed approximately 250 people: this is a reminder of the dangers of producing sour gas. A paper in this volume discusses the potential for acid gas injection in China[8].
7. The Gulf of Thailand – South China Sea region is famous for high-CO_2 gas fields. In the news recently was a report of a project to study the development of the K5 Field offshore near the Malaysian state of Sarawak[9]. This field is 70% CO_2.
8. These are just a few examples, but they show that the occurrence of sour gas is widespread throughout the world.

Acid Gas

Acid gas, a mixture composed mostly of H_2S and CO_2, is the by-product of the processing of the raw gas. Handling this stream is one of the difficulties in the exploitation of these resources. Acid

gas injection has become a way to monetize some of these sour fields, particularly the small and remote ones.

In addition to being more toxic than sweet gas, there are other problems associated with producing sour gas. In combination with water, H_2S and CO_2 are corrosive, and require special material selection and corrosion inhibition programs.

In Summary...

The world's thirst for energy will continue to increase, and natural gas will probably plan an important role in quenching it. As reserves of sweet gas diminish, sour gas will play a more important role.

References

1. ———, "Sour Gas," http://www.ercb.ca/portal/server.pt/gateway/PTARGS_0_0_315_247_0_43/http%3B/ercbContent/publishedcontent/publish/ercb_home/public_zone/sour_gas/, Energy Resources Conservation Board, Edmonton, AB, Canada, (2009).
2. Hatcher, N., Alvis, A.S., and Weiland, R., "A Holistic Look Gas Treating Simulation," in Wu, Y. and Carroll, J.J. (eds.), *Sour Gas and Related Technologies*, Scrivener Publishing, (2012).
3. ———, "Sour Gas," http://www.capp.ca/environmentCommunity/airClimateChange/Pages/SourGas.aspx, Canadian Association of Petroleum Producers CAPP, Calgary, AB, Canada, (2009).
4. Huang, N.S., Aho, G.E., Baker, B.H., Matthews, T.R., and Pottorf, R.J., "Integrated Reservoir Modeling of a Large Sour-Gas Field with High Concentrations of Inerts," *SPE Res Eval Eng*, **14** (4): 398–412, (2011).
5. Zhao, X., Carroll, J.J. and Wu, Y., "Acid Gas Injection for a Waste Stream with Heavy Hydrocarbons and Mercaptans," in Wu, Y. and Carroll, J.J. (eds.), *Sour Gas and Related Technologies*, Scrivener Publishing, (2012).
6. Schulte, D., Graham, C., Nielsen, D., Almuhairi, A.H., and N. Kassamali, "The Shah Gas Development (SGD) Project – A New Benchmark," *Sour Oil & Gas Advanced Technology (SOGAT) Conference*, Abu Dhabi, U.A.E., March 31-April 1, (2009).
7. Wu, Y. and Carroll, J.J., "A Review of Recent Natural Gas Discoveries in China," *Sour Oil & Gas Advanced Technology (SOGAT) Conference*, Abu Dhabi, U.A.E., April 27-May 1, (2008).
8. Li, Q., Li, X., Du, L., Liu, G., Liu, X., and Wei, N., "Potential Sites and Early Opportunities of Acid Gas Re-injection in China," in Wu, Y. and Carroll, J.J. (eds.), *Sour Gas and Related Technologies*, Scrivener Publishing, (2012).
9. ———, "Petronas, Total to study potential of CO2 field," *The Star Malaysia*, March 29, 2012.

PART 1

DATA: EXPERIMENTS AND CORRELATION

Ying (Alice) Wu, John J. Carroll and Weiyao Zhu (eds.) Sour Gas and Related Technologies, (3–20)

1

Equilibrium Water Content Measurements for Acid Gas at High Pressures and Temperatures

Francis Bernard[‡], Robert A. Marriott[†], and Binod R. Giri

Alberta Sulphur Research Ltd., Calgary, AB, Canada
[‡]fbernard@ucalgary.ca
[†]rob.marriott@ucalgary.ca

Abstract

The design of safe and reliable acid gas compression, injection, and transport facilities requires a good understanding of the phase behavior of acid gas and water. Although many data are available for natural gas systems in open literature, there are limited reported data on the $H_2S + H_2O$ system at pressures relevant to injection schemes and target reservoir pressures.

For the past ten years, Alberta Sulphur Research Ltd. (ASRL) has been developing techniques for the measurement of water carrying capacity of gases, liquids, and supercritical fluids. With the current experimental method, water carrying capacity measurements at pressures up to 100 MPa and at temperatures up to 150°C are being carried out. Difficulties associated with this type of experiment will be discussed.

Initial measurements have been completed for $H_2S + H_2O$ at $T = 50$ and 100°C, and from $p = 3.8$ to 70.5 MPa. These new measurements serve to add information at conditions which are not covered by the existing literature, including extending available experimental values above $p = 30$ MPa. These new values, together with literature water content and H_2S solubility and volumetric data, have been combined to calibrate a model for calculating equilibrium between H_2O and H_2S up to $T = 200$°C and $p = 70$ MPa. Model parameters have been reported, along with ASRL's future experimental and modeling plans in this area.

Ying (Alice) Wu, John J. Carroll and Weiyao Zhu (eds.) Sour Gas and Related Technologies, (3–20)

1.1 Introduction

The need for the accurate calculation of the water carrying capacity in acid gas injectates has been discussed by several authors [1, 2]. For example the ability to estimate the saturation water content within multiple compression stages is used to determine the extent of dehydration before fluids are sent to injection [3]. A considerable amount of time and money can be saved if an acid gas can be injected without the condensation of free water or production of a hydrate phase, *e.g.*, no free water upon compression discharge can alleviate the need for expensive corrosion resistant metallurgy in transport lines.

In a previous paper [4], we illustrated how compression can be used to partially dehydrate an acid gas, Figure 1.1. Figure 1.1 shows the estimated water dew points for a 50:50 H_2S/CO_2 acid gas and a simplified four cycle compression scheme [5, 6]. Note that the hydrate formation curve has not been included. For the scheme in Figure 1.1, within the second and third inter-stage cooling, the water content is reduced from 2.0 to 0.7 % H_2O and 0.7 to 0.3% H_2O. Upon cooling after the 4th stage compression cycle, the 0.3% fluid

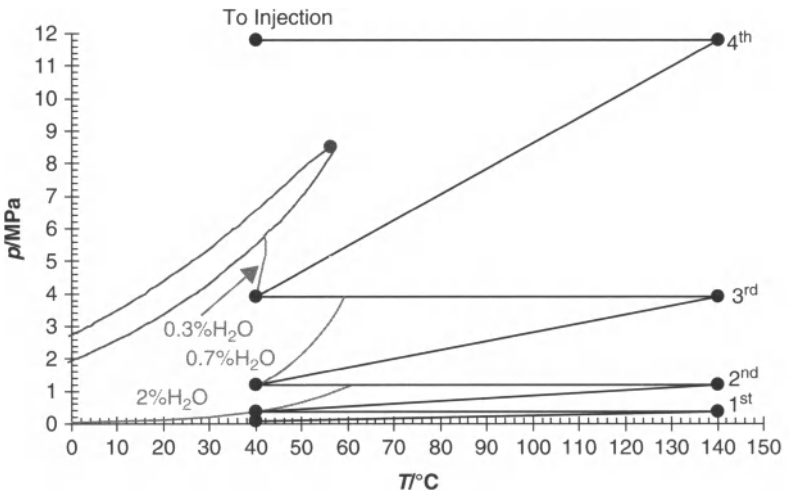

Figure 1.1 A simplified schematic for four stages of compression of a 50:50 H_2S/CO_2 acid gas mixture showing the estimated drop in dew point at each suction condition. The dry phase pockets have been calculated using VMGSim 2.8.0 [5] and the water dew point phase pockets have been calculated using AQUAlibrium 3.0. [6].

is under-saturated with water at the conditions labeled 'to injection'. While the final condition in Figure 1.1 represents a possible wellhead condition, the degree of subsaturation in the near wellbore region also is of interest to reservoir modeling, because as the fluid arrives in the reservoir, it will have the capacity to take up additional reservoir water. Therefore, the range of interest in water and acid gas equilibria can extend up to 75 MPa or, in other words, beyond the compression discharge pressures.

The calculated aqueous equilibria in Figure 1.1 are difficult to model, especially when they involve gaseous, liquid and supercritical acid gas phases. In general, calibration of these types of models are difficult because published experimental data for pure H_2S and other components are sparse and the pressure range of interest is very large. For example, Figure 1.2 (also presented in the previous paper) [4] shows the conditions for published H_2S water content data. [7–10] There are no data above *ca.* 30 MPa and experimental data in the liquid H_2S region are primarily those of Gillespie and Wilson [8]. The scarcity of data is due, in large part, to the experimental difficulties in obtaining representative samples of equilibrated dense phase acid gases (liquids and supercritical fluids).

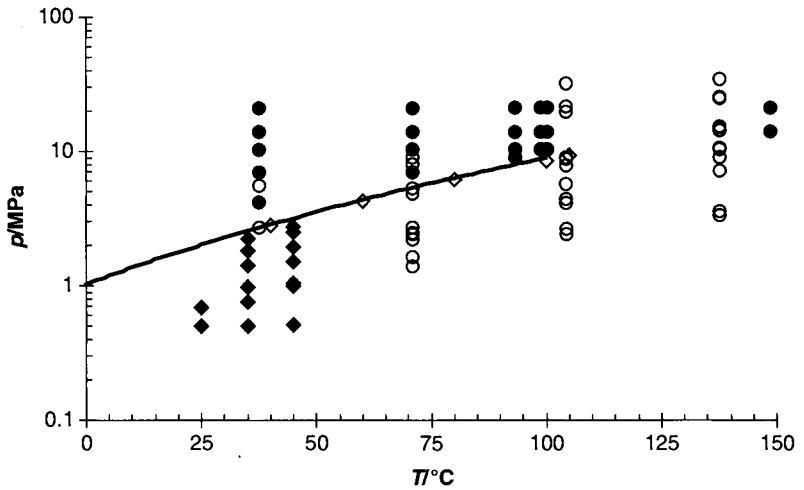

Figure 1.2 Conditions for H_2S water content data reported in the literature. ♦, Chapoy *et al.* [7]; •, Gillespie and Wilson [8]; ◊, Carroll and Mather [9]; ○, Selleck *et al.* [10]; ——, vapour pressure from the Lemmon and Span EOS [11]. Note that the conditions for the Wright and Maass [12] and Lee and Mather [13] data are missing from this figure.

The risks involved in working with high pressure hydrogen sulfide also explains why only a handful of laboratories around the world are equipped to perform these types of measurements.

The need for more published data for the H_2S-H_2O system prompted our laboratory to pursue an experimental program specifically aimed at measuring the water carrying capacity of high-pressure hydrogen sulfide fluids. The experimental method consists of a custom automated sampling/injection system that allows us to take microliter size high-pressure samples and expand them directly onto a gas chromatography column. Although this paper does not to report all the data measured to date, it is used to share our experience with these difficult measurements and identify future improvements.

Finally, using new water content data up to p = 70.4 MPa, we report a preliminary thermodynamic model which can be used to calculate the partitioning of H_2S and H_2O over a wide range of temperatures and pressures. In order to work in the liquid-liquid regime at very high pressures, this model utilizes high accuracy reduced Helmholtz energy equations of state for the pure components. For example the equation of state for H_2O, is self consistent with the current steam tables [15].The model limitations and estimated error have been discussed by evaluating water content of H_2S and H_2S solubility in water.

1.2 Experimental

In the past, ASRL has used different techniques to measure water content data [4]. These techniques have evolved as we attempt to measure phase behaviours in T-p regions that were more troublesome. Our current technique consists of a high pressure equilibrium vessel sampled through a capillary dip-tube and into a gas chromatograph (GC) (see Figure 1.3). The chromatographic column is a CP-RT-U-PLOT and we are using a thermal conductivity detector (TCD).

The most difficult issue for measuring water content in an acid gas sample is the transfer of the high-pressure sample to the low-pressure analytical GC. As the depressurizing fluid is flashed to the gaseous pressure region, there is a minimum in the water carrying capacity. If not properly considered, the water within the high-pressure equilibrium element will not continue with the other sampled components.

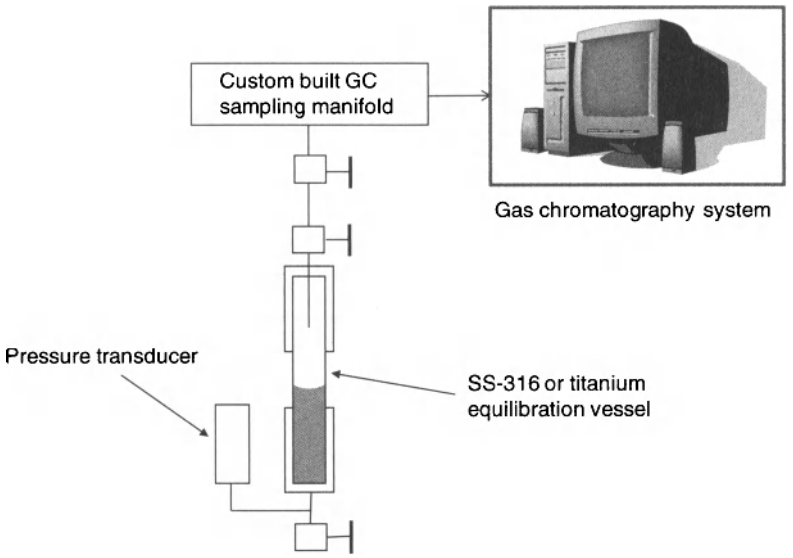

Figure 1.3 A schematic of the ASRL water content measurement technique.

Heat must consequently be supplied to allow the water to stay in the gas phase and overcome the Joule-Thompson cooling effect and the latent heat lost due to re-evaporation.

One option is to heat a liquid fluid sample 40 to 50°C above its equilibration temperature during sampling. The high sampling temperature can create problems with the temperature control of the equilibrium vessel itself. Our experience shows that some of the heat can be carried over to the sampling tip of the capillary tube and create an area of localized high temperature equilibrium. This in turn, causes the water content to be artificially high in the superheated zone.

To avoid superheating of the sample, ASRL now injects the high pressure fluid directly onto the GC column. This allows us to keep the sample loop at the same temperature as the equilibration vessel. While some of the water contained in the sample may condense in the transfer line upon depressurization, the GC carrier gas re-evaporates and carries the water to the column within a few seconds and without any sample loss. The transfer line to the GC is kept at *ca.* 100°C to ensure a complete and quick transfer to the GC.

In order to perform high-pressure sampling, we had to build a custom sampling manifold (see Figure 1.4) with microliter size sample loops. It gives us the capability to inject variable amounts

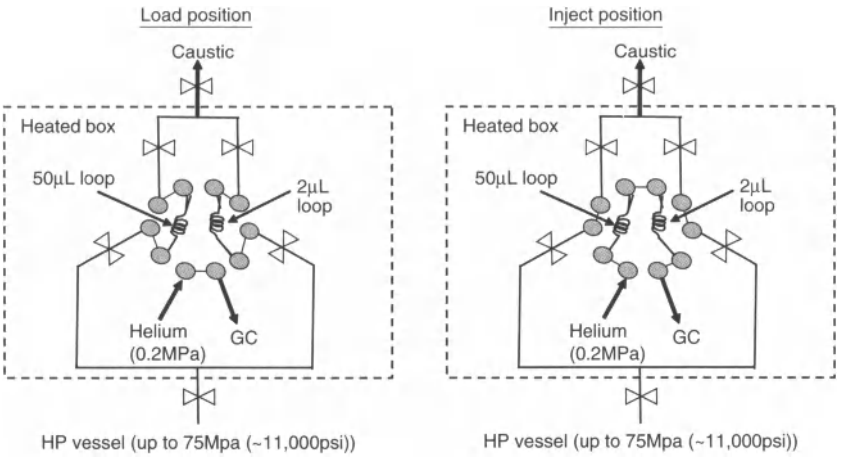

Figure 1.4 Schematics of the custom built GC injection valve used by ASRL.

of pressurized sample and avoids perturbing the equilibrium in the vessel. We use a Hastelloy C-276 high pressure liquid chromatography (HPLC) valve coupled with 2 sample loops, a 2μL loop that allows us to inject samples at up to $p = 75$ Mpa and a 50μL loop that can be used for calibration and for low density samples. All of the sampling components are kept at the same temperature as the sampling vessel by using resistive heaters and PID temperature control. The helium carrier gas also is pre-heated for improved temperature control.

Once the vessel is safely connected to the sampling manifold, valves are opened in order to place the sample in direct communication with the GC sampling valve. The fact that the vessel valve remains open allows us to perform automated injections over extended periods of time. Through small injection volumes we are able to keep the pressure drop to a minimum. Our current method involves injecting samples every 20 minutes and each equilibrium point normally is measured with *ca.* 10 samples. The HPLC valve was designed to be used with liquid samples as opposed to supercritical fluids. This makes it subject to blistering and leakage (see Figure 1.5) at high pressures when the temperature is higher than *ca.* 75°C. This is even more prominent with the use of high-pressure CO_2.

In each of the gravimetrically prepared calibration standards, we include some carbon dioxide to serve as an internal standard. This

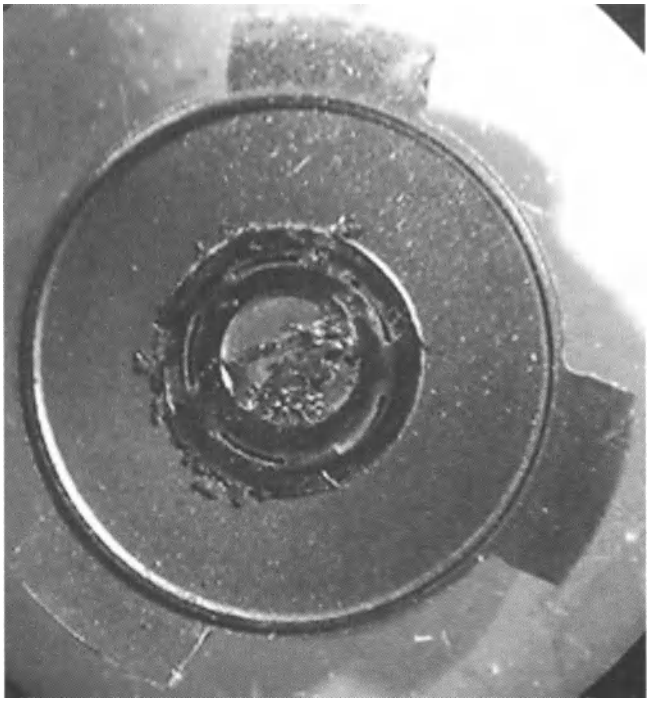

Figure 1.5 Photograph of a severely blistered GC valve rotor as seen under a microscope. Blistering took place after sampling H_2S and CO_2 for a few weeks at 100°C.

makes it possible to calibrate the GC by varying injection pressure instead of concentration and allows us to use fewer calibration mixtures for a broad range of detector response.

Calibration is a lengthy process that can take weeks, but due to the stability and linearity of the thermal conductivity detector, we can normally use the same calibration for several months, *i.e.*, periodically checking the calibration is much less time-consuming than re-running a complete calibration package. Gravimetric water standards tend to change slowing over long time periods and for that reason, it is difficult to re-use the same calibration standard twice. So far, we have used standards made of water in gaseous CO_2. The mixtures are stored at *ca.* 120°C for the water to remain in the vapour phase.

We recently have tested the use of water standards in dense phase CO_2. Due to the higher water carrying capacity of CO_2 at higher pressures, the standards don't need to be heated to remain

single-phase. This may provide more stability to the water standards, allowing us to check our calibration more frequently.

1.3 Recent Results and Modelling

Water content measurements for pure H_2S have been completed for $T = 50$ and 100°C and $p = 3.8$ to 70.5 MPa. These new experimental data are shown in Figure 1.6 along with the calculated water content using three different models (i) AQUAlibrium 3.0 [6, 9], (ii) the semi-empirical model of Alami *et al.*, [2] and (iii) the new model discussed within this study. As Figure 1.6 shows, the models show large differences in the high-pressure dense-phase region. Recall that the literature extends to less that $p = 30$ MPa; therefore, only the new model has been calibrated in the higher-pressure region. Often, the difficulty in this region arises from the use of cubic equations of state, which may not be robust at very high pressures. To overcome this limitation our model relies on the reduced dimensionless Helmholtz energy equations compiled by the NIST [14]. The two equations used here are those of Wagner and Pruss [15] for H_2O [T = 273.16–2000 K; p < 1000 MPa] and Lemmon and Span [11]

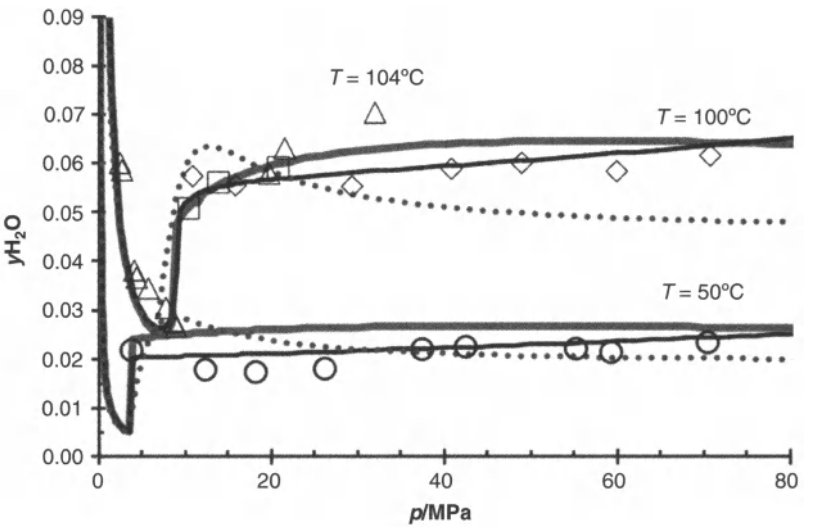

Figure 1.6 The experimental and calculated water content of H_2S at $T = 50$ and 100°C. ○, this study ($T = 50.1 \pm 0.2$°C); ◊, this study ($T = 100.1 \pm 0.3$°C); Δ, Selleck *et al* [10]. ($T = 104.4$°C); □, Gillespie and Wilson [8] ($T = 100$°C); —(grey), AQUAlibrium; – – –, this study, model; ·····, Alami *et al* [2].

for H_2S [T = 187.7–760 K; p < 170 MPa]. For each minor component in a phase, infinite dilution properties have been used to calculate solution properties. The modeling approach is similar to AQUAlibrium [6, 9] and Suleimenov and Krupp [16]. Two primary differences include: (1) fugacity coefficients do not rely on the Peng and Robison equation of state [23] and (2) activity in the aqueous phase is calculated using Pitzer theory for low-dissociating solutes.

To begin, the fugacities for H_2S and H_2O must meet the following equality at equilibrium:

$$f_i^b = f_i^{aq} \tag{1.1}$$

where f_i^b is the fugacity of component i in phase b and f_i^{aq} is the fugacity of component i in the aqueous phase ($i = H_2O$ or H_2S). Note that only the two phase system will be discussed here; therefore, phase b is the H_2S rich phase or non-aqueous phase which can be gaseous, liquid or supercritical. All concentrations in the aqueous phase are denoted by x_i (mole fraction) and concentrations in the non-aqueous phase are denoted by y_i.

1.3.1 Partitioning of Hydrogen Sulfide (H_2S Solubility in Water)

Using Equation (1.1), for H_2S one can show that

$$\varphi_{H_2S} y_{H_2S} p = \gamma_{H_sS} x_{H_2S} K_H e^{v^{\infty}_{H_2S}(p - p^0_{H_2O})/RT} \tag{1.2}$$

where φ_{H_2S} is the fugacity coefficient for H_2S in the non-aqueous phase, y_{H_2S} is the mole fraction of H_2S is the in the non-aqueous phase, p is the total pressure, γ_{H_2S} is the rational activity coefficient for aqueous H_2S, x_{H_2S} is the mole fraction of aqueous H_2S, K_H is the Henry's law constant for total H_2S dissolution in water, $v_{H_2S}^{\infty}$ partial molar volume of aqueous H_2S at infinite dilution, $p_{H_2O}^{\circ}$ is the vapour pressure for pure water, R is the ideal gas constant (R = 8.314472 J K^{-1} mol^{-1}) and T is the absolute temperature.

As will be discussed with water, the fugacity coefficients for the non-aqueous phase are established at infinite dilution of H_2O; therefore, the fugacity coefficient of H_2S in the non-aqueous phase is calculated under pure fluid conditions (standard state; $\varphi_{H_2S} = \varphi_{H_2S}^{\circ}$ as $y_{H_2O} \rightarrow 0$) using the Lemmon and Span equation of state [11].

Following Suleimenov and Krupp [16] and Edwards *et al.*, [18] the activity coefficient for H_2S is calculated using Pitzer theory for an H_2S solute with negligible dissociation [17, 18]:

$$\gamma^{x}_{H_2S} = e^{2\beta_{aa} m_{H_2S}} (1 + 0.0180152 \cdot m_{H_2S}) \tag{1.3}$$

where β_{aa} is the molecular-molecular interaction parameter and m_{H_2S} is the molality [$m_{H_2S} = 55.5087 \cdot x_{H_2S} / (1 - x_{H_2S})$]. Negligible dissociation is a significant simplification for aqueous H_2S ($pK_{a,H_2S} \approx 7$). In this respect, our model can be improved upon in future efforts, where changes in *p*H and ionic activity can influence the total solubility of H_2S. For simplicity in this model, the Henry's law solubility relationship is able to empirically compensate for neglecting the ionic activity. Using this simplification Edwards *et al* [18]. have reported the temperature dependence of β_{aa} for aqueous H_2S:

$$\beta_{aa} = -0.2106 + \frac{61.56}{T} \tag{1.4}$$

Again following Suleimenov and Krupp [16], we have used the Clark and Glew [19] method to correlate the Henry's Law constant. However, we have only used the first three terms in the Taylor series expansion of the heat capacity, whereas Suleimenov and Krupp [16] used four. The overall temperature dependant equation for the Henry's Law constant is then

$$\begin{aligned} R \ln K_H = &-\frac{\Delta G^o_{T_r}}{T_r} + \Delta H^o_{T_r}\left[\frac{1}{T_r} - \frac{1}{T}\right] + \Delta C^o_{p,T_r}\left[\frac{T_r}{T} - 1 + \ln\left(\frac{T}{T_r}\right)\right] \\ &+ \frac{T_r}{2}\left(\frac{d\Delta C^o_p}{dT}\right)_{T_r}\left[\frac{T}{T_r} - \frac{T_r}{T} - 2\ln\left(\frac{T}{T_r}\right)\right] \\ &+ \frac{T_r^2}{12}\left(\frac{d^2\Delta C^o_p}{dT^2}\right)_{T_r}\left[\left(\frac{T}{T_r}\right)^2 - 6\frac{T}{T_r} + 3 + 2\frac{T_r}{T} + 6\ln\left(\frac{T}{T_r}\right)\right] \end{aligned} \tag{1.5}$$

The reference temperature for Equation (1.5) is $T_r = 298.15$ K. All standard thermodynamic property changes were optimized to fit the available solubility data, with the exception of the change in the heat capacity which was measured by Barbero *et al* [20]. [$\Delta C^{\circ}_{p\,Tr} = -144.3$ J K^{-1} mol^{-1}].

The vapour pressure for pure water is calculated using the equation of Wagner and Pruss [15] and the molar volume at infinite dilution is calculated using the density and compressibility correlation shown by O'Connell *et al* [21].:

$$v^{\infty}_{H_2S} = \frac{1}{\rho^{o}_{H_2O}} + \rho^{o}_{H_2O}\kappa^{o}_{T,H_2O}RT\left[a_v + b_v\left(e^{90\rho^{o}_{H_2O}} - 1\right)\right]. \qquad (1.6)$$

For Equation (1.6), $\rho^{\circ}_{H_2O}$ is the density of pure water (mol m^{-3}) [15] and $\kappa_T{}^{\circ}_{H_2S}$ is the isothermal compressibility of pure water (Pa^{-1}) [15]. Parameters a_v and b_v were fit to the volumetric measurement data of Hnědkovsky *et al* [22]. and Barbero *et al.*, [20] which cover a large range of conditions (T = 10 to 431.85°C and p = 0.1 to 35 MPa). A correlation plot for the fitting of Equation (1.6) is shown in Figure 1.7 and the fitted parameters have been reported in Table 1.1.

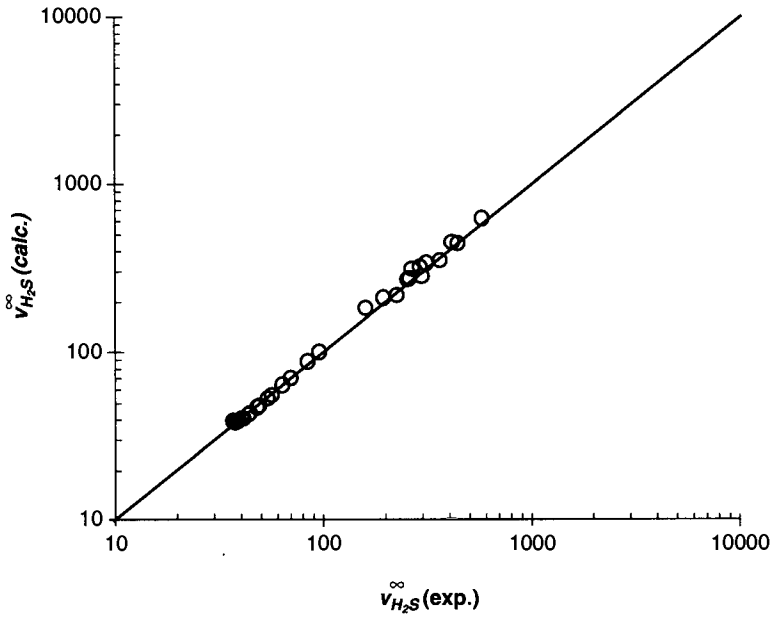

Figure 1.7 The calculated versus experimental partial molar volume of aqueous H_2S at infinite dilution from T = 10 to 431.85°C and p = 0.1 to 35 MPa. Calculation uses Equation (1.6); ○, Hnědkovsky *et al.* [22]; •, Barbero *et al.* [20]; $v_{H_2S}{}^{\infty}$ (exp.) = −2.4 ± 5.6 + 0.998 ± 0.015· $v_{H_2S}{}^{\infty}$ (calc.).

Table 1.1 The parameters for Equations (5), (6), (11) and (12) used for calculating the high-pressure $H_2S + H_2O$ equilibrium concentrations.

Parameter	Value
a_v / ($cm^3\ mol^{-2}$)	49.6 [lit. 47.9] [21]
b_v / ($cm^3\ mol^{-2}$)	1.37 [lit.1.7] [21]
$\frac{\Delta G^o_{T_r}}{T_r}$ / ($J\ mol^{-1}\ K^{-1}$)	147.9208 ± 0.0402
$\Delta H^o_{T_r}$ / ($J\ mol^{-1}$)	16539 ± 157
$\Delta C^o_{p,T_r}$ / ($J\ mol^{-1}\ K^{-1}$)	−144.3 [20]
$\frac{T_r}{2}\left(\frac{d\Delta C^o_p}{dT}\right)_{T_r}$ / ($J\ mol^{-1}\ K^{-1}$)	188.5 ± 20.8
$\frac{T_r^2}{12}\left(\frac{d^2\Delta C^o_p}{dT^2}\right)_{T_r}$ / ($J\ mol^{-1}\ K^{-1}$)	−71.7 ± 17.6
$10^4 \times a_{12}$ / ($m^3\ mol^{-1}$)	1.110 ± 0.279
b_{12} ($m^3\ K\ mol^{-1}$)	-0.1024 ± 0.0107
$10^9 \times a_{122}$ ($m^6\ K\ mol^{-2}$)	1.88 ± 1.73
$10^6 \times b_{122}$ ($m^6\ K\ mol^{-2}$)	2.619 ± 0.648

Partial molar volumes for Equation (1.2) were calculated at the saturation vapour pressure of water at the temperature of interest, despite that Equation (1.6) is valid for a broad range of conditions. Note that Equation (1.6) was derived as a generalized Krichevskii parameter. Through fluctuation solution theory, a rearrangement of the Krichevskii parameter can be integrated to yield the fugacity coefficient at infinite dilution [21]. The correlation with density is similar to the infinite dilution virial equation correlation used here for the non-aqueous phase. In fact, we investigated the use of fluctuation solution theory for both phases, which would simplify the model considerably. Perhaps if molar volumes of H_2O in high pressure H_2S become available, this will become a reasonable approach.

1.3.2 Partitioning of Water (Water Content in H_2S)

Up to this point our model is nearly identical to that of Suleimenov and Krupp [16] who, like Carroll and Mather [9], have used the Peng and Robinson equation of state [23] for the fugacities in the non-aqueous phase. For our model, the fugacity coefficients for the non-aqueous phase are established at infinite dilution of H_2O:

$$\varphi^{\infty}_{H_2O} y_{H_2O} p = a_{H_2O} f^{o}_{H_2O} \tag{1.7}$$

where $\varphi_{H_2O}{}^{\infty}$ is the infinite dilution fugacity coefficient for H_2O in the H_2S rich phase, $f_{H_2O}{}^{\circ}$ is the fugacity of pure water [15], and a_{H_2O} is the activity of H_2O. Through the Gibbs-Duhem relationship, the H_2O activity is calculated from the activity of H_2S, *i.e.*, using Pitzer theory, Equation (1.4) and H_2S solubility from Equation (1.2):

$$a_{H_2O} = \frac{x^2_{H_sS}(1-55.5087\beta_{aa}) - x_{H_sS}}{(1-x_{H_sS})^2}. \tag{1.8}$$

The fugacities for water in the H_2S rich phase are calculated using the volume explicit virial equation,

$$\ln Z\varphi_1 = 2\rho\sum_i y_i B_{1i} + \frac{3}{2}\rho^2 \sum_i \sum_j y_i y_j C_{1ij} + \ldots \tag{1.9}$$

For the $H_2S + H_2O$ system at infinite dilution of H_2O, a truncated Equation (1.9) simplifies to

$$\ln \varphi^{\infty}_{H_2O} = 2B_{12}\rho_{H_2S} + \frac{3}{2} C_{122}\rho^2_{H_2S} - \ln Z\,. \tag{1.10}$$

For Equation (1.10), ρ_{H_2S} is the molar density of pure H_2S [11] and Z is the compressibility factor for the pure H_2S. B_{12} and C_{122} are the second and third virial coefficients, respectively. These virial coefficients are only temperature dependant and were found to be well represented by the temperature dependent functions of

$$B_{12} = a_{12} + \frac{b_{12}}{T} \tag{1.11}$$

and

$$C_{122} = a_{122} + \frac{b_{122}}{T}\,. \tag{1.12}$$

The fitted coefficients for Equation (1.11), Equation (1.12) and their respective 95% errors are reported in Table 1.1.

1.3.3 Discussion of Results

The optimization of coefficients required to solve Equations (1.2) and (1.7) was as follows:

(i) the infinite dilution fugacity coefficient for water [Equation (1.7)] was fit by least squares regression to the water content literature data [7, 8, 10] and data from this study assuming an initial water activity of unity, $a_{H_2O}=1$;
(ii) the composition of H_2S in the vapour phase was established for each experimental solubility using Equation (1.7) and used to calculate experimental Henry's law constants for all literature data, [8, 10, 16, 24, 25–35] and then Equation (1.6) was fit by least square regression;
(iii) the infinite dilution fugacity coefficient for water [Equation (1.7)] was fit by least squares regression to the water content literature data and data from this study using the calculated water activity;
(iv) steps (ii) and (iii) were repeated until the coefficients converged [this required four iterations].

With the optimized coefficients, Equation (1.2) and (1.7) can be used by successive substitution to solve for both the H_2S and H_2O partitioning at equilibrium.

Figure 1.8 shows the calculated versus the experimental H_2S solubilities used to calibrate the model. Overall the calculated solubility data show a small bias when compared to the experimental [x_{H_2S}(exp.) = –0.00037 ± 0.00040 + 1.055 ± 0.005·x_{H_2S}(calc.)]. However, this bias does not exist for data where $x_{H_2S} < 0.3$. The average error was found to be $\delta x_{H_2S}/x_{H_2S} = 3.7\%$ for $x_{H_2S} < 0.3$ and $\delta x_{H_2S}/x_{H_2S} = 5.7\%$ for $x_{H_2S} > 0.3$. Note that at some conditions for $T > 200°C$, the equations do not converge. Both the instability at high-temperature and the bias at high concentration are likely due to the simplification of negligible dissociation in the activity coefficient and partial molar volume. A high temperature of $T = 200°C$ is sufficient for most acid

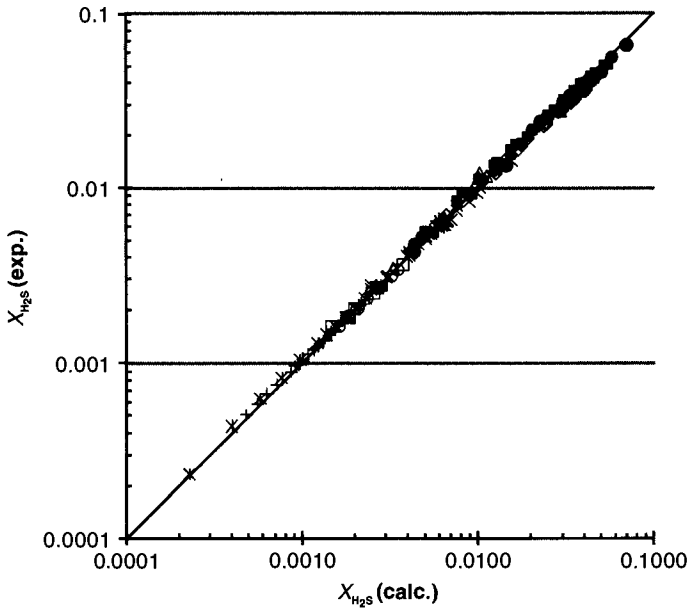

Figure 1.8 The calculated versus experimental H_2S solubilities in water from $T = 0$ to 266°C and $p = 0.05$ to 20.6 MPa. •, Gillespie and Wilson [8]; ■, Selleck *et al.* [10]; ◊, Chapoy [24]; Δ, Davis *et al.* [25]; ×, Suleimenov and Krupp [16]; ✳, Winkler [26]; +, Clarke and Glew [27]; ○, Doabul and Riley [35]; □, various smaller studies [28–34].

gas injection reservoirs of interest. Future modeling effort should take into account dissociation and other species such as CO_2 and CH_4. The equations proposed here would still apply to an acid gas or sour gas mixture, because accurate densities for acid gas mixtures can be calculated using the reduced Helmholtz energy equations of state. Finally, it should be noted that there is a high pressure solubility limit for the experimental data, $p < 20.6$ MPa; whereas, solubilities at higher target pressures could be explored in the future.

Figure 1.9 is a correlation plot for the calculated water contents from $T = 25$ to 260°C and $p = 0.5$ to 70.4 MPa. Unlike the H_2S solubility calculation, the water content calculation is not significantly biased with respect to the experimental data [y_{H_2O}(exp.) = –0.00047 ± 0.00070 + 1.02 ± 0.01 · y_{H_2O}(calc.)]. The averaged error is $\delta y_{H_2O}/y_{H_2O} = 8.3\%$, which compares favourably with $\delta y_{H_2O}/y_{H_2O} = 10.8\%$ for AQUIlibrium and the same data set. Again, at high-temperature conditions the model does not converge. This is a result of the solubility limitations discussed earlier.

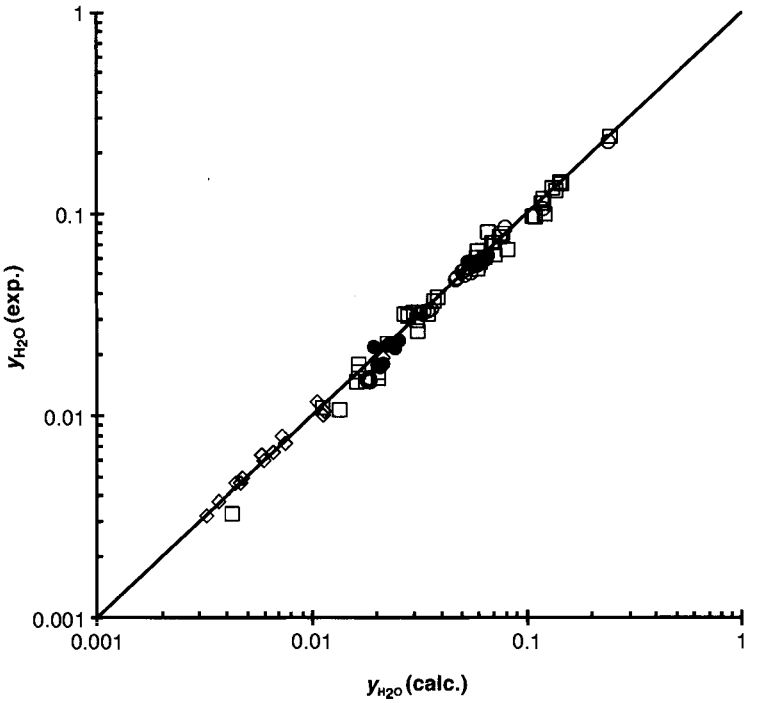

Figure 1.9 The calculated versus experimental water content of H_2S from $T = 25$ to 260°C and $p = 0.5$ to 70.4 MPa. ○, Gillespie and Wilson [8]; □, Selleck *et al.* [10]; ◊, Chapoy *et al.* [7]; •, this study.

Figure 1.9 and Figure 1.6 both show that AQUAlibrium and this model tend to overestimate our new data at $T = 50$ and 100°C. This suggests that our water contents are slightly below those reported by other authors in the high-pressure region. We note that these authors have used desiccants to trap and analyze water versus gas chromatography. Chapoy *et al.* [7] have used GC methods, but their measurements were at lower pressures (gas phase H_2S) and therefore could not be directly compared to ours.

A short note on current developments for our technique is related to measuring water contents for more complicated sour gases. Given the large peak sizes we have to deal with for some of our samples, it is very difficult to separate water from all hydrocarbons. While it is possible to separate them with increase split ratios to reduce peak sizes, it induces a much larger error in the water content results. With our current column and method, butane and water cannot be separated. To alleviate this problem, we recently

ordered a mass spectrometer (MS). By using a mass specific detector instead of a TCD, we should be able to quantify co-eluting chemicals, as long as there is no interference from other mass fragments. For complex mixtures, the MS will be the detector used after the GC. In the case of simple mixtures, it may be possible to sample straight into the mass spectrometer, without using a GC to first separate the components. This would speed-up acquisition time considerably and facilitate the publication of some much needed water content data in H_2S.

1.4 Conclusions

The current methods use by ASRL to measure water + gas, liquid or supercritical equilibria have been described. The custom high-pressure sampling system now injects the entire sample into a GC stream splitter, which resides just upstream of the GC column. This has allowed for better temperature control and access to a larger range of experimental conditions. Future directions were described, where ASRL is experimenting with dense-phase water content standards and installing a quadrupole MS detector which allows us to access more complex systems.

Initial measurements for H_2S and H_2O up to $p = 70$ MPa have been added to existing literature data and used to calibrate a thermodynamic model. The parameters for the model have been reported and the performance was evaluated for water content in H_2S and H_2S solubility in water. Water content for H_2S up to $p = 70$ MPa was estimated with an average deviation of $\delta y_{H_2O}/y_{H_2O} = 8.3\%$, whereas H_2S solubility was estimated with an average deviation of $\delta x_{H_2S}/x_{H_2S} = 3.7\%$ for $x_{H_2S} < 0.3$ and $\delta x_{H_2S}/x_{H_2S} = 5.7\%$ for $x_{H_2S} > 0.3$. Future modeling improvement may include ionic activity, which allows for the inclusion of CO_2 and salt solutions.

References

1. M.A. Clark, *Experimentally Obtained Saturated Water Content, Phase Behavior and Density of Acid Gas Mixtures*, MSc Thesis, University of Calgary (1999).
2. I.A. Alami, W.D. Monnery, and W.Y. Svrcek, *Oil & Gas Journal* 103(26), 48–54 (2005).
3. J.R. Maddocks, M. Conacher, and L. Dixon, *SOGAT Proceedings*, 235–253, May (2007).

4. R.A. Marriott, E. Fitzpatrick, F. Bernard, H.H. Wan, K.L. Lesage, P.M. Davis, and P.D. Clark, "Equilibrium Water Content Measurements For Acid Gas Mixtures," *Acid Gas Injection and Related Technologies*, 3–20 (2011).
5. VMGSim 2.8.0, Virtual Materials Inc., Calgary, AB.
6. AQUAlibrium 3.0, FlowPhase Inc., Calgary, AB.
7. A. Chapoy, A.H. Mohammadi, A. Chareton, B. Tohidi, and D. Richon, *Ind. Eng. Chem. Res.* 43, 1794–1802 (2004).
8. P.C. Gillespie and G.M. Wilson, *GPA Research Report RR-48*, Tulsa, OK (1982).
9. J.J. Carroll and A.E. Mather, *Can. J. Chem. Eng.* 67, 468–470 (1989).
10. F.T. Selleck, L.T. Carmichael, and B.H. Sage, *Ind. Eng. Chem.* 44, 2219–2226 (1952) [note that raw experimental data was used, not smoothed data].
11. E.W. Lemmon and R. Span, *J. Chem. Eng. Data* 51, 785–850 (2006).
12. R.H. Wright and O. Maass, *Can. J. Research.* 6, 94–101 (1932).
13. J.I. Lee and A.E. Mather, *Ber Bunsen-Ges. Phys. Chem.* 81, 1021–1023 (1977).
14. Eric W. Lemmon, Mark O. McLinden, and Marcia L. Huber, REFPROP 9.0, NIST, Bolder Co. (2010).
15. W. Wagner and A. Pruss, *J. Phys. Chem. Ref. Data* 31, 387–535 (2002).
16. O.M. Suleimenov and R.E. Krupp, *Geochim. Cosmochim. Acta.* 58, 2433–2444 (1994).
17. K.S. Pitzer, *J. Phys. Chem.* 77, 268–277 (1973).
18. T.J. Edwards, J. Newman, and J.M. Prausnitz, *AIChE J.* 21, 248–259 (1975).
19. E.C. Clark and D.N. Glew, *Trans. Faraday Soc.* 62, 539–547 (1966).
20. J.A. Barbero, K.G. McCurdy, and P.R. Tremaine, *Can. J. Chem.* 60, 1872–1880 (1982).
21. J.P. O'Connell, A.V. Sharygin, and R.H. Wood, *Ind. Eng. Chem. Res.* 35, 2808–2812 (1996).
22. L. Hnědkovsky, R.H. Wood, and V. Majer, *J. Chem. Thermodyn.* 28, 125–142 (1996).
23. D.-Y. Peng and D.B. Robinson, *Ind. Eng. Chem. Fund.* 15, 59–64 (1976).
24. A. Chapoy, "Thèse pour obtenir le grade de Docteur de l'École des Mines de Paris," Spécialité "Génie des Procédés," (2004).
25. P.M. Davis, P.D. Clark, E. Fitzpatrick, C.S.C. Lau, and K. Lesage, *ASRL Quarterly Bull.* XXXV, No. 2, 17–35 (1998).
26. L.W. Winkler, *Z. Phys. Chem.* 55, 344–354 (1906).
27. E.C.W. Clarke and D.N. Glew, *Can. J. Chem.* 49 (1971).
28. A.C. Harkness and B.A. Kelman, *TAPPI* 50, 13 (1967).
29. A.F. Kapustinsky and B.I. Anvaer, *Compt. Rend. Acad. Sci. URSS.* 30, 625–628 (1941).
30. A.V. Kiss, I. Lajtai, and G. Thury, *Z. Anorg. Allg. Chem.* 223, 346–352 (1937).
31. F. Pollitzer, *Z. Anorg. Chem.* 64, 121–148 (1909).
32. H. Gamsjäger, W. Rainer, and P. Schindler, *Monatsh. Chem.* 98, 1793–1802 (1967).
33. J. Kendall and J. C. Andrews, *J. Am. Chem. Soc.* 43, 1545–1560, (1921)
34. W. Gerrard, *J. Appl. Chem. Biotechnol.* 22, 623–650 (1972).
35. A.A. Doabul and J.P. Riley, *Deep-Sea Res.* 26A, 259–268 (1979).

2

Comparative Study on Gas Deviation Factor Calculating Models for CO_2 Rich Gas Reservoirs

Nan Zhang, Xiao Guo, Qiang Zhang, Rentian Yan, and Yan Ran

State Key Laboratory of Oil and Gas Reservoir Geology and Exploitation
Southwest Petroleum University
Chengdu 610500 China

Abstract

The application of traditional classical equations of state to calculate the physical property parameters of a sour gas mixture can result in significant errors. Therefore, a study is performed to investigate the common methods for calculating the deviation factor for a gas reservoir rich in CO_2. The following methods are used: Dranchuk-Purvis-Robinson (DPR), Dranchuk-Abu Kassem (DAK), Hall-Yarborough (HY), Beggs and Brill (BB), Sarem, Papay, Zhang Guodong (ZGD), and Li Xiangfang (LXF). The following correction methods are also examined: Guo Xuqiang (GXQ), Wichert-Aziz (WA), and Carr-Kobayashi-Burrows (CKB).

The gas deviation coefficient has been calculated and compared with experimental values, and then the adaptability of the calculating model for gas deviation factor of sour gas reservoirs has been evaluated. Results show that: (1) with consideration of the influence on critical pressure and temperature of the mixture caused by sour components, the correction models have a higher calculation accuracy than the uncorrected ones; (2) compared with GXQ correction method, WA and CKB correction methods will result in more errors; and (3) using the DPR model or the DAK model, combined with the GXQ correction method, to calculate sour mixture deviation factor will produce relatively accurate results, and the HY and BB models come next. However, the models of Sarem, Papay, ZGD and LXF will cause relatively great errors, which are not suitable for calculating the deviation coefficient of sour gas.

Ying (Alice) Wu, John J. Carroll and Weiyao Zhu (eds.) Sour Gas and Related Technologies, (21–36)

2.1 Introduction

In recent years, many high CO_2 (5 to 90%) natural gas reservoirs have been found. Physical parameters of natural gas include gas deviation factor (Z-factor), compressibility coefficient, volume factor, and viscosity, and all of these depend upon the amount of CO_2 in the gas. The gas deviation factor is the foundation of calculating high-pressure physical properties of natural gas and an indispensable parameter for resource calculation and dynamic prediction of natural gas reservoirs. It is true that compressibility coefficient, volume factor and viscosity are all functions of deviation factor, so their accuracies in the solution process are all dependent on the gas deviation factor.

Compared with conventional gas reservoirs, fluid phase behavior characteristics of acid gas reservoir are particular and complex. Because of low content CO_2 in conventional natural gas, the application of chart method, state equation and empirical formulas to calculate the deviation factor can meet the required precision in a certain range. However, natural gas reservoirs with rich CO_2 have been found successively in recent years. Due to differences of CO_2 and hydrocarbon gases, the increase of CO_2 content in the gas will affect computational accuracy of deviation factor. Therefore, many domestic and foreign well-known scholars have made extensive research in this field [1–6]. According to gas compositions in literatures [7, 8], different deviation factors were calculated with DPR, DAK, HY, BB, Sarem, Papay, ZGD and LXF models, as well as the GXQ, WA and CKB correction methods respectively, and then adaptability of deviation factor calculating models were evaluated through comparison between computational results and experimental results.

2.2 Deviation Factor Correlations

The gas deviation factor of compressibility factor is an important physical property for natural gas mixtures. It is defined as

$$Z = \frac{pv}{RT} \tag{2.1}$$

where:

Z is the deviation factor
p is the total pressure
R is the gas constant
T is the absolute temperature

For an ideal gas the deviation factor is exactly but for real gas mixtures the z-factor can be less than or greater than one depending upon the pressure and temperature.

The basis for the deviation factor calculations in the natural gas business is the chart of Standing and Katz, which was constructed in 1942. There have been many methods proposed over the years for calculating compressibility factors. Some of these are reviewed here.

2.2.1 Empirical Formulas

There are many empirical formula methods to calculate acid gas compressibility factor. Nowadays, more commonly used methods mainly include: DPR, DAK, HY, BB, Sarem, Papay, Li Xiangfang and Zhang Guodong methods. These methods are given in the sections that follow.

2.2.1.1 Dranchuk-Purvis-Robinsion (DPR) Model

Based on the Benedict-Webb-Rubin state equation, Dranchuk, Purvis and Robinsion [9] proposed a function of reduced pressure and reduced temperature for the deviation factor. The empirical formula has eight constants is expressed as follows:

$$Z = 1 + \left(A_1 + \frac{A_2}{T_{pr}} + \frac{A_3}{T_{pr}^3} \right) \rho_{pr} + \left(A_4 + \frac{A_5}{T_{pr}} \right) \rho_{pr}^2 + \left(\frac{A_5 A_6}{T_{pr}} \right) \rho_{pr}^5 + \frac{A_7}{T_{pr}^3} \rho_{pr}^2 \left(1 + A_8 \rho_{pr}^2 \right) EXP\left(-A_8 \rho_{pr}^2 \right) \tag{2.2}$$

$$\rho_{pr} = 0.27 p_{pr} / (Z T_{pr}) \tag{2.3}$$

where:

A_i are the various correlation coefficients
p_{pr} is the pseudo-reduced pressure
T_{pr} is the pseudo-reduced temperature
ρ_{pr} is the pseudo-reduced density

Since this equation is implicit in the deviation factor, the Newton-Raphson iteration method to solve this equation.

This method is reasonable under certain conditions as follows:

$$1.05 \le T_{pr} \le 3 \text{ and } 0.2 \le p_{pr} \le 30$$

2.2.1.2 *Dranchuk-Abu-Kassem (DAK) Model [10]*

The fundamentals of the Dranchuk, Abu Kassem empirical formula and Dranchuk-Purvis-Robinsion are basically the same. However, the DAK is slightly more complicated and has eleven parameters. The DAK equation is as follows:

$$Z = 1 + \left(A_1 + \frac{A_2}{T_{pr}} + \frac{A_3}{T_{pr}^3} + \frac{A_4}{T_{pr}^4} + \frac{A_5}{T_{pr}^5} \right) \rho_{pr} + \left(A_6 + \frac{A_7}{T_{pr}} + \frac{A_8}{T_{pr}^2} \right) \rho_{pr}^2$$
$$- A_9 \left(\frac{A_7}{T_{pr}} + \frac{A_8}{T_{pr}^2} \right) \rho_{pr}^5 + \frac{A_{10}}{T_{pr}^3} \rho_{pr}^2 \left(1 + A_{11} \rho_{pr}^2 \right) \exp\left(1 - A_{11} \rho_{pr}^2 \right) \tag{2.4}$$

where: A_i are the various correlation coefficients and are different from the previous method

Again this equation is implicit in the deviation factor and must be solved using the Newton-Raphson method.

This method is reasonably accurate for the following conditions:

$$1.0 \le T_{pr} \le 3;\ 0.2 \le p_{pr} \le 30 \text{ or } 0.7 \le T_{pr} \le 1.0;\ p_{pr} < 1.0$$

2.2.1.3 *Hall-Yarborough (HY) Model [11]*

Based on Starling-Carnahan state equation, The Hall-Yarborough equation is based on the Starling-Carnahan state equation by fitting the Standing-Katz chart. The HY model is:

$$Z = 0.06125 \left(p_{pr} / \rho_{pr} T_{pr} \right) \exp\left[-1.2 (1 - 1/T_{pr})^2 \right] \tag{2.5}$$

where: ρ_{pr} is pseudo-reduced density, which can be derived from the following formula using Newton's iteration method.

$$\frac{\rho_{pr} + \rho_{pr}^2 + \rho_{pr}^3 - \rho_{pr}^4}{(1 - \rho_{pr})^3} - (14.76 / T_{pr} - 9.76 / T_{pr}^2 + 4.58 / T_{pr}^3) \rho_{pr}^2$$
$$+ (90.7 / T_{pr} - 242.2 / T_{pr}^2 + 42.4 / T_{pr}^3) \rho_{pr}^{(2.18 + 2.82/T_{pr})}$$
$$- 0.06152 (p_{pr} / T_{pr}) \exp\left[-1.2 (1 - 1/T_{pr})^2 \right] = 0 \tag{2.6}$$

The HY method is stated to be accurate for the following conditions:

$$1.2 \le T_{pr} \le 3 \text{ and } 0.1 \le p_{pr} \le 24.0$$

2.2.1.4 *Beggs and Brill (BB) Model [12]*

This empirical formula method for calculating deviation factor made by Beggs and Brill can be expressed by the following formula:

$$Z = A + \frac{1-A}{e^B} + Cp_r^D \tag{2.7}$$

where: A, B, C and D are functions of reduced pressure and the reduced temperature.

2.2.1.5 *Sarem Model [13]*

The Sarem model is basically a Legendre polynomial fit of the deviation factor as a function of the reduced pressure and reduced temperature. The empirical formula was obtained by using least square method to fit Standing-Katz chart, which can be expressed as follows:

$$Z = \sum_{m=0}^{5} \sum_{n=0}^{5} A_{mn} p_m(x) p_n(y) \tag{2.8}$$

where:

A_{mn}—given coefficient
$p_m(x)$—pseudoreduced pressure
$p_n(y)$—pseudoreduced temperature Legeadre multinomial

This method is reasonable under certain conditions as follows:

$$1.05 \le T_{pr} \le 2.95;\ 0.1 \le p_{pr} \le 14.9 \text{ or } 0.7 \le T_{pr} \le 1.0;\ p_{pr} < 1.0.$$

2.2.1.6 *Papay Model*

$$Z = 1 - \frac{3.52 p_{pr}}{10^{0.9813 T_{pr}}} + \frac{0.274 p_{pr}^2}{10^{0.8157 T_{pr}}} \tag{2.9}$$

2.2.1.7 *Li Xiangfang (LXF) Model [14]*

Most of previous empirical formula methods mainly are applicable to calculate compressibility factor under normal pressure, and will bring about big errors under high pressure. To improve the

accuracy of calculated results under high pressure, Li derived the following formula through fitting Standing Katz chart.

$$Z = X_1 p_{pr} + X_2 \tag{2.10}$$

where X_1 and X_2 can be calculated using different specific relationships respectively when $1.05 \le T_{pr} \le 3.0; 8 \le p_{pr} \le 15.0$ and $1.5 \le T_{pr} \le 3.0; 15 \le p_{pr} \le 30.0$.

2.2.1.8 *Zhang Guodong Model [15]*

This method is also suitable for calculating deviation factor under high pressure. When $1.05 \le T_{pr} < 3.0$; $8 \le p_{pr} < 15.0$, the deviation factor is given by:

$$\begin{aligned} Z = {} & (-0.003165868T_{pr}^4 + 0.0225556934T_{pr}^3 - 0.0329265839T_{pr}^2 \\ & - 0.0736585418T_{pr} + 0.1972508148)p_{pr} + (0.1173881178T_{pr}^4 \\ & - 1.0108778348T_{pr}^3 + 2.963273024T_{pr}^2 - 3.0624663198T_{pr} \\ & + 1.1482706381) \end{aligned} \tag{2.11}$$

When $1.05 \le T_{pr} < 3.0$; $15 \le p_{pr} < 30$ it is:

$$\begin{aligned} Z = {} & (-0.021T_{pr}^4 + 0.1994107738T_{pr}^3 - 0.690946968T_{pr}^2 \\ & - 1.080656683T_{pr} + 0.6985828272)p_{pr} + (-0.3338068182T_{pr}^4 \\ & + 3.0659722222T_{pr}^3 - 10.3983901516T_{pr}^2 + 15.6767658731T_{pr} \\ & - 8.296469697) \end{aligned} \tag{2.12}$$

2.2.2 Correction Methods

As the presence of CO_2 can affect critical temperature and critical pressure of natural gas, which will cause increase of gas deviation factor and further result in errors of other calculations. Therefore, it is very necessary to correct critical parameters of CO_2 rich natural gas. At present, there are two main deviation factor correction methods for critical parameters of the acid gas as follows:

2.2.2.1 *Guo Xuqiang Method [5]*

In order to improve the accuracy of deviation factor calculated values in acid gas reservoir, Guo suggests that critical parameters should be corrected, and the relationship can be expressed by the following formulas:

$$T_c = T_m - C_{wa} \tag{2.13}$$

$$p_c = T_c \sum (x_i p_{ci}) / [T_c + x_1(1-x_1)C_{wa}] \tag{2.14}$$

$$T_m = \sum_{i=1}^{n} (x_i T_{ci}) \tag{2.15}$$

$$C_{wa} = \frac{1}{14.5038} \left| 120 \times \left| (x_1 + x_2)^{0.9} - (x_1 + x_2)^{1.6} \right| + 15(x_1^{0.5} - x_1^4) \right| \tag{2.16}$$

where: x_1 is the H_2S mole fraction in the system and x_2 is the CO_2 mole fraction in the system.

2.2.2.2 *Carr-Kobayshi-Burrows Correction Method*

This method not only considers corrections of CO_2 and H_2S, but also takes the influence of N_2 into account. The pseudoreduced critical parameters are given as:

$$T'_{pc} = T_{pc} - 44.4y_{co_2} + 72.2y_{h_2s} - 138.9y_{n_2} \tag{2.16}$$

$$p'_{pc} = p_{pc} + 3.034y_{co_2} + 4.137y_{h_2s} - 1.172y_{n_2} \tag{2.17}$$

where: y_{co_2}, y_{h_2s} and y_{n_2} are CO_2, H_2S and N_2 mole fraction in the system respectively.

2.2.2.3 *Wichert-Aziz Correction Method [16]*

In 1972, in order to make up defects of common computational methods, Wicher-Aziz introduced parameter ε mainly considering effects of some common polar molecules such as H_2S, CO_2. The relationship of Parameter ε can be expressed by the following formula:

$$\varepsilon = 15(M - M^2) + 4.167(N^{0.5} - N^2) \tag{2.18}$$

where:

M—mole fraction sum of H_2S and CO_2 in gas mixture
N—mole fraction of H_2S in gas mixture

According to Wichert-Aziz's point of view, the critical temperature and critical pressure of each component should be related with the parameter ε, and their correction relationships are as follows:

$$T'_{ci} = T_{ci} - \varepsilon \tag{2.19}$$

$$p'_{ci} = p_{ci} T'_{ci} / T_{ci} \tag{2.20}$$

where:

T_{ci}—critical temperature of component i, K
P_{ci}—critical pressure of component i, kPa
T'_{ci}—corrected critical temperature of component i, K
P'_{ci}—corrected critical pressure of component i, kPa

Meanwhile, Wicher-Aziz proposed a practical range of pressure of correction equation, which is 0-17240 kPa. In addition, it is necessary to correct temperature in the range of pressure application, whose relationship is as follows:

$$T' = T + 1.94(p / 2760 - 2.1 \times 10^{-8} p^2) \tag{2.21}$$

2.3 Model Optimization

According to gas compositions in literatures [7, 8], different deviation factors were calculated with DPR, DAK, HY, BB, Cranmer, Sarem, Papay, ZGD and LXF models, as well as the GXQ, WA and CKB correction methods respectively, and then the comparison was made between computational results and experimental results. Fluid compositions and characteristic parameters in literatures are shown in Table 2.1.

Critical temperature and critical pressure of heavy components in every composition are calculated by Lee-Kesler empirical formula [17]. For critical temperature and critical pressure of mixture in each composition, which are obtained using simple mixing rule. Finally, comparison results of deviation factor by reach method are shown in Table 2.2, Table 2.3, Table 2.4 and Table 2.5.

Absolute average error is defined as follows:

$$AAD\% = \frac{1}{N_p} \sum_j \left| \frac{Z_{cal} - Z_{\exp}}{Z_{\exp}} \right| \times 100 \tag{2.22}$$

where:

Z_{cal}—calculated value of deviation factor
$Z_{\exp}$—experimental value of deviation factor

Table 2.1 Composition of the various samples.

Component	C1	C2	C3	i-C4	n-C4	iC-C5	n-C5	n-C6	n-C7	n-C8	n-C9	n-C10	CO_2	H_2S	N_2
Sample 1	39.016	4.710	0.661	0.162	0.142	0.051	0.030	0.391	0.000	0.000	0.000	0.000	44.654	0.000	10.183
Sample 2	25.492	6.011	1.562	0.081	0.090	0.030	0.022	0.031	0.000	0.000	0.000	0.000	61.248	0.000	5.433
Sample 3	14.186	5.191	1.059	0.045	0.046	0.004	0.002	0.006	0.000	0.000	0.000	0.000	76.880	0.000	2.581
Sample 4	9.108	1.894	0.538	0.028	0.028	0.009	0.004	0.000	0.000	0.000	0.000	0.000	86.642	0.000	1.749
Sample 5	1.273	0.532	0.000	0.000	0.000	0.000	0.000	0.000	0.000	0.000	0.000	0.000	98.144	0.000	0.051
Sample 6	74.580	4.740	0.000	0.000	0.000	0.000	0.000	0.000	0.000	0.000	0.000	0.000	20.160	0.000	0.520
Sample 7	96.533	0.248	0.028	0.000	0.000	0.000	0.000	0.000	0.000	0.000	0.000	0.000	1.126	0.675	1.390
Sample 8	75.950	6.520	2.660	0.520	0.490	0.610	0.410	0.940	0.520	0.300	0.240	0.160	8.190	0.000	0.780
Sample 9	79.840	7.400	2.570	0.610	0.630	0.390	0.290	0.500	0.170	0.310	0.110	0.090	6.000	0.000	0.710

Table 2.2 Calculated deviation factors without correction.

Sample number	Pressure	Temperature	Experimental values	Calculated values							
	MPa	K		DPR	DAK	HY	BB	Sarem	Papay	ZGD	LXF
1	5	318.2	0.8572	0.8603	0.8613	0.8580	0.8679	0.5139	0.8571	0.3679	0.5033
	10	318.2	0.7602	0.7211	0.7230	0.7236	0.7393	0.5892	0.7490	0.4428	0.5775
	20	318.2	0.6959	0.6385	0.6386	0.6369	0.6293	0.7114	0.6369	0.5925	0.7259
	30	318.2	0.7829	0.7458	0.7468	0.7456	0.7563	0.7983	0.6638	0.7423	0.8743
	40	318.2	0.9035	0.8891	0.8912	0.8910	0.9035	0.8594	0.8296	0.8920	1.0227
	50	318.2	1.0347	1.0385	1.0413	1.0424	1.0492	0.9054	1.1343	1.0417	1.1712
	40	388.2	0.95	0.9424	0.9403	0.9406	0.9266	0.9140	0.9740	0.9275	1.1603
2	50	318.2	0.9855	0.9854	0.9874	0.9850	0.9987	0.8725	0.9115	0.9883	1.0863
3	40	318.2	0.8019	0.7856	0.7862	0.7800	0.7831	0.8005	0.4848	0.7961	0.8746
4	40	408.2	0.8627	0.8132	0.8127	0.8121	0.8132	0.8320	0.7760	0.8000	0.9624
5	40	388.2	0.7494	0.7568	0.7583	0.7569	0.7709	0.8040	0.6534	0.7582	0.8828
6	20.9	310.93	0.778	0.7340	0.7329	0.7302	0.7307	0.7563	0.7272	0.6717	0.8430
7	47.7	378.15	1.153	1.1545	1.1511	1.1510	1.1406	1.0585	1.2554	1.1547	1.5743
8	42.1	440.95	1.018	1.0846	1.0809	1.0801	1.0623	1.0387	1.1355	1.0794	1.4891
9	29.3	441.45	0.979	0.9947	0.9918	0.9897	0.9771	1.0110	0.9960	0.9646	1.4172

Table 2.3 Calculated deviation factor with the correction method of Wichert-Aziz.

Sample number	Pressure	Temperature	Experimental values	Calculated values							
	MPa	K		DPR	DAK	HY	BB	Sarem	Papay	ZGD	LXF
1	5	318.2	0.8572	0.9273	0.9278	0.9253	0.9338	0.4835	0.9199	0.3453	0.4877
	10	318.2	0.7602	0.8524	0.8536	0.8504	0.8599	0.5277	0.8502	0.3862	0.5283
	20	318.2	0.6959	0.7133	0.7150	0.7161	0.7314	0.6087	0.7419	0.4682	0.6095
	30	318.2	0.7829	0.6495	0.6499	0.6498	0.6574	0.6784	0.6751	0.5502	0.6906
	40	318.2	0.9035	0.6687	0.6686	0.6665	0.6603	0.7368	0.6497	0.6322	0.7718
	50	318.2	1.0347	0.7260	0.7265	0.7250	0.7296	0.7850	0.6658	0.7142	0.8529
	40	388.2	0.95	0.8332	0.8316	0.8292	0.8208	0.9166	0.8378	0.7290	0.9765
2	50	318.2	0.9855	0.7620	0.7639	0.7610	0.7761	0.8022	0.5845	0.7708	0.8733
3	40	318.2	0.8019	0.6810	0.6819	0.6766	0.6791	0.7556	0.4272	0.6975	0.7782
4	40	408.2	0.8627	0.7735	0.7777	0.7762	0.7735	0.8085	0.7472	0.7544	0.9204
5	40	388.2	0.7494	0.7576	0.7590	0.7577	0.7716	0.8044	0.6550	0.7588	0.8837
6	20.9	310.93	0.778	0.7447	0.7434	0.7407	0.7410	0.7609	0.7388	0.6802	0.8571
7	47.7	378.15	1.153	1.1564	1.1529	1.1528	1.1430	1.0603	1.2563	1.1566	1.5801
8	42.1	440.95	1.018	0.9388	0.9391	0.9418	0.9461	0.8450	0.9410	0.7518	1.1737
9	29.3	441.45	0.979	0.9625	0.9630	0.9657	0.9701	0.8692	0.9638	0.7334	1.1942

Table 2.4 Calculated deviation factor with the correction method of Carr-Kobayashi-Burrows.

Sample number	Pressure	Temperature	Experimental values	Calculated values							
	MPa	K		DPR	DAK	HY	BB	Sarem	Papay	ZGD	LXF
1	5	318.2	0.8572	0.9323	0.9329	0.9316	0.9375	0.5654	0.9262	0.4668	0.6780
	10	318.2	0.7602	0.8700	0.8709	0.8698	0.8734	0.6083	0.8681	0.5181	0.7284
	20	318.2	0.6959	0.7899	0.7898	0.7887	0.7892	0.7012	0.7990	0.6209	0.8292
	30	318.2	0.7829	0.7945	0.7927	0.7897	0.7856	0.7863	0.7928	0.7236	0.9299
	40	318.2	0.9035	0.8539	0.8521	0.8508	0.8427	0.8539	0.8495	0.8264	1.0307
	50	318.2	1.0347	0.9376	0.9368	0.9379	0.9297	0.9032	0.9690	0.9291	1.1315
	40	388.2	0.95	0.9514	0.9484	0.9460	0.9270	0.9437	0.9593	0.9097	1.2680
2	50	318.2	0.9855	0.8384	0.8392	0.8392	0.8464	0.8447	0.7921	0.8341	0.9854
3	40	318.2	0.8019	0.6798	0.6805	0.6787	0.6834	0.7600	0.6176	0.6700	0.7975
4	40	408.2	0.8627	0.8274	0.8402	0.8375	0.8274	0.8027	0.8461	0.7517	1.0039
5	40	388.2	0.7494	0.7750	0.7736	0.7708	0.7698	0.7595	0.7768	0.6866	0.8860
6	20.9	310.93	0.778	0.7655	0.7644	0.7619	0.7628	0.7415	0.7704	0.6622	0.8578
7	47.7	378.15	1.153	1.1510	1.1474	1.1471	1.1377	1.0626	1.2401	1.1510	1.5834
8	42.1	440.95	1.018	1.0687	1.0649	1.0634	1.0474	1.0455	1.0971	1.0607	1.5012
9	29.3	441.45	0.979	0.9934	0.9907	0.9889	0.9799	1.0183	0.9914	0.9606	1.4369

Table 2.5 Calculated deviation factor with the correction method of Guo Xuqiang.

Sample number	Pressure	Temperature	Experimental values	Calculated values							
	MPa	K		DPR	DAK	HY	BB	Sarem	Papay	ZGD	LXF
1	5	318.2	0.8572	0.8638	0.8649	0.8616	0.8713	0.5162	0.8602	0.3725	0.5110
	10	318.2	0.7602	0.7292	0.7310	0.7313	0.7463	0.5910	0.7545	0.4468	0.5845
	20	318.2	0.6959	0.6457	0.6457	0.6440	0.6381	0.7127	0.6454	0.5953	0.7317
	30	318.2	0.7829	0.7490	0.7499	0.7487	0.7583	0.7996	0.6729	0.7439	0.8789
	40	318.2	0.9035	0.8900	0.8920	0.8920	0.9039	0.8608	0.8368	0.8925	1.0260
	50	318.2	1.0347	1.0378	1.0405	1.0418	1.0479	0.9068	1.1372	1.0410	1.1732
	40	388.2	0.95	0.9450	0.9428	0.9430	0.9282	0.7838	0.9772	0.9296	1.1670
2	50	318.2	0.9855	0.9844	0.9865	0.9844	0.9980	0.8733	0.9173	0.9874	1.0873
3	40	318.2	0.8019	0.7855	0.7862	0.7802	0.7842	0.8011	0.4916	0.7959	0.8755
4	40	408.2	0.8627	0.8138	0.8138	0.8132	0.8138	0.8325	0.7784	0.8007	0.9642
5	40	388.2	0.7494	0.7570	0.7584	0.7571	0.7710	0.8041	0.6539	0.7583	0.8830
6	20.9	310.93	0.778	0.7391	0.7379	0.7352	0.7359	0.7575	0.7334	0.6744	0.8488
7	47.7	378.15	1.153	1.1547	1.1512	1.1512	1.1409	1.0592	1.2544	1.1549	1.5764
8	42.1	440.95	1.018	1.0854	1.0816	1.0808	1.0634	1.0406	1.1346	1.0802	1.4943
9	29.3	441.45	0.979	0.9956	0.9927	0.9907	0.9784	1.0129	0.9965	0.9656	1.4218

Table 2.6 Comparison of deviation factor calculated by different methods (ADD%).

	DPR	DAK	HY	BB	Sarem	Papay	ZGD	LXF
Without correction	2.93	2.92	2.96	2.99	8.45	9.61	10.26	20.96
WA correction	11.41	11.40	11.45	11.78	14.84	16.77	24.56	17.08
CKB correction	6.61	6.49	6.46	6.62	8.08	7.83	12.86	19.79
GXQ correction	2.73	2.71	2.76	2.77	9.33	9.23	10.10	21.18

N_p—experimental number
$AAD\%$—absolute average error

Absolute average errors obtained from comparison between calculated values and experimental values are shown in Table 2.6.

Some conclusions can be obtained from Table 2.6: For the accuracy of gas deviation factor, results obtained from correction methods are commonly more accurate and reliable than empirical formulas that are not corrected, which is mainly because the former have considered the impact of acid components of sour gas on critical pressure and critical temperature; In the three correction methods, it is clear that GXQ Correction method can more effectively enhance the precision of gas deviation factor in CO_2 rich nature gas reservoirs; Among all empirical formulas, DAK method is the most accurate in predicting the compressibility factor, with the absolute average error is 2.71%, followed by DPR, HY, and BB methods, while Sarem, Papay, ZGD and LXF methods all have larger errors and so they are not suitable for determining deviation factor in nature gas reservoirs with rich CO_2.

2.4 Conclusions

1. Calculated values of acid gas deviation factor by corrected models are commonly more accurate compared with uncorrected models.

2. GXQ correction method can more effectively enhance the precision of deviation factor compared with WA and CBA Correction methods.
3. DAK model combined with GXQ correction method is the best one to predict compressibility factor, followed by DPR, HY, and BB methods, while Sarem, Papay, ZGD and LXF methods all have larger errors and so they are not suitable for determining the acid gas deviation factor.

References

1. Wichert, E. and Aziz, K. "Calculation of Z's for Sour Gases," *Hydrocarbon Processing*, 1972, 51(5): 119–12.
2. Li, Q. and Guo, T. M. "A study on the supercompressibility and compressibility factors of natural gas mixtures," *J. Pet. Sci. & Eng*, 6, 1991, 235–247.
3. Mohsen-Nia, M., Moddaress, H., and Mansoori, G. "A Sour natural gas and liquid equation of state," *J. Pet. Sci. & Eng*, 1994, 12: 127–136.
4. Li Qun, Gu Minxin, Chen Weidong, *et al.* "Experimental Measurement and Model Prediction of the Phase Behavior of H_2S-Rich Sour Natural Gases [J]," *Journal of Chemical Engineering of Chinese Universities*, 1994, 8(3): 219–215.
5. Guo Xuqiang, Yan Wei Chen Shuang, *et al.* "Comparion of Methods for Calculating Compressibility Factor of Natural Gas at Elevated High Pressure [J]," *Journal of the University of Petroleum*, 2000, 24(6): 36–39.
6. Wang Zhouhua, Guo Ping, Li Haiping, *et al.* "Contrasting and Analyzing the Utility Arithmetic for Calculating the Z-Factor of Sour Gas [J]," *Journal of Southwest Petroleum Institute*, 2004, 26(1): 47–50.
7. Zhang Dihong, Yan Youjun, Xiang Xinhua, *et al.* "Experimental Research on the Deviation Factor of Natural Gas [J]," *Natural Gas Industry*, 2002, 22(SU): 107–109.
8. Liu Jianyi, Li Shilun, Guo Ping, *et al.* "Measurement of Gas Deviation Factor [J]," *Natural Gas Industry*, 2002, 22(2): 63–65.
9. Tarek Ahmeb. *Hydrocarbon Phase Behavior*. Gulf Publishing Company, 1989: 101-106.
10. Dranchuk, P.M. and Abou-Kassem, J.H. "Calculation of Z factors for natural gases using equation of state[J]," *JCPT*, 1975: 34–36.
11. Yarborough, L. and Hall, K.R. "How to solve equation of state for Z-factor calculations," *OGJ*, 1973: 82–91.
12. Yuan Zixue. "Optimizing Empirical Formula for Calculating Deviation Factor [J]," *Xinjiang Petroleum Geology*, 1996, 17(2): 163–167.
13. Li Xiangfang, Zhuang Xiangqi, Gang Tao, *et al.* "Comprehensive Appraisal and Selection for Gas Compressibility Factor Calculating Model [J]," *Oil Drilling & Production Technology*, 2001, 23(2): 42–46.
14. Li Xiangfang, Gang Tao, Zhuang Xiangqi, *et al.* "Analytic Model with High Precision for Calculating Compressibility Factor of High-Pressure Gas [J]," *Journal of the University of Petroleum*, 2001, 25(6): 45–51.

15. Zhang Guodong, Li Min, and Bai Dongling. "Practical Calculating Model of Gas Deviation Factor with High and Super-High Pressure [J]," *Natural Gas Industry*, 2005, 25(8): 79–80.
16. *Theory and Practice of the Testing of Gas Wells*, third edition, Energy Resources Conservation Board, 1975.
17. K.S. Pedersen and Aa. Fredenslund. *Properties of Oils and Natural Gases*. Gulf Publishing Company. Houston, 1989.

3

H_2S Viscosities and Densities at High-Temperatures and Pressures

Binod R. Giri, Robert A. Marriott*, and Pierre Blais

Alberta Sulphur Research Ltd.
University of Calgary, University Research Centre, AB, Canada
**rob.marriott@ucalgary.ca*

Abstract

New high-pressure and high-temperature viscosity and density values for pure H_2S were measured using a Cambridge oscillating piston viscometer and an Anton Paar vibrating tube densimeter, respectively. Viscosities and densities were measured for temperatures from $T = 273$ K to 423 K, and pressures up to $p = 100$ MPa covering the sub- and supercritical region. Within the low density region, our values for densities match reasonably well with the existing literature data, and within our estimated error of ±1.2 kg m^{-3}, whereas beyond supercritical density ($\rho_c = 347.28$ kg m^{-3}), the data showed a larger deviation, of about ±10 kg m^{-3}. However, the deviation of such magnitude also discussed in the reports by other groups with respect to the high density region. Our viscosity data also compared well with the existing experimental data that are limited to low pressure region. Though the performance of a recent reference viscosity model proposed by Schmidt *et al.* [1] was capable of estimating the viscosities of H_2S within an AAD of about 5% in relation to our measured data for all conditions, it generally over-predicted our data, with a deviation as large as +15%. For this study, a simple empirical model that correlates viscosity with the density is proposed. This viscosity correlation can estimate viscosities of pure H_2S within an AAD below 5% for $T = 220 - 483$ K and $p = 0.1$ to 100 MPa.

Ying (Alice) Wu, John J. Carroll and Weiyao Zhu (eds.) Sour Gas and Related Technologies, (37–48)

3.1 Introduction

There is considerable interest in obtaining reliable physical properties for injectate gaseous, supercritical and low-viscosity liquid fluids over a broad range of conditions ($273 < T/K < 423$; $0.1 < p/MPa < 100$). These conditions span a large range of process, compression and reservoir conditions, *e.g.*, gaseous fluids which are compressed and transported as liquid and supercritical injectates. Unfortunately, there are significant gaps in the available literature data for acid gas fluids, especially for the high-pressure and high-temperature regions. Fit-for-purpose models suffer from this lack of available literature data and even the available data can be either inaccurate or studied at industrially irrelevant temperatures and pressures. Extrapolations of these models to extreme conditions of pressures and temperatures may inadvertently create large uncertainties in estimated values.

While density and viscosity properties for pure CO_2 and CH_4 appear to have well been established, they were used to assess the accuracy and reproducibility of our high pressure measurements. The results of these measurements have been reported previously [2]. Hydrogen sulfide is an industrial byproduct resulting from the sweetening of the natural gas. An option for both carbon and sulfur management is the injection of acid gas/mixtures into depleted reservoirs, where the design of the acid gas injection (AGI) schemes requires accurate knowledge of the thermo-physical properties for determining the feasibility of the operation and size of equipment. Densities of hydrogen sulfide covering a broad range of experimental conditions have been reported by several research groups [3–8]. In a recent study, Ihmels and Gmehling [8] measured the density of H_2S using a computer controlled high-temperature high-pressure vibrating tube densimeter (DMA-HDT) covering a temperature range from $T = 273$ K to 623 K and a pressure up to $p = 40$ MPa. The accuracy of their density data, particularly at the higher end of their experimental conditions, was estimated to be ± 0.3 kg m^{-3}. This suggests that densities of hydrogen sulfide at sub- and supercritical regions seem to have been well established. The viscosity data for H_2S at industrially relevant conditions are still sparse, particularly at elevated pressures. A notable exception, are Monteil *et al.* [9] who have reported some H_2S viscosities at high-pressures and temperatures ($p = 10$ to 50 MPa; $T = 338$ to 413 K) in the late 1960's, after which no other studies appeared to have been carried out. It should

be noted here that the data set from Monteil *et al.* [9] was discarded by a recent reference H_2S viscosity model of Schmidt *et al.* [1] due to inconsistency of their data with the rest of the literature data set. All the other data [10–17] which were considered to be reliable and included in their reference viscosity model, are confined in the low pressure region, *i.e.*, either in the gas phase or the saturated liquid.

The reference viscosity model developed by Schmidt *et al.* [1] was found to deliver superior results to reproduce the existing experimental data for H_2S. However, due to lack of reliable experimental data at the elevated pressures, their model has not been calibrated at high-pressure conditions relevant to acid gas injections (T = 273–423 K and p = 10–50 MPa). Therefore, Schmidt *et al.* [1] identified regions where additional data for H_2S would be required to resolve the discrepancies of existing data sets. This supports the importance of additional experimental studies for the determination of viscosities and densities for H_2S and other acid gas mixtures at elevated temperatures and pressures to broaden the range of data and improve the accuracy of the reference models.

This study intends to expand the literature data to fill the void regions by providing the reliable data for density and viscosity of H_2S covering a wide range of conditions $T = 273 - 423$ K and $p = 0.6 - 100$ MPa. The results are discussed and compared with the existing literature data. As for H_2S viscosity, values at high-pressures are compared to the reference viscosity model by Schmidt *et al.* [1] In addition, we propose a viscosity correlation in order to estimate the viscosity of H_2S over a wide range of thermodynamic conditions.

3.2 Experimental

A schematic of the experimental set up has been shown in Figure 3.1. The details of the measurement principles and calibration procedure can be found elsewhere [2]. Only a brief description of the instrumentation is given here. An Anton Paar DMA HPM vibrating tube densimeter (VTD) was employed to carry out the density measurements; whereas, viscosities were measured using an oscillating piston viscometer commercialized by Cambridge Viscosity Inc.; henceforth referred to as Cambridge viscometer. The densimeter has Hastelloy C-276 wetted parts, a working temperature range of T = 263 to 473 K and a pressure limit of p = 140 MPa. The Cambridge viscometer was designed for high-viscosity fluids;

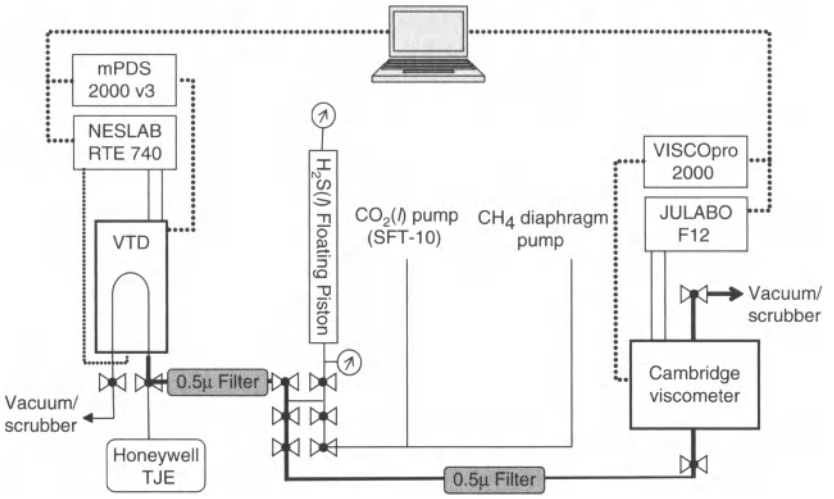

Figure 3.1 A schematic of the anton paar vibrating tube densimeter (VTD) and an oscillating cylinder cambridge viscometer system. Component details can be found in the text.

however, by using a hollow cylinder with less tolerance between the cylinder and vessel wall, it has been possible to reduce minimum measurable viscosity. The primary advantage of this viscometer is its small internal volume and broad viscosity range, *e.g.*, other pistons can be purchased to accommodate very viscous fluids. No modifications other than the installation of high pressure 0.5μ Supelco Inline Filter upstream of the both instruments were made. This small change reduced the need for frequent cleaning of the viscometer.

Before the measurements were made, calibration parameters were checked in a regular interval of time using laser grade CO_2 (PRAXAIR 99.9995%), CH_4 (PRAXAIR 99.999%) and C_5H_{12} (BDH > 99%). Pure CO_2 was charged using a liquid CO_2 pump (SFT-10, Supercritical Fluid Technology) and pure methane was delivered using an air operated diaphragm gas compressor (p_{max} = 75 MPa; Supperpressure Inc. 46-14025-1). H_2S was charged at a desired pressure up to 70 MPa through a custom built SS-316 hydraulic floating piston (*ca.* 250 cm^3). At high-pressures up to 100 MPa, fine pressure tuning was achieved by adjusting the stem position of the high-pressure autoclave valves. Ethylene glycol hydraulic fluid was delivered using a Waters High Performance Liquid Chromatography (HPLC) pump.

Pressure was measured *via* a Hastelloy Honeywell Sensotec TJE pressure transducer with a maximum calibrated pressure of $p = 140$ MPa. All valves and tubing were SS-316 ($p_{max} = 210$ MPa). As shown in Figure 3.1, extra autoclave valves were installed for fine tuning of pressure, *i.e.*, by displacement of the fluid by adjusting the valve stem position. All measurements were completed for static fluids after the delivery lines and instruments were flushed at least three times with the fluid to be measured. The temperature of the VTD unit was controlled using NESLAB RTE-740 circulating baths that controls to within ± 0.01 K from $T = 233$ to 473 K. Temperature was measured at the VTD using an internal platinum resistance thermometer, PRT, and a second PRT (100 Ω, 3 wire) inserted into the face plate between the unit inlet and outlet. This second PRT was previously calibrated using the triple point of pure water and melting point of pure indium (99.9999%) according to ITS-90 ($T_{t,H_2O} = 273.16$ K; $T_{m,\,In} = 429.7185$ K) [18]. The calibrations for both PRTs were checked by slowly melting distilled water which had been frozen inside the VTD. The inflection in density/time period upon melting was within ± 0.02 K for both PRTs. The temperature of the viscometer was controlled using a Julabo-F12 bath that has a range of $T = 253$ to 463 K and a stability of ± 0.03 K. The viscometer temperature was measured with a built-in resistant temperature detector (RTD) mounted to the base of the Inconel-718 measurement chamber.

3.3 Results and Discussion

As stated earlier, the performance of the instruments including the accuracy and reproducibility of the measurements previously have been assessed and discussed in detail [2]. Based on our earlier work with pure CO_2 and CH_4, the Cambridge Viscometer was found to be accurate within an uncertainty of 2 to 6%, where as the VTD measurements were within 1.2 kg m^{-3} for the entire range of temperatures and pressures covered in this study ($T = 273$ to 423 K and $p \leq 100$ MPa).

Figure (3.2) shows the density isotherms measured at $T = 273$, 323, 373 and 423 K and at pressures up to $p = 100$ MPa. The figure also shows the calculated values derived from the reference equation of Lemmon and Span EoS [6]. An AAD of 0.9% was observed for the density of H_2S. However, we note here that the uncertainty

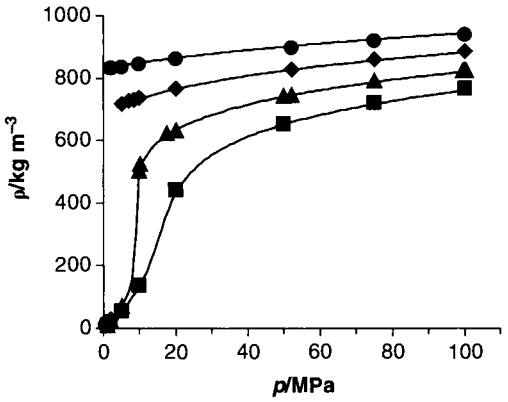

Figure 3.2 Density isotherms for hydrogen sulfide. (●), this work at $T = 273$ K; (◆), this work at $T = 323$ K; (▲), this work at $T = 373$ K; (■) this work at $T = 423$ K; (——), calculated densities from Lemmon and Span Equation of State (EoS) [6].

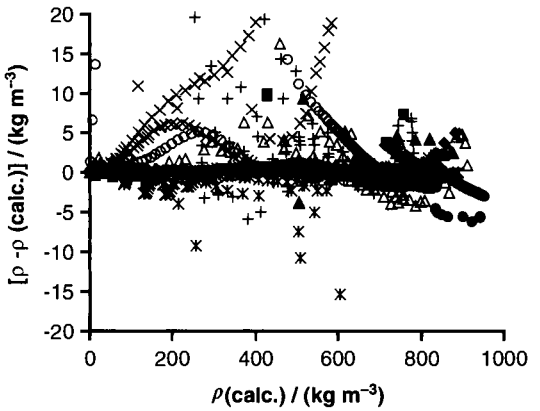

Figure 3.3 The relative difference between the experimental and calculated H_2S densities. Calculated densities are from Lemmon and Span; [6] (●), this work at $T = 273$ K; (◆), this work at $T = 323$ K; (▲), this work at $T = 373$ K; (■) this work at $T = 423$ K; (), Reamer *et al.* [3] ; (+), Lewis and Fredericks [4]; (×), Liu [5]; (*), Ihmels and Gmehling [8]; (○), Sakoda and Uematsu EoS [7].

of the values calculated from the reference equation of Lemmon and Span [6] is reported to be as large as 0.4% in the vapor phase and 1% at or above supercritical temperature. Additionally, Figure (3.3) displays the comparison of our data with some of the available literature data in terms of density difference plot. As can be seen, our data below the supercritical density ($\rho_c = 347.28$ kg m^{-3}) lie within

the expected uncertainty of 1.2 kg m^{-3}. However, the uncertainty was found to be as large as 10 kg m^{-3} at higher densities. In particular this deviation is more appartent at and beyond supercritical region (T_c = 373.05 K and p_c = 9.0 MPa). The literature data shows deviations of similar magnitude at high pressures. The densities calculated from using Sàkoda and Uematsu EoS [7] also show large deviations from the one calculated from Lemmon and Span EoS [6] at and beyond the supercritical region. As for our data, a better accuracy of the results can be achieved by a larger averaging the oscillation time periods; whereas, the current work uses the time period averaged reported by the Anton Paar instrument to calculate the density. As expected, larger deviations were observed near the critical point because of the strong pressure dependence on the densities in this region. A similar observation was made by Ihmels and Gmehling [8] during the calibration of their vibrating tube densimeter (DMA-HDT). They reported an error of about ± 2% in the region near the critical point.

Figures (3.4) shows viscosity isotherms for H_2S measured at T = 273, 323, 373 and 423 K and pressure up to p = 100 MPa. The solid lines show the results of simple empirical viscosity correlation discussed later in this section. Our data compare reasonably well to the limited data available in the literature within the quoted uncertainties. As mentioned earlier, outside of the co-existence liquid and low pressure vapor regions, there are no other reliable H_2S

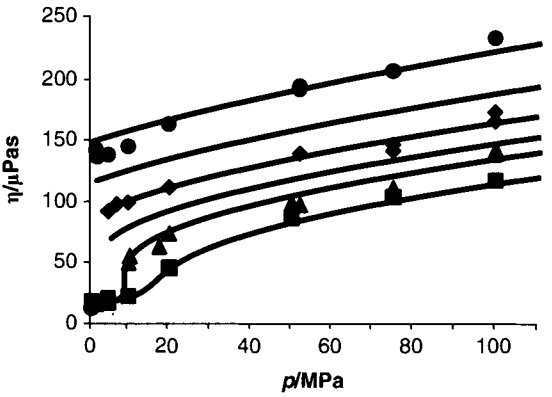

Figure 3.4 Viscosity isotherms for hydrogen sulfide. (●), this work at T = 273 K; (˙), this work at T = 323 K; (◆), this work at T = 373 K; (■) this work at T = 423 K; (——), calculated viscosities isotherms from the viscosity correlation based on equation (3.1) for T = 273, 298, 323, 348, 373 and 423 K (from top to bottom).

viscosity data to compare with. Despite of the limited experimental data, Schmidt *et al.* [1] recently developed a reference model that can predict viscosities for H_2S in a wide range of temperatures and pressures with a special focus on the industrially relevant operating conditions, *e.g.*, for acid gas injection schemes ($p = 0.1$ to 75 MPa and $T = 273$ to 423 K). The author reported that their model can deliver a reasonable performance for pressures up to $p = 10$ MPa and further indicated that an extrapolation beyond this pressure may show a deviation as large as ± 20%. Despite their report for larger deviations at higher pressures, we observed a close match between our experimental values and the predicted values from the reference viscosity model by Schmidt *et al.* [1] at all pressures within an AAD of 5.2%. However, we note here that the model of Schmidt *et al.* [1] under-predicted our experimental viscosities in general.

To provide an updated estimation of H_2S viscosity, a simple empirical viscosity model was optimized for all the experimental data available in the literature, including the entire data sets from the current work. As the viscosity of a fluid (η) is a strong function of the density (ρ) and reciprocal of temperature, we employed equation (3.1) for H_2S viscosity correlation that is explicit in ρ,

$$\left(\frac{\eta}{\mu Pas}\right) = a_0 + a_1\left(\frac{T}{K}\right)\exp\left[\left(a_2 + \frac{a_3}{(T/K)} + \frac{a_4}{(T/K)^2}\right)\bullet\left(\frac{\rho(T,p)}{kgm^{-3}}\right)\right], \tag{3.1}$$

where a_0 through a_4 ($a_0 = 5.448325$, $a_1 = 0.022148$, $a_2 = 0.002784$, $a_3 = 0.007225$, $a_5 = 72.73416$) are temperature and density independent fitting coefficients. The density, r, is calculated using of Lemmon and Span [6]. These tuned coefficients are valid for the conditions from $T = 221$ to 483 K and $p = 0.1$ to 100 MPa. The results of the model performance are shown in Figures (3.4) and (3.5). The viscosity correlation estimated the viscosities of H_2S reasonably well within the stated range of validity. The viscosity correlation agrees to all data set slightly better than that of the predicted values from the reference equation of Schmidt *et al.* [1] with an average absolute deviation below 5%. In general, our data shows larger deviation for small viscosities ($\eta < 20$ µPa s), see Figure (3.5) for the viscosity deviation plot.

The estimated error is found to increase at low viscosities as the cylinder travel time is very small at low density gas, thus increasing the variance within averaged measurements. The performance

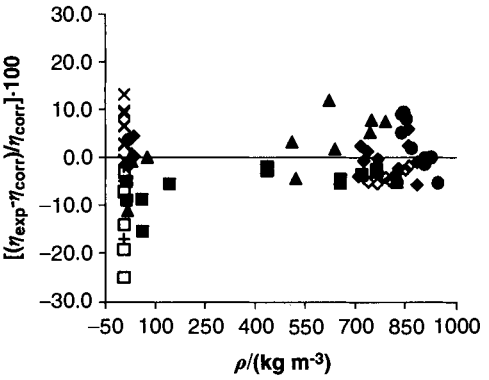

Figure 3.5 The relative deviations of the experimental viscosities from the one calculated using viscosity correlation (equation (3.1)) developed for H_2S in this work. Closed symbols: the experimental data from this work for the conditions identified in Figure (3.4); (+), from ref. (10); (◊), from ref. (11); (■), from ref. [12, 13]; (×), from ref. [13, 14].

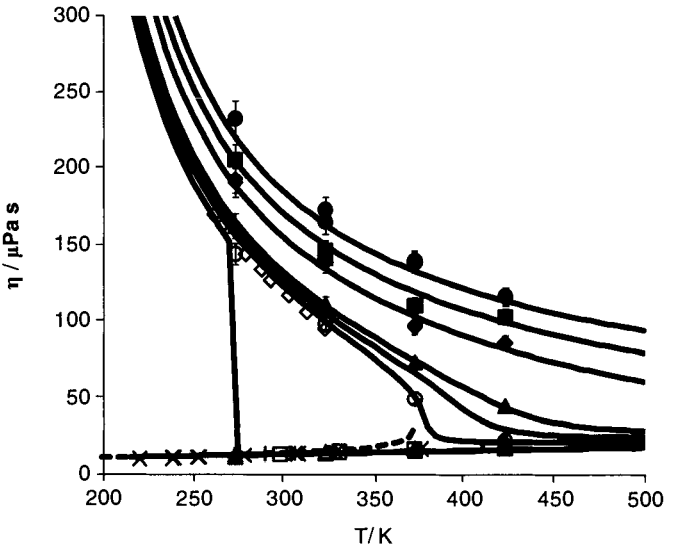

Figure 3.6 Viscosity plotted as a function of temperature for selected isobars to demonstrate the performance of the proposed viscosity correlation described in this work. (——), isobaric curves for p = 0.1, 1, 10, 15, 20, 50, 75 and 100 MPa (from bottom to top); (– – –), equilibrium phase curves; (●), this work at p = 100 MPa; (■), this work at p = 75 MPa; (◆), this work at p = 50 MPa; (▲), this work at p = 20 MPa; (○), this work at p = 10 MPa; (Δ), low pressure viscosity data from this work; (+), Rankin and Smith [10]; (◊), Hennel and Krynicki [11]; (*), Pal and Barua [12]; (□), Pal and Bhattacharya [13]; (×), Bhattacharya *et al.* [14, 15].

of the proposed viscosity correlation for H_2S is further illustrated in Figure (3.6) with few selected isobaric curves, equilibrium phase curves along with the available experimental data.

3.4 Conclusions and Outlook

The thermo-physical properties of pure H_2S, some acid gas mixtures and sour gas mixtures are of great importance for the design of high pressure acid gas injection schemes. Previous to this work, the literature data available for pure H_2S were confined to the low pressure region and there remain no studies to be found for the mixture of acid and/or sour gas mixtures at industrially relevant conditions. Recently, a reference viscosity model was developed by Schmidt *et al.* [1] using the generalized friction theory to estimate the viscosity of H_2S for a broad range of conditions. Their model was shown to accurately reproduce the available experimental viscosities for H_2S within the stated uncertainties of the respective experiments; however, the reference model could not be tested at high pressures due to aforementioned reason. With the aim to fill the void regions, we have conducted experiments to deliver reliable results on viscosities and densities for H_2S at elevated temperatures and pressures (T = 272 to 423 K and p = 0.6 to 100 MPa). Our values for density, particularly at low density region, compared very well with the available literature data. Our data showed a larger deviation ($\delta\rho = \pm$ 5 kg m^{-3}) at and beyond the supercritical region. Similar observations were made by other studies beyond the supercritical density of H_2S. As for the viscosities of H_2S, our values are in line with existing experimental viscosities and also with the estimates of Schmidt *et al.* [1] reference model as well. Though the match between our experiments and reference viscosity model of Schmidt *et al.* [1] for all pressures and temperatures is within the quoted uncertainty of both works, their values were found to overpredict our experimental results at all conditions in general. For an estimation of H_2S viscosity, a simple empirical viscosity model was developed and reported in this work which can be used to calculate viscosities for H_2S within an average absolute deviation below 5% for conditions T = 221 to 483 K and p = 0.1 to 100 MPa. For future work, we have begun to measure the thermo-physical properties for acid gas mixtures at conditions that are applicable to the design of acid gas injection schemes.

3.5 Acknowledgement

Alberta Sulphur Research Limited would like to acknowledge its member companies for their financial support.

References

1. K.A.G. Schmidt, S.E. Quinones-Cisnores, J.J. Carroll, and B. Kvamme, *Energy and Fuels*, 22, 3424–3434 (2008).
2. R.A. Marriott, E. Fitzpatrick, F. Bernard, H.H. Wan, K.L. Lesage, P.M. Davis, and P.D. Clark, "Chapter 1. Equilibrium water content measurements for acid gas mixtures," in J.J. Carroll and W. Ying, eds., *Acid gas injection and related technologies*, Wiley (2011).
3. H.H. Reamer, B.H. Sage, and W.N. Lacey, *Ind. Eng. Chem.* 42, 140-143 (1950).
4. L.C. Lewis and W.J. Fredericks, *J. Chem. Eng. Data* 13, 482-485 (1968).
5. C.H. Liu, *Experimental densities, entropies and energies for pure H2S and equimolar mixtures of H2S/CH4 and H2S/CO2 between 300 and 500 K.* M.S thesis, Texas A&M University, College Station, TX, 1985.
6. E.W. Lemmon and R. Span, *J. Chem. Eng. Data*, 51, 785-850 (2006).
7. N. Sakoda and M. Uematsu, *Int. J. Thermophys.* 25, 709 (2004).
8. E.C. Ihmels and J. Gmehling, *Ind. Eng. Chem. Res.* 40, 4470-4477 (2001).
9. J.M. Monteil, F. Lazarre, J. Salvinien, and P. Viallet, *J. Chim. Phys. Phys.-Chim. Biol.* **66**, 1673 (1969).
10. A.O. Rankine and C.J. Smith, *Philos. Mag.* 42, 615-620 (1921).
11. J.W. Hennel and K. Krynicki, *Acta Phys. Pol.* 18, 523-526 (1959).
12. A.K. Pal and A.K. Barua, *Trans. Faraday Soc.* 63, 341-346 (1967).
13. A.K. Pal and P.K. Bhattacharya, *J. Chem. Phys.* 51, 828-831 (1969).
14. P.K. Bhattacharya, A.K. Ghosh, and A.K. Barua, *J. Phys. B.*, 3, 526-535 (1970).
15. P.K. Bhattacharya, *J. Chem. Phys.* 53, 893-895 (1970).
16. B.D. Steele, D. McIntosh, and E.H. Archibald, *Z.Phys.Chem.* 55, 129-199 (1906).
17. G. Jung and H. Schmick, *Z.Phys.Chem.* 7, 130-147 (1930).
18. H. Preston-Thomas, "The International Temperature Scale of 1990 (ITS-90)," *Metrologia* 27, 3-10 (1990).

4

Solubility of Methane in Propylene Carbonate

Fang-Yuan Jou, Kurt A.G. Schmidt,[1] and Alan E. Mather*

Department of Chemical and Materials Engineering
University of Alberta, Edmonton, AB Canada
[1]Present address: Schlumberger-DBR Technology Center, Edmonton, Alberta
**To whom correspondence should be addressed.*
E-mail alan.mather@ualberta.ca

Abstract

The solubility of methane in propylene carbonate has been measured over a range of temperatures from 244 to 373 K. Pressures varied between 0.1 and 11.2 MPa. The data were correlated using the Peng-Robinson equation of state, and values of the binary interaction parameters were obtained from the experimental data. Using the expressions relating the binary interaction parameters with the parameters of the Krichevsky-Ilinskaya equation, Henry's constant for the solute was obtained. The calculated Henry's constant obtained in this study is compared with previously reported Henry's constants.

4.1 Introduction

Over the years, a number of removal techniques have been proposed to remove acid gas components (H_2S and CO_2) from gas streams. One technique is to use propylene carbonate to strip these components from the gas stream. There is a large amount of published solubility data for carbon dioxide and hydrogen sulfide in these solvents. This is, however, not the case for the solubility of the hydrocarbon components.

Ying (Alice) Wu, John J. Carroll and Weiyao Zhu (eds.) Sour Gas and Related Technologies, (49–56)

The solubility of the light hydrocarbons in propylene carbonate is important, as the dissolved hydrocarbons constitute a loss to the process, and may result in hydrocarbon emissions to the atmosphere. Despite this importance, there are only a limited number of experimental data sets dealing with the solubility of the hydrocarbons in propylene carbonate. This work is a continuation of the experimental work performed by this laboratory on the solubility of light hydrocarbons (particularly methane) in acid gas removal and gas dehydration solvents [1–9].

The physical properties of propylene carbonate allow for the acid gas removal process to operate at low temperatures which has been proposed to enhance acid gas removal design considerations and operations. Lower operation temperatures can reach 245 K while stripping temperatures are usually limited to 365 K due to solvent and acid gas solute stability issues [10]. Limited solubility data are available in the literature for hydrocarbons in propylene carbonate. In the case of methane, the only available data have been measured in the limited temperature range of 283–323 K. Recently, this laboratory has expanded the solubility data set over the temperature ranges found in acid gas removal processes using propylene carbonate [11].

There are four experimental data sets available in the open literature for the binary methane – propylene carbonate system. Rusz [12] and Shakhova and Zubchenko [13] experimentally determined the solubility of methane at elevated pressures while Lenoir *et al.* [14] and Parcher *et al.* [15] determined the Henry's constant by gas chromatography at a number of temperatures.

4.2 Results and Discussion

The apparatus and experimental technique that were used are similar to those described by Jou *et al.* [16]. The solubility of methane in propylene carbonate was measured at the temperatures of (244.26, 248.15, 255.37, 266.48, 273.15, 298.15, 333.15 and 373.15) K and at pressures up to 11.2 MPa. The experimental data are shown in Figure 4.1.

The equilibrium data were correlated in the manner described by Jou *et al.* [9]. The method requires that an equation of state valid for the solvent and dilute solutions of the solute in the solvent be

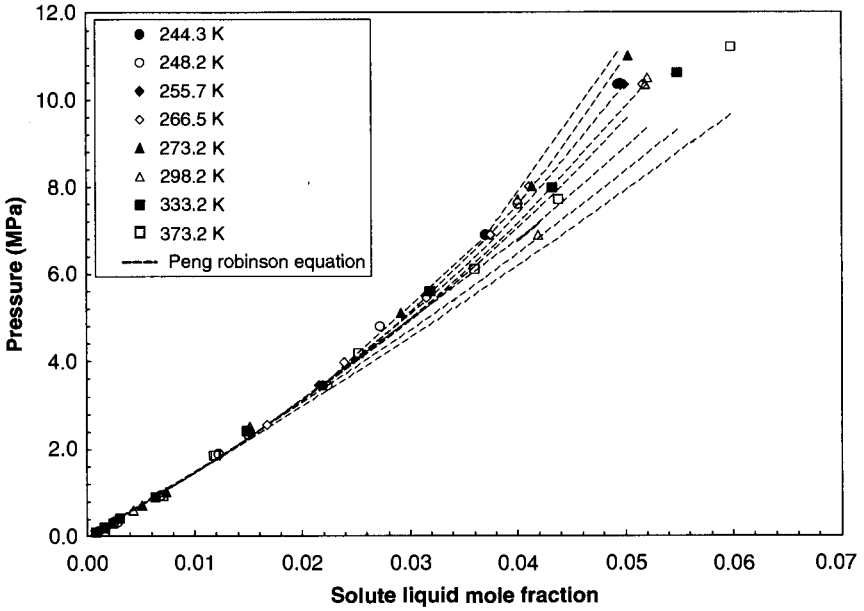

Figure 4.1 Experimental data for the Propylene Carbonate (1) + Methane (2) system compared with correlated values using the Peng-Robinson equation of state.

available. The Peng–Robinson [17] equation of state was used in the calculations. The parameters a_{22} and b_2 of methane were obtained from the critical constants presented in Rowley *et al.* [18].

The parameters a_{11} and b_1 for propylene carbonate were obtained over the complete temperature range with the vapor pressure and liquid density equations and their associated parameters which were obtained from the compilation of Rowley *et al.* [18]. The isothermal flash routine algorithm presented by Whitson and Brulé [19] was used to calculate the solubility of methane at each temperature and pressure of interest. The binary interaction parameter, k_{12}, which appears in the mixing rule of the equation of state:

$$a_{12} = (a_{11}a_{22})^{1/2}(1-k_{12}) \tag{4.1}$$

was iteratively modified until the deviations between the calculated liquid mole fraction and the experimental value were less than the set tolerance.

Values of k_{12} were found to have a slight dependence on temperature and the model reproduces the experimental data quite well. The other two experimental data sets, Rusz [12] and Shakhova and Zubchenko [13], are plotted in Figure 4.2 with the results calculated from the Peng-Robinson equation of state and the binary interaction parameter obtained in this investigation. As can be seen, the results obtained in this investigation match the data of Shakhova and Zubchenko [13] quite well with some deviations at higher pressures. The data of Rusz [12] are inconsistent with both the data obtained in this investigation and those of Shakhova and Zubchenko [13]. According to Clever and Young [20] there was not an exact procedure for calculating the solubility of this data set. The obtained binary interaction parameter calculates the solubility of methane in propylene carbonate determined by Shakhova and Zubchenko [13] to within a similar deviation as the new data set.

Bender *et al.* [21] have shown the connection between the Peng-Robinson equation of state, the binary interaction parameter and the three parameters in the Krichevsky-Ilinskaya equation. This

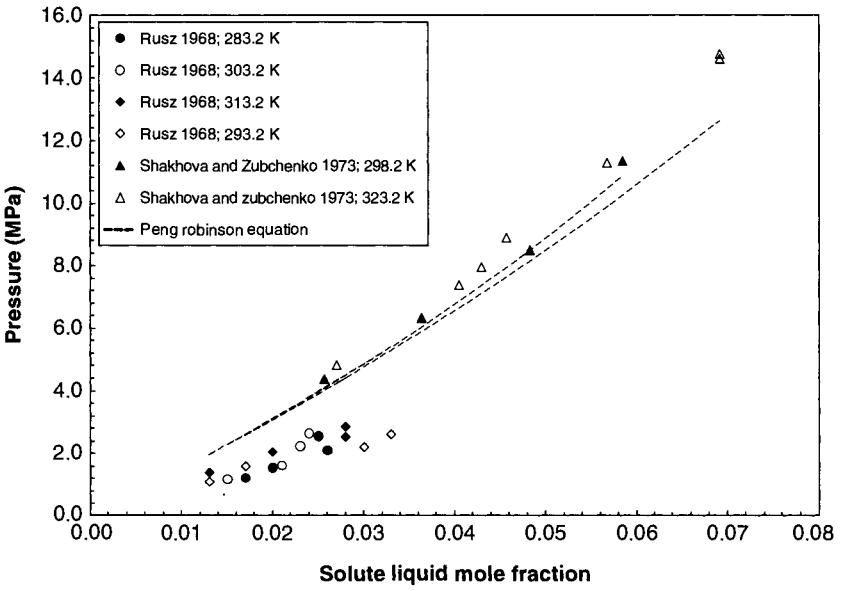

Figure 4.2 Experimental data for the Propylene Carbonate (1) + Methane (2) system of Rusz [12] and Shakhova and Zubchenko [13] compared with correlated values using the Peng-Robinson equation of state.

equation is discussed in the book by Prausnitz *et al.* [22] and is given by:

$$\ln\left(\hat{f}_2 / x_2\right) = \ln H_{21} + \frac{\overline{v}_2^{\infty}(P - P_1^s)}{RT} + \frac{A}{RT}(x_1^2 - 1) \qquad (4.2)$$

The three parameters are the Henry's constant, H_{21}, the partial molar volume at infinite dilution, and the Margules parameter, A. Schmidt [23] has corrected the equations which relate these parameters to the binary interaction parameter in the Peng-Robinson equation of state. The obtained Henry's constant for methane in propylene carbonate is plotted in Figure 4.3 for comparison with those obtained by Lenoir *et al.* [14] and Parcher *et al.* [15]. The calculated Henry's constants are closer to those obtained by Parcher *et al.* [15] than to those obtained by Lenoir *et al.* [14].

The Henry's constant for methane has a maximum, indicating that the solubility of methane has a minimum at around 333 K. At lower pressures (P < 7 MPa) the solubility of methane in propylene

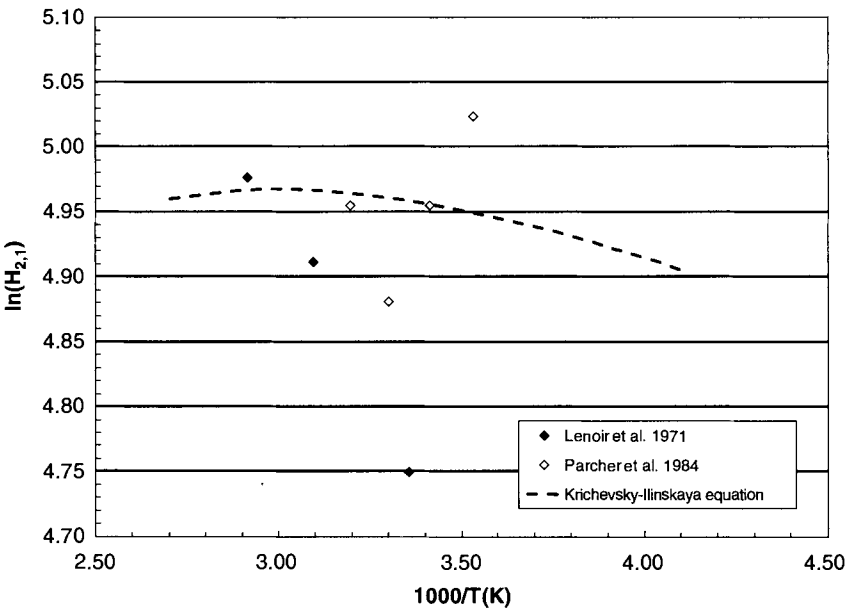

Figure 4.3 Temperature dependence of the Henry's constants for Methane (2) in Propylene Carbonate (1).

carbonate can almost be considered independent of temperature. The effect of temperature increases at higher pressures.

4.3 Nomenclature

a	parameter in the Peng-Robinson equation, $Pa \cdot m^6/mol^2$
A	Margules parameter, J/mol
b	parameter in the Peng-Robinson equation, cm^3/mol
$\hat{f}_i$	fugacity of component i in a mixture, MPa
H_{21}	Henry's constant of solute 2 in solvent 1 at P_1^s, MPa
k_{12}	binary interaction parameter in the Peng-Robinson equation
P_i^s	pressure of component i, MPa
P	pressure, MPa
R	gas constant, J/mol·K
T	absolute temperature, K
$\overline{v}_2^{\infty}$	partial molar volume at infinite dilution, cm^3/mol
x_i	mole fraction of component i in the liquid phase
y_i	mole fraction of component i in the vapor phase

4.4 Acknowledgement

The authors are grateful to the Natural Sciences and Engineering Research Council of Canada for financial support of this research.

References

1. Jou, F.-Y; Carroll, J.J.; Mather, A.E.; and Otto, F.D. "Solubility of Methane and Ethane in Aqueous Solutions of Methyldiethanolamine," *J. Chem. Eng. Data* 1998, *43*, 781–784.
2. Carroll, J.J.; Jou, F.-Y; Mather, A.E.; and Otto, F.D. "The Solubility of Methane in Aqueous Solutions of Monoethanolamine, Diethanolamine and Triethanolamine," *Can. J. Chem. Eng.* 1998, *76*, 945–951.
3. Jou, F.-Y; and Mather, A.E. "Solubility of Methane in Methyldiethanolamine," *J. Chem. Eng. Data* 2006, *51*, 1429–1430.
4. Schmidt, K.A.G.; Jou, F.-Y; and Mather, A.E. "Solubility of Methane in an Aqueous Methyldiethanolamine Solution (Mass Fraction 50%)," *J. Chem. Eng. Data* 2008, *53*, 1725–1727.

5. Jou, F.-Y; Carroll, J.J.; Otto, F.D.; and Mather, A.E. "Solubility of Methane in Aqueous Solutions of 2-(2-Aminoethoxy)ethanol," *Ind. Eng. Chem. Res.* 1998, *37*, 3519–3523.
6. Henni, A.; and Mather, A.E. "The Solubility of Methane in Triethylene Glycol Monomethyl Ether," *Fluid Phase Equil.* 1995, *108*, 213–218.
7. Jou, F.-Y; Otto, F.D.; and Mather, A.E. "Solubility of Methane in Glycols at Elevated Pressures," *Can. J. Chem. Eng.* 1994, *72*, 130–133.
8. Jou, F.-Y.; Deshmukh, R.D.; Otto, F.D.; and Mather, A.E. "Solubility of H_2S, CO_2, CH_4 and C_2H_6 in Sulfolane at Elevated Pressures," *Fluid Phase Equil.* 1990, *56*, 313–324.
9. Jou, F.-Y.; Deshmukh, R.D.; Otto, F.D.; and Mather, A.E. "Solubility of H_2S, CO_2 and CH_4 in n-Formyl Morpholine," *J.Chem. Soc.- Faraday Trans. I* 1989, *85*, 2675–2682.
10. Mak, J.; Nielsen, D.; and Schulte, D. "An Update of the Fluor™ Solvent Process," *Proceedings of the Laurance Reid Gas Conditioning Conference*, Norman, OK, February 25–28, (2007).
11. Schmidt, K.A.G.; Jou, F.-Y; and Mather, A.E. "Solubility of Methane in Propylene Carbonate," in preparation for *J. Chem. Eng. Data* 2010.
12. Rusz, L. "Gas Absorption Studies XX. The Decarbonatization of the Synthesis Gas with Propylene Carbonate on High Pressures," *Veszp. Veg. Egy. Kőz.* 1968, *11*, 169–180.
13. Shakhova, S.F.; and Zubchenko, Yu.P. "Solubility of Methane and Argon in Organic Solvents," *Khim. Prom.* 1973, *49 (8)*, 595–596.
14. Lenoir, J.-Y.; Renault, P.; and Renon, H. "Gas Chromatographic Determination of Henry's Constants of 12 Gases in 19 Solvents," *J. Chem. Eng. Data* 1971, *16*, 340–342.
15. Parcher, J.F.; Bell, M.L.; and Lin, P.J. "Determination of the Solubility of Gases in Liquids by Gas-Liquid Chromatography," in J.G. Giddings, ed., *Advances in Chromatography*, 1984, *24*, 227–246.
16. Jou, F.-Y.; Carroll, J.J.; Mather, A.E.; and Otto, F.D. "The Solubility of Nitrous Oxide in Water at High Temperatures and Pressures." *Zeit. f. phys. Chem.*, 1992, *177*, 225–239.
17. Peng, D.-Y.; and Robinson, D.B. "A New Two-Constant Equation of State." *Ind. Eng. Chem. Fundam.* 1976, *15*, 59–64.
18. Rowley, R.L.; Wilding, W.V.; Oscarson, J.L.; Yang, Y.; Zundel, N.A.; Daubert, T.E.; and Danner, R.P. *DIPPR Data Compilation of Pure Component Properties*, Design Inst. Phys. Prop., AIChE, NY (2003).
19. Whitson, C.H.; and Brulé, M.R., "Phase Behavior," *SPE Monograph Series* 20, Soc. Petroleum Eng., Richardson, TX (2000).
20. Clever, H.L.; and Young, C.L.; eds. *IUPAC Solubility Data Series*, Volume 27/28, Methane, Pergamon Press, New York, NY (1987).
21. Bender, E.; Klein, U.; Schmitt, W.Ph.; and Prausnitz, J.M. "Thermodynamics of Gas Solubility: Relation Between Equation-of-State and Activity-Coefficient Models," *Fluid Phase Equil.* 1984, *15*, 241–255.
22. Prausnitz, J.M.; Lichtenthaler, R.N.; and de Azevedo, E.G. *Molecular Thermodynamics of Fluid-Phase Equilibria*, 3rd ed., Prentice-Hall, Englewood Cliffs, NJ, U.S.A. (1999).
23. Schmidt, K.A.G. "Letter to the Editor," *Fluid Phase Equil.* 2005, *236*, 268–269.

PART 2
PROCESS

Ying (Alice) Wu, John J. Carroll and Weiyao Zhu (eds.) Sour Gas and Related Technologies, (3–20) © 2012 Scrivener Publishing LLC

5

A Holistic Look at Gas Treating Simulation

Nathan A. Hatcher[1], R. Scott Alvis[2], and Ralph H. Weiland[3]

[1]*Optimized Gas Treating, Inc., Buda, TX, USA*
nate.hatcher@ogtrt.com
[2]*Optimized Gas Treating, Inc., Houston, TX, USA*
scott.alvis@ogtrt.com
[3]*Optimized Gas Treating, Inc., Clarita, OK, USA*
ralph.weiland@ogtrt.com

Abstract

Next to native intelligence and critical thinking, perhaps the most powerful tool an engineer can bring to bear on a gas treating problem is a reliable, proven, fundamentals-based process simulator. Troubleshooting gas treating plants can be challenging. Failure to treat products to specification can be triggered by multiple layers of problems. Besides the equipment disappearing due to corrosion, there are also problems with fouling, plugging, carryover, and foaming. In addition, amine units have chemical reactions that need to be well understood before some difficulties yield to analysis. Indeed, the tough-to-solve problems in gas treating are often rooted in either process chemistry or surface chemistry.

This paper deals first with a real process operations troubleshooting case study, in which the root causes of malperformance were really quite simple, but evaded detection for quite some time. The second focal point is an understanding of how MEA and piperazine-promoted MDEA perform in CO_2 removal in an NGL plant, an ammonia plant, and a CO_2 capture facility. To uncover the fundamental behaviors in these cases, the treating unit had to be analyzed from a holistic perspective, considering *all* of the equipment in the plant and all of the factors influencing tower performance, as well as the condition of the solvent. When interpreted from this vantage, the important factors become glaringly obvious. In particular, it is shown how utilizing a model that can account for the

Ying (Alice) Wu, John J. Carroll and Weiyao Zhu (eds.) Sour Gas and Related Technologies, (59–78)

real chemistry of contamination (dirty solvents) and actual mass transfer hardware removes significant guesswork from both troubleshooting and unit design.

The interpretation of column temperature and composition profiles is shown to be an effective tool in analyzing gas treating plants. Accounting for the real column internals as they actually exist in the plant eliminates an opaque shroud of uncertainty simply because "guessing" overall tray efficiencies, Murphree vapour efficiencies, numbers of ideal stages, residence times per theoretical stage, and stage thermal efficiencies do not form part of a genuinely mass-transfer rate based simulation model. Several aspects will be explored that are quite revealing. Learning whether a treating plant is lean-end pinched, rich-pinched, or bulge-pinched can often point the way to solutions to problems, in addition to providing a significantly improved understanding of performance.

5.1 Introduction

Developing a good understanding of the behaviour and performance of any gas treating plant depends on being able to look at the plant in its entirety as opposed to focusing too soon on some specific detail or set of details. This is especially the case in troubleshooting, but it applies equally well even to grass roots plant design. The foundational footing for this discussion is the kind of *mass transfer rate* simulation that creates a virtual plant on a computer. This virtual plant is a digital image of the real plant on a scale and to a level of detail that permits performance and behaviour to be examined as under a microscope. As will be seen, what such a model is capable of revealing can be quite intricate and detailed, and very satisfying from an engineering science perspective. Perhaps of more pragmatic importance, it can lead inexorably to the solution of a difficult troubleshooting exercise, on the one hand, or to the selection of correct operating conditions for a new plant on the other. The discussion centres around two case studies. The first is a refinery fuel gas unit in which the heat stable salt (HSS) levels revealed by solvent analysis had a profound effect on the H_2S content of the treated fuel gas. Here, chemistry played a key role. The second set of cases was concerned with CO_2 removal in an LNG plant, an ammonia plant, and a CO_2 capture plant, all inextricably linked by the commonality of a fairly reactive solvent, namely, piperazine-promoted MDEA or generic MEA.

5.2 Clean Versus Dirty Solvents: Heat Stable Salts

A refinery MDEA fuel gas treater was experiencing a steady decline in treating performance. Prior to February 2005, the amine contactor was consistently treating H_2S down to levels of 1–3 ppmv in the vent gas. From February to May of 2005, the H_2S gradually increased to around 17 ppmv in the treated gas. After ruling out foaming and lean/rich exchanger leaks as potential causes, the plant contacted their corporate Treating/Sulfur Processing Network for troubleshooting and simulation assistance.

Table 5.1 presents a summary of the absorber feeds and operational data. To facilitate the troubleshooting effort, a feed gas sample was analyzed by gas chromatography. Lean and rich amine samples were taken concurrently for strength and loading analysis. Table 5.2 provides further analytical breakdown of the lean amine solution over time from ion chromatography analysis. In looking at just the data in Tables 5.1 and 5.2, a number of explanations could be formulated to explain the deterioration in performance, among them:

1. The Absorber was overloaded and rich-amine-loading pinched,
2. Lean amine feed temperature increased as ambient temperature climbed from February to May,
3. Regenerator performance declined as indicated by the lean loading increase. This could have been caused by a host of potential causes, among them: tray damage, exchanger fouling, lower reboiler heat input, or decreased heat stable salts.

The picture was further complicated by the results of initial material balance screening calculations around the absorber which showed a nominal 30% inconsistency between the measured rich amine loading and the rich amine loading that would result from a material balance using the inlet gas composition and the metered feed gas and rich amine flows. Consequently, two sets of simulations were developed for the system based upon the assumptions that either flow and GC data, or lean and rich amine lab loadings, were

Table 5.1 Absorber feed and treating performance summary.

Parameter	May 2005 operations		February 2005 operations	
	Absorber feed gas	**Absorber treated gas**	**Absorber feed gas**	**Absorber treated gas**
Temperature (°F)	100.5	115.3	99–100	108–110
Pressure (psig)	174.3	172.4	176	178
Flowrate (MMscfd)	54.5	Not Available	53.5–55.5	Not Available
Composition (Dry Mole %)	**Lab GC**	**Online GC**	**Lab GC**	**Online GC**
H_2S	17.04	17 ppmv		1–3 ppmv
CO_2	1.21	0.104		0.11–0.12
H_2	11.04	17.7		20.4–20.8
N_2	3.65	3.25		2.5–2.7
CH_4	39.28	49.3	Not Available	46.5–46.9
C_2H_4	3.43	4.1		4.8–5.0
C_2H_6	15.02	17.0		16.8–17.0
C_3H_6	1.98	2.37		2.8–2.9
C_3H_8	3.18	3.94		2.8–3.0
C_4+	2.47	2.18		2.4–2.5
Lean Amine				
Flowrate (gpm)	847–853		766–772	
Lean Loading (mole/mole)				
H_2S	0.0046		0.0007–0.0010	
CO_2	0.0009		Not Available	
Total	0.0055		Not Available	
Temperature (°F)	115		108.6–110.0	

correct. Table 5.3 presents further operating data around the absorber and principle regenerator on the circuit under these two assumptions outlined above together with a number of simulation results.

Figure 5.1 provides an overview of the amine system together with some data pertinent to the May, 2005 operation (see Table 5.3). It was fortuitous that this particular unit was well instrumented. A number of the absorber trays had thermocouples located in the liquid flow path to establish an internal temperature profile (see Table 5.3). The rich amine temperature was also known allowing the absorber energy balance to be used to reconcile the plant data.

Table 5.2 Lean amine analyses by ion chromatography.

Date of sample	11/10/04	12/8/04	1/12/05	2/9/05	3/9/05	4/13/05
Component						
Free amine (wt%)	40.7	42.5	37.5	40	44.1	42.3
Bound amine (wt%)	2	1.8	1.4	1.1	1.3	0.9
Total amine (wt%)	42.70	44.30	38.90	41.10	45.40	43.20
Ions, ppmw						
Sodium (Na^+)	1,573	1,044	1,336	1,401	1,461	1,212
Formate ($HCOO^-$)	7,768	7,935	7,263	6,406	6,159	4,864
Acetate (CH_3COO^-)	885	672	605	591	370	463
Chloride (Cl^-)	46	87	72	54	57	42
Sulfate ($SO_4^=$)	0	0	0	0	0	0
Thiosulfate ($S_2O_3^=$)	38	27	60	0	43	198
Thiocyanate (SCN^-)	4,184	1,844	755	638	665	378
Total Anions	12,921	10,566	8,754	7,689	7,293	5,945
Cation Equiv. (meq/g)	0.2365	0.1966	0.1757	0.1533	0.1728	0.1283
Anion Equiv. (meq/g)	0.2617	0.2225	0.1878	0.1649	0.1570	0.1272
DEA (% of total amine)	0.9	1.3	1.2	1.2	0.9	1.2

The amine loading change across the regenerator could also be found from the rich amine flow to the regenerator and metered acid gas rate.

Simulations (Table 5.3) of May operations were run for two sets of conditions using a number of tools to evaluate the operating data. For the sake of brevity, only the results from the ProTreat® simulator are shown. ProTreat is the name of a commercial mass and heat transfer rate based amine simulator capable of accounting for the effect of specific HSSs and other ions on treating. It uses rigorous mass-transfer-rate calculations to evaluate absorber and regenerator performance on an actual tray basis.

It was immediately clear from running ProTreat that the metered gas flow rate was in error. Referring to Table 5.3, the metered feed gas flow led to an unrealistic temperature profile as well as CO_2 and H_2S slip. It was also found as noted in Table 5.3 that the Regenerator

®ProTreat is a registered trade name of Optimized Gas Treating, Inc.

Table 5.3 Simulation comparison to may 2005 plant data.

Parameter	Simulations per GC and metered gas feed		Simulations per lab H_2S loads and material-balanced gas feeds	
	May/05 Data	Protreat®	Protreat	ProTreat w/o HSS & Na
Absorber tray No.	Tray temperatures (°F)		Tray temperatures (°F)	
30 (Top)	115.3	119.1	115.2	115.2
25	115.4	153.2	115.5	115.5
20	116.5	175.2	115.9	116.0
11	117.2	177.2	116.9	116.9
7	121.2	177.2	118.5	118.4
3	142.7	174.0	138.6	138.3
1 (Bottom)	144.9	159.3	147.6	147.6
H_2S leak (ppmv)	17	5,610	15	23
CO_2 slip (%)	6.9–7.6* /33.0	69.6	32.6	32.3
Lean mole loading	Lab			
H_2S	0.0046	0.0022	0.0023	0.0079
CO_2	0.0009	0.0003	0.0005	0.0010
Total	0.0055	0.0025	0.0028	0.0089
Rich mole loading	Lab			
H_2S	0.446	0.638	0.446	0.453
CO_2	0.022	0.015	0.022	0.022
Total	0.468	0.653	0.468	0.475
Total per Reg MB¶	0.46–0.47			

*per GC analysis; CO_2 slip is 33% per loading measurements.

¶Indicates total loading obtained via a material balance around the regenerator.

acid gas balance was in agreement with a lower Absorber feed flowrate. The evidence was fairly convincing that the feed gas flow meter was reading some 30% high. However, we still have not explained why the treating performance deteriorated.

To answer this question, a sensitivity analysis was conducted using ProTreat. The following variables were changed in cumulative succession from the May, 2005 calibration model to conditions

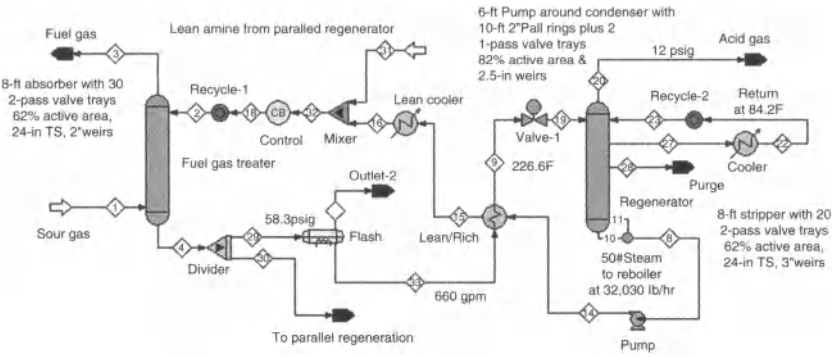

Figure 5.1 PFD of fuel gas circuit.

corresponding to February, 2005 operations, and the results are presented in Table 5.4:

1. Lean amine temperature and to a lesser extent, feed gas temperature were dropped,
2. Amine strength was raised,
3. Regenerator reboiler steam was increased nominally by 10%,
4. Heat stable salt and sodium ion concentrations were increased.

The results suggested that the lean amine temperature increase from February to May played at most a very slight role in hindering treating performance. The higher amine strength in February would have worked marginally in the wrong direction, increasing both the lean loading and the H_2S leak from the absorber; whereas, both were actually lower in February than in May. This suggested that the contactor's treating performance was not limited by a rich end loading pinch. However, in practice the rich loading must be limited to minimize corrosion in the carbon steel equipment. The reboiler steam rate was higher in February than in May, and ProTreat predicted that this would have quite a positive effect on the H_2S leak and the lean loading of H_2S. However, even the increased reboiler duty was insufficient to reduce the H_2S leak to match the measured February performance. Furthermore, tower hydraulic rating indicated that the regenerator already operated close to jet flood in both February and May (~80% at 0.65 system factor), which constrains the increased steam flow that could be used to reduce emissions.

Table 5.4 H_2S Treat sensitivity analysis—proTreat® predictions.

Case	Base may, 2005 operation	Lower temp	Higher amine strength	Higher reboiler steam	Higher HSS	Other sim w/o HSS & Na
Feed Gas Temp (°F)	100.5	100	100	100	100	100
Lean Amine Temp (°F)	115	109.3	109.3	109.3	109.3	109.3
Reboiler Steam (lb/gal)	0.8	0.8	0.8	0.89	0.89	0.89
Total MDEA (wt%)	43.2	43.2	44.2	44.2	44.2	44.8
HSS & Na^+ Ions as per	May, 05*	May, 05*	May, 05§	May, 05§	Feb, 05¶	N/A Clean
Calc Lean H_2S Loading	0.0023	0.0023	0.0023	0.0014	0.0006	0.0005
Absorber Performance						
H_2S (ppmv)	15	13	14	8.3	4.6	21
CO_2 slip (%)	32.6	31.0	31.3	31.3	8.0	40.6

*May, 2005 analysis; § May, 2005 analysis increased proportional to strength; ¶ Feb, 2005 analysis.

However, when the HSSs and sodium contaminants per the detailed solution analysis were included in the solvent description, Table 5.4 shows that *ProTreat predicted very nearly the exact performance observed in February.* The observed H_2S leak was 1–3 ppmv versus a predicted leak of 4.6 ppmv; predicted 31.5% CO_2 slip versus 33% measured; predicted 0.0006 H_2S lean mole load versus 0.0007–0.001 observed lean load. The high HSS level in February, combined with a higher reboiler steam flow, allowed the plant to produce 3 ppmv H_2S gas. *The drop in HSS level hurt plant performance!* Another simulation tool (without HSS and Na chemistry capabilities) missed both the reboiler steam benefit and the HSS effect. It also predicted a CO_2 slip significantly greater than observed.

Lessons Learned

1. A simulation can only be as accurate as the data on which it is built. In this particular case study, the simulation itself (through the temperature profile), provided a measure of verification.
2. Complete solution ion chemistry must be taken into account for accurate modeling of treating down to low H_2S levels at low lean loadings. If the solvent contains contaminants, the simulation *must* account for *the actual contaminants.*
3. It is insufficient just to have an accurate absorber model. Rigorous mass transfer rate simulation for the regenerator is absolutely critical to predict plant performance accurately. Thus, a holistic approach is necessary.

5.2.1 CO_2 Removal Using MEA, and MDEA Promoted With Piperazine

MDEA does not react with CO_2, so as the sole amine constituent of a solvent, it has very limited ability to remove CO_2. At best, MDEA might be said to catalyse CO_2 hydrolysis by providing a more alkaline environment than water, i.e., a higher hydroxyl ion concentration to hydrolyse CO_2, but real lack of reactivity makes it incapable of removing CO_2 quickly. For this reason it simply cannot reduce CO_2 to low concentrations. This makes it an excellent choice for *slipping* CO_2 but a bad choice even for moderately deep CO_2 removal. Piperazine,

on the other hand, reacts extremely rapidly with CO_2 (some 10 times faster than MEA) which makes it an excellent promoter when used in relatively small concentrations with MDEA. Thus, piperazine promoted MDEA is a very commonly used solvent in LNG, and syngas (hydrogen and ammonia plant) applications. It is offered by all the major solvent vendors under a variety of trade or brand names.

5.2.2 Piperazine-promoted MDEA in an Ammonia Plant

It has already been established[1,2] that there is a boundary limiting the stable operating region in the sense that there is an operational cliff when using piperazine-MDEA blends too close to this boundary. For example, in the ammonia-plant two-stage syngas absorber shown in Figure 5.2, operating the unit at higher and higher *semi*-lean temperatures leads to the performance curve shown in Figure 5.3.

As long as the semi-lean temperature is kept below about 78°C, the treated gas will more than meet a 500 ppmv CO_2 treating specification, and by a wide margin. But it is not possible to operate this unit with a semi-lean feed much above 78°C stably because the Lean Absorber goes immediately from being lean-end to rich-end pinched. This can be seen in the two temperature profiles shown in Figure 5.4 where the semi-lean temperatures are separated by only 0.25°C. When the semi-lean temperature is slightly too high, the bulk absorber cannot adequately handle the CO_2 load and the excess CO_2 spills over into the Lean absorber, immediately overwhelming it into a rich-end pinch condition and sending the CO_2 in the final treated gas from 10 ppmv to some 700 ppmv. Operation with a semi-lean temperature of 78°C is completely unstable in the sense that even the slightest variation of inlet CO_2 content, solvent rate, gas rate, or temperature in the wrong direction would cause the outlet gas to go completely off specification.

As shown in References 1 and 2, this can also occur in LNG applications using piperazine promoted MDEA where a slight reduction in solvent flow too close to the stable operating limit can send the treated gas from a few ppmv CO_2 to well over 1,000 ppmv. This

[1] Weiland, R.H. and Hatcher, N.A., Foundations of Failure, Hydrocarbon Engineering, December (2011).
[2] Weiland, R.H. and Hatcher, N.A., Stable Operating Limits in Amine Treating Units, Proceedings of the Lawrence Reid Gas Conditioning Conference, Norman, Oklahoma, February, 2011.

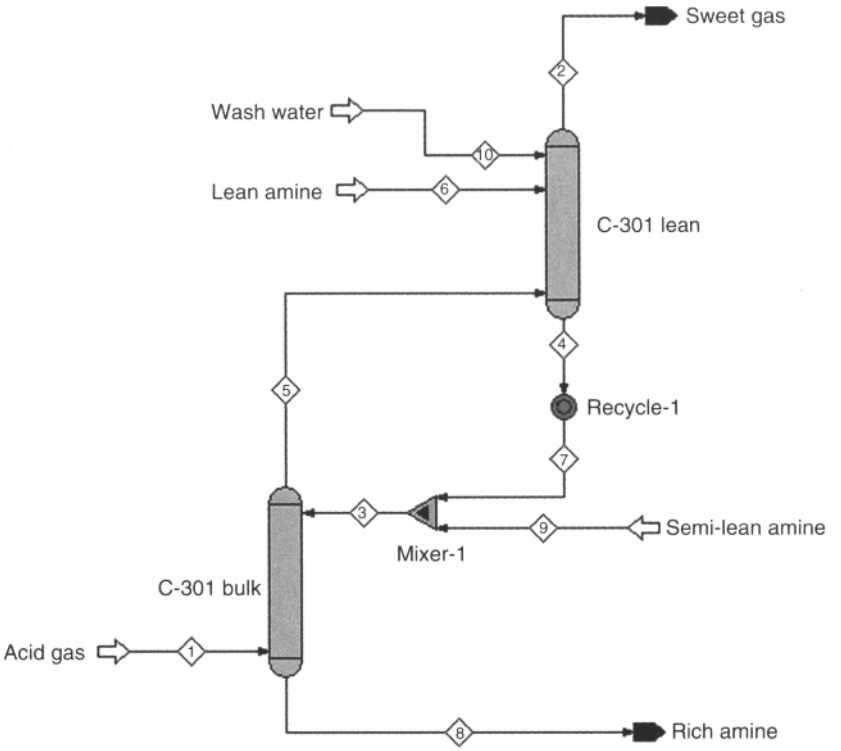

Figure 5.2 Two-Stage absorber for CO_2 removal in an ammonia syngas plant.

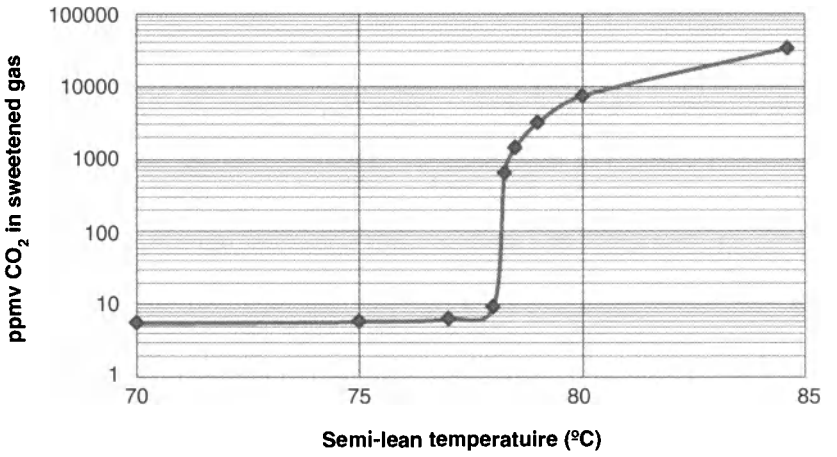

Figure 5.3 Effect of semi-lean temperature on performance of the two-stage absorber shown in figure 5.2.

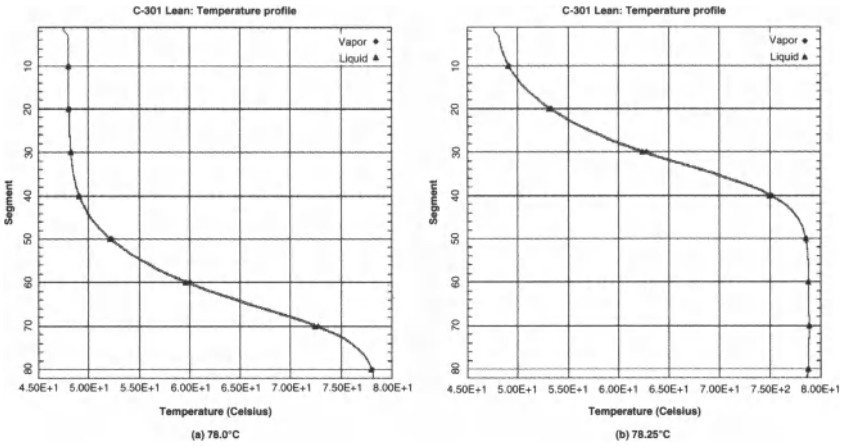

Figure 5.4 Transition from (a) Lean-end to (b) Rich-end Pinch Conditions in an Ammonia Syngas Lean Absorber.

kind of behaviour is apparently well-known, at least to the more astute solvent vendors and process licensors, but despite engineering contractors being repeatedly warned and encouraged not to provide designs that are too tight, winning a bid often takes precedence, with the result that plants are still being designed with built-in instabilities. But this is not the only kind of plant performance behaviour that can be found with piperazine activation.

5.2.3 Post-combustion CO_2 Capture

Figure 5.5 shows the processing scheme. The plan is to remove 90% of the CO_2 from the entering flue gas and the engineers were interested in exploring the extent to which reboiler duty (regeneration energy) depends on solvent circulation rate. The absorber contained 10 m of structured packing with specific surface area roughly 250 m^2/m^3. The cross exchanger was to operate with a 10°F temperature approach. When a series of simulations was run over the solvent flow range from 1,800 to 6,000 gpm and the reboiler duty was adjusted on each one to achieve 90% removal, the rather unusual looking curve shown in Figure 5.6 was obtained. There are two minima, a maximum, and two asymptotes at the far left and right hand sides. The engineers conducting the study initially believed that the ProTreat® simulator predictions were in gross error. They expected to see a single minimum in the reboiler duty followed by

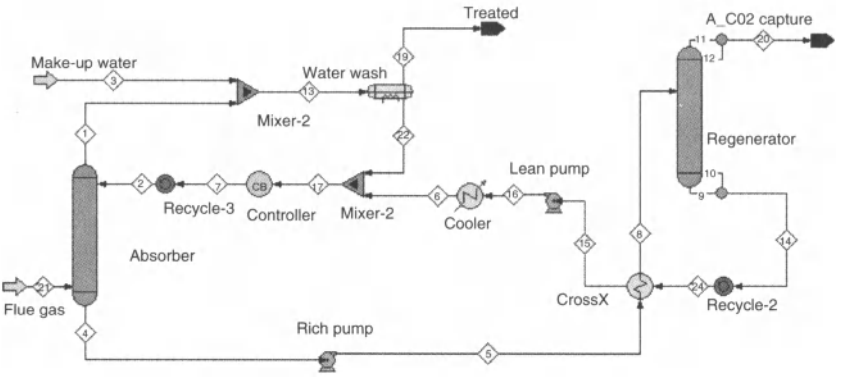

Figure 5.5 CO_2 capture pilot plant.

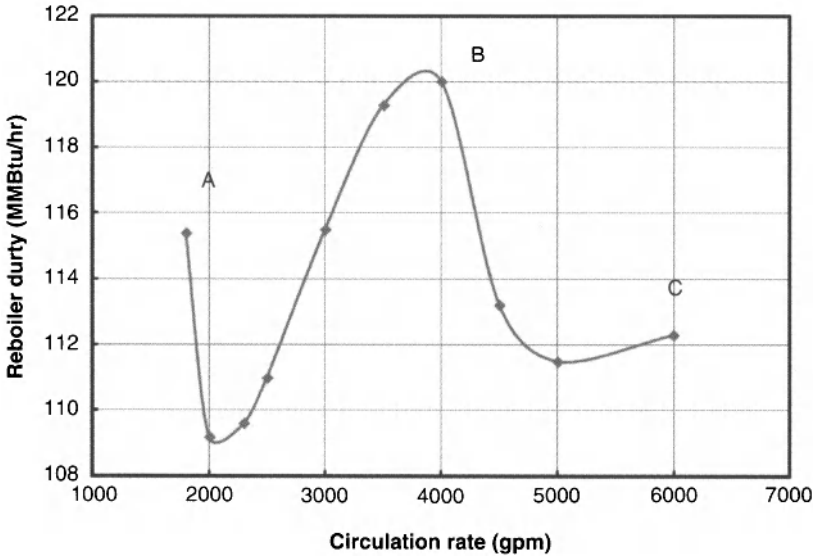

Figure 5.6 How reboiler duty and solvent flow rate interact to achieve 90% CO_2 removal in carbon-capture Pilot Plant.

a steady increase in reboiler energy input based upon results from an equilibrium stage, efficiency based simulator.

The reason for this seemingly strange behaviour is that the absorber moves from a rich-end pinch condition at the far left of Figure 5.6, which is the desired mode of operation for carbon capture, to a lean end pinch at the right. At the right hand side, far too much solvent is being used for only 90% CO_2 removal: this is

more typical of a conventional MEA column used to treat to low CO_2 levels, except that here the reboiler duty is much reduced so that the *equilibrium* partial pressure of CO_2 over the lean solvent is close to what is needed to remove only 90% of the CO_2. The regions marked A, B, and C in the figure signify regions where it might be worthwhile to look at temperature profiles for clues.[3] That the combination of low reboiler duty and low solvent rate is an efficient way to remove 90% of the CO_2 is no surprise—the rich end pinch produced by low solvent flow is used to limit CO_2 absorption. However, why does a higher solvent flow eventually require *more* reboiler energy to be expended? The answer is, that as solvent flow increases, the temperature bulge spreads to much of the interior of the column making the centre region so hot it can do less absorbing, thereby leaving more CO_2 in the gas, unless, that is, the solvent gets stripped cleaner by *more* reboiler steam. At point B the bulge temperature is nearly 170°F and only the ends of the column are effective in removing CO_2. As the solvent rate goes still higher, beyond the peak at 4,000 gpm, the bulge continues to move down the column and treating becomes increasingly lean-end pinched. Under lean-end pinch conditions, solvent lean loading controls the outlet CO_2 concentration and higher and higher lean loadings are adequate for treating to 90% CO_2 removal. Despite the fact that the solvent flow is higher so more reboiler energy will go into heating the rich fed to its bubble point on the stripper's feed tray, less stripping still requires less energy and the curve falls through another minimum. It should be apparent that to the left of the first minimum a further *decrease* in solvent rate will require a *substantial* decrease in lean loading, hence higher reboiler duty, and to the right of the second minimum a *higher* solvent flow will require a *gradually* increasing reboiler duty to heat the solvent to the feed tray temperature, the solvent lean loading being fairly constant beyond 6,000 gpm.

Maxima and minima are always caused by there being (at least) two factors opposing each other. The factors at play here are lean-end versus rich-end pinch, and solvent net loading capacity versus the solvent flowrate. So there are two pairs of factors. The situation is obviously complex and in part the complexity is related to

[3] It's amazing just how much information can be gleaned from a seemingly simple, temperature profile. Accurate temperature (and composition) profiles are the purview solely of a genuine mass transfer rate model, and they indicate quite accurately just how a give column is operating and where improvements, including what other treating strategies such as solvent additives, might be worthwhile.

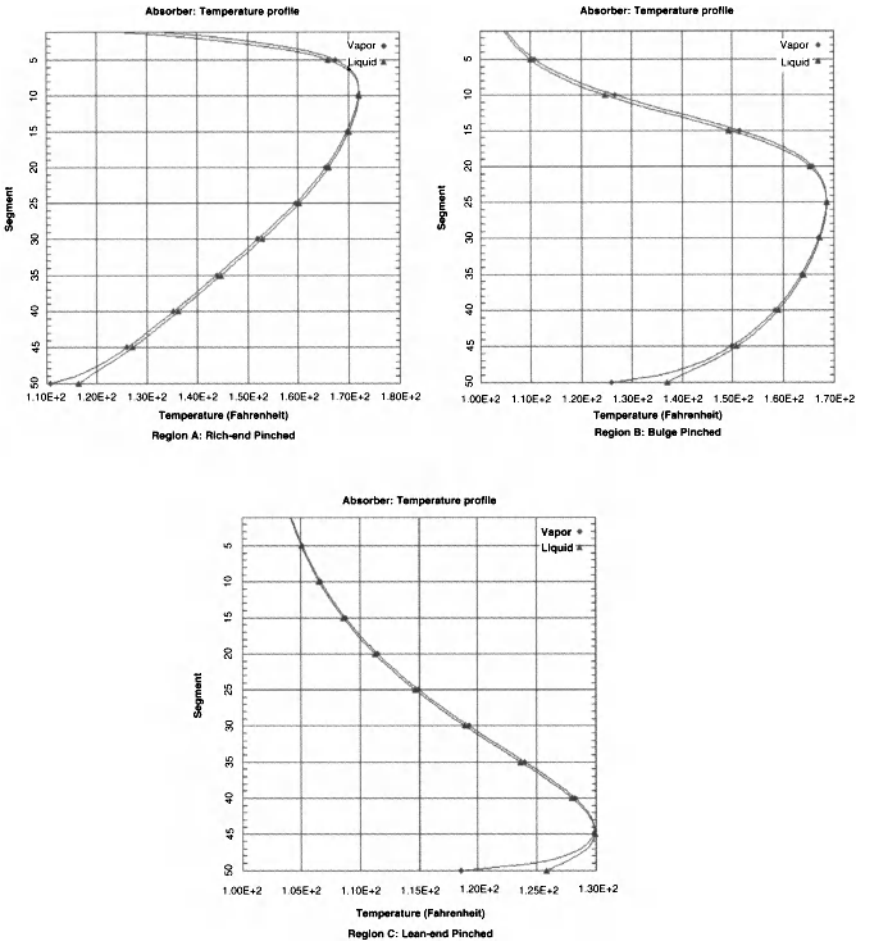

Figure 5.7 Temperature profiles in the three regions marked in figure 5.6.

whether one wants to do carbon capture (left hand side) or higher purity treating (right hand side). But if these two regions are considered separately from each other, a lot of the complexity goes away.

The performance curve shown in Figure 5.6 is for 30% MEA which is a fairly reactive solvent. There is no operational cliff. The fact of at least two regions of lowest energy treating is simply a result of lean-end versus rich-end pinching in the absorber. But to appreciate this, one must be able to look not just at the absorber, but at the whole treating plant, including the regenerator which plays just as important a part in determining the operating curve as the absorber does. Coming to terms with a

seemingly strangely shaped operating curve required a close look at how temperature profiles responded to changing solvent rates and reboiler duties.

5.2.4 LNG Absorber

This case focuses on an absorber in an LNG plant treating essentially methane (84%), ethane (10%), and propane (4%) containing 2% CO_2 on a dry basis to a specification of <50ppmv CO_2. The tower contained 60 feet of IMTP-50 random packing and it was sized in each simulation for 80% of flood. Three sets of simulations were run at a series of solvent rates, but with each set having a constant value of CO_2 lean loading, as shown by the legend in Figure 5.8. At each lean loading, the absorber failed to treat adequately if the solvent rate was too low. This is as one should expect, because at too low solvent flows the solvent has inadequate capacity and, more importantly, the column is rich-end pinched. The temperature profile at 500 gpm is shown in Figure 5.9. As solvent flow was increased, treating improved, and if the lean loading was low enough there was adequate capacity to achieve <50 ppmv CO_2. But as solvent flow was increased further, the temperature profile deformed into the shape in Figure 5.9 for 800 gpm. At this flow rate, the absorber was bulge pinched in that the temperature in the central part of the

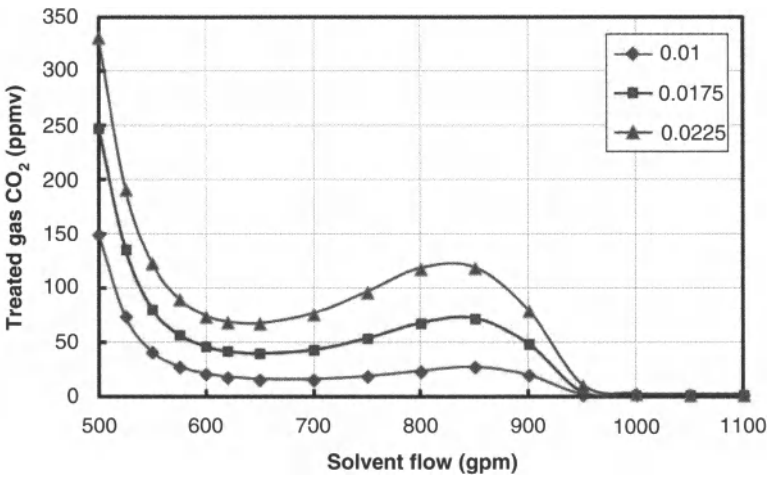

Figure 5.8 LNG absorber performance as a function of solvent rate at a series of solvent lean loadings (See Legend).

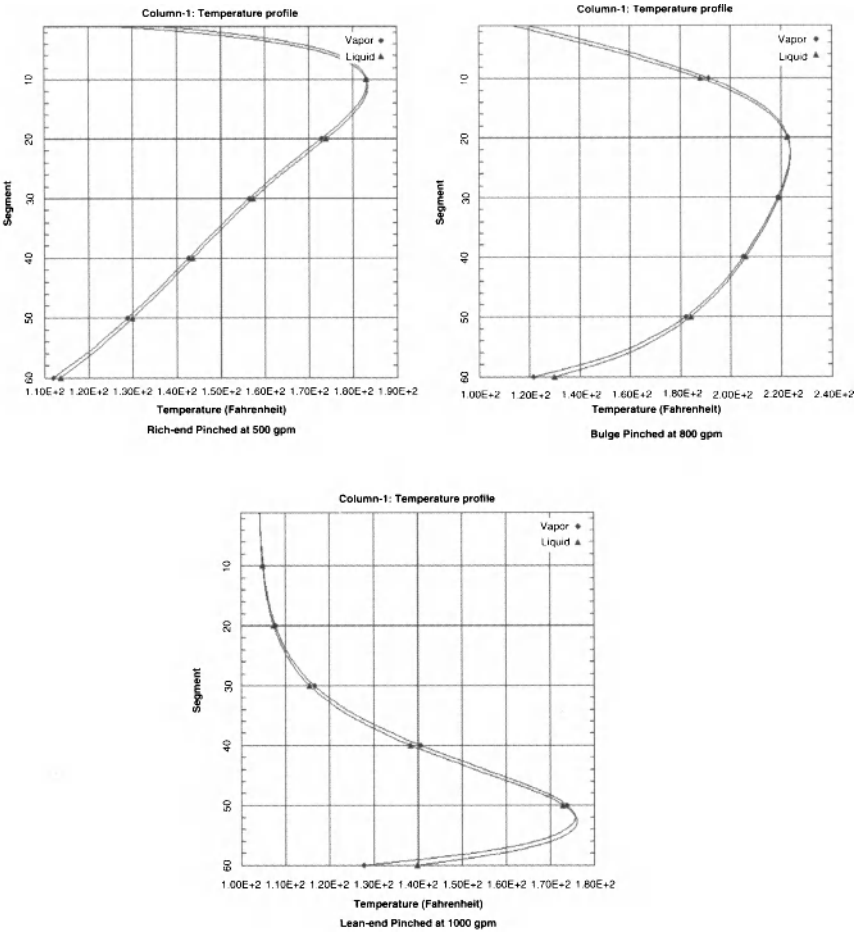

Figure 5.9 Temperature profiles corresponding to solvent flows in figure 5.8.

column was so high, only the ends were effect in removing CO_2, the centre part of the column did nothing, and the column behaved as though it had perhaps 30 or 40 feet of packing, not the 60 feet that was really there. As the solvent rate was increased further, the temperature bulge got pushed further down the column, and the absorber became lean-end pinched, where treating was determined primarily by the solvent's lean loading.

In this particular case, the treated gas was 40–45 ppmv CO_2 over the flow range from 600 to 700 gpm but the way to respond to the gas going off-specification may not be to increase solvent rate, but rather maybe to decrease it, or perhaps to increase reboiler steam

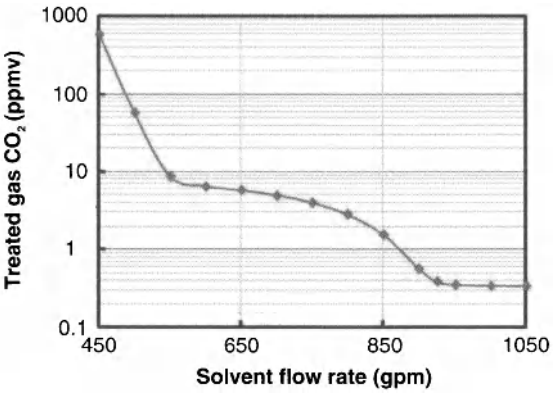

Figure 5.10 Performance of a trayed LNG absorber with 0.015 lean loading.

or hot oil flow. Without a detailed operating diagram such as the one in Figure 5.8, operations could probably not do much more than just guess at the correct response and hope for the best. And if the engineering contractor uses an equilibrium stage simulator of whatever ilk (ideal stages with Murphree efficiencies, or ideal stages with kinetic corrections and user-estimates of ideal stage residence times[4] and stage thermal efficiencies), none of this would be apparent at all and the design would have an unwelcome element of uncertainty and surprise.

The behaviour of packed columns is a little different from trays. With packing, as the solvent flow is increased, the wetted, interfacial area rises as well, and the mass rate therefore increases with solvent flow for this reason. With trays, gas-liquid interfacial area for mass transfer is only a relatively *weak* function of liquid rate and the performance curve typically looks like Figure 5.10. Note the logarithmic scale. There is no maximum because the liquid-rate dependence of area is insufficient to drive higher absorption rates and exacerbate the central, flat region into becoming a peak. Nevertheless, there are still lean-end, bulge, and rich-end pinch conditions at the low, medium and high solvent rates shown in Figure 5.10. Under the conditions of the simulation results shown in Figure 5.10, none of this really matters; however, if the lean loading

[4] The residence time of an ideal stage is quite elusive. Although the liquid flow rate may be stated, there is no known way to determine the volume of an ideal stage. The volume is an essential part of the definition of residence time. Indeed, the volume of a theoretical stage is just as meaningless as its residence time.

were to become too high, one might have to operate at nearly twice the flow of very lean solvent to achieve the <50 ppmv specification.

The difference between packing and trays and, indeed the effect of packing type and size can be very important in the design of an LNG facility. If your simulator is not genuinely *mass transfer* rate-based, all of this will be missed, all trays and packings will all be treated as ideal stages, the differences will not be apparent, the design will be subject to considerable uncertainty and the plant may not work at all.

5.3 Summary

Plant simulation and analysis are holistic when the entire treating plant is examined all at once, or at least the isolated equipment item is examined and analysed using a simulation tool that is based on considering *all* the factors that affect performance, without idealizations or unwarranted approximations. Using ideal stages or any approach that refers to ideal stages immediately leaves the simulation analysis open to debate because guesswork was inherently involved, either in assumed or calculated efficiencies or through the number of ideal stages assumed or even sometimes insofar as introducing a phony residence time per hypothetical stage. Regardless of the exact approach, when ideal stages underlie a model, at least two assumptions have to be made, and there is no way to prove an assumption was valid unless the answer is already known. This immediately disqualifies the resulting analysis as nothing more than a gross approximation to the truth, and frequently a completely faulty one.

Using an ideal stage model with Murphree efficiencies begs the question, 'Where do the efficiencies come from?' Neither tables of efficiencies nor reliable correlations of such efficiencies exist, so they can come only from what is termed 'experience'. Efficiencies vary widely from tray to tray, from component to component and with specific operating conditions of temperature, pressure and flow rates as well as the tower internals details (tray design, packing type and size). Experience will not necessarily come in handy to solve new problems or problems when the answer is not already known. Therefore simulation based on necessarily overall or component efficiencies will yield results that can leave an unsettled feeling when the analysis is completed.

There is no longer any need to use such antiquated and unreliable models. Modern computing power is more than enough to solve columns and flowsheets in only a few seconds using models very soundly based in engineering science. The ProTreat® simulator is the only available, proven, commercial tool that allows this to be done for gas treating in a computationally robust and reliable manner. There is no reason to continue taking the risk for failure using inadequate tools to develop unreliable designs when the right tool is available at quite modest cost.

This paper has shown how a holistic approach was necessary to solve a rather complex troubleshooting problem by isolating the problem into one of chemistry. This required use of a simulation tool that correctly accounted for the *real* heat stable salts and other contaminants in the treating solution. Confident prediction of the real tray internal temperature profiles provided additional evidence to understand better a material and energy balance discrepancy around the absorber, eliminating some degree of guesswork from the plant troubleshooting exercise.

In the other case studies, the ProTreat® mass transfer rate model showed some rather exotic behaviours in both a CO_2 capture plant environment as well as an ammonia plant and an LNG facility. Performance behaviour was analysed and understood by using the tray-to-tray and packed-segment to packed-segment temperature profiles that were generated as an integral part of genuine mass transfer rate simulation. Thus, the columns themselves were examined holistically because the fundamental model used in the simulations accounted for all the factors that affected treating performance.

6

Controlled Freeze Zone™ Commercial Demonstration Plant Advances Technology for the Commercialization of North American Sour Gas Resources

R.H. Oelfke, R.D. Denton, and J.A. Valencia

ExxonMobil Upstream Research Company, Houston, TX, USA

Abstract

The CFZ™ technology provides for the single-step removal and liquefaction of CO_2 as well as other acid gas components present in sour natural gases. The resulting high pressure liquid can then be readily reinjected for geosequestration or EOR purposes. The CFZ™ technology will allow sour gas resources with 8 mol% or more CO_2 to be economically developed when coupled with subsurface acid gas injection, while protecting the environment from excessive greenhouse gas emissions, and without having to dispose of a sulfur byproduct.

During the last year, ExxonMobil has successfully started up a 14 Mscfd commercial demonstration plant (CDP) at our Shute Creek Treating Facility in Wyoming, USA. The CDP is designed to process feed streams with CO_2 contents ranging from 15 to 65% and H_2S contents of 0 to 35%, at pressures up to 600 psig. The CDP also demonstrates the advantages of discharging the sour gas components as a high pressure liquid stream by re-injecting the acid gas components via an existing acid gas injection (AGI) facility.

This paper will provide a review of the CFZ™ technology and initial data from the CDP baseline run at 600 psig (42 barg), and a discussion about the types of sour gas reserves where use of this technology might be applicable.

Ying (Alice) Wu, John J. Carroll and Weiyao Zhu (eds.) Sour Gas and Related Technologies, (79–90)

6.1 Introduction – Gas Demand and Sour Gas Challenges

ExxonMobil believes that natural gas demand growth will continue to outstrip other competing energy resources and that natural gas production will grow by about 60% over current levels of production by 2040. Its overall abundance and clean burning characteristics will continue to justify its expanded use in power generation, which is forecast to represent over 40% of the entire global energy demand in 2040. In addition, since natural gas fired power generation releases less CO_2 than power generated from other fossil fuels, its increasing use will be critical to help the world slow and then reverse the growth in greenhouse gas emissions. By 2040, ExxonMobil forecasts that natural gas will supply 27% of the world's total energy demand up from approximately 22% today.

A significant increase in gas production will be needed to meet this large increase in demand. Many new resources have substantial amounts of CO_2 and H_2S. Therefore, this will also result in a significant increase in CO_2 produced and, if not sequestered, vented.

In order to moderate the greenhouse gas emission effects from producing these additional sour natural gas volumes, geosequestration, possibly via enhanced oil recovery projects, will be required for at least some of the incremental CO_2 produced. Commercial application of a technology like the ExxonMobil Controlled Freeze Zone (CFZ™) process can help meet that goal at a significantly lower cost than the other competing technologies available today.

6.2 Acid Gas Injection

When acid gas injection is called for in the processing of sour gas resources, the relative advantages of the various types of treatment processes shifts towards options that release the acid gases removed from the natural gas at a relatively high pressure (especially as a liquid) and dehydrated. Natural gas fractionation can be designed to recover the acid gases at high pressure, at least partially as a liquid in some cases, and dry. This minimizes

the power required for compression or pumping for reinjection of the waste acid gases and the need for acid gas dehydration facilities.

Fractionation based processes rely on the relative volatility of the components in the sour natural gas stream. Bulk fractionation uses a single refrigerated tower for the bulk removal of acid gas compounds, but the overhead "sweet" product has a residual CO_2 content of 15% or more to prevent CO_2 solidification from occurring in the distillation column. Therefore, further treatment, usually with a solvent process, is needed to achieve the quality specifications normally required for natural gas sales to transmission systems.

The Ryan-Holmes process is capable of achieving the required high natural gas purity via a multi-tower fractionation process. This process uses a heavier hydrocarbon liquid additive to suppress the CO_2 freezing during the distillation process. This hydrocarbon additive reduces the freezing point of CO_2 in the first column and is recovered in later columns and recycled. While effective, this process requires that the recovered acid gas be vaporized during recovery of the hydrocarbon liquid additive.

The Controlled Freeze Zone (CFZ™) technology is capable of achieving a high quality sales gas product, like the Ryan-Holmes process; however, no hydrocarbon additive is required to effect the desired separation, so the second distillation step to recover the additive is not required. As a result, the acid gas can be recovered as a high pressure liquid, so pumping, rather than costlier compression, can be used for reinjection.

6.3 Controlled Freeze Zone™ — Single Step Removal of CO_2 and H_2S

CFZ™ is a cryogenic process for the single step separation of CO_2 and H_2S from natural gas involving the controlled freezing and re-melting of CO_2. A simplified schematic of the process is shown in Figure 6.1. In a novel approach, rather than avoiding the solidification of CO_2 as is the case in conventional and other cryogenic treating processes, the Controlled Freeze Zone™ process allows CO_2 to freeze, albeit under carefully controlled conditions and in a specially designed section. High purity methane product and a by-product liquid acid gas stream with low methane content are

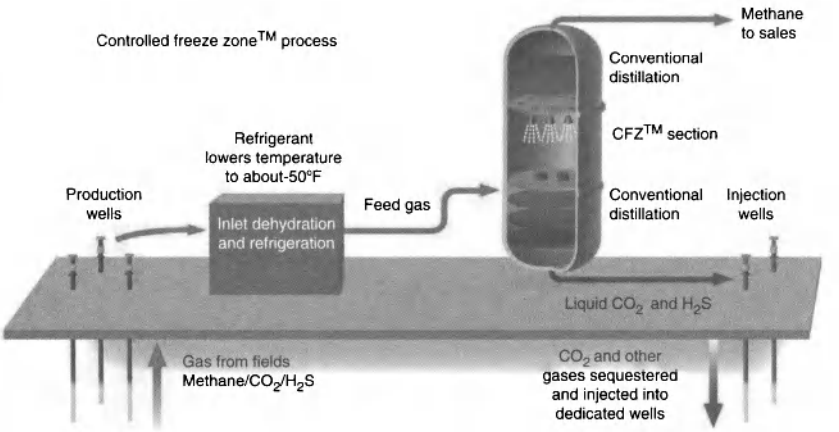

Figure 6.1 Simplified process – CFZ™ from Wellhead to Market.

produced by combining traditional distillation techniques with the CFZ™section.

To separate methane at high purity from acid gas (CO_2, H_2S) compounds, a Controlled Freeze Zone™ tower normally will use 3 zones: the specially designed CFZ™ section that addresses the solidification region in the phase equilibrium (pressure-temperature-composition) envelope, and two conventional distillation sections for rectifying and stripping, that cover the vapor-liquid areas above and below the CO_2 solidification region. The relationship between the three sections of the CFZ™ column and the methane-CO_2 phase envelope is illustrated in Figure 6.2 In the lower portion of the tower, below the CFZ™ section, methane is stripped from the bottoms liquid stream, which contains CO_2 and other acid gas contaminants, via conventional distillation. Above the CFZ™ section, the CO_2 content of the methane product stream is further reduced as required to meet the required export sales criteria again via conventional distillation in a rectifying section.

Liquid from the upper conventional distillation section, that is about to enter solidification conditions, is sprayed into the CFZ™ section, which is designed to provide an unobstructed volume for generation of the solid CO_2 formed. As the liquid droplets fall, they encounter warmer temperatures. Methane and any lighter components such as nitrogen, if present, vaporize. The residual concentration of CO_2 in the droplets increases, leading to

solidification. The solids that form then fall onto a liquid layer at the bottom of the CFZ™ section that is maintained above solidification temperatures. A liquid, now warmer than the threshold solidification temperature, emerges from the bottom of the CFZ™ section and is fed to the stripper section below to recover the methane fraction still dissolved in the liquid leaving the CFZ™ section.

The vapors from the bottom conventional distillation (stripper) section, rise through the CFZ™ section and encounter colder temperatures. CO_2 condenses or frosts onto the falling spray droplets or solid crystals. The solids formed in the CFZ™ section are pure CO_2, thus providing greater separation factors and higher efficiency for this section than conventional, vapor-liquid distillation could achieve. Their removal from the vapor stream results in a product exiting the top of the CFZ™ section that is significantly depleted in CO_2, and which can be fed to an upper distillation section, if further reduction of residual CO_2 is needed.

The Controlled Freeze Zone™ tower normally would include all three sections; however, depending on the sales gas specifications and inlet composition, the rectifying section may not be necessary in all cases.

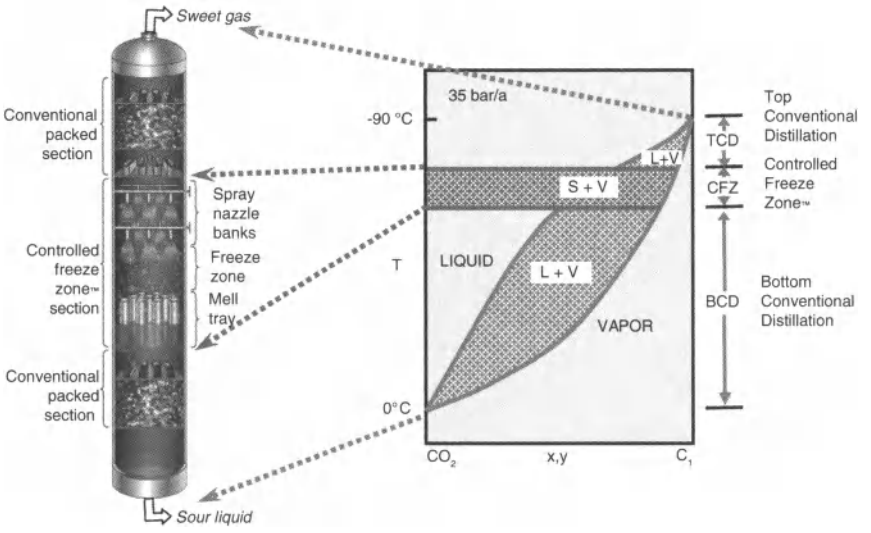

Figure 6.2 The controlled freeze zone™ tower.

Fundamentally, the CFZ™ technology provides the ability to more economically process natural gas without imposing limitations on the level of CO_2 or H_2S contamination. The CO_2, and any other acid gas components present, is separated into a liquid stream that can be easily pumped for geo-sequestration or for use in enhanced oil recovery operations, while yielding a high quality methane product.

6.4 Development Scenarios Suitable for Utilizing CFZ™ Technology

Over the past several years ExxonMobil has studied the potential application of the CFZ™ technology for the development of several sour gas resources using acid gas reinjection. Based on this work, we have determined ranges where the technology offers significant cost advantages over other gas processing alternatives.

Figure 6.3 below shows the results of four gas fields that were studied to compare CFZ™ technology with other acid gas removal technology. The variables & ranges are:

- The feed gas CO_2 content ranges from 70% to 8%. All included varying H_2S levels.
- Various alternative technologies were studied, including: Ryan-Holmes separation, bulk fractionation with DMPEG solvent treating, and amine treating.
- Sales gas specifications were both pipeline-quality and LNG-quality.
- Feed gases very lean and very rich in ethane-plus were considered.

One unexpected result is that the percentage cost advantage enjoyed by CFZ™ technology did not change much with varying feed gas CO_2 content or sales gas specification. Another significant result is the importance of the ethane-plus content of the feed gas. Ethane and CO_2 can form an azeotrope and liquefy at similar conditions. Any ethane will be removed with the CO_2 in a CFZ™, or other cryogenic separation process. This economic loss is usually unacceptable. Additional facilities are needed to

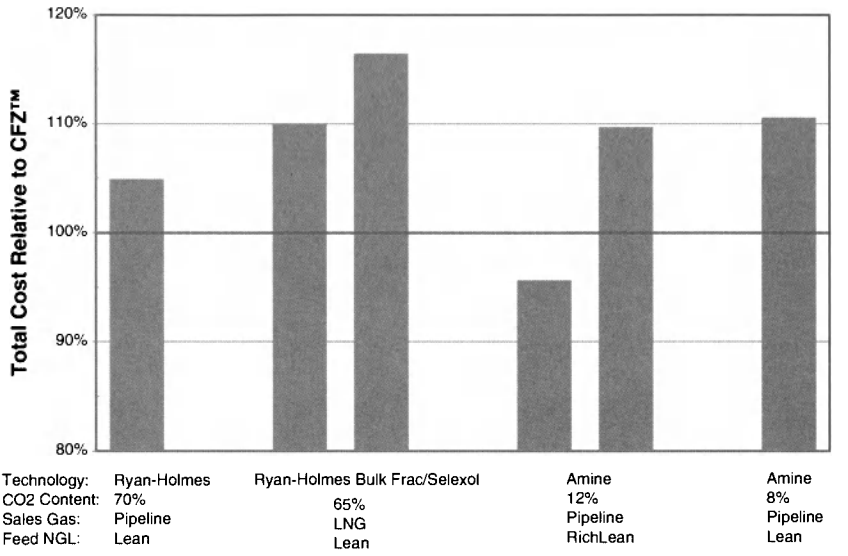

Figure 6.3 The controlled freeze zone™ cost comparison.

recovery the heavy hydrocarbons from the acid gas, which will increase costs.

Sour gas production opportunities where the CFZ™ technology has a clear advantage over other gas processing options, include the following:

- Raw gas with more than 8% CO_2 and any amount of H_2S
- Lean raw gas with minimal C_2+ present (<1 mol%) or where recovery of NGLs is not needed
- Developments where acid gas injection is required due to:
  - Lack of market for sulfur
  - GHG emission limitations or mandated reductions
  - Availability of EOR opportunities

A feed gas with as little as 8 mol% CO_2 can be efficiently separated using the CFZ™ technology. Such an application requires careful attention to heat integration and refrigeration system design, and will be dependent to some extent on the amount of co-produced H_2S that is present in the feed gas.

6.5 Commercial Demonstration Plant Design & Initial Performance Data

The CFZ™ Commercial Demonstration Plant (CDP) is now operating and the testing program is underway. The CDP is located at ExxonMobil's Shute Creek Treating Facility near LaBarge, Wyoming. The facility is schematically shown in Figure. 6.4

Three sources of feed are blended to provide the desired feed composition flexibility for testing. These streams consist of a methane stream (with a minor amount of nitrogen), a CO_2 stream, and an acid gas stream made up roughly of $^2/_3$ H_2S and $^1/_3$ CO_2. The feed dehydration system has been designed to allow the adjustment of the moisture content in the CFZ™ feed stream. The deployment of distillation towers in offshore applications involves additional wave motion and structural considerations that may pose limitations in tower height. So while a single tower can be used, the CDP incorporates a split-tower design to better understand and prepare for potential offshore applications. One column includes the stripping and CFZ™ sections. The other column includes the rectifying section. This arrangement also allows the demonstration of self-sufficiency in the stripper and CFZ™ sections in reaching pipeline-quality gas (~2 mol% CO_2) without a rectifying section.

The CDP as shown in Figure 6.5 has been started up and the initial baseline runs have been completed. The initial runs were

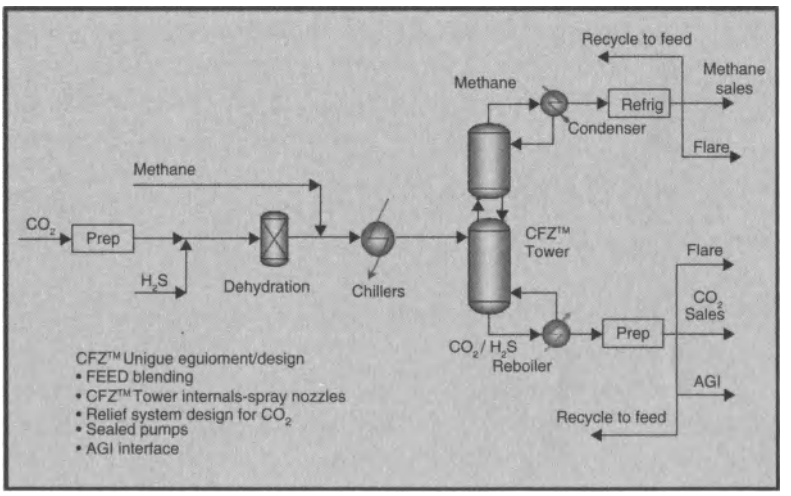

Figure 6.4 CFZ™ CDP process schematic.

Figure 6.5 CFZ™ commercial demonstration plant at night.

done with a nominal 60% CO_2 feed at pressures from 550 to 600 psig. The testing program is anticipated to run through the end of 2012.

To date, acid gas CO_2 concentrations have been over 99 mol% CO_2 with methane concentrations always below 0.5 mol%, while the gas product is usually less than 1.2 mol% and in some cases has been as low as 100 ppmv.

As an example, Figure 6.6 shows the temperature profile from a seven day run of the unit's two towers using the following feed composition:

CO_2	62 mol%
CH_4	37 mol%
N_2	1 mol%

As can be seen, the melt tray operates at about –75°F (–60°C) over a range of ± 1°C. The top of the freeze zone at these pressure conditions operates at –113°F (–80°C). During the whole week while this baseline run was underway the unit performed very stably with only modest fluctuations in temperature.

In Figure 6.7, CO_2 concentration data at several locations in the columns is displayed for the same one week time period. After some

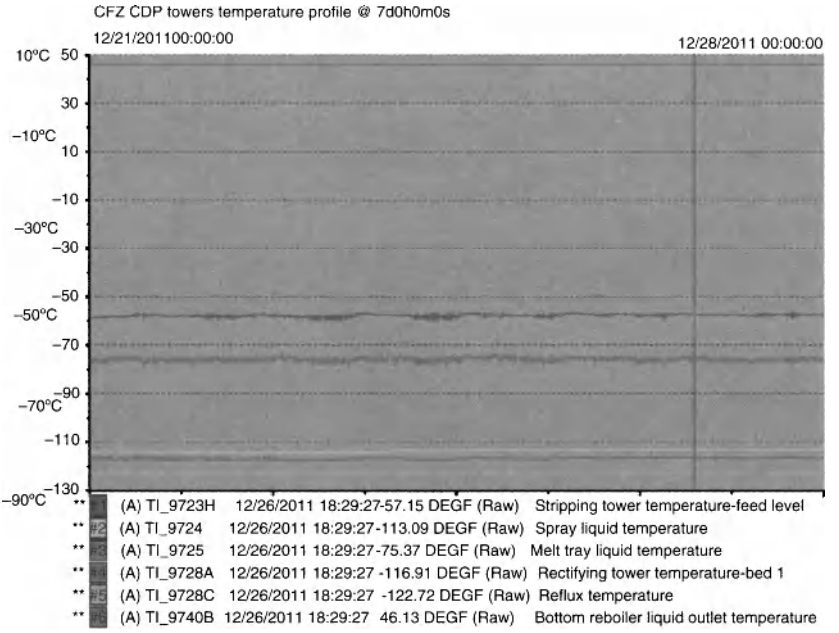

Figure 6.6 CFZ™ CDP towers temperature profile.

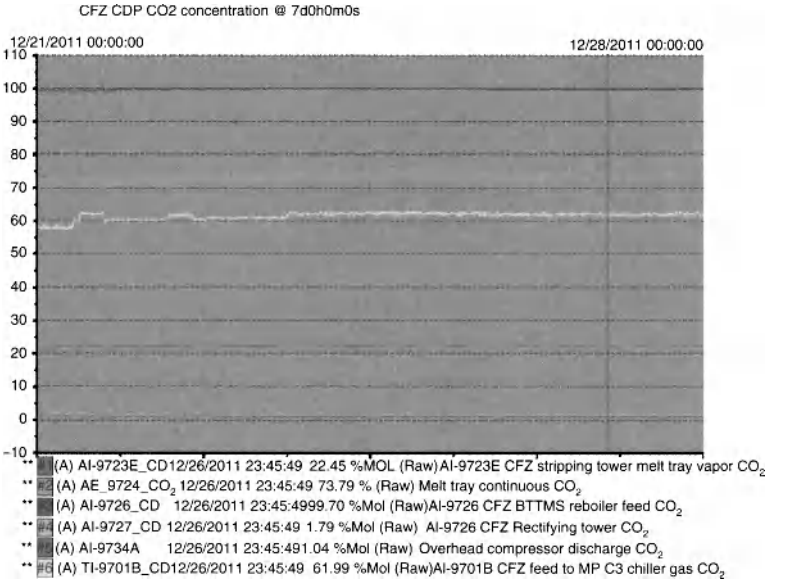

Figure 6.7 CFZ™ CDP Towers CO_2 concentration profile.

initial, modest adjustments in the feed composition, the CO_2 profiles in both the CFZ/stripper column and the Rectifier were very stable. As noted previously the overhead products were remarkably stable with 1 mol% CO_2 in the vapor product and 99.5+ mol% CO_2 in the bottom product.

6.6 Conclusions and Forward Plans

The Controlled Freeze Zone™ technology is a single step process for the separation of acid gas components from methane in sour natural gas resources, offering capital cost, operating expense and process efficiency advantages. This is ExxonMobil's proprietary technology for the development of increasingly sour gas reserves around the world. There is no technical limit on the amount of CO_2 or H_2S in the sour natural gas when treating with CFZ™ technology. In addition to the economic benefits for this technology, further environmental benefits can be realized since the acid gas by-product stream is discharged as a high pressure liquid. This provides a more economical reinjection option compared to compression of a low pressure acid gas stream characteristic of other gas treating process options.

The commercial demonstration plant is now in its testing phase. For the remainder of this year the CDP will be used to demonstrate the applicability of the technology for a wide range of opportunities and will provide the information required for scale up and deployment of the technology to develop sour gas resources around the globe.

Bibliography

1. Clark, W.E. and Kurata, F.: "Freezing CO_2 from Natural Gas," *Petroleum Refiner*, vol. 38, no. 6, pp. 249–251, 1959.
2. Donnelly, H.G. and Katz, Donald L.: "Phase Equilibria in the Carbon Dioxide –Methane System," *Industrial and Engineering Chemistry*, vol. 46, no. 3, pp. 511–517, 1954.
3. Mart, C.J., Valencia, J.A., and Northrup, P.S.: "Developing Sour Gas Resources: Controlled Freeze Zone™ Technology with Integrated Acid Gas Management," Sour Oil & Gas Advanced Technology 2010, March 28–April 1, 2010, Abu Dhabi, UAE.
4. Denton, R.D., Valencia, J.A., and Oelfke, R.H.: "The Controlled Freeze Zone™ Technology for the Commercialization of Middle East Sour Gas Resources," Sour Oil & Gas Advanced Technology 2011, March 27–31, 2011, Abu Dhabi, UAE.

5. Thomas, E.R. and Denton, R.D.: "Conceptual Studies for CO_2/Natural Gas Separation Using the Controlled Freeze Zone Process," *Gas Separation and Purification*, vol. 2, pp. 84–89, June 9, 1992.
6. Valencia, J.A. and Denton, R.D.: Method and Apparatus for Separating Carbon Dioxide and Other Acid Gases from Methane by the Use of Distillation and a Controlled Freeze Zone, U.S. Patent 4, 583, 372, August 6, 1985.
7. Valencia, J.A., Northrop, P.S., and Mart, C.J.: "Controlled Freeze Zone™ Technology for Enabling Processing of High CO_2 and H_2S Gas Reserves," International Petroleum Technology Conference, Dec. 3–5, 2008, Kuala Lampur, Malaysia.
8. Valencia, J.A., Northrop, P.S., and Mart, C.J.: "Controlled Freeze Zone™ Technology for Developing Sour Gas Reserves," GasTech 2009 Conference, 2009, Abu Dhabi, UAE.

7

Acid Gas Dehydration – A DexPro™ Technology Update

Jim Maddocks, Wayne McKay, and Vaughn Hansen

Gas Liquids Engineering Ltd., Calgary, AB, Canada

Abstract

The dehydration of acid gas is an important design and operating consideration for design engineering teams and owners of high pressure CO_2/H_2S systems. This paper will:

- Review the need for acid gas dehydration as a function of composition;
- Review dehydration criteria from several points of view;
- Provide an overview of existing acid gas dehydration technology, with benefits and drawbacks;
- Provide information and operating data from a new acid gas dehydration technology that can be applied to carbon capture projects as well; and
- Provide an update on the applied technology and discuss operating data.

7.1 Introduction

Acid gas is composed of a mixture of H_2S and/or CO_2 and often water vapour. Acid gas, a byproduct of gas treating systems, is usually considered to be a simplistic binary mixture of H_2S and CO_2. There are often other contaminants including methane, BTEX's, amine, and other hydrocarbon components. Carbon capture streams are typically pure CO_2 although there are other contaminants co-captured with the carbon dioxide. For the remainder of this paper,

Ying (Alice) Wu, John J. Carroll and Weiyao Zhu (eds.) Sour Gas and Related Technologies, (91–116)

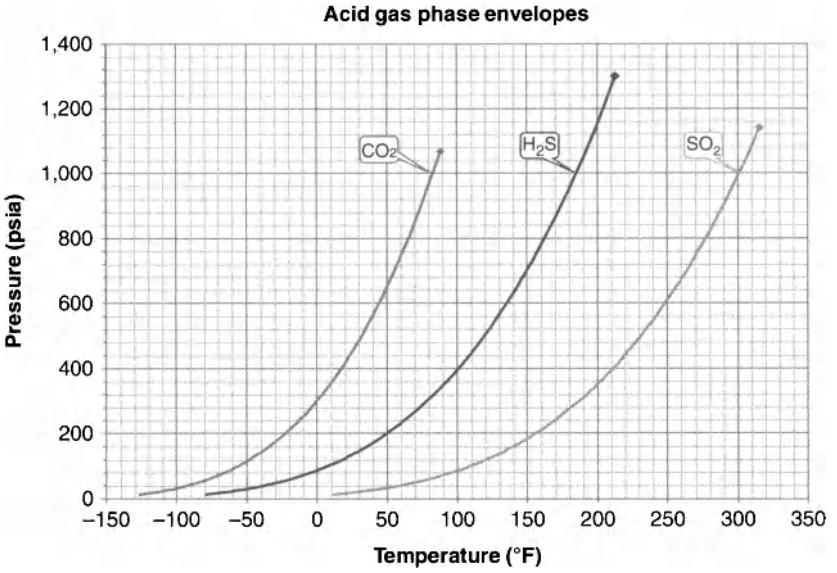

Figure 7.1 Phase behavior–typical acid gas.

the term acid gas will be used interchangeably to describe either the acid gas from a sweetening process or the waste gas from a carbon capture scheme. Produced gas from an EOR scheme will be discussed briefly as it behaves somewhat differently. A simplistic PT plot is shown below for some typical acid gas fluids:

7.2 Necessity of Dehydration

The acid gas streams are often captured at low pressure from either a gas treating facility or a carbon capture system. In any case, the low pressure acid gas, often below 1 bar(g), is water saturated at the regeneration pressure and temperature. As the fluid is compressed up to the necessary injection or disposal pressure (or potentially for EOR usage or other receipt point), some water will begin to condense. However, depending on the composition, operating conditions, and specifications, this fluid may require supplemental dehydration.

It's well known that high H_2S content acid gas streams can be managed to provide a measure of dehydration due to the increased water handling capacity of the fluid at high pressures[1]. This effect is less pronounced with CO_2 and depending on interstage conditions and desired water content, may or may not provide sufficient dehydration.

Acid gases, when combined with water, will produce hydrates (at elevated pressures), as well as produce an acidic aqueous phase contributing to corrosion concerns. While corrosion concerns can usually be countered with proper materials selection and corrosion monitoring programs, this is often costly and impractical depending on the process scheme, injection receipt points, and design considerations. The use of stainless steels is typical in a "wet" acid gas system, but this would almost certainly be economically prohibitive in any kind of pipeline application beyond 1 km in length.

Hydrate avoidance is critically important from a personnel safety and production (operational reliability) management standpoint. The formation of hydrates is preventable by:

- Managing system temperatures and pressures to enable maximum water dropout to suppress the hydrate formation temperature
- Partial or total removal of water from the system
- Injection of hydrate inhibitors such as methanol & KHI's

The plot below shows the hydrate temperature of CO_2 with varying water content:

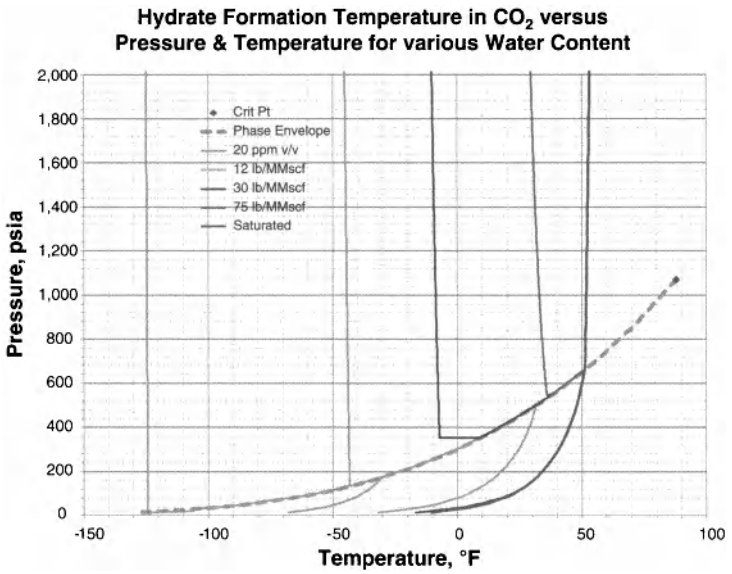

Figure 7.2 CO_2–Water Content.

7.3 Dehydration Criteria

Water content is usually set by a combination of contract requirements, hydrate avoidance criteria, or prevention of an aqueous fluid during transmission or handling. Typically, natural gas dehydration criteria is stated as a water content value; usually 4 #/MMSCF (64 mg/m^3) or 7 #/MMSCF (112.1 mg/m^3). This criteria was developed decades ago and is likely based on the McKetta-Wehe[2] moisture prediction chart to avoid the formation of hydrates and an aqueous phase during the transmission of natural gas. These informal criteria have been widely adopted for use within the natural gas industry. However, this moisture prediction methodology is not applicable or appropriate for use within sour gas systems. Alternative criteria and prediction methods have been established using correlations, specifically Wichert's correlation[3]. The nature of moisture content in acid gas is such that the water content criteria and hydrate formation temperature no longer remain connected to these traditional criteria. For example, pure methane at a water content of 64 mg/m^3 has a predicted hydrate formation temperature of –6°C at 5,000 kPa. This gas has a water dewpoint of –8.5°C.

The same pressure and water content criteria on a 50/50 H_2S/CO_2 mixture has a predicted hydrate formation temperature of –69°C while the pure H_2S stream has a predicted hydrate formation temperature of –75°C. These predictions are based on the PR equation of state. This is due, in large part, to the behavior of water and acid gas systems. See Figure 7.3 below to show how the system performance can vary as a result of composition:

This anomaly shows that traditional dehydration criteria may be too stringent for acid gas systems. Rather than applying commonly accepted dehydration or water content criteria, each system and case must be evaluated to establish moisture content that will suit the requirements of that particular project, whether that is pipeline moisture content, contract requirements, or hydrate avoidance during handling.

As a large transporter of CO_2, Kinder Morgan has set the maximum water content at 30 lb/MMSCF (632 ppm_v) for their EOR systems. While this is certainly adequate for most applications, lower ambient temperatures may require a more stringent specification of 12 Lb/MMSCF (250 ppm_v). In plant piping where sufficient

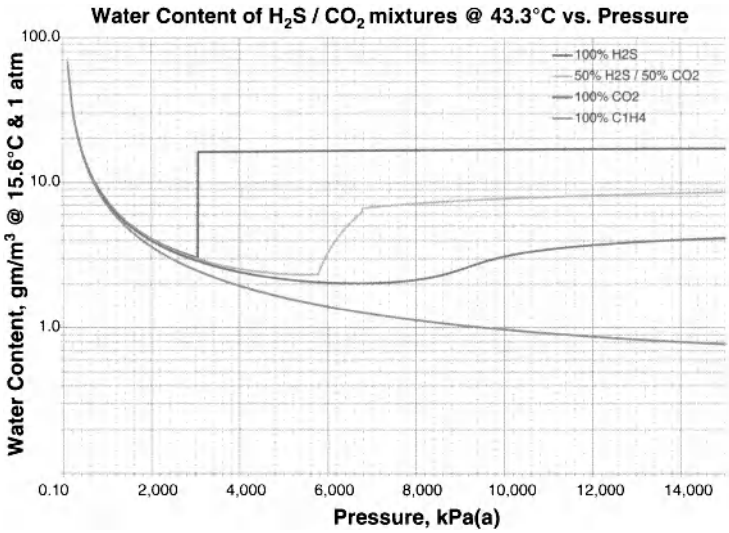

Figure 7.3 Acid gas water behavior.

tracing and insulation exists, the designer might well be satisfied with a water content of 75 Lb/MMSCF (1,580 ppm_v).

A recent DNV report (DNV-RP-J202, April 2010) states:

Note: 500 ppm(mol%) = 500 ppm_v ⟶ equates to 23.74 lb/MMscf

While there is no definitive standard for CO_2 water content, it's clear that it must be determined for each individual application. For the purpose of most applications, we will utilize the 30 Lb/MMSCF (approx 632 ppm_v) for comparison purposes.

Reference	*Maximum water content*				*Source of CO_2*
	1b/ MMScf	ppm W	ppm V	ppm Mol%	
/M. Mohitpour/	18 - 30	157 – 261			-
/KMCO_2/	30	261			CO_2 reservoir
/Statoil operated Snøhvit/			50		CO_4 + Stream
/DYNAMIS/				500	CCS

Figure 7.4 DNV Water Table (RP-J202).

7.4 Acid Gas – Water Phase Behaviour

The behavior of water in acid gas (at least at relatively low pressures) is a well known phenomena and varies widely as a function of acid gas composition. Pure H_2S (per the above diagram), exhibits a dramatic shift in water capacity. This shift, allows the pure H_2S to hold a lot more water once it condenses. The figure below shows the water isotherms from 3.3°C to 49°C for pure H_2S.

This dramatic increase in water capacity allows the system to be under saturated with water as it exits the compression system going to either injection or pipeline. Depending on the interstage pressures of the compressor, the system can be designed to achieve an interstage pressure near the water minima for the design interstage temperature. Once the gas is compressed further, the acid gas mixture has capacity to hold substantially more water; consequently, it is undersaturated.

As seen above (Fig 7.3), the water capacity varies dramatically as composition varies and does not exhibit a minimum in the pure methane system. The highest offset in water capacity is shown by the pure H_2S case while pure CO_2 shows a lesser water capacity offset. The presence of hydrocarbons will decrease the offset and move it closer to a steadily declining water capacity.

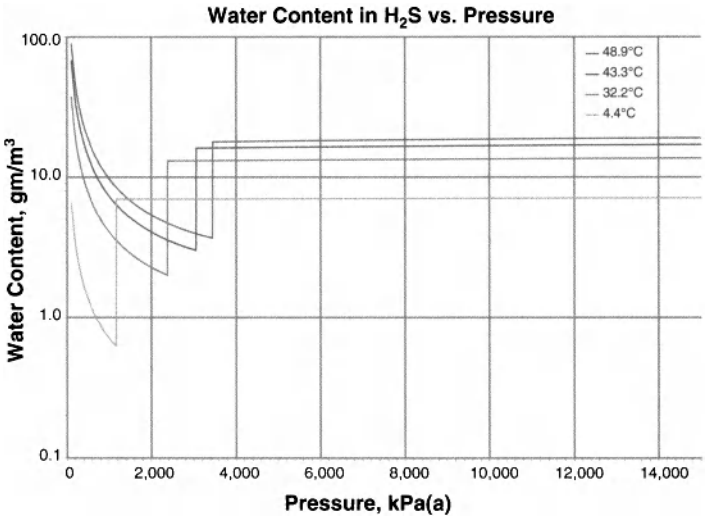

Figure 7.5 H_2S Water Isotherms.

This "natural" dehydration allows the process design engineer to essentially custom fit the dehydration process to the composition of the acid gas. However, this means that what works for 75% H_2S may not work for 25% H_2S if the composition varies widely within

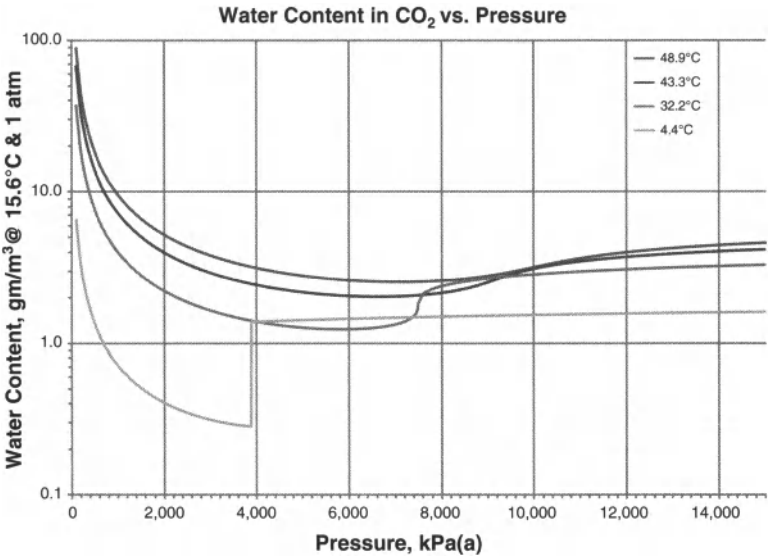

Figure 7.6 CO_2 Water Isotherms.

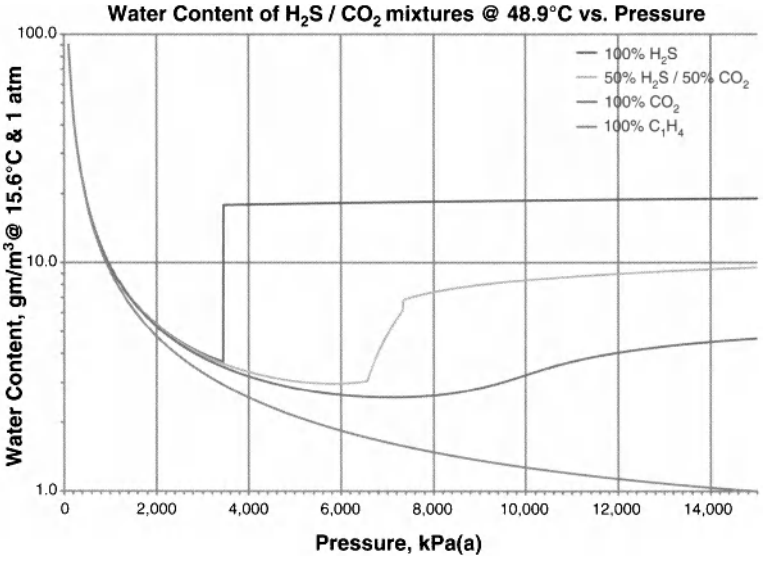

Figure 7.7 Acid gas mixture water behavior at 48.9°C.

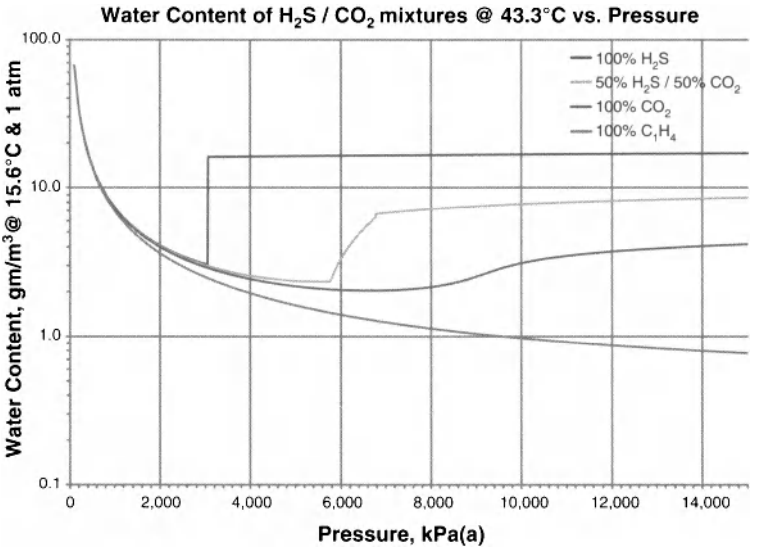

Figure 7.8 Acid gas mixture behavior at 43.3°C.

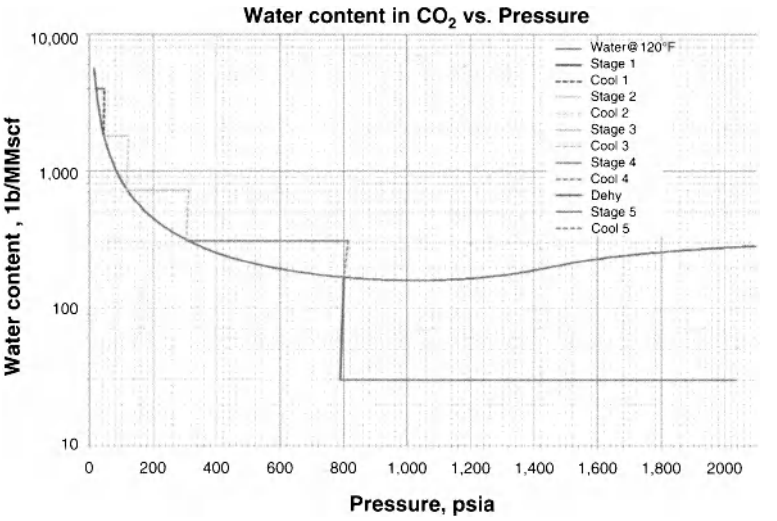

Figure 7.9 Dehydration via compression.

the system. Thus, for widely varying acid gas compositions, it may be necessary to plan for a more robust or worst case dehydration process. As well, the system performance varies as the temperatures vary – see below for the graph of mixed system performance at 48.9°C.

At a reduced temperature of 43.3°C, the water behavior is slightly different as shown below:

A typical CO_2 phase behavior curve is shown below to illustrate this feature. The minor hydrate shift is clearly seen as providing for some degree of "natural" dehydration during the compression process:

Several interesting anomalies are noted with this "natural" or auto-dehydration process:

- The addition of hydrocarbons will widen the phase envelope and will suppress the bubble point – the dewpoint will remain largely unchanged unless the % of hydrocarbons is significant or unless the hydrocarbons being added are heavy or contain BTEX's.
- The addition of natural gas and/or LPG to this mixture will raise the hydrate point and can potentially result in the formation of an aqueous phase.
- The auto-dehydration effect is not a suitable candidate for EOR based systems where the hydrocarbon fraction in the CO_2 stream can vary widely. For this reason, EOR based schemes typically utilize TEG dehydration due to its compositional flexibility.

7.5 Conventional Dehydration Methods

Dehydration methodologies can be divided into several groups:

- Desiccant Technology:
  - Adsorption – This process group includes mole sieve, silica gel, carbon bed, and other dry material based processes.
  - Absorption – This group includes TEG, DEG, glycerol, and other hygroscopic fluid based processes.
- Separation – membrane based processes
- Avoidance – hydrate inhibitors
- Thermodynamic/Refrigerative
  - External – closed loop processes such as ammonia or propane.
  - Internal – choke plant, JT processes, DexPro

7.5.1 Desiccant Adsorption

Although adsorption technology would seem to be a natural fit for acid gas dehydration, these dry material based processes will often over-dehydrate the acid gas mixtures. This does not cause any process issues, however, the capital cost and operating costs of these processes usually eliminates them from further consideration unless the specification requires extreme moisture removal. This can be the case for systems requiring food grade CO_2, or client receivers with unusually stringent moisture content specifications. These processes can require considerable plot space, piping, valving, and controls. Additional requirements include regeneration heat/cooling requirements, gas filtration, and media disposal. Fugitive emissions are low as the regeneration water scrubber off-gas can be recycled into an upstream scrubber. Utilizing this technology for multiple compressors may require some relatively complex valving to allow for each compressor to access the dehydration equipment. With limited moving parts, reliability is relatively strong, although replacement of the desiccant media is required as is replacement of main gas and regeneration gas filter elements on a periodic basis. Depending on the type of regeneration heater chosen, additional maintenance may be required. Switching valves will also require periodic servicing as they are in a difficult service. The adsorption process can be placed in any part of the compression cycle – the higher the pressure, the lower the water load but the higher the required equipment design pressure. The units must be protected from contamination by either liquid water or lube oils.

7.5.2 Desiccant Absorption

Absorption technology is commonly selected for acid gas dehydration for a number of reasons:

- Proven technology, operating history and commonly used gas process
- Relatively simple technology with a perceived low labour component
- Is not compositionally dependant although there may be some acid gas solubility concerns.

This fluid based technology is typically modeled after a simplistic gas dehydration system utilizing a hygroscopic fluid in a vertical

contactor. The process does have some drawbacks including fluid makeup, filter handling, regeneration offgas recycle handling, regeneration heat requirements, and the use of stainless steels. These systems are typically TEG based although several design papers often reference the use of glycerol[4] to limit the glycol solubility in the CO_2, particularly at or near dense phase operating pressures.

Dehydration with these glycol based fluids usually takes place at an interstage pressure to allow for maximum pre-removal of water load while still maintaining a gas phase. The gas undergoes anywhere from 2–4 stages of compression before being dehydrated and then is compressed in a final stage of the compressor or potentially even injection/transfer pumps before exiting the system.

Similar to the solid desiccant based processes, these processes do have additional equipment footprint requirements, and will require the same degree of complex valving to allow multiple compressors to access a single contactor. It may be more advantageous to design a single contactor for each compressor with a single regeneration train. Gas entering the units should have some type of lube oil removal prior to the TEG unit to prevent the contamination of glycol with compressor lube oil.

Equipment in the TEG unit is typically manufactured using stainless steel although there may be an alternative design utilizing a stainless steel precontactor mixer that would reduce the effective water saturation content to less than 60%. This pre-treatment may allow the use of a carbon steel contactor, although the remaining equipment would likely require stainless steel materials. Depending on treating pressure, gas/glycol ratio's, and system temperatures, it may be necessary to cool the gas after the TEG unit to keep final discharge pressures in line with requirements. As well, the high level of CO_2 may require solution pH control, buffering, and filtration.

Although the desired water content may not require deep level dehydration, the co-absorption of acid gases leaves a water saturated near-atmospheric acid gas stream (still column vapours). This will need to be managed with a cooler/condenser, separator, and a recompressor or vacuum/educator system to return these acid gas vapours to the inlet of the acid gas compressor. Operations and maintenance of these systems can be challenging – particularly in cold environments.

The below chart shows a pure CO_2 system with either TEG dehydration or mole sieve:

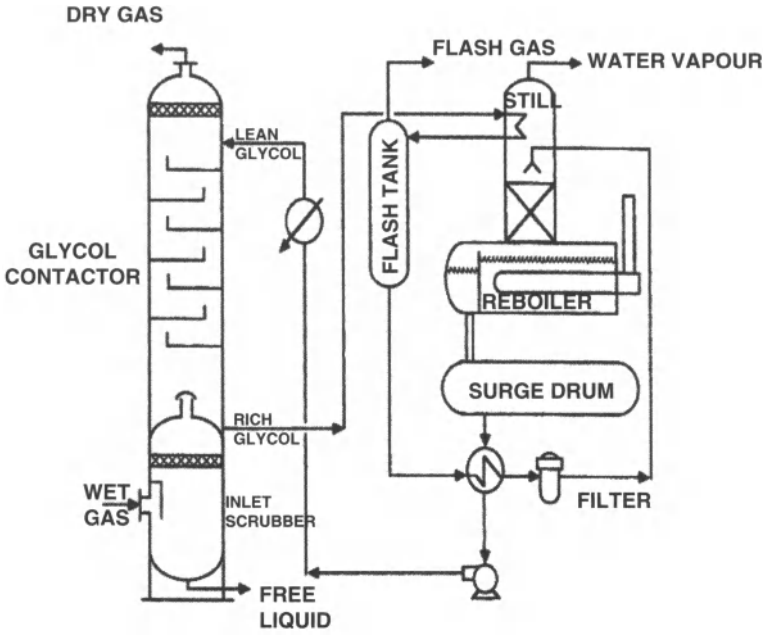

Figure 7.10 Typical TEG dehydration schematic.

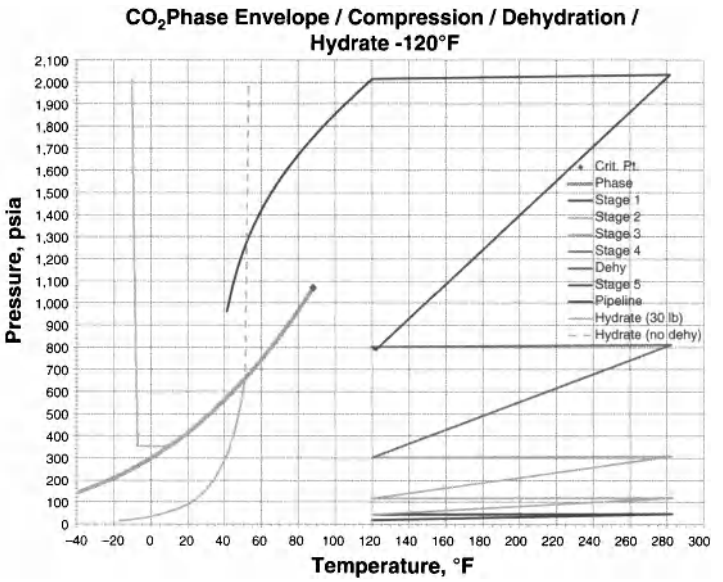

Figure 7.11 Pure CO_2 - TEG/Mole sieve dehydration.

7.5.3 Separation Based Processes

Separation based processes like membrane technology, to date, have not proven suitable for this application. While this may change, the acid gas tends to permeate reasonably easily as well meaning that several membrane stages may be required. As well, the permeate fluid may contain large volumes of CO_2 and H_2S that would require recompression and retreatment. While rubbery membranes may provide some promise, we are unaware of any updates allowing for economic membrane based water removal.

7.5.4 Avoidance Based Processes

Methanol and other hydrate inhibitors can be used to prevent the formation of hydrates in the pipeline. However, they do not ultimately reduce the water content and are not suitable for any type of contractual water requirement. They are only suitable for use in small short distance injection schemes where hydrate prevention is the key criteria. A key exception is the use of methanol in conjunction with other processes may provide incremental dehydration. Maintenance and footprint requirements are minimal although there is a continuing operating cost for the chemical consumption. Material selection and corrosion concerns still play a role within these systems. Many of the other dehydration schemes may augment their systems with methanol injection to ward off hydrates in the event of an excursion. Short, small volume, acid gas injection systems may elect to utilize a stainless steel pipeline with methanol injection to manage the risk of hydrates.

7.5.5 Thermodynamic/Refrigerative Based Processes

Refrigerative based processes can be divided into two(2) categories; external and internal. External processes utilize a closed loop of refrigerant, typically ammonia or propane, to cool the acid gas and provide temperature based water dropout. Conditions within the chiller must be controlled carefully to prevent the formation of hydrates and freezing of water on the surface of the tubes. Depending on the composition and desired final water content specification, it may be necessary to continuously inject methanol. Chilling may also be necessary in a hybrid process or physical solvent process where significant amounts of hydrocarbon are co-adsorbed. The presence of hydrocarbons can create an artificially

high hydrate point. In addition to this, they can represent a possible revenue stream that is being rejected to either EOR or disposal.

This closed loop process requires refrigeration compression, condensing, a JT valve, a stainless steel gas refrigerant chiller, and refrigerant suction scrubber. While this can be more equipment intensive, it may be a less costly adder in a facility already equipped with a refrigeration utility. As well, this chilling process may be more economical than a TEG based process depending on the type of offgas handling. This chilling process takes place at an intermediate pressure; ideally high enough to avoid hydrate temperatures but low enough to maximize water dropout in the downstream scrubber. This is usually done in between Stage 2 and Stage 3 of the compression cycle. Chilling on suction or on stage 1 discharge would be costly due to considerable water loads/duty, and would require large gas equipment to prevent unreasonable pressure drops.

While multiple compressors can be served with a single chiller, the valving and logic can be prohibitively expensive; it may be more economical to provide for a single acid gas chiller for each compressor. If a new refrigeration process module is required, it can take up plot space equivalent to that of the acid gas compressor.

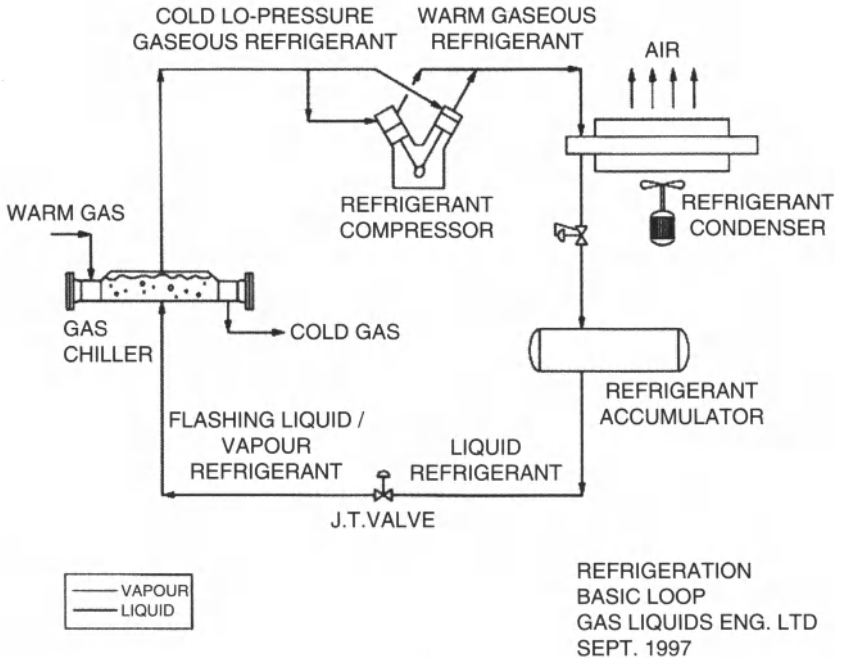

Figure 7.12 Typical simple cycle refrigeration loop.

As well, it will require a refrigerant condenser, lube systems, power, gas detection, and capacity/shutdown controls. Maintenance of the refrigerant system would be per normal equipment requirements. A typical closed loop refrigeration process is shown below:

Internal refrigeration processes are based on using the process fluid as the refrigerant. This can be accomplished in several ways including:

- JT or "choke" type arrangement with a gas/gas exchanger.
- DexPro[5]

Hydrogen sulphide, carbon dioxide and sulphur dioxide all display excellent refrigerant properties. Comparing the JT coefficients of typical process fluids in an unusual format shows:

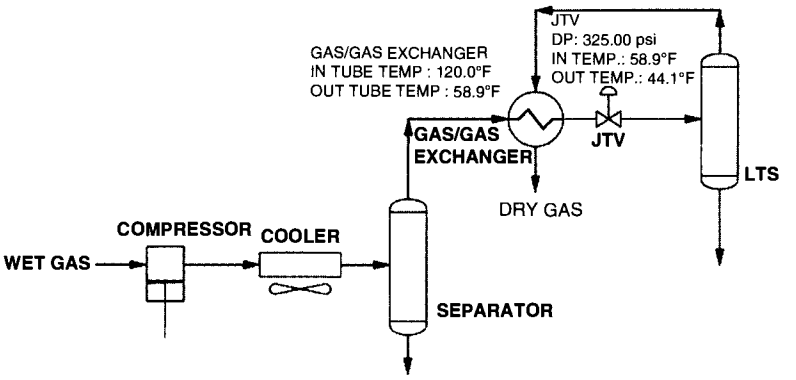

Figure 7.13 Simple natural gas JT process schematic.

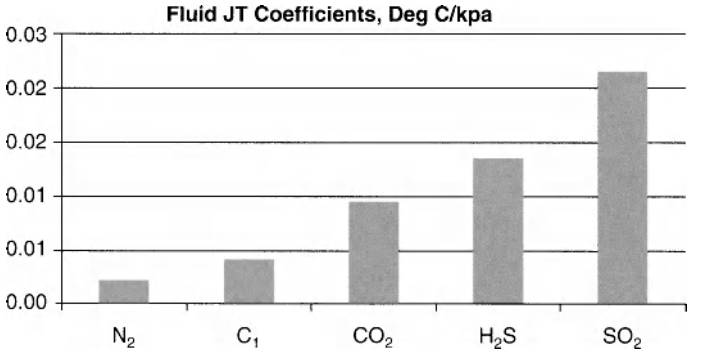

Figure 7.14 Process fluids, comparative JT coefficients[1].

[1] At a temperature of 50°C & pressure of 652 kPaa.

Several process fluids exhibit outstanding JT coefficients resulting in a significant cooling effect across the JT valve. Hydrogen and helium do not always display a temperature drop across a JT valve. If the starting temperature of the fluid is below the JT (joule thomson) inversion temperature, then the fluid will cool. If the fluid starting temperature is above the JT inversion temperature (of that fluid), then the fluid will warm on expansion. Nitrogen has an inversion temperature of 348°C – consequently, almost all nitrogen gas mixtures will cool on expansion. The inversion temperature of helium is –222°C – consequently, most helium mixtures will warm on expansion.

Barring the safety issues of cryogenic hydrogen sulphide, this fluid has outstanding refrigerant properties. In its most simplistic form, the basic process would overcompress the final fluid to allow for a JT effect and then use the cooled fluid to chill the process gas at an intermediate pressure – the basic "choke" plant arrangement. Alternately, a small system (comprising of a separator or receiver and pump) could pump a slipstream of the final fluid up to an elevated pressure prior to the JT valve. This basically provides a similar effect to the external refrigeration process. A better way to illustrate this point is with a simple P-H diagram of carbon dioxide:

The below plot shows the compressor performance, hydrate curves, and phase behavior of a pure CO_2 system:

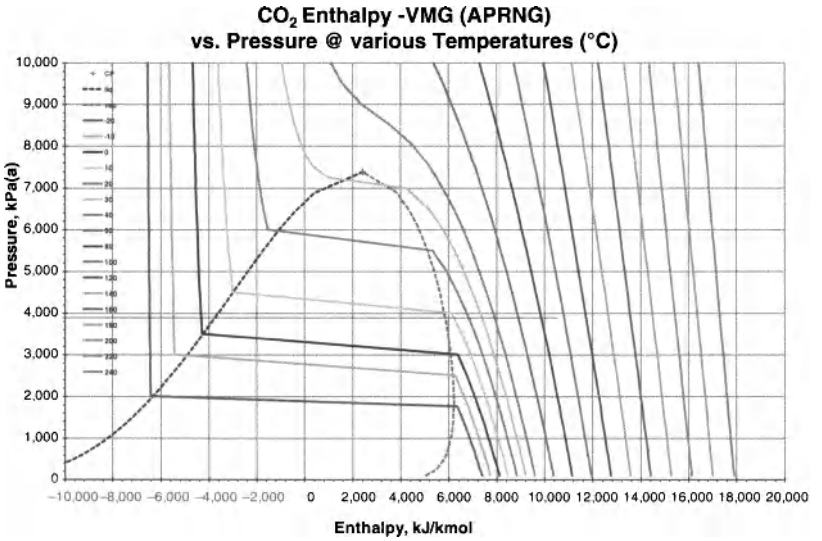

Figure 7.15 PH Diagram for CO_2.

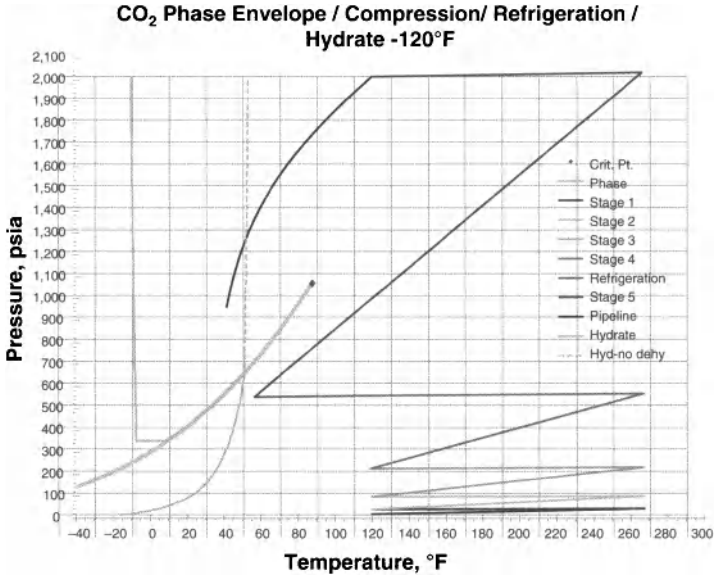

Figure 7.16 Temperature based CO_2 system performance.

7.6 Development of DexPro

The natural extension to this concept is the DexPro™ process. The basic premise of the system is that a small slipstream (typically 10-20%) of the dense phase final acid gas fluid is passed through a temperature control JT valve and reinjects it into the proprietary DexPro module upstream of the final stage suction scrubber.

This system requires multistage compression with the interstage pressures being (ideally) optimized to allow for maximum water dropout in accordance with normal CO_2/water behavior. This DexPro module allows for proper mixing of the streams while minimizing the potential of hydrate formation. The mixing of the now dry acid gas with warm wet acid gas on either 4th stage or final stage suction allows the resulting mixture to cool sufficiently to drop out the desired amount of water. There are some important design considerations:

- The process is compositionally dependent. The higher the CO_2 content, the less of a natural dehydration effect is achieved and more refrigeration effect is

necessary to achieve water extraction. However, the process is also self-adjusting to achieve the required water content.

- The process can be adjusted to earlier stages with several mixing stations to achieve lower water content and hydrocarbon removal.
- Higher H_2S content streams require less refrigeration to achieve satisfactory water content, but more attention must be paid to avoid excursions into the phase envelope.
- Hydrate formation temperature of the DexPro fluid must be avoided after expansion – methanol can be used to boot-strap the process until the system achieves specification water content.
- Special attention must be paid to the phase behavior and hydrate formation temperatures – for maximum water removal, the system should operate as close to the fluid dewpoint line as possible without hitting the hydrate point.
- Temperature control of a number of elements of the process is important to avoid excursions into potential hydrate zones.
- The mixing pressure, should ideally take place at or near the lowest point of the water content curve for that particular fluid. This allows for the highest offset between the water content and the possible saturation water content. This reduces the amount of work that either of the refrigeration based process are required to do.

As the colder reinjection fluid is mixed with the hotter fluid from the intercooler, the resulting temperature is reduced and excess water drops out in the downstream compressor suction scrubber (downstream of the DexPro module). The resulting cooled acid gas is then compressed in the final stage of compression and aftercooled for either injection requirements or pipeline. The resulting water content at the higher pressure is much lower and typically meets the 30 #/MMSCF criteria.

An interesting side effect is that the colder final stage suction temperature allows for adjusted compression ratios on the higher stages. This allows for reduced operating temperatures and an improved thermodynamic efficiency resulting in an almost net zero theoretical horsepower addition due to lowered cylinder temperatures.

This process has a number of advantages including:

- Very small equipment (physical) footprint – can be done usually within the compression package (makes use of existing compressor building utilities and safety systems).
- No incremental rotating equipment with the exception of the methanol injection pump – only required during startup or during low residual water criteria scenario's.
- Low capital cost
- Negligible operating costs
- Very small environmental footprint
- No hygroscopic fluid carryover to impact corrosion integrity
- No fugitive emissions or off-gas handling
- Extreme turndown

In order to maximize the system opportunities and design performance of DexPro, it is critical that it be integrated into the overall performance and design of the compressor. Thus, selection of the DexPro process is best done at the time of the compressor selection for optimal cylinder or compressor selection and proper inter/aftercooling engineering. Off design conditions must be considered along with turndown, future cases, and ambient variations. As well, a number of compression system operating data points are required to be passed back and forth to the DexPro control system; it is important to engage the compressor packager/designer in the early aspects of the DexPro equipment. The use of DexPro may alter cylinder selections, turndown considerations, control systems, and scrubbers/LCV's. It should be noted that the current design is based on cascading scrubber dumps for optimum degassing, two(2) stage warm/cold recycle system, and advanced cooler controls.

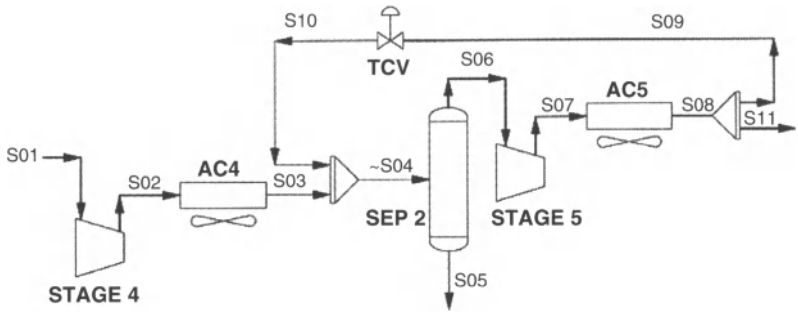

Figure 7.17 Basic dexpro configuration.

The DexPro system utilizes an Ametek (5100 series) laser based moisture analyzer that will allow for control parameter tracking as well as monitoring system CO_2 (and/or H_2S) content for algorithm management. This laser analyzer, along with a mass flow meter is mounted inside the compressor package. Inputs from this and other process devices go into an advanced control system and are housed in a separate PLC control system. This control system enables a high degree of automation.

The DexPro module is fabricated of stainless steel and is usually fitted in upstream of the final stage suction scrubber. It utilizes proprietary internal technology to prevent hydrate formation as well as ensuring adequate mixing of the process fluids.

The first two(2) commercial DexPro pilot units have recently been installed at Murphy Oil Company Ltd's Tupper West Gas Plant near Dawson Creek, British Columbia. Each 100% duty compressor is designed to move a maximum of 24 e3m3/day of nearly pure CO_2 into an injection line and to a nearby disposal well approximately 2 km away. Given the high level of integration with the compressors, it was decided that each compressor package would be equipped with its own dedicated DexPro system. This would provide for full redundancy as well as ensuring minimal interaction during backup unit performance. In the event of a compressor or DexPro problem, the standby compressor could be quickly warmed up, and put on line.

This large natural gas plant was commissioned this past winter and came online with sales gas Feb 22, 2011.

These two (2) initial units were commissioned early in 2011 and are currently in operation. Although the startup took place during intensely cold weather conditions (typically –30 to –40°C), the first years' performance is promising. Water content is settling out well below the desired 30 #/MMSCF, although fine tuning has yet to

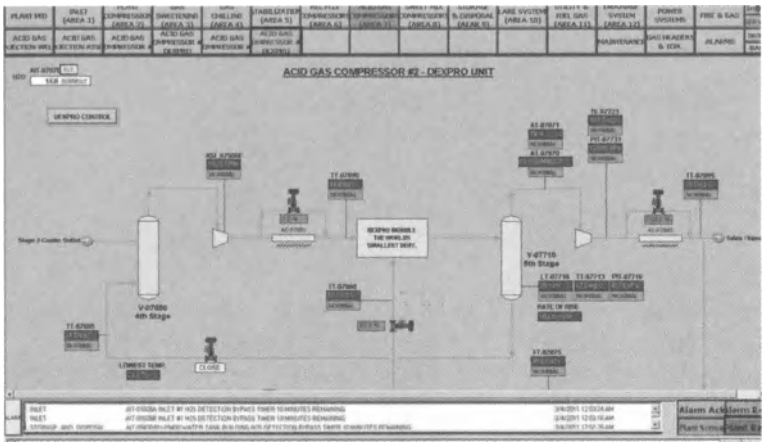

Figure 7.18 Screen capture at tupper west.

take place. Acid gas injection is taking place and the system is performing as expected. The below screen shots were from the evening of initiation of acid gas injection – Mar 3, 2011:

The DexPro system at Murphy Oil Company Ltd's Tupper West facility is online, working well, and dehydrating the acid gas to below the required specifications. This may (in part) be due to lowered ambient temperatures resulting in better pre-dropout of water, slightly higher H_2S content during the initiation, and possibly higher DexPro rates and methanol injection to result in a "safe" zone. The current level of acid gas dehydration is about 16–20 lb/MMSCF.

Remote monitoring of the system is being setup for home office monitoring of the system performance and optimization.

A comparison of dehydration technologies (for a 10 MMSCFD pure CO_2 stream) is shown in the below table:

	CAPEX	OPEX	NPV
DexPro	$574,047	$37,230	$968,462
Refrig	$985,050	$76,039	$1,790,608
TEG	$1,443,250	$111,187	$2,621,167
TEG+VRU	$1,809,500	$112,063	$2,996,697

Figure 7.19 NPV for 10 MMSCFD CO_2 Dehydration[2].

[2] Does not include license fees. Based on 7% discount rate over 20 years, Cdn $.

DexPro is an excellent candidate for carbon capture and sequestration:

- Carbon dioxide has excellent properties for use within DexPro and is a predictable fluid.
- Allows for minimum footprint and customized dehydration – does not over-dehydrate fluid.
- No fugitive emissions, maintenance, fluids, and/or filters to change.
- Integrated design with compression system
- Minimal energy usage, and operating costs.
- Very small environmental footprint
- No hygroscopic fluid carryover
- Can be integrated with cooling water system for precise process control
- Excellent turndown

7.7 DexPro Operating Update

Considerable testing has taken place at the Tupper West facility throughout varying analyses, ambient conditions and flowrates. As per the figure below, the system continues to perform well and easily meets the 30 lb/MMSCF water content specification.

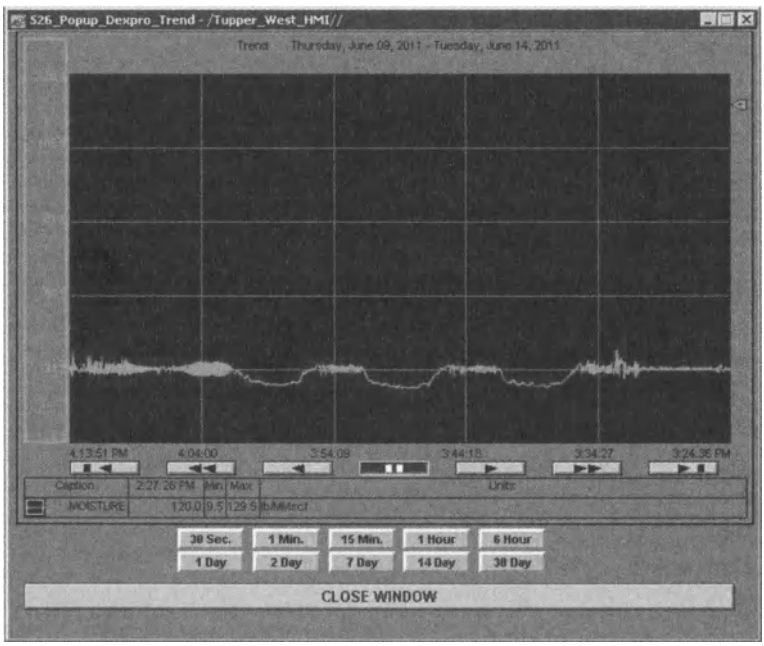

Figure 7.20 System performance.

Operator intervention is minimal with no dewpoint excursions. Control system tuning continues intermittently with some analyzer issues with regards to lube oil contamination as well as ambient temperature variations. The site operations team is very pleased with the units and their lack of maintenance – essentially this is a hands-off operation.

7.8 DexPro Next Steps

Integration with a real-time process simulator is being planned to allow for online prediction of phase envelope dewpoints and hydrate temperatures – currently this fluid is being modeled as a binary fluid with CO_2 as the primary test fluid. Although composition can often vary in gas processing facilities, the variation is typically a binary function with H_2S and CO_2 content; other components are generally considered to be relatively constant and the predictions can be adjusted with a minor correction.

Development of advanced versions of DexPro to allow for lower water contents; including development of a fulltime methanol assisted DexPro to allow for dramatically lower water content. As well, DexPro engineering development is showing promise for EOR based CO_2 dehydration as well as variants that can result in incremental hydrocarbon liquids recovery.

Offshore acid gas applications look promising due to substantially lowered physical parameters of DexPro systems compared to conventional systems. The result is a dehydration package that is less than 7% of the weight and 11% of the footprint when compared to a conventional dehydration system[6].

As well, a retrofit version has been developed that can allow better integration into an existing compressor application.

7.9 Murphy Tupper – 2012 Update

After 13 months of online performance, the two(2) initial DexPro units continue to operate with minimal operator involvement. Water content remains low and system stability is strong. The chart shown below illustrates acid gas water content on December 27, 2011. Analyzer response swings have been eliminated with regulator temperature control and finer regulator pressure control.

The below screen shot is a snapshot view of the DexPro control systems screen in normal operation:

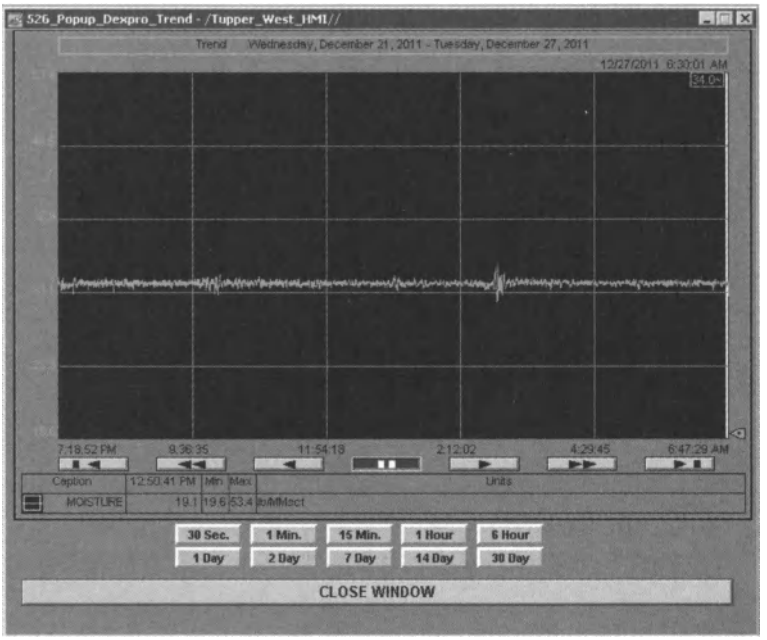

Figure 7.21 December 2011 water content.

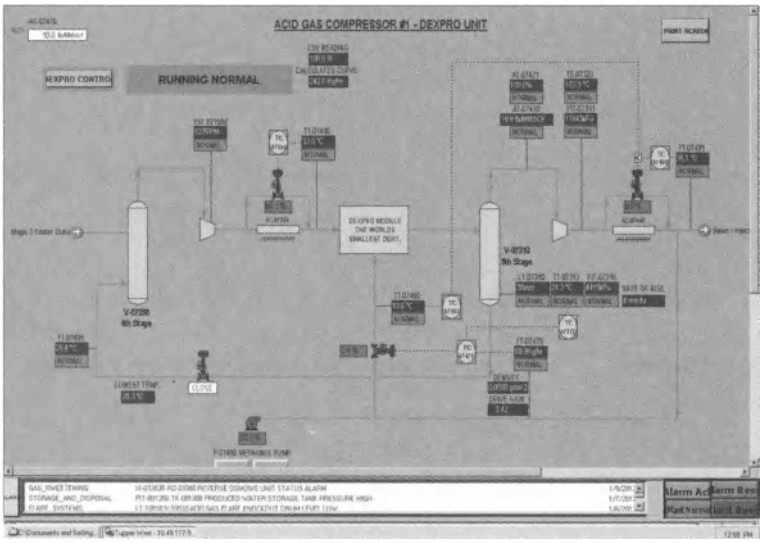

Figure 7.22 DexPro control screen.

7.10 Acknowledgements

1. Carroll, "Phase Equilibria Relevant to Acid Gas Injection," CGPA, May, 1999.
2. McKetta – Wehe, *Petroleum Refiner*, August 1958.
3. Wichert, G.C. and Wichert, E., "Chart Estimates Water Content of Sour Natural Gas," *Oil & Gas J.*
4. Wallace, C.B., "Dehydration of Supercritical CO2," *Proceedings 1985 LRGCC Gas Conditioning Conference*, Univ. of Oklahoma, Norman, OK.
5. Canadian Patent Issued, J. Maddocks, Wayne McKay.
6. McKay, W., "CO2 Dehydration... is there a better way?" *Carbon Capture Journal*, 2011.

8

A Look at Solid CO_2 Formation in Several High CO_2 Concentration Depressuring Scenarios

James van der Lee[1], John J. Carroll[2], and Marco Satyro[1]

[1]*Virtual Materials Group Inc., Calgary, AB, Canada*
[2]*Gas Liquids Engineering Ltd., Calgary, AB, Canada*

Abstract

In recent years, there has been an increase in processes dealing with high concentrations of CO_2 at high pressures, such as carbon sequestration, enhanced oil recovery, and supercritical CO_2 extraction processes. Given these conditions, there are questions about the expected behavior when these systems experience substantial pressure drops, specifically whether solid CO_2 formation will occur. These pressure drops could be either an integral part of the typical process operation, or during a depressuring or relief scenario. This paper will investigate the behavior of several typical pressure drop scenarios at a variety of conditions and compositions, with the intent of highlighting areas that may be of concern.

The investigation will be based on a number of steady state and dynamics simulations, which will make use of a thermodynamic model that was specifically built to be able to predict both the conditions at which solid CO_2 will form, as well as the amount. An overview of the basis of the thermodynamic model and the basis of the simulation methodology will be provided. A summary of whether CO_2 solid will form in each scenario investigated will be presented.

8.1 Introduction

The study focuses on the blow down of CO_2 storage vessels; which are becoming increasingly prevalent due to EOR activity throughout the world. The intent of this work is not to provide a basis for

Ying (Alice) Wu, John J. Carroll and Weiyao Zhu (eds.) Sour Gas and Related Technologies, (117–128)

the design or safety issues related to the blow down of such vessels, but rather to illustrate some circumstances where CO_2 solid may form during the course of a blow down. These could in turn be used as a guideline to determine when a more detailed investigation may be warranted.

Three different pressures of saturated CO_2 are examined in this work, along with the effect of a liquid or vapour draw during the blow down.

8.2 Methodology

This study was conducted by developing models of the various blowdown scenarios in the process simulator VMGSim. VMGSim is capable of performing rigorous steady state and dynamic simulations. The dynamic simulation engine in VMGSim solves for a series of dynamic states where each state is calculated at a user-set step size. Rather than solving unit operations in sequential order (as in steady state), the dynamics engine solves pressures and flows using a network (simultaneous) solver, and energy and composition balances on a per unit operation basis. This provided the ideal basis to conduct a study of this type. Another important consideration in the development of the models used in this study is the thermodynamics property package, specifically its ability to predict the phase equilibrium when solid CO_2 may form in the course of the blow down.

8.3 Thermodynamic Property Package Description

The APRCO2 property package is based on the APR package with special handling of CO_2; the package can predict the formation of solid CO_2. All results for SLVE are predictions based on the APR model and a rigorous model for the fugacity of solid CO_2. The thermodynamic basis for thermodynamic equilibrium calculations is given by equation 8.1.

$$f^{v}_{CO_2} = f^{l}_{CO_2} = f^{s}_{CO_2}. \tag{8.1}$$

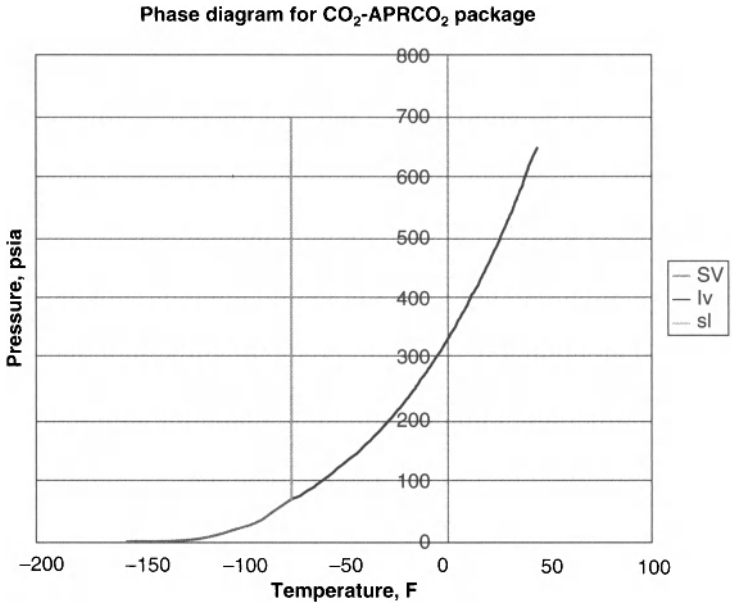

Figure 8.1 Phase diagram for CO_2 – APRCO2 package. Phase boundaries calculated using APRCO2. Note that the SL boundary was located by trial and error.

Fugacities of all other components in the solid phase are set to an arbitrarily large value ensuring the solid phase contains essentially only CO_2. Necessary modifications for the calculation of enthalpies and densities of a solid CO_2 phase were also added to the package. The ability to predict the existence of a solid phase allows for a more complete depiction of the phase diagram of a pure substance. In standard property packages the phase boundaries are always vapour-liquid or liquid-liquid. With an active solid phase we can also have vapour-solid as well as liquid-solid boundaries. This behaviour is shown in Figure 8.1, the phase diagram for CO_2.

The triple point calculated by APRCO2 is equal to 216.73 K and 513.31 kPa. The recommended values are 216.59 K and 517.88 kPa (RefProp).

8.4 Model Configuration

All cases assume that the initial inventory of the vessel is 100 tonnes and is contained in a vessel that is of the same size. The liquid level was adjusted so that the total inventory (saturated vapour and

saturated liquid) was 100 tonnes. The vessel size was set to be 15-m in length and 3.75-m in diameter, the vessel was assumed to have flat heads. The thickness of the vessel shell was assumed to be 2-in and a 4-in layer of insulation. The initial wall temperature of the vessel shell was assumed to be the same as the saturation temperature at the three pressures.

The relief devices used were valves that were sized using a CO_2 stream at the initial condition that would be experienced during the blow down and a flow rate of 400000 kg/h, with a downstream pressure of 1 bara. The valve sizes for the different scenarios are shown in Table 8.1.

Figure 8.2 shows a process schematic of the dynamic models used in this study, where the primary difference in the configuration in

Table 8.1 Summary of the valve Cv for the different blowdown scenarios.

P (bara)	20	40	60
Vapour Draw Cv	1500	750	250
Liquid Draw Cv	200	150	75

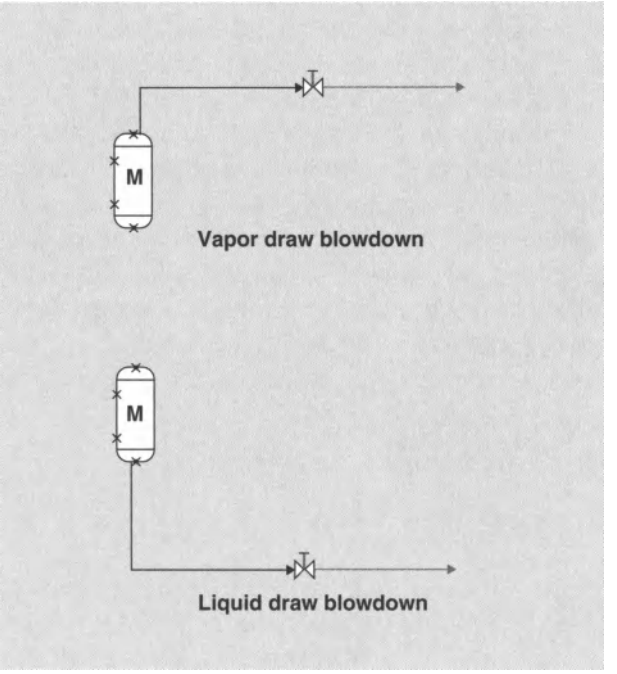

Figure 8.2 Process schematic of the simulation model used in this study.

the model being whether the draw was taken from the liquid or the vapour. The configuration of the vessel was such that if the liquid level was lower than 5%, the draw stream would contain both vapour and liquid. The valve would then relieve the pressure of a two-phase stream.

8.5 Results

The following are the results from the blow down of the CO_2 present as a saturated liquid with an initial pressure of 20, 40 and 60 bars, in which the draw was taken either from the vapour or liquid phase. The results presented for each scenario show the vessel holdup temperature, the downstream valve temperature and the holdup pressure in the plot labelled A. The plot labelled B shows the molar flow rates of the vapour and solid CO_2 phase downstream of the let down valve. While the plot labelled C shows the total mass inventory of the vessel, including the mass of all of the phases contained in the vessel.

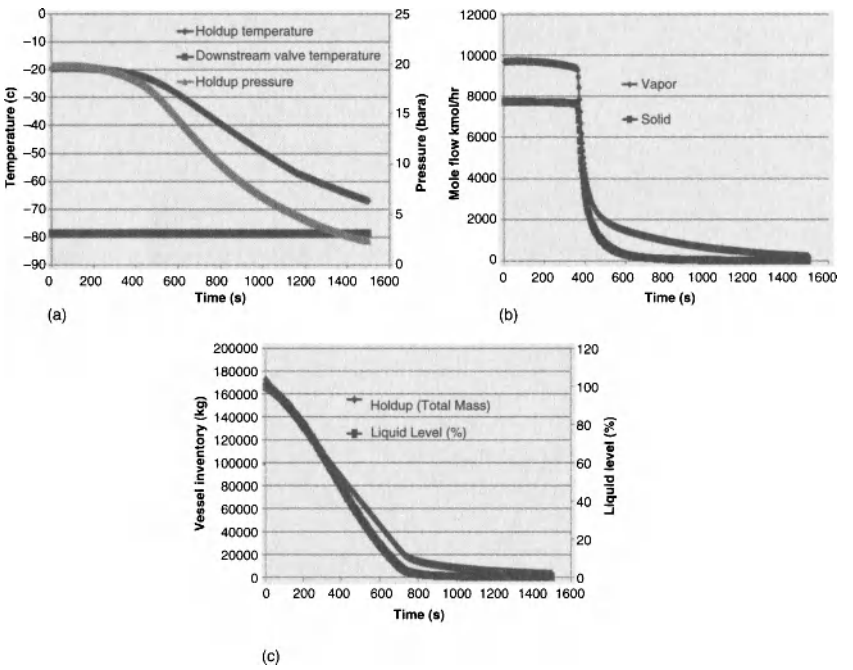

Figure 8.3 20 bara blow down using liquid draw.

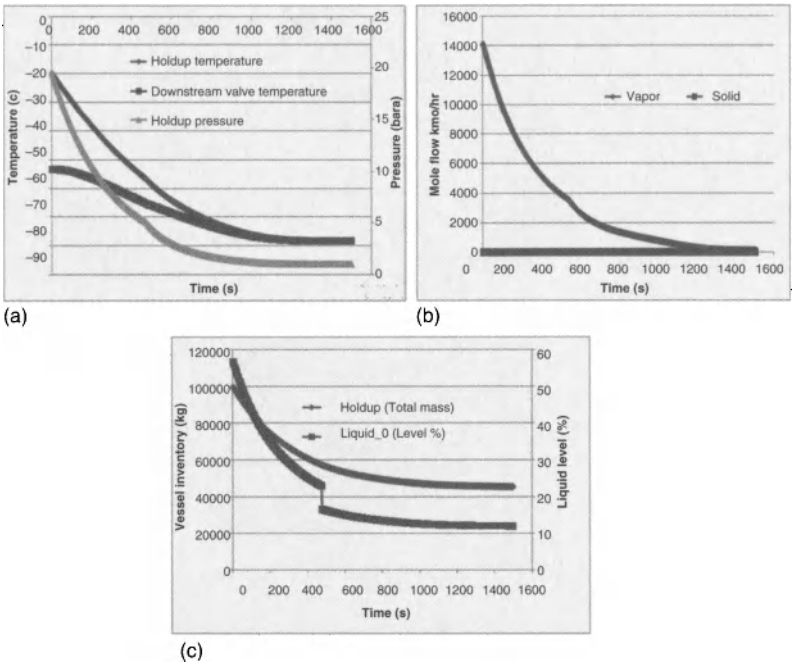

Figure 8.4 20 bara blow down using vapour draw.

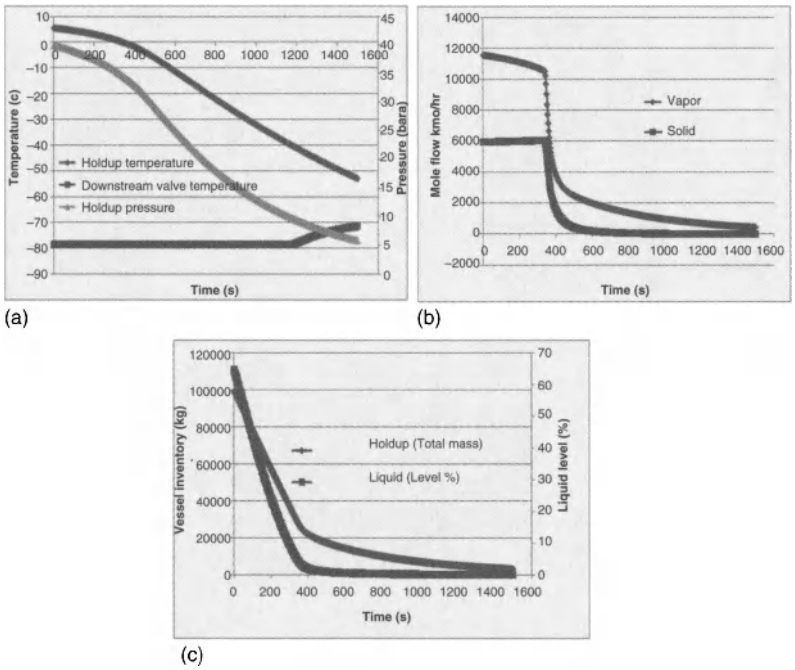

Figure 8.5 40 bara blow down using liquid draw

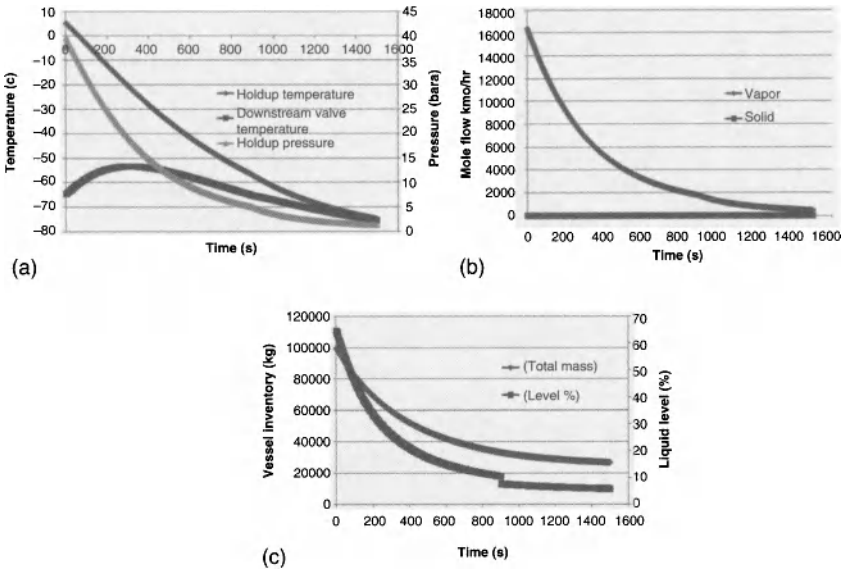

Figure 8.6 40 bara blow down using vapour draw.

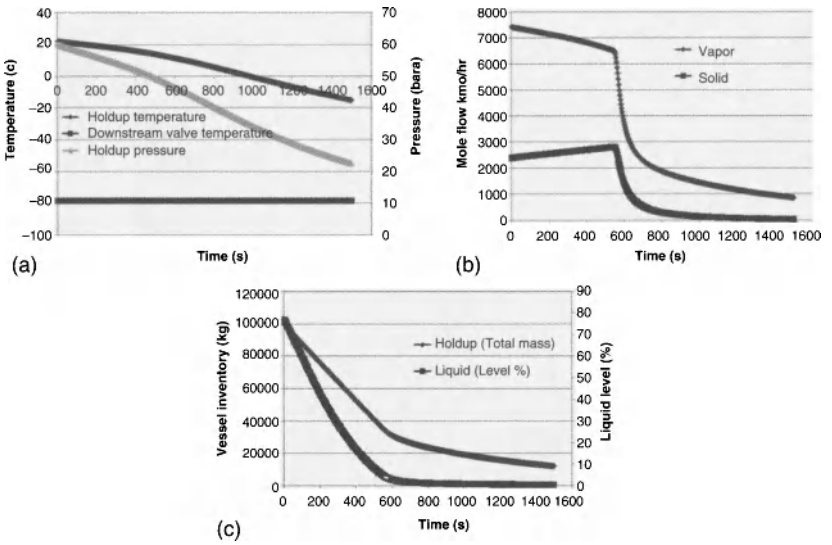

Figure 8.7 60 bara blow down using liquid draw.

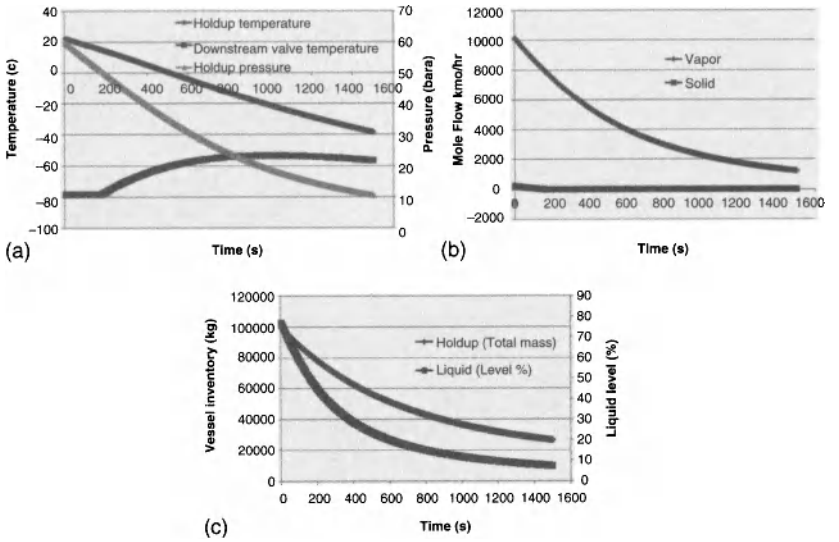

Figure 8.8 60 bara blow down using vapour draw.

8.6 Discussion

8.6.1 20 bar

8.6.1.1 Vapour Blow Down

Looking at Figure 8.4A it can be seen that the hold up pressure and temperature drops significantly over the course of the blow down. This is largely attributed to the fact that the heat required to vaporize the CO_2 leaving through the vapour letdown valve is provided by a sensible heat decrease in the CO_2 hold up temperature. Figure 8.4A and Figure 8.4B also show a distinct change in slope in the holdup pressure curve and downstream vapour flow rates at around 460s into the blow down. It is also worth noting that solid CO_2 is not formed downstream of the letdown valve during the course of the blow down. At this same time, Figure 8.4C shows a sudden drop in the liquid level in the vessel which indicates that the liquid contained in the vessel has transferred to the solid phase, this is confirmed by observing that the hold up pressure at this time is approximately the triple point pressure. It is interesting to see that during the final stages of the blow down in this scenario, inventory reduction occurred via the sublimation of CO_2 into the vapour phase.

8.6.1.2 Liquid Blow Down

Looking at Figure 8.3A, the temperature of the hold up for the duration of the blow down is significantly higher than that of the vapour blow down case. Figure 8.3B shows there is a significant amount of solid CO_2 produced downstream of the letdown valve during the first portion of the blow down, which is characterized by a predicted outlet valve temperature of approximately -80C. This corresponds to the temperature of CO_2 vapour and solid and liquid in equilibrium with each other at 1 bara. There is a substantial amount of inventory that leaves the vessel during the first portion of the blowdown. During the later stages of the blowdown there is a significant drop in the solid CO_2 flow rate after the letdown valve, this corresponds to the vessel liquid level approaching 5%; at this point a significant amount of vapour will be leaving through the liquid draw. The rate at which material can pass through the letdown valve drops significantly thus the slowing of the rate of vessel inventory.

8.6.2 40 bar

8.6.2.1 Vapour Blow Down

Looking at Figure 8.6 it can be seen that the blow down behaviour with a vapour draw and an initial vessel pressure of 40 bara is similar to the blow down with a vapour draw and an initial vessel pressure of 20 bara.

8.6.2.2 Liquid Blow Down

Looking at Figure 8.5 it can be seen that the blow down behaviour with a liquid draw and an initial vessel pressure of 40 bara is similar to the blowdown with a liquid draw and an initial vessel pressure of 20 bara.

8.6.3 60 bar

8.6.3.1 Vapour Blow Down

Looking at Figures 8.8A and B it can be seen that there is solid CO_2 formed on the downstream side of the blow down in the case with an initial pressure of 60 bara and a vapour draw. As the blow down

proceeds the vessel hold up temperature and pressure drops and, perhaps somewhat counter intuitively at around 200s after the blow down started, solid CO_2 is no longer formed at the outlet of the blow down valve. In this case it is informative to look at several points in time of the blow down on a PH diagram (Figure 8.10).

The area labelled Vapour + Liquid in Figure 8.9 indicates the phase boundary where vapour and liquid will be in equilibrium with one another. The line as the triple point line indicates where the three phases can coexist; the temperature and pressure at this

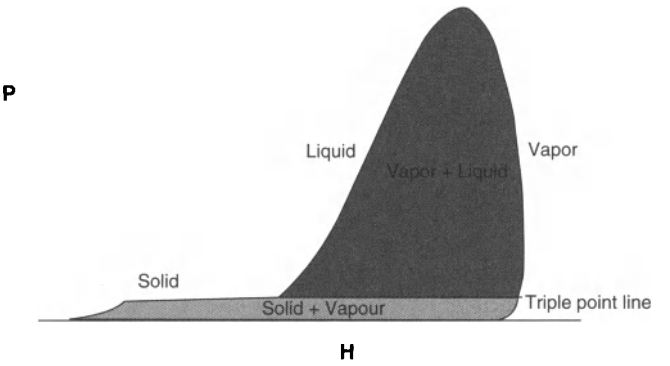

Figure 8.9 PH diagram for CO_2 with vapour + liquid and vapour + solid phase regions.

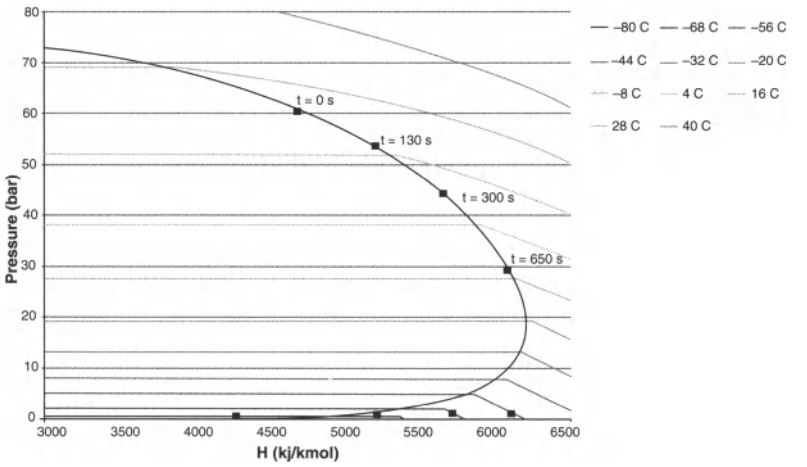

Figure 8.10 Isenthalpic pressure drop at different points in time for 60 bara initial, vapour draw blowdown on plotted on s PH diagram.

point is fixed. The area labelled Solid + Vapour indicates the phase boundary where vapour and solid will be in equilibrium with one another. In this region, dry ice will only sublimate into vapour CO_2. As the low pressure side of the letdown valve was assumed to be 1 bara, only vapour and solid phases could occur here.

While the overall blowdown process cannot necessarily be simplified as being isentropic or isenthalpic. The pressure drop across the letdown valve at any given time can be well represented by an isenthalpic pressure drop. Figure 8.10 shows such an isenthalpic pressure drop for a number of different points during the 60 bara initial pressure vapour draw blow down scenario.

The point labelled t = 0 s on Figure 8.10 shows the isenthalpic pressure drop from a saturated vapour at 60 bara to 1 bara. This isenthalpic pressure drop from 60 bara results in the 1 bara point being in the vapour solid two phase region, which corresponds to the results seen in Figures 8.8A and 8.8B. The point labelled t = 130 s shows the pressure at which isenthalpic pressure drop to 1 bara will fall just on the vapour boundary when drawing from a saturated vapour. This is the lowest pressure in which an isenthalpic pressure drop to 1 bara could result in the formation of solid CO_2 on the downstream side of a letdown valve. The points at t = 300 and 650 s show an isenthalpic pressure drop to 1 bar that will result in only a vapour phase being present downstream of the letdown valve despite the cooler hold up temperatures.

8.6.3.2 Liquid Blow Down

Looking at Figure 8.7 it can be seen that the blow down behaviour with a liquid draw and an initial vessel pressure of 60 bara is similar to the blow down with a liquid draw and an initial vessel pressure of 20 bara.

8.7 Conclusions

The blow down of a saturated CO_2 vessel in general leads to several interesting scenarios. If a strictly vapour blow down is conducted the formation of solid CO_2 is mitigated, if not completely, during the blow down, depending on the pressure. Although inventory reduction is possible with a strictly vapour phase blow down, it is limited by the accelerated cooling of the vessel contents due to the

fact that there is a heat of vaporization. On the other hand, a liquid draw blow down will result in significant quantities of dry ice being formed on the outlet of the letdown valve for the duration of the blow down. This would require special design considerations in order to be able to handle these quantities of dry ice in the blow-down lines. Also, given the fact that the majority of the inventory removed was in the liquid phase, the temperatures experienced within the vessel are significantly higher than that of a vapour phase blow down. This results in a significantly higher residual pressure within the holdup vessel. Perhaps a blow down system which makes use of both vapour and liquid draws at various points in time of the blow down should be considered.

References

1. RefProp ver 8.0, National Institute of Standards and Technology, Boulder, Colorado, USA.
2. VMGSim 6.5b10, Virtual Materials Group Inc., Calgary, Alberta, Canada.

PART 3
ACID GAS INJECTION

Ying (Alice) Wu, John J. Carroll and Weiyao Zhu (eds.) Sour Gas and Related Technologies, (3–20)

9

Potential Sites and Early Opportunities of Acid Gas Re-injection in China

Qi Li[1,2], Xiaochun Li[1,2], Lei Du[3], Guizhen Liu[2], Xuehao Liu[2], Ning Wei[2]

[1]*State Key Laboratory of Geomechanics and Geotechnical Engineering, Institute of Rock and Soil Mechanics (IRSM), Chinese Academy of Sciences(CAS), Wuhan, China*
[2]*Energy and Waste Underground Storage Research Center, IRSM, CAS, Wuhan, China*
[3]*China Petroleum Engineering Southwest Company, Chengdu, China*

Abstract

In this paper, some key problems of acid gas re-injection are generally revealed, at first for co-storage situations of CO_2 and the strong acid gas H_2S/SO_2 into subsurface reservoirs. Then, under the limits of acid gas re-injection benefits and drawbacks, the potential sites suitable for acid gas re-injection in China are analyzed by using the developed CCS integrated database on the platform of ESRI ArcGIS. The potential storage sedimentary basins and deep saline aquifers are focused to be investigated for acid gas re-injection. In general, sedimentary basins usually are the oil, gas, and/or coal reservoirs. Except for EOR, EGR, and ECBM by injection of CO_2, the depleted reservoirs are suitable for sequestration of acid gases. The insights of potential sites are gained by source-site matching analysis in ESRI ArcGIS and some tailored numerical simulations. Preliminary study shows that there are enough potential storage sites for acid gas re-injection, particularly in the mid-developed regions of China. Furthermore, with considerations of aforementioned constraints and boundary conditions, some early opportunities can be listed for the implementation of acid gas re-injection in China. The analysis suggests that there are many early opportunities. The potential acid gas re-injection projects with early opportunities can be different combinations of high purity CO_2 and/or

Ying (Alice) Wu, John J. Carroll and Weiyao Zhu (eds.) Sour Gas and Related Technologies, (131–142)

H_2S/SO_2 sources, good storage sites, and value-added byproducts. These early opportunities will provide China chances to have a quantum leap on CCS technologies, from early stage to commercial operation. Finally, the feasibilities and difficulties of implementing acid gas re-injection are concluded for the current stage in China.

9.1 Introduction

In terms of total emissions, China has overtaken the USA as the largest CO_2 emitter in the world. This is mainly due to China's relatively high energy intensity compared to developed countries during latest impressive growth [1]. China will reduce the intensity of carbon dioxide emissions per unit of GDP in 2020 by 40 to 45% compared with the level of 2005. Even as a lower carbon economics future is being transited in China, fossil fuels will still continue to play a major role in the energy structure for many years. Carbon dioxide capture and storage (CCS) is being widely accepted as one of main solutions to mitigate global warming. China is planning to play a more active role in the CCS field. However, the still-very-high cost and potential risks of CCS are some ones of the major concerns to block its implementation, in particular in the developing countries like China. In the other hand, emission control of SO_2 and COD (Chemical Oxygen Demand) has specific reduction target in the latest Five-Year Plan of China [2], just because both of them heavily impact the public health and sustainable use of energy and environment in comparison with greenhouse gases (GHG) such as CO_2. In particular, the acid rain cause serious economic losses for the most developed area of East China during China's impressive growth in the past. Therefore, re-injection of acid gases (AG), such as CO_2 and H_2S/SO_2, into subsurface reservoirs may be an effective way to reduce CCS cost, to meet the environmental control policy, and at the same time to boost up CCS to gain an early opportunity of operational industrial deployment [3].

Therefore, acid gas re-injection (AGI), i.e. capture and storage of CO_2 and H_2S/SO_2 together (SCCS), may be an effective solution to reduce CCS cost, e.g. due to saving the de-sulphur device, and power CCS to gain an early deployment opportunity in China. In the regime of SCCS, two sections can be investigated to integrate into current CCS implementation. The one is to do during the capture stage, and the other is to finish during the sequestration

stage [3]. If CO_2 and SO_2 can be captured together and be sequestered into the same potential reservoir, it will greatly increase the implementation of CCS. According to China's near-zero emission plan, SO_2 must be captured from industrial sour gases. In China, the captured H_2S/SO_2 from the sour gases was usually processed into sulphur. Furthermore, the processed sulphur faces the acute fluctuation of price in the marketplace, e.g. with the firm restriction of its usage in the food processing industry, a large consumer, for sake of safety. However, in the prospected future, the clear reduction control of CO_2 still has a long way to climb up. Whatever, there are some potential demands to cheaply sequester the acid gases mainly from industrial sector in the present and in the future. With consideration of China's economic and energy structures, SCCS would be a potential better solution to sequester SO_2 and CO_2 together rather than CCS. In particular, this technology could be extended to capture a significant fraction of the natural gas-associated CO_2 stream at low cost based on a cursory economic analysis in Canada [4].

Faced with the challenge of reducing atmospheric emissions of H_2S produced from sour hydrocarbon pools, oil and gas producers in western Canada, AGI into deep geological formations for the SCCS occurs over a wide range of aquifer and reservoir characteristics, acid gas compositions, and operating conditions since 1990 [5]. To date, there are more than 45 AGI schemes in Western Canada. The AGI technology is steadily developing in Canada [6]. In China, there is not yet AGI project under plan. As known, China's policy and characters of sedimentary basins are very different from those of Canada. With mitigating GHG emissions and growing environmental concerns, AGI also shows indeed promising as an option to eliminate the release of carbon dioxide and sulfur oxides to the atmosphere. Sulfur plants emit all of the CO_2 to the atmosphere and even the most efficient emit small amounts of SO_2. Since the very complicated tectonic structure of China in comparison with Canada', the whole subsurface part of SCCS faces some challenges, e.g., high fault density and low permeability of sediments. Furthermore, Co-storage of CO_2 with SO_2 results in a larger and more strongly acidified zone, and alteration differs substantially from that caused by the injection of CO_2 only [3, 7]. For the implementation of AGI into deep sedimentary basins in China, a thorough assessment of the disposal reservoirs is prerequisite, in particular the mechanical stability of the sequestered formation

during and after the injection of acid gases [8]. The study in this paper examines the potential storage sites of SO_2 co-storage with CO_2 into deep brine or sedimentary basins.

9.2 Potential Storage Capacity for CCS

This first-ever comprehensive survey of the potential for large scale CCS deployment in China finds that China has adequate deep geological storage capacity to meet likely demand for more than 100 years. Furthermore, the potential reservoirs are in good proximity to a large fraction of major stationary CO_2 point sources in China. This may significantly lower the cost of large scale greenhouse gas abatement [9, 10]. The calculation methodology of CO_2 emissions is mainly referred to the IPCC Guidelines for National Greenhouse Gas Inventories [11]. The methodology to be applied in storage capacity estimation, and the types and level of detail of the necessary data vary, depending on the scale and resolution of the assessment itself [12]. The storage capacity assessment methodology was constructed at the basin level. The emission estimation indicates that there are over 1,620 large stationary CO_2 point sources in China that each emits at least 100,000 metric tons of CO_2 per year. The total annual emissions from these sources are estimated over 3,890 million tons ($MtCO_2$). There are also 629 power plants emitting 72% of the total emissions [9, 13].

9.3 Emission Sources of Acid Gases

In general, the CO_2 point sources are also the emitter of other acid gases or greenhouse gases such as H_2S, SO_2 and NO_2. As know, industrial sectors are the largest contributor of AG/GHG in China [9]. With the examination study within the scope of coal-fired power plants, cement, iron and steel, petroleum refineries, ammonia, ethylene, ethylene oxide, and hydrogen industry, the locations of major acid gas emission sources are mapped in Figure 9.1. The majority of AG point sources are concentrated along the developed coastal zones of China and the heavily industrialized North China. This corresponds to the impact area of acid rain [14]. Power plants, iron-steel plants and petroleum refineries are the big three of AG

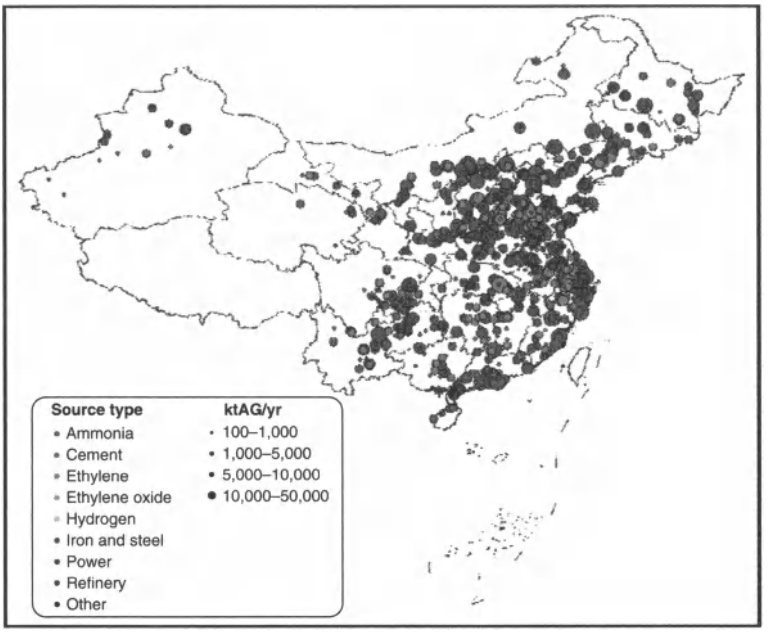

Figure 9.1 Location map of large AG point sources in China.

contributions in China. Heavy dependence of coal is the major origins of the AG emissions.

9.4 Distribution of High H_2S Bearing Gas Field

In general, there are different H_2S concentrations in natural gas resources. However, natural gas reserves with H_2S concentrations of more than 1% accounts for 1/4 of China's natural gas reserves [15]. The spatial distribution of sour natural gas fields in the sedimentary basins is apparently nonuniform in China. H_2S concentrations generally reach 10%–17% in the gas fields explored at Dukouhe, Luojiazhai and Puguang in the Northeastern Sichuan Basin which adds great difficulty to production safety and increases cost of capture and process of H_2S. Table 9.1 listed some major high H_2S bearing gas fields in China [16–18]. According to the classification criteria of sulfur gas fields as issued by the State Reserves Committee in 2005, a high sulfur gas field means that its H_2S content is no less than 30 g/m^3. The high sulfur gas fields are mainly in the northwest and northeast Sichuan Basin.

Table 9.1 High H_2S bearing gas fields in china

Basin	Gas field	H_2S Content	
		%	g/m^3
Sichuan	Zhongba	4.90	95.80–105.90
	Jinzhuping	-	92.30
	Dukouhe	15.27	231.93–244.05
	Luojiazhai	7.13–10.49	102.07–150.01
	Gunziping	13.74	196.57–203.93
	Tieshanpo	14.19	203.00–207.53
	Puguang	15.66–24.12	224.56–345.88
	Wolonghe	4.00–31.95	57.40–491.49
Bohai Bay	Luojia	4.35–6.50	62.38–93.21
	Zhaolanzhuang	63.00–92.00	903.42–1319.28

9.5 Systematic Screening of Potential Sites

It covers many factors to do a systematic screening of potential sites for AGI. The screening and selection of storage sites facilitates the management of uncertainties and minimization of risks associated with AG storage. The risks and uncertainties primarily arise from the subsurface characteristics. The processes should be examined and expressed in terms of costs that can be incorporated into the decision-making process. On the basis of different assessment flow, a range of different methods for site screening and selection are developed for CCS up to now, e.g. [19–24]. The evaluation methodology for AGI projects considers the most important factors involved in large-scale deployment of CCS projects and available data. In general, the factors included in the screening can be categorized as the following:

1. Capacity. Can potential sites hold as much AG as needed?
2. Injectivity. Can the storage site be filled at the required rate?
3. Risks related to long-term safety. Will stored AG remain safely in place?
4. Economics. Will the projects be economically feasible?

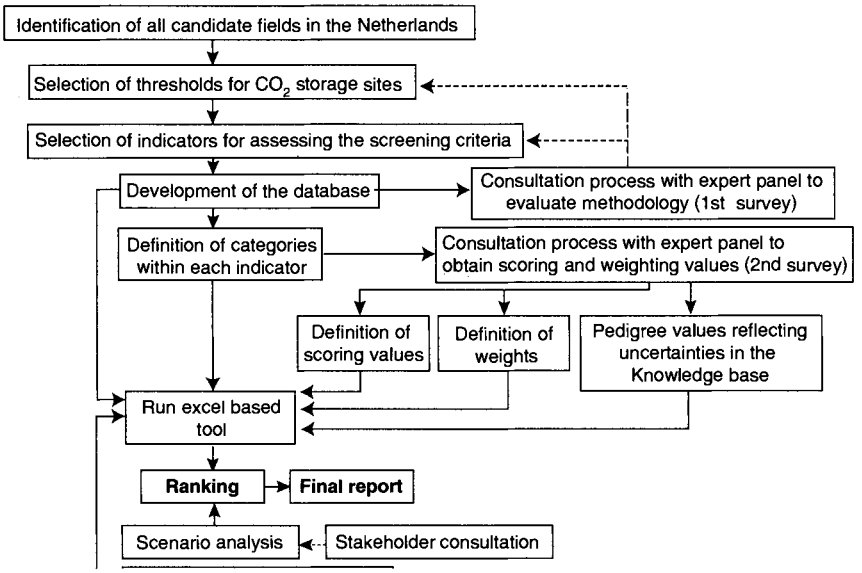

Figure 9.2 Schematic diagram of the methodology used in this research [24].

The screening of potential sites should include the management of qualitative and quantitative data and parameters. The process is based on a set of four priority objectives as follows:

1. Storage optimization in terms of capacity and injectivity;
2. Risk minimization, storage confinement and migration pathways;
3. Adherence to regulations, environmental constraints, existing land-use and underground use patterns;
4. Consideration of economic and social aspects.

Figure 9.2 shows a schematic screening flowchart used to develop the framework of site assessment .

9.6 Early Deployment Opportunities of AGI

To date, aquifer sequestration of CO_2 is still expensive, due mainly to the cost of CO_2 capture, purification and compression, and secondarily due to required field facilities and risk monitoring. Although there are many possibilities to reduce CO_2 emissions that are more

economically attractive, saline aquifer storage remains as one of the largest disposal sinks available for CO_2, and may be utilized if other less expensive options are exhausted [25]. As aforementioned causes in the introduction, capture and storage of CO_2 and SO_2 together (SCCS), may be a potential solution to reduce total cost of CCS, and it may provide an effective solution to gain the early chance to implement CCS in China. It also leads to an innovation of industrialization and localization during stepping on the SCCS.

The first acid gas re-injection (AGI) operation in the world was started in 1989 on the outskirts of Edmonton, Alberta, Canada [26]. It is no different from large-scale injection of CO_2 into depleted oil and gas reservoirs and into deep saline aquifers. AG such as H_2S and SO_2 is usually more toxic and corrosive than CO_2. The understanding of the nature of AG in the subsurface, such as rate and magnitude of geochemical reactions, is great important to evaluate storage capacity and injectivity of potential reservoirs. Before implementation of greenhouse gas geological sequestration, a series of questions need to be addressed. The most important ones are related to the short- and long-term fate of the injected AG. Such investigations ensure the operational aspects of co-storage into possible formations over a long period of time [3]. The success of the acid gas injection operations in Canada indicates that the engineering technology for CO_2 geological sequestration is well developed and ready for large-scale deployment.

In this paper, the potential storage sedimentary basins and deep saline aquifers are investigated for AGI in China. In general, sedimentary basins usually are the oil, gas and/or coal reservoirs. Except for EOR, EGR and ECBM, the depleted reservoirs are suitable for sequestration of GHG and AG. Figure 9.3 depicts the distribution of sedimentary basins of China. With comparison to Figure 9.1, it can be founded that the mainland sedimentary basins cannot provide adequate storage capacity for the high developed coastal zones in South China and Yangtze River delta. The marine sedimentary basins may be reasonable alternatives for these areas. On the other hand, if considering the option of deep saline aquifers (Figure 9.4) with a source-site matching analysis, it offers the largest potential storage capacity for AGI in China. The detail of the proposed analysis will be addressed in the following publication. Whatever, there is significant potential of storage capacity to meet the sequestration demand of SCCS and/or CCS.

Figure 9.3 Map of sedimentary basins in China.

Figure 9.4 Map of deep saline aquifers in China.

9.7 Conclusions

As aforementioned analyses, it looks at both the storage capacity and locations confirm that China has the theoretical capacity to

store the GHG and/or AG produced from its major point sources. Some concluding remarks can be addressed as follows:

1. Coal will remain at the centre of China's energy structure at least for some decades.
2. There appears to be enough storage capacity in China to store the majority of China's GHG/AG emissions from large point sources. However, more site-specific work is needed to facet this understanding.
3. AGI should be seen as one ambitious solution overall to motivate low-carbon energy strategy and domestic industrialization reform. SCCS is not a substitute for the CCS, and it is a potential solution to power CCS to gain early implementation chances.
4. Experience of Canada's AGI operations shows a certain confidence to the public on the geological sequestration of GHG/AG. However, it still has a lot of research work to do for the situations of AGI in China.

9.8 Acknowledgements

This research is partially funded by the Hundred Talent Program of Chinese Academy of Sciences and the China Australia Geological Storage (CAGS) Project.

References

1. OECD/IEA. *World energy outlook 2010.* International Energy Agency: Paris, France, p. 738, (2010).
2. Z. Wang; L. Pan. "Thinking on 11th five-year plan for SO_2 control at existing thermal power plants." *Electric Power (China)* 38, (11), (2005).
3. Q. Li; X.C. Li; N. Wei; Z.M. Fang. "Possibilities and potentials of geological co-storage CO_2 and SO_2 in China." *Energy Procedia* 4, 6015–6020, (2011).
4. S. Wong; D. Keith; E. Wichert; B. Gunter; T. McCann. "Economics of acid gas reinjection: An innovative CO_2 storage opportunity." *Greenhouse Gas Control Technologies, Vols I and II, Proceedings*, 1661–1664, (2003).
5. S. Bachu; W.D. Gunter. "Overview of acid-gas injection operations in western Canada." In *Seventh International Conference on Greenhouse Gas Control Technologies (GHGT-7)*, Vancouver, Canada, pp. 1–6, (2004).
6. J.J. Carroll. *Acid gas injection and carbon dioxide sequestration.* Wiley-Scrivener: Salem, Massachusetts, USA, p. 277, (2010).

7. T. Xu; J.A. Apps; K. Pruess; H. Yamamoto. "Numerical modeling of injection and mineral trapping of CO_2 with H_2S and SO_2 in a sandstone formation." *Chem Geol* 242, (3–4), 319–346, (2007).
8. Q. Li; Z.S. Wu; Y.L. Bai; X.C. Yin; X.C. Li. "Thermo-hydro-mechanical modeling of CO_2 sequestration system around fault environment." *Pure Appl Geophys* 163, (11–12), 2585–2593, (2006).
9. X.C. Li; N. Wei; Y.F. Liu; Z.M. Fang; R.T. Dahowski; C.L. Davidson. "CO_2 point emission and geological storage capacity in China." *Energy Procedia* 1, (1), 2793–2800, (2009).
10. R.T. Dahowski; X.C. Li; C.L. Davidson; N. Wei; J.J. Dooley; R.H. Gentile. "A preliminary cost curve assessment of carbon dioxide capture and storage potential in China." *Energy Procedia* 1, (1), 2849–2856, (2009).
11. IPCC. *Revised 1996 IPCC guidelines for national greenhouse gas inventories.* IPCC: Bracknell, UK, (1997).
12. S. Bachu; D. Bonijoly; J. Bradshaw; R. Burruss; S. Holloway; N.P. Christensen; O.M. Mathiassen. "CO_2 storage capacity estimation: Methodology and gaps." *International Journal of Greenhouse Gas Control* 1, (4), 430–443, (2007).
13. X.C. Li; N. Wei; Y.F. Liu; Z.M. Fang; B. Bai; R. Dahowski; C. Davidson. "CO_2 point emission and geological storage capacity in China." *IOP Conference Series: Earth and Environmental Science* 6, (17), 172026, (2009).
14. R.Q. Sun. "Pollution situation and control measures of sulphur dioxide in China." *Energy of China* 25, (7), 25–28, (2003).
15. W. Liu; Tenger; B. Gao; Z. Zhang; J. Zhang; D. Zhang; M. Fan; X. Fu; L. Zheng; Q. Liu. "H_2S formation and enrichment mechanisms in medium to large scale natural gas fields (reservoirs) in the sichuan basin." *Petroleum Exploration and Development* 37, (5), 513–522, (2010).
16. X. Ma. "High sulfur gasfields in China: Current status of exploration & development, and the challenges." In *7th Sino-US Oil and Gas Industry Forum*, UESA: Hangzhou, China, (2006).
17. G.Y. Zhu; S.C. Zhang; J. Li; Q. Jin. "Formation and distribution of hydrogen sulfide bearing gas in China." *Petroleum Exploration and Development* 31, (3), 18–21, (2004).
18. J. Zhao. "Key points on drilling and production safely with high efficiency in high H_2S and CO_2 gas reservoirs in China." *Natural Gas Industry* 27, (2), 141–144, (2007).
19. National Energy Technology Laboratory. *Best practices for: Site screening, selection, and initial characterization for storage of CO2 in deep geologic formations*; National Energy Technology Laboratory: p. 110, (2010).
20. CO_2CRC. *Storage capacity estimation, site selection and characterisation for CO_2 storage projects*; Cooperative Research Centre for Greenhouse Gas Technologies: Canberra, Australia, p. 52, (2008).
21. C.M. Oldenburg. *Health, safety, and environmental screening and ranking framework for geologic CO_2 storage site selection*; Lawrence Berkeley National Laboratory: Berkeley, CA, p. 22, (2006).
22. Det Norske Veritas. *CO_2QUALSTORE: Guideline for selection and qualification of sites and projects for geological storage of CO_2*; Det Norske Veritas: Hovik, Norway, p. 77, (2009).

23. S. Bachu. "Screening and ranking of sedimentary basins for sequestration of CO_2 in geological media in response to climate change." *Environmental Geology* 44, (3), 277–289, (2003).
24. A. Ramírez; S. Hagedoorn; L. Kramers; T. Wildenborg; C. Hendriks. "Screening CO_2 storage options in the Netherlands." *Int J Greenhouse Gas Control* 4, (2), 367–380, (2010).
25. W.D. Gunter; S. Bachu; D.H.S. Law; V. Marwaha; D.L. Drysdale; D.E. MacDonald; T.J. McCann. "Technical and economic feasibility of CO_2 disposal in aquifers within the Alberta sedimentary basin, Canada." *Energy Conversion and Management* 37, (6–8), 1135–1142, (1996).
26. S. Bachu; J.J. Adams; K. Michael; B.E. Buschkuehle. "Acid gas injection in the Alberta basin: A commercial-scale analogue for CO_2 geological sequestration in sedimentary basins." In *Second Annual Conference on Carbon Sequestration: Developing & Validating the Technology Base to Reduce Carbon Intensity*, NETL: Alexandria, VA, pp. 1–11, (2003).

10

Acid Gas Injection for a Waste Stream with Heavy Hydrocarbons and Mercaptans

Xingyuan Zhao[1], John J. Carroll[2], and Ying Wu[3]

[1]*China Petroleum Engineering Southwest Company, Chengdu, China*
[2]*Gas Liquids Engineering, Calgary, Canada*
[3]*Sphere Technology Connection, Calgary, Canada*

Abstract

The third phase of Zhanazhol Oil Field in Kazakhstan was put into production, and a conceptual design for the acid gas injection scheme was undertaken. The acid gas stream is unusual because of its high hydrocarbon (C_4+ is about 1.75 mol%) and mercaptan (3 mol%) content.

These components add challenges to the design of a traditional injection process. One difficulty is the condensation of this stream during the compression and cooling. One solution is to use additional cooling on the interstage. This produces a sour condensate stream that can be recycled back to the front of the plant. This also results in a dehydrated acid gas stream, and therefore reduces the chance of corrosion problems and hydrate formation during the transport and injection of this stream.

10.1 Basis

The acid gas stream from the solvent regeneration tower is at the following conditions: 40°C and 0.07 MPa[g] and at an average flow rate of 765.6 kmol/h or equivalently 41.2×10^4 m^3/d (approximately 15 MMSCFD). According to the client's requirement, the injection pressure was specified to be 6.8MPa. Estimation of the injection pressure was not part of this study.

Ying (Alice) Wu, John J. Carroll and Weiyao Zhu (eds.) Sour Gas and Related Technologies, (143–152)

The composition of the acid gas is given in Table 10.1. This acid gas stream is somewhat unusual because it contains a large amount of hydrocarbons and heavier hydrocarbons in particular, The total hydrocarbon is about 3 mol%, which is not that extraordinary, but the heavy hydrocarbon (C_4+) is about 1.75 mol% which is very high and it is these heavier hydrocarbons that can have a significant effect on the process design.

The stream also contains about 3 mol% mercaptans, which is also very high and can have a significant effect on the process design. Such compounds can adversely affect an acid gas injection scheme because they are easily condensed. They can also adversely affect a sulfur plant. The hydrocarbons lead to catalyst poisoning and also the "black sulfur", a poorer grade of sulfur which may not be saleable.

10.2 Phase Envelope

Figure 10.1 shows the phase envelope for the acid gas mixture (solid line). The presence of the heavy hydrocarbons and mercaptans

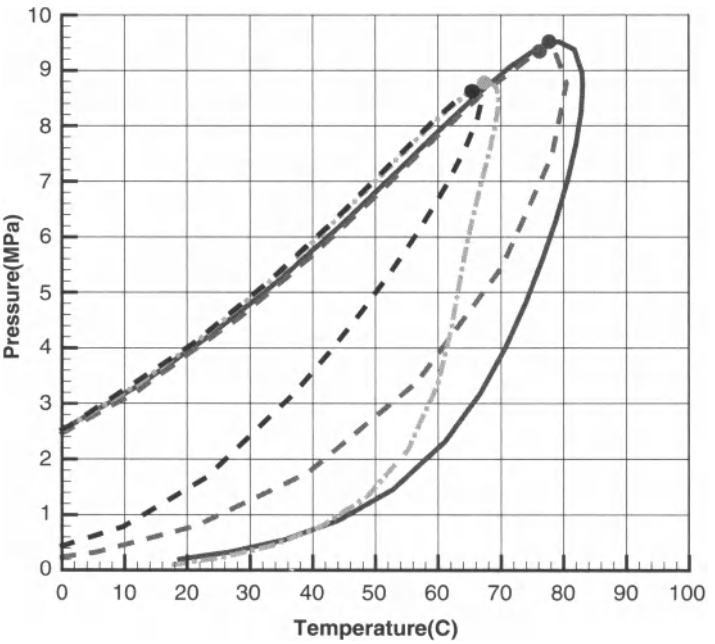

Figure 10.1 Phase envelopes. Solid line: full composition; Dashed line: full composition without heavy hydrocarbons; Dash dot line: full composition without mercaptans; full composition without heavy hydrocarbons and mercaptans.

Table 10.1 Composition of the acid gas mixture.

Component	mol%	Component	mol%
Carbon Dioxide	35.7840	Heptane	0.1912
H_2S	54.2152	Octane	0.1230
Methane	0.4328	Nonane	0.0864
Ethane	0.3054	Decane	0.0044
Propane	0.6344	$C_{11}+$	0.0027
i-Butane	0.2802	Nitrogen	0.0018
n-Butane	0.4458	CH_3SH	0.8822
i-Pentane	0.1072	C_2H_5SH	1.4258
n-Pentane	0.2465	CH_3SHCH_3	0.6212
Hexane	0.2589	Water	3.9511

results in a much broader phase envelope than for a typical acid gas. The estimated critical point for this mixture is 78°C and 9.4 MPa. The phase envelope was calculated using Aspen HYSYS.

To study the influence of heavy hydrocarbons and mercaptans on phase envelope, either C8~C11 fractions or mercaptan components, or both, were removed from the full composition list, and the corresponding envelopes were shown in Fig. 10.1. It can be seen that if the heavy hydrocarbons are removed, the envelope become thinner (the dashed line in Fig. 10.1), and the dew point at the pressure of 3 MPa, which could be a inters-stage pressure of compression, decreases from 65°C to 52°C. If the mercaptan components are removed (the dash-dot line in Fig. 10.1), the critical point noticeably changes its position in the p-T envelope, with both the critical pressure and critical temperature decreasing about 10%. Nevertheless, the dew point at 3 MPa does not crease so much as that when the heavy hydrocarbons are removed.

If the C8~C11 fractions and mercaptan components are both removed, the phase envelope become much thinner, which is more like the typical one reported in literatures. This indicates the high mercaptan and heavy hydrocarbon content has a remarkable influence on the phase envelope, increasing the critical pressure and the dew point temperature significantly. The broaden phase envelope could be a problem for the design of acid gas compression and dehydration.

10.3 Water Content

The water content calculations were performed using AQUAlibrium. The accuracy of AQUAlibium for predicting water content of acid gas mixtures is well established (see for example Carroll, 2002).

The component database in AQUAlibrium is not as large as most process simulation packages. Thus sum component lumping is required in order to use this software. The mercaptan components were lumped with the hydrogen sulfide. This is believed to give a better water content calculation but worse non-aqueous phase equilibrium. For the non-aqueous equilibrium it is better to lump the mercaptans with the hydrocarbon with similar boiling points. The hydrocarbons heptanes through undecane were lump with the hexane to make a C_6+ fraction, which is assumed to have the properties of n-hexane.

The resultant composition is given in Table 10.2. From the lumped composition the water content for this stream was calculated and the results are presented in Figure 10.2.

The steep curves at low pressure represent the water content in the gas phase. The somewhat shallower curves at high pressure are the water content in the liquid phase. The broken line connecting the two is the water where the water content curve passes through the phase envelope and does not actually represent the water content at these conditions. It should be noted that the non-aqueous dew and bubble points shown in Figure 10.1 are for the original gas composition and not for the lumped mixture.

Table 10.2 Lumped acid gas composition for AQU Alibrium calculations.

Component	mol%	Component	mol%
CO_2	35.78396	n-Butane	0.44580
H_2S	57.14433	i-Pentane	0.10715
Methane	0.43282	n-Pentance	0.24645
Ethane	0.30543	C_6^+	0.66655
Propane	0.63443	Nitrogen	0.00177
i-Butane	0.28017	Water	3.95112

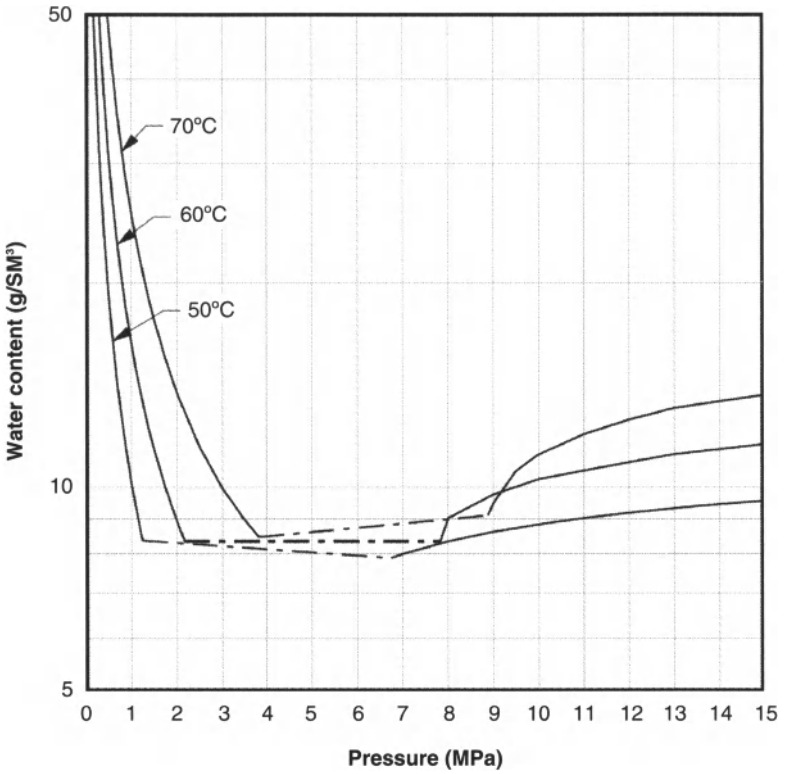

Figure 10.2 Water content of the acid gas mixture.

These curves do not show the dramatic difference in the water capacity between the gas phase and the liquid phase that is typical of an acid gas mixture. This is because of the relatively low dew point pressures for these mixtures. And again the low dew points are due to the high mercaptan and heavy hydrocarbon content.

It is estimated that the lumping used in this case has a negligibly small effect on the water content calculations in this case.

10.4 Hydrates

Figure 10.3 shows the hydrate curve for the mixture as given in Table 10.1 and was calculated using VMGSim under the condition that saturated water exists in the acid gas mixture. The region where hydrates are possible is to the left and above this hydrate curve (i.e. pressure greater and temperature less than the hydrate curve).

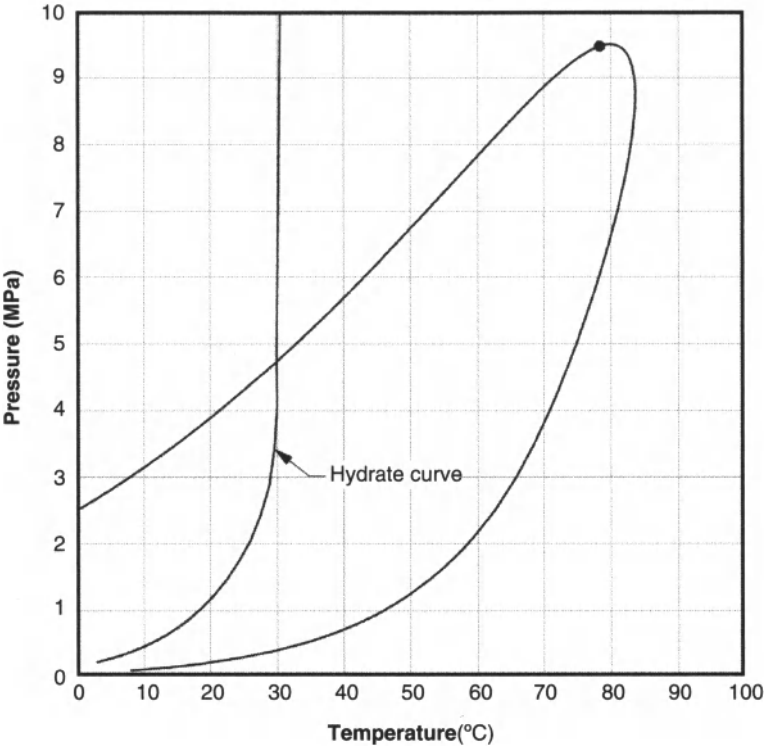

Figure 10.3 Approximate hydrate curve for acid gas given in Table 10.1.

The predicted hydrate curve for this mixture extends out to 30°C. It reaches this temperature at a pressure of about 4 MPa.

Reducing the water content of a gas mixture below some threshold level reduces the temperature at which a hydrate will form for a given pressure. For acid gas mixtures this effect is significantly larger for the liquid phase than for the gas phase. For example, reducing the water content to 2 g/sm3 is predicted to reduce the hydrate temperature from about 30°C to about +10°C. Further reducing it 1 g/Sm3 reduces this to –6°C. These calculations were performed using CSMGem with the lumped composition.

As the aerial temperature in Kazakhstan is very low in winter, the temperature in the transportation pipe could be as low as near 0°C. Thus the water content in the acid gas should be decreased in order to avoid water condensation or hydrate formation. For extra safety consideration, the acid gas should be dehydrated to reduce the water content to 1 g/sm3.

10.5 Dehydration and Compression

The acid gas composition for this case is unusual and thus requires special considerations over a more conventional acid gas injection scheme.

The phase diagrams presented earlier show that the compression of this stream requires careful consideration.

First, from Fig. 10.1 it can be seen that merely cooling to 50°C will result in condensation of the acid gas on the interstage. The acid gas dew point at 50°C is approximately 1.25 MPa. Second, from Fig. 10.2 the use of compression and cooling alone will not result in a sufficiently dehydrated stream. A combination of compression and chilling result is a dehydrated stream and eliminates problems with condensation of the acid gas.

Figure 10.4 shows a process flow diagram for this four stage compression and chilling process. The process was modeled using VMGSim.

First the gas is compressed and cold through an aerial cooler to 50°C. This stream is blended with methanol and cooled to 0°C in a chiller. Refrigerant (usually propane) boils on the shell side of the reboiler while the acid gas cools (and partially condenses) on the tube side. Methanol is injected at a rate of 275 kg/h in order to prevent hydrates from forming in the tubes of the reboiler. At this point the stream has been dehydrated to about 1 g/Sm3 and thus additional condensation of water is not a concern. There is a methanol-water byproduct stream (labeled "Aqueous Waste") that can be

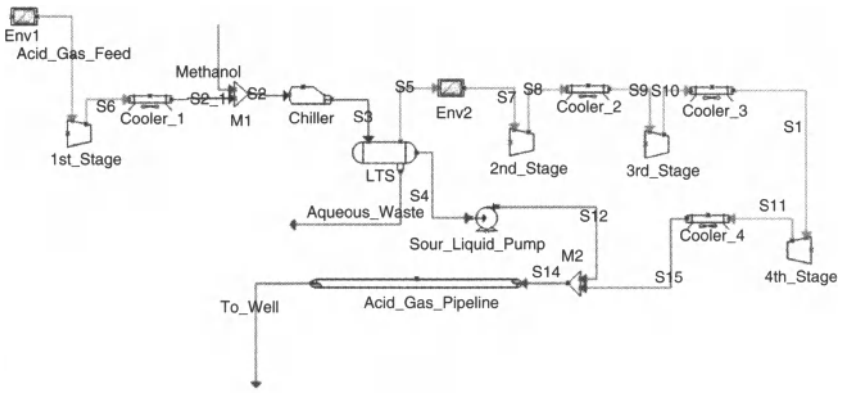

Figure 10.4 Process flow diagram for the compressor plus chiller process.

disposed with any aqueous waste. However it is probably wish to recover this methanol and reuse it.

The condensation of a portion of the acid gas changes the phase envelope. The phase envelopes for the original acid gas and the lightened acid gas are shown in Fig. 10.5. At pressure below 7 MPa the dew point temperature for the mixture has been reduced by about 10 to 25 Celsius degrees. On the other hand the bubble points are almost unaffected by this change in composition.

The estimated compression power for this scheme is about 2.5 MW and the required chiller duty is 0.75 MW. These values are for the full flow rate of the acid gas.

A significant amount of the heavier components are also condensed. In the PFD shown, this stream is pumped to a high pressure and blended with the compressed acid gas stream and the combined stream is injected. This stream can be recycled back to the

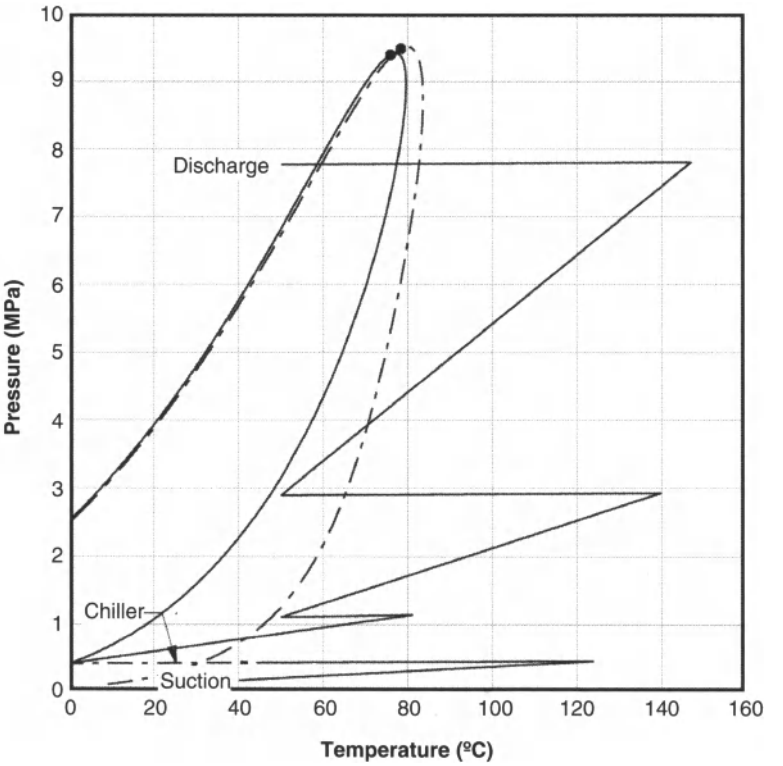

Figure 10.5 Graphical representation of the compression-chilling process.

inlet of the plant and blended with the raw liquids in the inlet. This stream contains about 8 t/d of hydrocarbon (oil) and represents a potential source of income rather than simply a waste product. A review of the entire plant may reveal a point where this stream can be returned for further processing and thus recovery of this potentially lost product.

This process is similar to that use at the South Rosevear Plant that was designed by Gas Liquids Engineering (see Maddocks *et al.*, 2008).

10.6 Discussion

The chilling process can also be achieved after the second stage compression. The gas is compressed at the first stage and cold to 50°C in an aerial cooler. After the condensate is removed by the interstage scrubber the gas is again compressed at the second stage and cold through an aerial cooler to 50°C. This stream is blended with methanol and cooled to 18°C through a gas-gas exchanger and a chiller.

The conventional refrigeration loop can be modified to include a gas-gas exchanger and a separator after it. This separator removes liquid water and any hydrocarbons that condense. The liquid water is returned to the amine plant and the condensed hydrocarbon is sent o the condensate stabilization system.

Since the gas-gas exchanger is maintained above the hydrate temperature, methanol does not have to be injected into the exchanger and thus the water from the first separator contains no methanol. Methanol is only injected after the separator.

With the above changes of the process, the stream has been dehydrated to about 1 g/Sm3, and the duty on the chiller is greatly lessened. The estimated compression power for this scheme is still about 2.5 MW but the required chiller duty decreases to about 0.3 MW, and methanol is injected at a rate of only 35 kg/h in order to prevent hydrates from forming in the tubes of the reboiler.

10.7 Conclusion

The high mercaptan and heavy hydrocarbon content has a remarkable influence on the phase envelope, increasing the critical pressure and the dew point temperature significantly. The broaden

phase envelope causes problems for the design of acid gas compression and dehydration. Merely cooling to 50°C will result in condensation of the acid gas on the interstage, and the use of compression and cooling alone will not result in a sufficiently dehydrated stream.

A combination of compression, chilling and separation result is a dehydrated stream and eliminates problems with condensation of the acid gas. With an optimized process design by adding a gas-gas exchanger and scrubbers to remove the condensate, this scheme can be energy-saving and obtain extra heavy hydrocarbon (oil) recovery.

References

1. Carroll, J.J., "The Water Content of Acid Gas and Sour Gas from 100° to 220°F and Pressures to 10,000 psia," *81st Annual GPA Convention*, Dallas, TX, March 11–13, (2002).
2. Maddocks, J.R., Conacher, M., and Dixon, L., "Conversion of Suncor's South Rosevear Facility to Acid Gas Injection," *SOGAT*, Abu Dhabi, U.A.E., Apr. 27- May 1, (2008).

11

Compression of Acid Gas and CO_2 with Reciprocating Compressors and Diaphragm Pumps for Storage and Enhanced Oil Recovery

Anke Braun[1], Josef Jarosch[1], Rainer Dübi[2], and Luzi Valär[2]

[1]LEWA GmbH, Ulmer Strasse 10, 71229 Leonberg, Germany
[2]Burckhardt Compression, Im Link 5, 8404 Winterthur, Switzerland

The concept of controlling the level of CO_2 in the atmosphere includes a variety of strategies to reduce carbon emissions. One effort being pursued to lessen the release of greenhouse gases is capture and long term storage of CO_2.

There is an increasing interest in injecting CO_2 from large CO_2-producing single sources, e.g., fossil-fueled power plants, oil refineries, cement works, and steel production. The oil and gas industry is increasingly faced with the disposal of fossil CO_2 received from low-quality gas streams, which are sometimes characterized by more than 10% CO_2.

Injection of CO_2 has taken place for many years as a consequence of pressing CO_2 into oil fields to enhance oil recovery (EOR). Faced with sour sources of natural gas, acid gas injection is employed by oil and gas producers in Canada to reduce emissions of H_2S to the atmosphere. Since CO_2 often represents the largest component in acid gas streams and it is costly to separate the two gases, large volumes of CO_2 are injected together with H_2S into geological formations [1], [2]. The methods and technologies used for the sequestration of pure CO_2 are analogous to those developed for the acid gas injection.

Ying (Alice) Wu, John J. Carroll and Weiyao Zhu (eds.) Sour Gas and Related Technologies, (153–164)

Today the main priority for the development and wide spread deployment of CO_2 capture and storage technology is to reduce the cost for capture, compression and transport.

In all these Capture and Storage schemes the compression represents an important process step. It requires significant compression power to boost the pressure of the CO_2 after capture to typical pipeline levels. Reduction of the cost and power requirements for compression will encourage injection of CO_2 both for existing and future power plants and other large CO_2 producing processes. Therefore current R&D activities are focused on developing and improving the energy- and cost-intensive sub processes of separation and compression. Also in the fields of enhanced oil recovery and acid gas injection, oil and gas producers will benefit from an optimized compression scheme.

For high pressure applications depending on the specific characteristics of the injection process, it can be reasonable to utilize new concepts with part compression followed by liquefaction and pumping [3], [4]. Significant power savings in the compression step can be achieved with this tandem approach [5].

With renewable energies taking up a higher percentage of the energy mix in the future, more flexibility will be required for fossil fuelled power plants. By employing reciprocating compressors and pumps, high efficiencies can be obtained at part-load.

Beside the efficiency improvement also the corrosion behaviour of CO_2 at higher pressure has to be considered. Conventional compressor technology can be harmed by the special behaviour of the CO_2 and H_2S mixtures especially at pressures above 100 bara. The

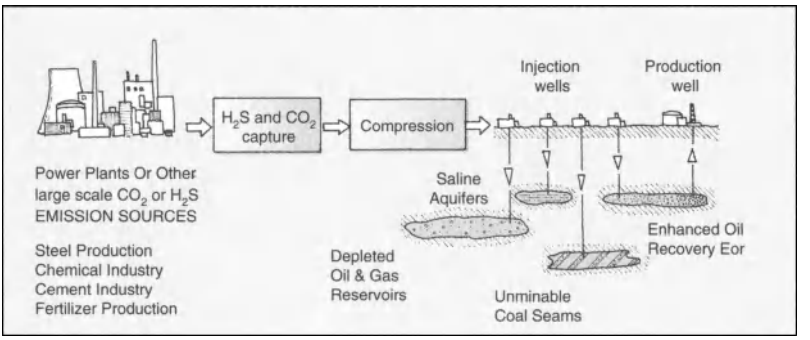

Figure 11.1 Acid gas and CO_2 capture, compression & storage.

actual technologies are extremely cost-intensive and therefore new concepts are requested.

This paper will show the plant layout and demonstrate the high overall efficiency of this approach which combines semi-isothermal compression with reciprocating compressors, cooling, liquefaction and pumping with diaphragm pumps, and display the possible energy savings, illustrated by an example for compressing 30t/h CO_2 from 2 bara to 200 bara.

It will address the special behaviour of CO_2 and H_2S in regard to compression and the related corrosion mitigation and will give an overview over reciprocating compressors and pumps and their benefits.

Figure 11.2 shows two ways of compressing 30t/h CO_2 from 2 bara to 200 bara. One process, indicated by the solid black line, describes the conventional semi-isothermal compression with multistage compression and inter-stage cooling for reciprocating compressors. The compression ratio is in a range of 3–4. This compression path requires five compression stages and results in a power demand of 3 MW for this application.

The hybrid approach, indicated by the open white line, combines semi-isothermal compression, cooling, liquefaction and increasing the pressure in a final single step to the pipeline condition by a pump. Since compression in the liquid state consumes less power than in the gaseous state, this combined path of compression reduces the power demand by 0,5 MW. The CO_2 is compressed to 70 bar by a reciprocating compressor with three stages, subcooled to 25°C and boosted to the final pressure of 200 bar by a triplex diaphragm pump. However, there will be no universally valid solution to CO_2 and acid gas compression duties. Specific storage site conditions such as location, ambient air temperatures, availability of cooling medium etc. will play a decisive role in determining the optimum configuration.

This is why only the shaft power is considered in this energy balance. The power consumption of the liquefaction depends on the ambient conditions. Figure 11.3 shows the condensation temperatures of acid gas at 65 and 70 bar. It can be seen that for pure CO_2, a temperature of about 20°C is required for the cooling agent which can be achieved with cooling water. Hence, if cooling water is available at the site of compression, the overall power saving can be up to 15% because the power consumption of the liquefaction is negligible. If active cooling is required, the power saving is still

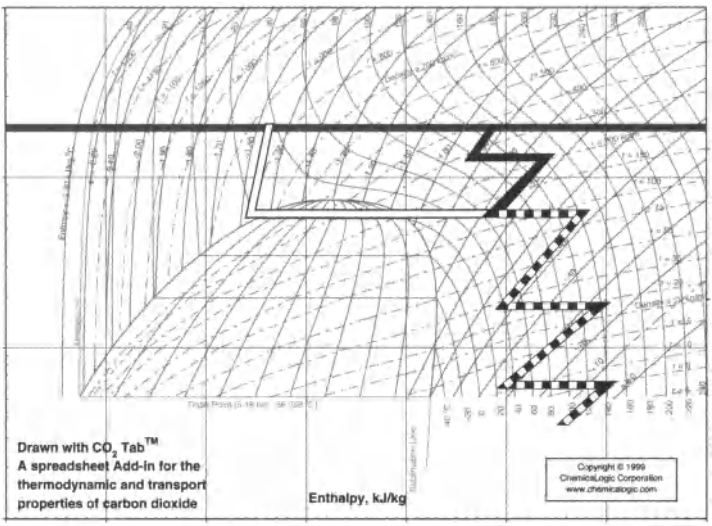

Figure 11.2 Compression schemes for CO_2.

in the range of 5–8%. With an increasing amount of hydrogen sulphide in the acid gas, the condensation temperature rises and thus the required temperature of the cooling liquid becomes less critical.

Figure 11.3 also shows the density of acid gas on the boiling curve. Since reciprocating compressors and pumps work on a volumetric base, the density and compressibility of the fluid determines the size of the machine. To be in an economic range for the capital costs of diaphragm pumps, the density of the pumped fluid should at least be 500 kg/m^3. As can be seen from the diagram, this minimum density can be attained if the acid gas is liquefied at a pressure around 70 bar.

Beside the efficiency improvement, the hybrid compression path also mitigates an important corrosion issue with acid gas. At higher pressure, the suction temperature is close to the two-phase region. At these conditions, there is a risk of corrosion if the acid gas decompresses in the packing and sealing elements and liquefies. This is illustrated in the p-h-diagram in Figure 11.4 which shows the limit in suction temperature for pure CO_2. To avoid this corrosion problem it is necessary to increase the suction temperature for the upper stages, which, as a result, increases the number of stages. For the case study which is presented here it concerns the suction temperature of stage 4 and 5. For acid gas with a high content of H_2S, this issue arises already at lower stages. As a consequence, the

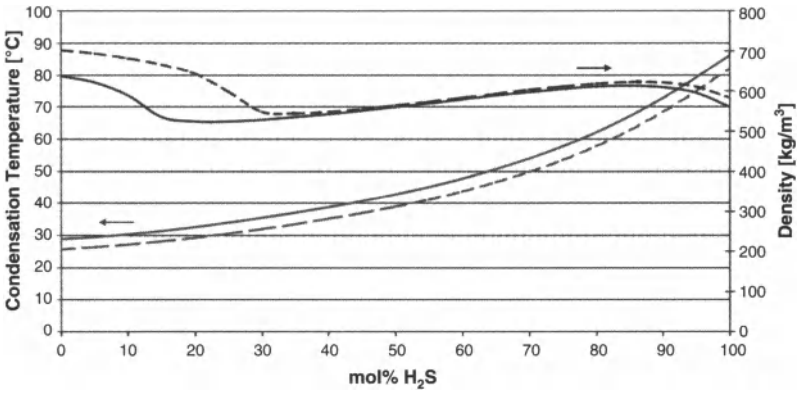

Figure 11.3 Condensation temperature and density of acid gas at 65 bar (---) and 70 bar (—).

combination of reciprocating compressors and pumps for acid gas compression also reduces corrosion issues for processes with discharge pressures above 100 bar for CO_2 and even lower discharge pressures for acid gas.

Additionally, reciprocating machines offer advantages where process flexibility is an important criterion. Reciprocating compressors can be adapted to varying mass flows by speed control in combination with valve unloading, and diaphragm pumps by speed control. In this way, for the compressor a turndown ratio of 1:4 is achieved and 1:4 or 1:5 for the pump, dependent on the pump size. By using speed control, reciprocating machines can deliver variable flow rates at a constant high efficiency.

Also varying gas compositions, occurring in Enhanced Oil Recovery and Acid Gas Injection, can be handled easily by reciprocating compressors and pumps. Varying compositions bring about changes in density and compressibility which result in changing volumetric flow rates. Again, this can be accomplished by speed control without loss in mechanical efficiency.

Finally, for all compression and storage operations it is a quite conceivable scenario that the discharge pressure will vary over time due to changes in the reservoir pressure. With the hybrid compression path, this case would not require any adaption of the installation since the fluid is boosted to the final pressure by the pump in one single step.

Figure 11.5 shows the process flow diagram for the example of compressing 30 t/h of CO_2 in a 3-stage reciprocating compressor

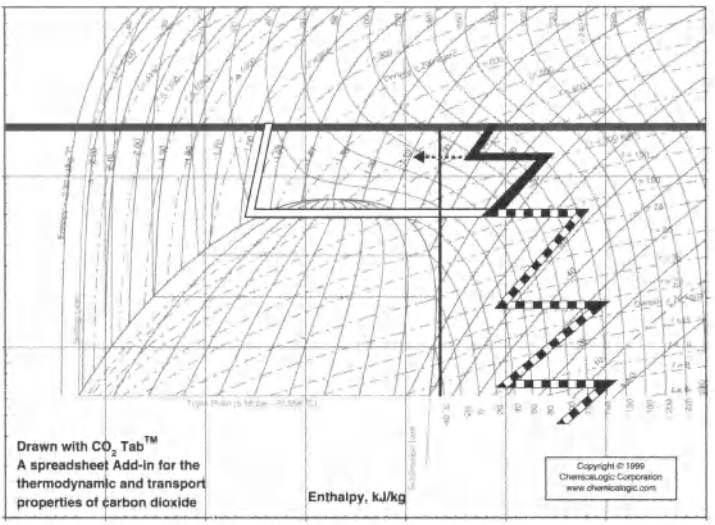

Figure 11.4 Corrosion issue and suction temperature for CO_2 compression.

and a diaphragm pump, including the interstage coolers and pulsation dampers for each stage. Figure 11.6 presents the plant layout for the same process. The first compressor stage requires two pistons, the second and third stage one piston each. After the compressor, the CO_2 is liquefied in the subcooler before it is boosted by the triplex diaphragm pump to the reservoir pressure.

The limit for piston compressors and diaphragm pumps lies at about 150 t/h of acid gas. In terms of carbon capture and storage, the CO_2 emissions of many CO_2 generating processes and fossil fuelled power plants of 200–300 MW can be handled with one set of machines. Power plants of 200–400 MW would need 2–3 sets of reciprocating machines operated in parallel. The range above - up to 1200 MW - would be the field of turbo compressors and turbo pumps, though with significant lower efficiency, especially at part load. For high-capacity power plants where concurrently high efficiency is required, it is conceivable to use turbo machines to cover the base load and reciprocating machines to accomplish the peak load at high efficiency.

The limit in discharge pressure for this hybrid solution is roughly 500 bar, depending on the actual flow rate, and the suction pressure needs to be at least atmospheric pressure. In low pressure

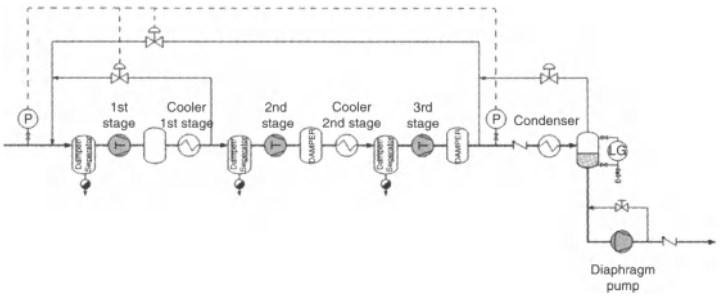

Figure 11.5 Process flow diagram for 3-stage reciprocating compressor and triplex diaphragm pump.

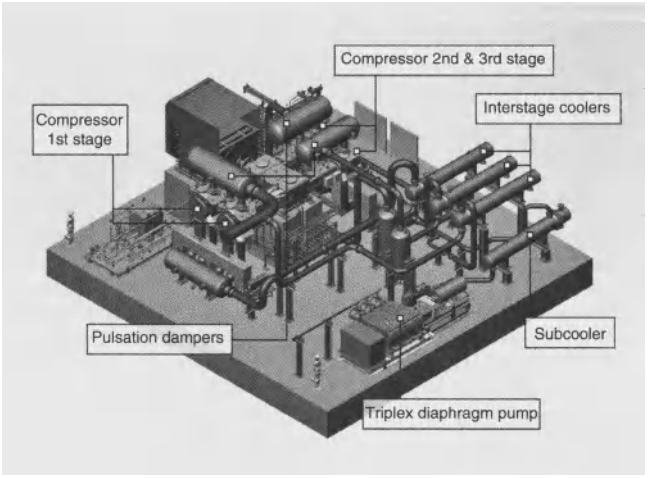

Figure 11.6 Plant layout for compressing 30 t/h CO_2.

applications, that is up to about 150 bar, the compression can be performed by multistage reciprocating compressors solely.

Ring sealed reciprocating compressors are widely applied for a very wide range of applications due to their very high efficiency also in part load operation and due to their ability to scope with a very large range of operation conditions. Burckhardt Compressions portfolio of ring sealed reciprocating compressors with crosshead (API 618) ranges from 200 to 31'000 kW and discharge pressures of up to 1'000 bar can be reached.

The advantages of crosshead reciprocating compressors (API 618) are the balancing of forces due to double acting pistons and

the strict separation of the process gas and the crank case. For high compression ratios, multiple stages are applied in order to improve the volumetric efficiency and to limit the gas temperature.

The sealing of the crank end side compression chamber is realized with a packing along the piston rod. The mechanical seal limits the leakage to a very small amount. For the compression of flammable, hazardous or toxic gases, a double compartment distance piece is installed between the cylinder and the compressor frame. The two chambers of the distance piece ensure that no frame lubrication oil is in contact with the process gas and no process gas is released to the crank case or to the atmosphere.

Figure 11.7 shows a schematic of compressor with a two-compartment distance piece. The leakage gas of the packing is fed to the suction side of the compressor (or to an external leakage system). The remaining leakage to the distance piece is diluted with inert gas and vent to the flare. Between the two compartments of the distance piece, an intermediate packing equipped with seal gas is installed to prevent the gas from entering the crank end compartment, which is vented to the atmosphere. This configuration guaranties that no contamination of the frame lube oil or the environment occurs.

Diaphragm pumps are mainly used for low to medium flow rates at medium to high pressures. They are predominantly known for low flow - high head applications and for fluids which have to be metered leak free with high accuracy. In the last 25 years however process diaphragm pumps were developed rather unnoticed from the general public to hydraulic powers of several hundred Kilowatts. Today the allowable physical values such as pressure, flow rate and viscosity cover several orders of magnitude.

The above mentioned process conditions are typical applications for plastic diaphragms. They are usually employed for pressures up to 400 bar at temperatures of –50°C to +150°C. Special designs are used in processes up to 800 bar.

Diaphragm pumps are absolutely leak-free because the hydraulically actuated diaphragm completely separates all susceptible parts of the pump from the process fluid. This is why they have found a wide field of applications in all industries which handle fluids with the potential to be hazardous, dangerous or toxic. Therefore the diaphragm pump technology is not only suitable to convey CO_2 for carbon capture and storage, but also acid gas, containing highly toxic H_2S, for sequestration or enhanced oil recovery.

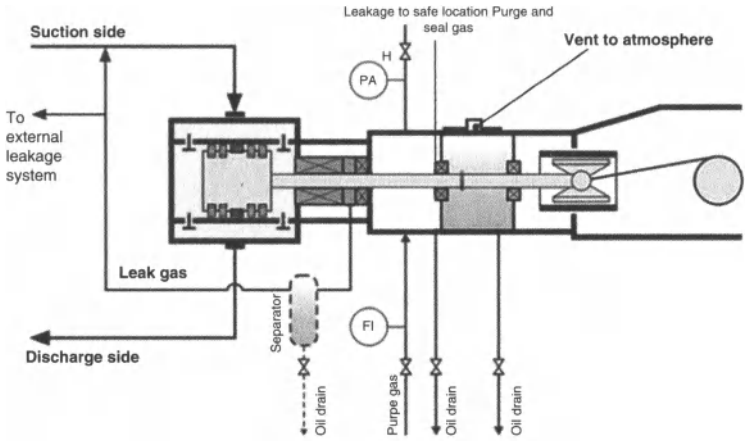

Figure 11.7 Schematic of reciprocating compressor.

Leakages in case of a damage are avoided by multilayered diaphragms with a diaphragm rupture indication. The fluid is still contained in the pump even if one diaphragm is damaged. For fluids that tend to diffuse through the diaphragm, especially CO_2, there is a special diaphragm rupture indication that differentiates between tiny leakages caused by diffusion and real damages of the diaphragm. Other safety features are implemented in the hydraulic part of the pump to render it inherently safe against up-set conditions such as overload or cavitation.

In addition to be leak-free, diaphragm pumps have all the advantages of reciprocating displacement pumps, such as high accuracy, high volumetric and mechanical efficiency and a pressure firm characteristics i.e., the capacity is nearly unaffected by the back-pressure. Linear capacity control is possible by speed adjustment and for some pump types also by stroke adjustment.

Worldwide there are more than 370 Burckhardt compressors installed for CO_2 and around 30 for H_2S services. The long term experience with the handling of such demanding gases enables Burckhardt Compression to judge the risks, choose the proper materials and adjust the process for trouble free operation of reciprocating compressors.

CO_2 is one of the most frequently pumped fluids by LEWA pumps. Many of these pumps are employed in low flow - high pressure applications. But also the biggest diaphragm pump ever built

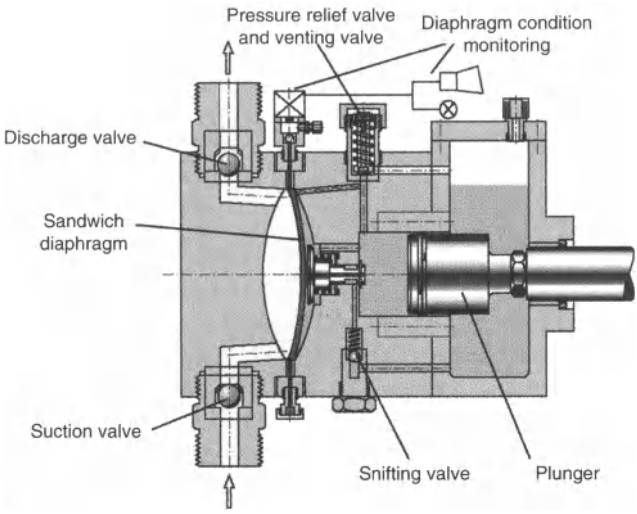

Figure 11.8 Schematic of diaphragm pump head.

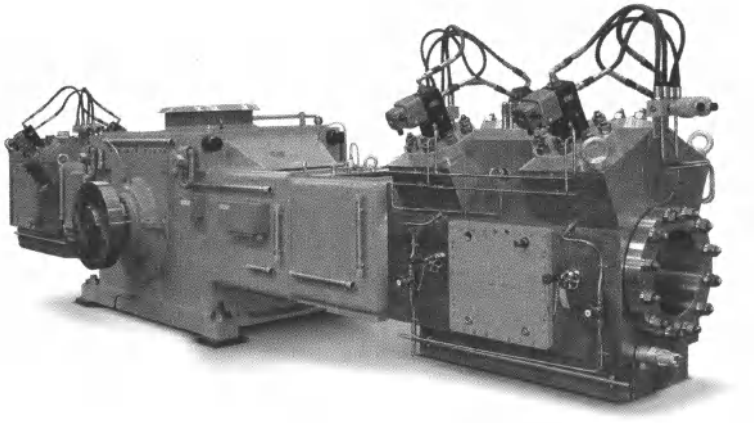

Figure 11.9 Burckhardt Compression BA Compressor for CO_2 compression 33 t/h CO_2 wet, 27 bara suction pressure, 235 bara discharge pressure, 3800 kW shaft power.

by LEWA conveys CO_2. It is placed at an LNG production facility in Norway where it compresses CO_2 contained in the natural gas for sequestration in a deep sub-sea formation beneath the gas field for final storage. The 4-headed diaphragm pump boosts 110 m^3/h CO_2 from 60 bar to 215 bar. In this case the hybrid compression

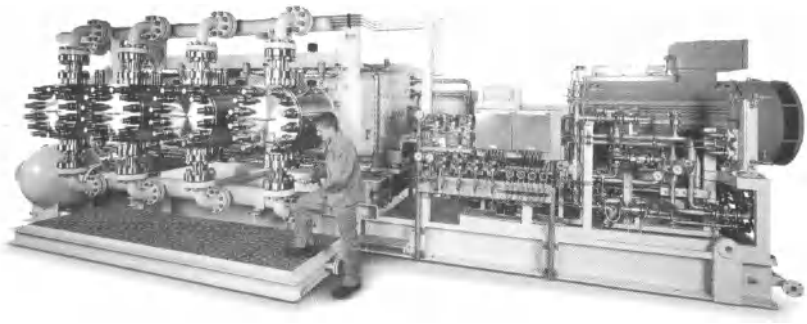

Figure 11.10 LEWA Diaphragm Pump G4T for CCS 100 t/h CO_2, 60 barg suction pressure, 215 barg discharge pressure, 650 kW hydraulic power.

consumes more than 1000 kW less than the conventional compressor process [6].

LEWA pumps are also employed for acid gas injection in Canada where underground storage of acid gas has taken place for many years to make sure that acid gas is not emitted to the atmosphere.

11.1 Conclusion

The process of capture and storage of CO_2 is the most promising to reduce greenhouse gas emissions since the world wide ever growing energy demand will probably be covered by fossil fuels for some more decades. The CCS technology can build on the experience gained in acid gas injection which has been taken place for more than 20 years in Canada to avoid the emission of highly toxic H_2S.

Both capture and compression of CO_2 and H_2S are energy-intensive steps. The overall acceptance of CCS will depend on a reduction of the cost and energy requirements for the whole process. Since the compression of a liquid consumes less energy than compression of a gas, the combination of a compressor and a pump can bring power consumption down. Depending on the ambient conditions, the energy saving can be as high as 15%. For the compression of up to 150 tonnes/h, the combination of a reciprocating compressor and a diaphragm pump offers further advantages regarding corrosion problem mitigation and the speed of response to changes of gas mass flow, gas composition and discharge pressure. To comply with varying flow rates a turn down ratio of 1 : 4 can be realised with high efficiency.

References

1. Stefan Bachu, William D. Gunter: "Overview of Acid-Gas Injection Operations in Western Canada;" Alberta Energy and Utilities Board, Edmonton, AB, T6B 2X3, Canada.
2. Edward M. Wichert: "Acid Gas Compression and Injection;" Course Notes, Frankfurt, October 25, 2002.
3. Dr. J. Jeffrey Moore, Ms. Marybeth Nored, Dr. Klaus Brun: "Novel Concepts for the Compression of Large Volumes of Carbon Dioxide;" Southwest Research Institute, *Oil & Gas Journal*, June 2007.
4. Simone Bertolo: "Four Post-Combustion CO2 Compression Strategies compared;" *Carbon Capture Journal*, Sept. – Oct. 2009.
5. Josef Jarosch: "Improving Efficiency of Compressing CO_2 for Re – Injection;" Carbon Capture and Storage: Making it Happen; Institution of Mechanical Engineers London, October 2009.
6. Matthias Müller: "The Goliath of Pumps;" *TCE Today*, November 2007.

12

Investigation of the Use of Choke Valves in Acid Gas Compression

James van der Lee[1], and Edward Wichert[2]

[1]*Virtual Materials Group Inc., Calgary, Canada*
[2]*Sogapro Engineering Ltd., Calgary, Canada*

Abstract

Throughout acid gas compression and injection systems, there are numerous significant pressure drops that can occur, including recycle gas from high pressure compression stages to low pressure compression stages, and choke valves between the final compression stage discharge and the wellhead. This paper will provide a brief review of the principles that allow sufficient amounts of water to be removed from acid gases with compression and cooling. The paper will also present a typical acid gas compression and injection system, in order to highlight potential issues related to using choke valves. The basis of the investigation will be a series of simulation cases, and as such, a summary of the validity of the models used will be presented.

The scenario that will be studied in detail in this paper will be to determine if a choke valve could be used to raise the pressure at which a four-stage acid gas compression and injection system runs, in order to be able to lower the water content of the acid gas sufficiently with compression and cooling. In four-stage compression systems, water content reaches a minimum at temperatures approaching the hydrate temperature after three stages of compression, or at the dewpoint temperature at the required injection pressure. For this to be effective for water content control, the required wellhead injection pressure must be above a certain level, depending to some extent on composition of the acid gas. The question to be analyzed is whether imposing an artificial higher pressure by means of a choke valve can be used to minimize the water content if the natural pressure for injection is relatively low. If the final injection pressure is purposely increased at these conditions, water content will be

Ying (Alice) Wu, John J. Carroll and Weiyao Zhu (eds.) Sour Gas and Related Technologies, (165–182)

reduced. However, the wellhead pressure will always revert to the actual pressure required for the particular well and injection zone conditions. If this pressure is not naturally high enough to minimize the water content sufficiently, then a water dehydration process has to be included in the facilities, at additional capital and operating costs. Given the fact that injection pressure is an important factor in whether an acid gas can be dehydrated with only compression and cooling, there may be a motivation to try to operate the acid gas compression train at a pressure higher than the required well head injection pressure in order to be able to take advantage of this. Several different examples with varying suction and injection pressures at several different compositions will be examined to see if this is possible, or if problems, such as formation of an aqueous water phase or hydrates, would occur once the pressure has been reduced to the injection pressure.

12.1 Introduction

Acid gas is a mixture of H_2S and CO_2 that is extracted from sour natural gas during sweetening of the sour gas to comply with the low content specifications of the acid gas components in the treated sales gas. When the acid gas mixture is separated from the sour gas in the treating process, it exits the separator fully saturated with water vapour at the separator pressure and temperature. One way of disposing of the acid gas stream is to compress it and inject it into a deep underground formation. In Western Canada there are over 50 such projects currently in operation.

Acid gas is very corrosive in an aqueous environment, and will also form hydrates at elevated pressures at temperatures considerably above the freezing temperature of water. In the further handling of the acid gas in compression and injection projects it is necessary to remove most of the water vapour from the acid gas so that the acid gas is highly undersaturated in water vapour content when it leaves the compressor site.

The conventional processes that can be used for dehydrating natural gas can also be applied to drying acid gas. This increases the capital cost and the operating cost of an acid gas injection project. If the injection pressure required by the injection well due to reservoir conditions of pressure and injectivity restrictions results in a high injection pressure, then the water content can be sufficiently reduced by interstage cooling. This is due to the fact that the acid gas exhibits a minimum water holding ability as the

pressure increases in the compression steps in the vapour phase. If the required pressure is high, then upon cooling after the final stage of compression the acid gas is condensed into the liquid phase. In the liquid state, at the same pressure but at a lower temperature, the acid gas can hold substantially more water in solution than in the vapour state. This behaviour of acid gas can be used to reduce the water content sufficiently, by cooling the acid gas to near its hydrate forming temperature after three stages of compression in a four-stage compression project. By lowering the water content in this manner, corrosion or hydrate formation will not be a problem. However, this method of water content reduction works only if the required injection pressure is at a high level. If not, then a dehydration process has to be applied.

The purpose of this paper is to examine whether or not it is feasible to install a choke valve after the final stage of compression to artificially raise the injection pressure so that water content is sufficiently minimized in situations where the actual required injection pressure in itself is not high enough.

12.2 Water Content Behaviour of Acid Gas

When dealing with natural gas mixtures that contain no or very minute amounts of acid gas components, the water vapour holding ability decreases with increasing pressure at a constant temperature. This holds true also for acid gas in the vapour state below the critical temperature but at different water contents than for sweet gas. However, acid gas can be readily liquefied at ambient temperature at high pressure. In the liquid state the acid gas can hold substantially more water in solution than in the gas state. This feature is illustrated in Figure 12.1 for an acid gas mixture containing 50% H_2S, 48% CO_2 and 2% methane. There always are small amounts of hydrocarbon components in acid gas mixtures, represented in this example by methane.

The plots in Figure 12.1 show the water content at 30°C and at 40°C for the indicated composition of acid gas. As the pressure increases, the water content drops until a certain pressure is reached for each of these temperatures. The water holding ability then takes a sudden upturn, and then levels off but continues to increase slightly as the pressure increases at these two example temperatures. This type of behaviour holds true for all acid gas mixtures, of course at

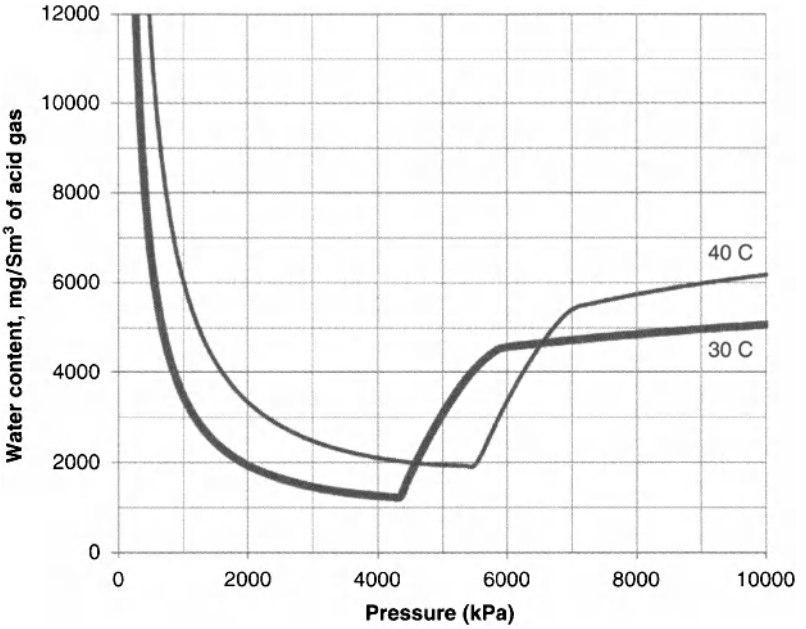

Figure 12.1 Water content of acid gas containing 50% H_2S, 48% CO_2, 2% C_1.

different water contents for different compositions. The pressure at which the sudden increase in water holding ability occurs is the dewpoint temperature of the acid gas mixture. The levelling off after the steep increase in water holding ability occurs at the bubble point temperature.

It can be seen in Figure 12.1 that by cooling the acid gas to 30°C or 40°C after three stage of compression at a pressure in the range of 2 500 to 5 000 kPa abs, the water content will be near the minimum. After the fourth stage of compression and cooling the acid gas can hold substantially more water in solution. This works well if the required wellhead pressure is high enough so that the pressure span indicated above is reached after three compression stages. When injecting into low pressure zones that may have been depleted by production of oil or gas, then the pressure after three stages of compression may not be high enough to reach the required pressure level for minimum water content as indicated in this example. Can the pressure be artificially raised by means of a choke valve after the final stage of compression to reach the required pressure level to minimize the water content sufficiently?

It must be recognised that ultimately the pressure will drop after the choke to that actually required for injection.

The above example pertains to this particular composition of the acid gas. Other compositions exhibit similar behaviour regarding water content, but at different levels of water content and pressure spans.

12.3 Test Cases to Ascertain the Effect of Choke Valves

Figure 12.2 shows the typical equipment installed in a four-stage acid gas compression train. The acid gas temperature increases after each stage of compression and is then cooled to around 30 to 40°C. The water content is reduced by cooling at each higher pressure step and the condensed water is removed in the next suction scrubber. If no dehydration method is included in the process, then the water content in the acid gas at the temperature of the suction scrubber to the fourth stage of compression must be low enough so that when the acid gas is cooled to the dewpoint temperature of the acid gas upon final compression it is undersaturated in water content. Once cooled and liquefied, it will be highly undersaturated in water. Thus cooling of the acid gas after three stages of compression is extremely important. However, there is a limit in the cooling that can be done at this point, and that is the hydrate forming temperature, as shown in Figure 12.3. The phase diagram, the hydrate temperature curve and the water holding ability of the acid gas will vary substantially with composition. In light of this, three different acid gas compositions will be tested

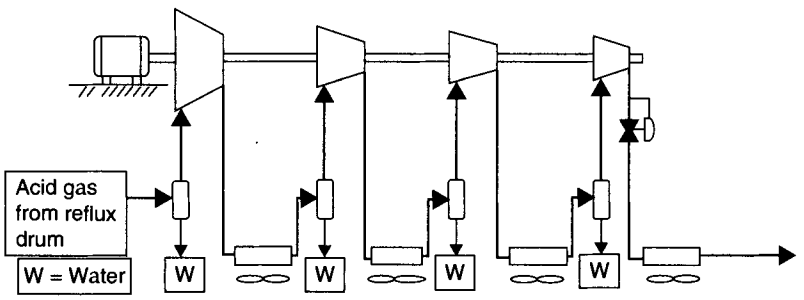

Figure 12.2 Typical equipment in a four-stage acid gas compression train.

to see if increasing the discharge pressure to raise the pressure in the fourth stage suction scrubber will be a useful method for minimizing water content sufficiently to avoid the installation of a dehydration unit in the compression train.

The three compositions that will be examined will each contain 2% methane, and will include 20%, 50% and 80% H_2S respectively, with the balance being CO_2. Different injection pressures will be assumed for the different cases, as required pressures also differ greatly with compositions for controlling water content to the required minimum. The basic requirements common to all cases will be that after the third stage of compression the acid gas has to be cooled to within 3°C of the hydrate temperature and that the water content at that condition is about the same as the water holding ability of the acid gas at the required final pressure and the acid gas dewpoint temperature. These limits impose the minimum margin of safety in water content reduction without dehydration by a different process. The evaluations will be made with the VMG suite of programs. It will be assumed for each case that the suction pressure to the first stage suction scrubber is 140 kPaa. Compression ratios will vary to reach the required pressure levels.

An injection pressure will be assumed in each case that is on the borderline of needing or not needing to use a dehydration process in the equipment train. If the actual injection pressure were somewhat higher than the assumed pressure in any of these cases, then there would be no need to install a choke valve to artificially raise the pressure. The exercise with the choke valve applies only to borderline cases where the water content after the third stage of compression and cooling to within 3°C of the hydrate temperature is about the same as the water content of the acid gas at the required injection pressure and the dewpoint temperature of the acid gas. The limit of cooling to within 3°C of the hydrate line leaves a small margin of safety in cooling of the acid gas without running into hydrate problems.

12.4 Test Case 1: 20% H_2S, 78% CO_2 and 2% C_1

In this case it is assumed that the required injection pressure at the injection rate is 6 203 kPaa. Figure 12.3 shows the phase diagram and the hydrate line as well as the pressure steps and the temperatures

after compression and after cooling. The compression ratio is (6 203/140)^.25 or 2.58. The pressure after three stages of compression is 140*(2.58)^3 or 2 404 kPaa. The gas after three stages of compression can be cooled to 22°C, with the hydrate temperature at this point being 19°C, as can be seen in Figure 12.3. At these conditions of pressure and temperature the water content of the acid gas is estimated to be 1 056 mg/Sm^3. At the required injection pressure of 6 203 kPaa and the dewpoint temperature of 28°C, the water holding ability of the gas, before it starts to liquefy, is 1 058 mg/Sm^3. Thus the gas has to be dehydrated, or perhaps by artificially and temporarily raising the pressure somewhat, the pressure after the third stage of compression may be enough to lower the water content.

Table 12.1 was generated to show the effect of increasing the pressure by means of a choke valve downstream of the fourth stage compression cylinder but ahead of the fourth stage cooler for four

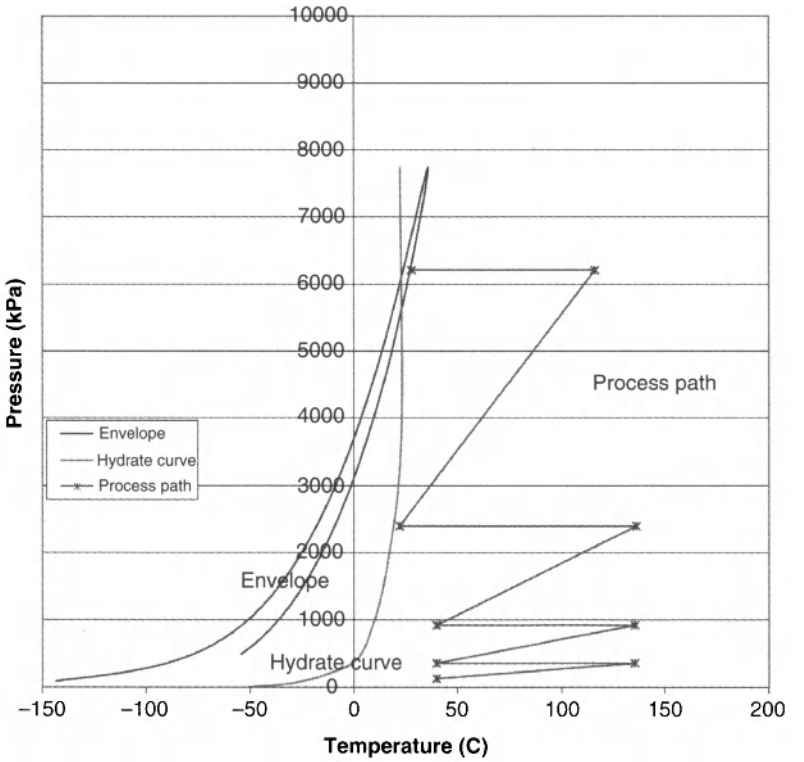

Figure 12.3 Phase diagram, hydrate and compression process path curves for 20% H_2S, 78% CO_2 and 2% C_1 with compression ratio of 2.58.

Table 12.1 Results of water content with pressure variations for an acid gas containing 20% H2S, 78% CO2 and 2% C_1.

Comp. Stage	Compr. Ratio	Pressure, kPaa	Temperature,°C	H_2O, mg/Sm³
4th stg suction	2.58	2 404	22	1 056
4th stg discharge	2.58	6 203		
After choke & cool	2.58	6 203	28	1 058
4th stg suction	2.60	2 460	23	1 102
4th stg discharge	2.60	6 460		
After choke & cool	2.60	6 203	28	1 058
4th stg suction	2.70	2756	24	1 082
4th stg discharge	2.70	7 440		
After choke & cool	2.70	6 203	28	1 058
4th stg suction	2.80	3 073	25	1 069
4th stg discharge	2.80	8 600		
After choke & cool	2.80	6 203	28	1 058
4th stg suction	2.90	3 414	25	1 006
4th stg discharge	2.90	9 900		
After choke & cool	2.90	6 203	28	1 058

higher test pressures. As can be seen, by increasing the compression ratio the water content in the fourth stage suction scrubber changed very little. This is due to the limitation imposed on the system to cool only to within 3°C of the hydrate temperature. As the pressure increases the hydrate forming temperature increases as well. Consequently the acid gas is cooled less as the pressure increases, resulting in insufficient change in the water content of the acid gas.

As can be seen from Table 12.1, increasing the discharge pressure slightly or considerably did not lower the water content sufficiently at the fourth stage scrubber conditions as compared with the water content at the dewpoint conditions of the acid gas at 28°C and 6203 kPaa. Figure 12.4 shows the pressure path for this particular

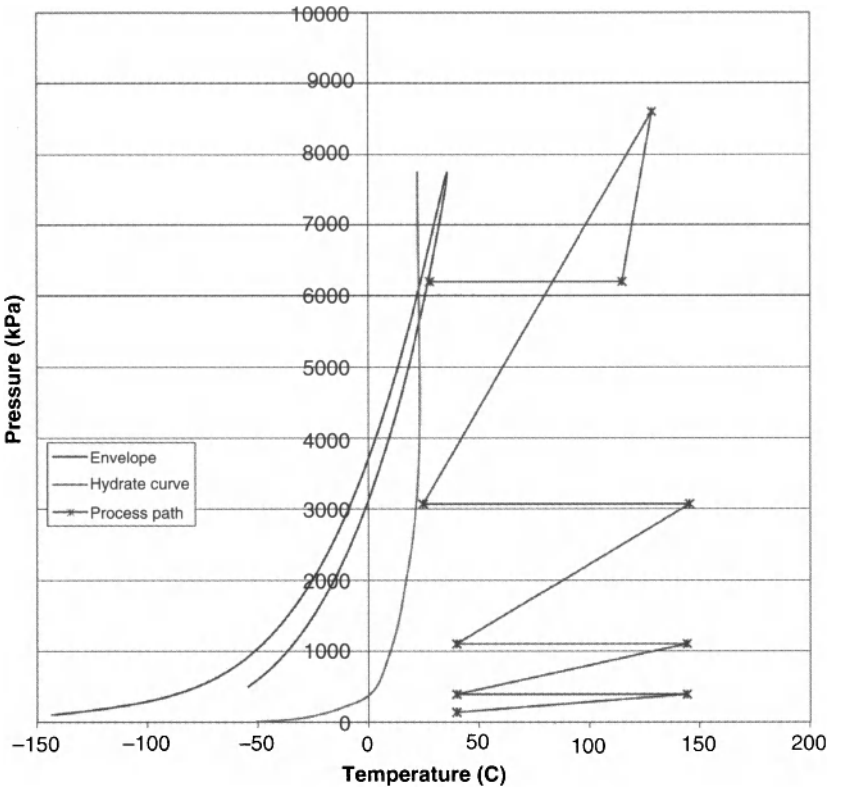

Figure 12.4 Phase diagram, hydrate and compression process path curves for 20% H_2S, 78% CO_2 and 2% C_1 with compression ratio of 2.8.

acid gas mixture at a compression ratio of 2.8. As can be seen in Table 12.1 at the 4th stage suction scrubber pressure of 3 073 kPaa and the cool-down temperature of 25°C, the water content is 1 069 mg/Sm^3. After the final stage of compression and pressure reduction to 6 203 kPaa, the water holding ability at the dewpoint temperature of 28°C is 1 058 mg/Sm^3. Thus nothing has been gained by increasing the pressure to this level, as far as water content reduction is concerned.

12.5 Test Case 2: 50% H_2S, 48% CO_2 and 2% C_1

Figure 12.5 shows the phase diagram and the hydrate line for this particular mixture. Both the hydrate curve and the phase diagram have moved to the right, to a higher temperature as compared to

the temperature relationship in Figure 12.4. The borderline pressure for this mixture is 5 044 kPaa. This means that at a somewhat higher well injection pressure there would be no need to dehydrate the gas as interstage cooling to within 3°C after the third stage of compression (fourth-stage suction scrubber pressure) would reduce the water content sufficiently.

Table 12.2 shows the results of the water content estimates at 5 044 kPaa and the cooling temperatures at various compression ratios. The results show again that increasing the pressure and then allowing the pressure to revert to the required pressure for the injection well has no benefit. For example, if the pressure were boosted by a compression ratio of 2.7 to a pressure of 7 440 kPaa, the third stage pressure would be 2 756 kPaa. The acid gas hydrate temperature at this pressure is 29°C. By cooling the acid gas to 32°C

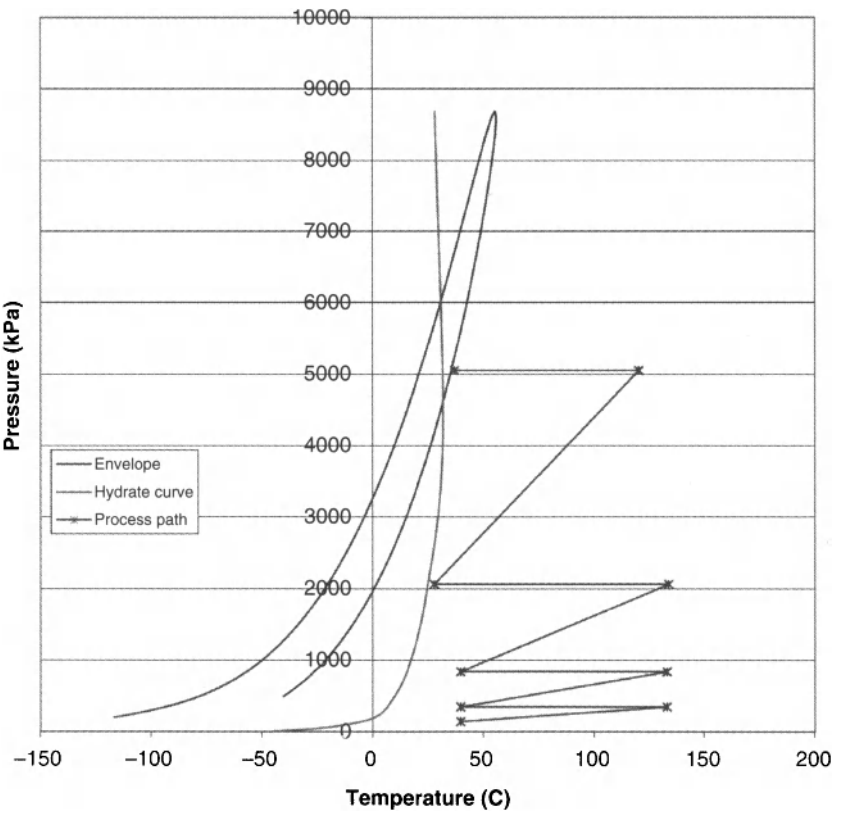

Figure 12.5 Phase diagram, hydrate and compression process path curves for 50% H_2S, 48% CO_2 and 2% C_1 with compression ratio of 2.45

Table 12.2 Results of water content with pressure variations for an acid Gas containing 50% H_2S, 48% CO_2 and 2% C_1.

Comp. Stage	Compr. Ratio	Pressure, kPaa	Temperature,°C	H_2O, mg/Sm³
4th stg suction	2.45	2 059	28	1 698
4th stg discharge	2.45	5 044		
After choke & cool	2.45	5 044	37	1 691
4th stg suction	2.50	2 188	29	1 718
4th stg discharge	2.50	5 470		
After choke & cool	2.50	5 044	37	1 691
4th stg suction	2.70	2 756	32	1 725
4th stg discharge	2.70	7 440		
After choke & cool	2.70	5 044	37	1 691
4th stg suction	2.90	3 414	34	1 685
4th stg discharge	2.90	9 900		
After choke & cool	2.90	5 044	37	1 691

at this pressure, the water content would be 1 725 mg/Sm³. This amount is slightly higher than what the water holding ability of the acid gas is at its dewpoint pressure of 5 044 kPaa and 37°C.

12.6 Test Case 3: 80% H_2S, 18% CO_2 and 2% C_1

At high concentrations of H_2S, the phase diagram shifts to a higher temperature on the P-T presentation. Figure 12.6 shows the phase diagram for the acid gas mixture of this Test Case. As can be seen, the hydrate temperature line also occurs at a higher temperature. The pressure selected for this case, 3 652 kPaa at a compression ratio of 2.26, again reflects the situation where the water content is in close balance between the water content after the third stage of compression and cooling and that at the dewpoint temperature and the required well injection pressure.

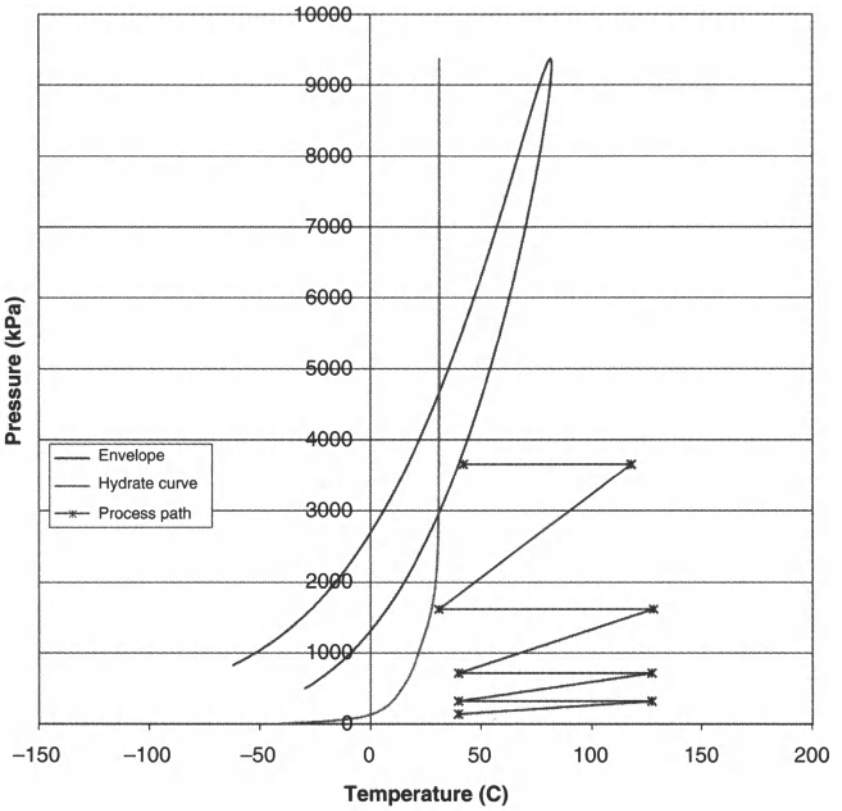

Figure 12.6 Phase diagram, hydrate and compression process path curves for 80% H_2S, 18% CO_2 and 2% C_1 with compression ratio of 2.26.

At the interstage pressure of 1 616 kPaa and within 3°C of the hydrate line, the water content is estimated at 2 445 mg/Sm^3, which is about 2% lower than the water holding ability of the acid gas at the pressure of 3 652 kPaa and 42°C, namely 2 486 mg/Sm^3. Again, this is too tight a margin of safety for a normal, trouble free operation of an acid gas injection system. The next step was to increase the pressure to 4 645 kPaa, with a compression ratio of 2.40. The results are summarized in Table 12.3. This represents a pressure increase of 27 %. At the new interstage pressure of 2 188 kPaa and a temperature of 32°C, the water content is 2 239 mg/Sm^3. This represents a water content of about 10% lower than the water holding ability of this acid gas mixture at the required injection pressure and the acid gas dewpoint temperature of 42°C.

This reduction in water content of the acid gas would be sufficient for a normal operation. However, if the cooling of the acid gas after the third stage of compression were to occur to only 34°C, the water content in the acid gas would be 2 500 mg/Sm^3, which would not be acceptable. Thus it is important to have excellent control over the degree of cooling of the acid gas after the third stage of compression.

Figures 12.7, 12.8 and 12.9 show the pressure-temperature relationships at compression ratios of 2.4, 2.6 and 2.8 respectively. The water content for the compression ratio case of 2.6, (Figure 12.8) shows that the pressure after three stages of compression is 2 756 kPaa, and by cooling to 33°C, the water content is only 1 983 mg/Sm^3.

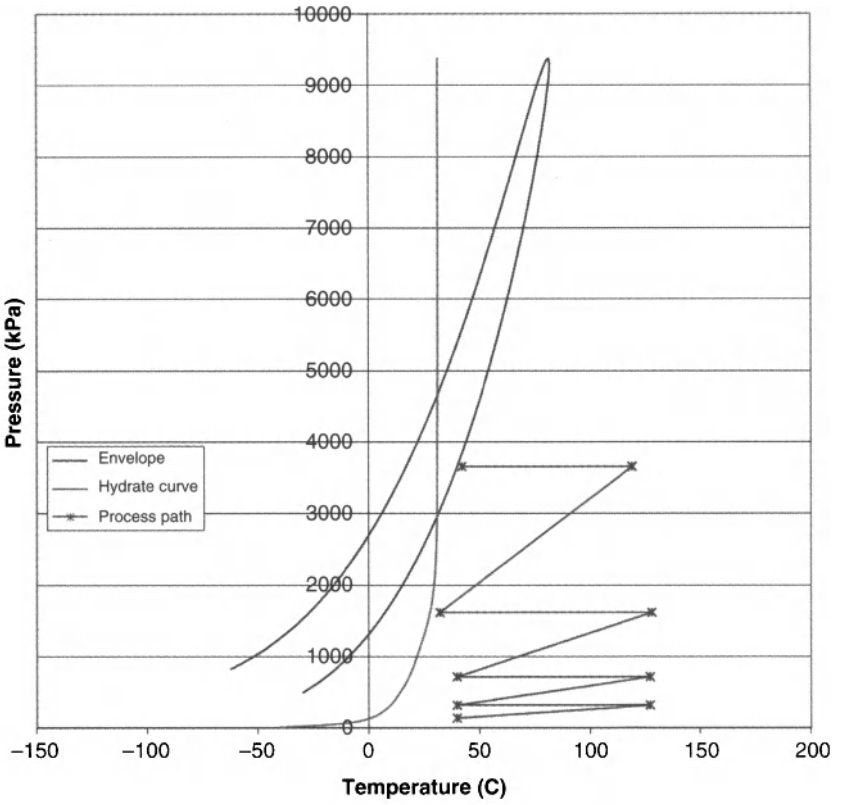

Figure 12.7 Diagram, hydrate and compression process path curves for 80% H_2S, 18% CO_2 and 2% C_1 with compression ratio of 2.4.

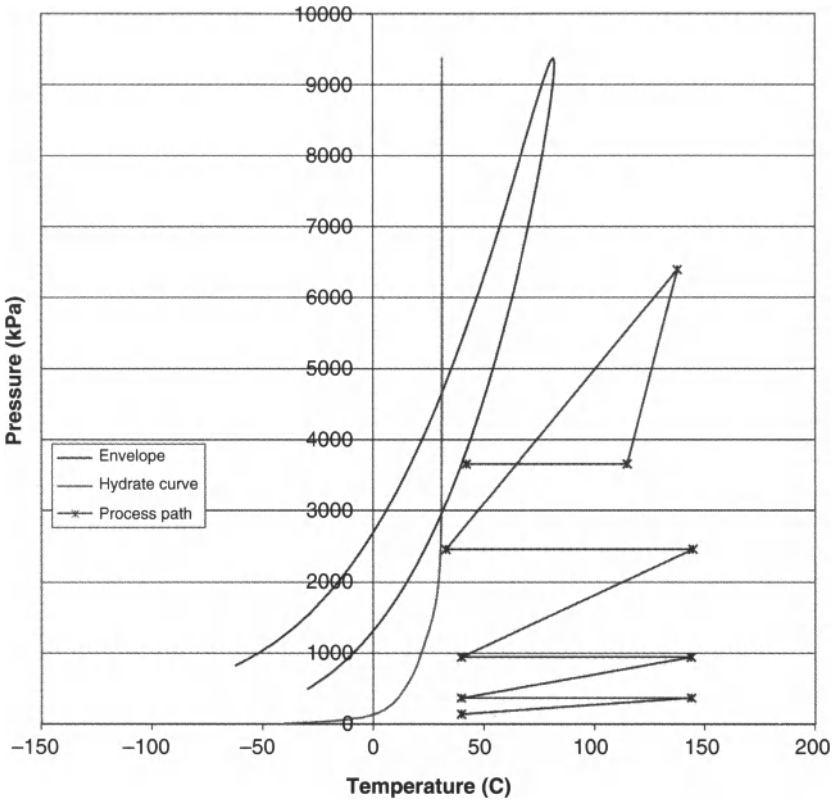

Figure 12.8 Diagram, hydrate and compression process path curves for 80% H_2S, 18% CO_2 and 2% C_1 with compression ratio of 2.6.

This again would be acceptable for water control by interstage cooling, provided the cooling level could be guaranteed. In Figure 12.9 it is seen that at the compression ratio of 2.8, the cooling limit after the third stagee of compression is not the hydrate temperature but the acid gas dewpoint temperature. This resulted in a somewhat higher water content in the acid gas than compared for the two lower compression ratio cases.

Acid gas mixtures that contain high concentrations of H_2S, as in this Test Case 3, lend themselves to water content control by interstage cooling much more readily than mixtures lean in H_2S. While the selected pressure of 3 652 kPaa did not lend itself readily for water control by interstage cooling, a pressure of 10% higher would have worked quite well in this regard.

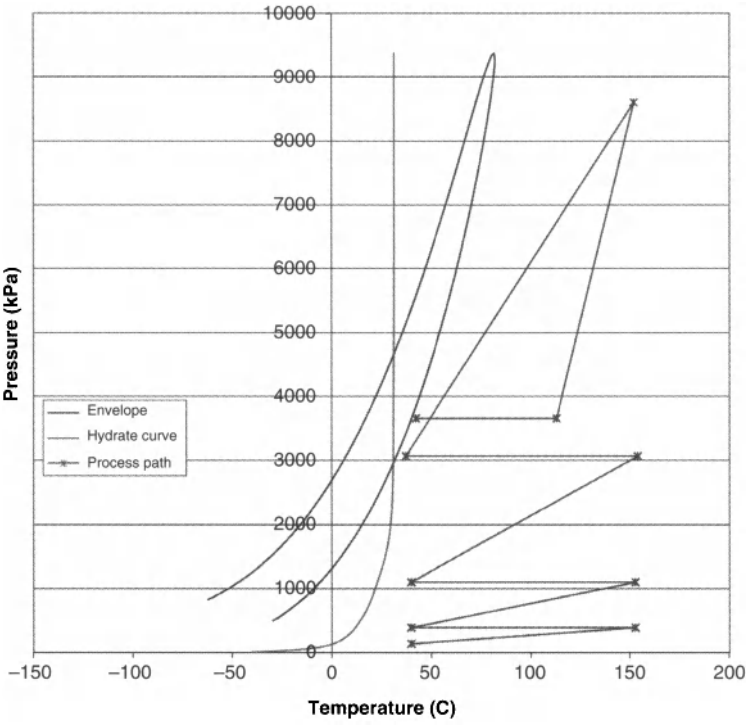

Figure 12.9 Phase diagram, hydrate and compression process path curves for 80% H_2S, 18% CO_2 and 2% C_1 with compression ratio of 2.8.

There is one other approach that can be taken with acid gas mixtures very rich in H_2S content and interstage cooling, as illustrated in Figure 12.10. The acid gas of Test Case 3, for example, can be compressed to a pressure of about 6 400 kPaa. By installing the choke valve at the wellhead instead of ahead of the cooler after the fourth stage of compression, the acid gas can be cooled as much as possible by the cooler, and then additionally cooled to about 10°C by the ground if the pipeline is long enough and the ground is cool enough. Then at the wellsite, the pressure can be reduced to the required injection pressure of 3 652 kPaa, as shown in Figure 12.10. Since the acid gas is now in the liquid state, and the injection pressure at a temperature of 10°C remains in the liquid state, no water will drop out. On the phase diagram in Figure 12.10, the bubble point temperature is 51°C at 6 400 kPaa and the water holding ability is 11 560 mg/Sm^3. The actual water content, as shown in Table 12.3 for the 2.60 compression ratio case, is

Table 12.3 Results of water content with pressure variations for an acid Gas containing 80% H_2S, 18% CO_2 and 2% C_1.

Comp. Stage	Compr. Ratio	Pressure, kPaa	Temperature, °C	H_2O, mg/Sm³
4th stg suction	2.26	1 616	31	2 445
4th stg discharge	2.26	3 652		
After choke & cool	2.26	3 652	42	2 486
4th stg suction	2.40	1 935	32	2 239
4th stg discharge	2.40	4 645		
After choke & cool	2.40	3 652	42	2 486
4th stg suction	2.60	2 461	33	1983
4th stg discharge	2.60	6 400		
After choke & cool	2.60	3 652	42	2 486
4th stg suction	2.80	3 073	37	2123
4th stg discharge	2.80	8 605		
After choke & cool	2.80	3 652	42	2 486

1983 mg/Sm³. At the injection pressure of 3 652 kPaa and 10°C, the water holding ability is 4 482 mg/Sm³. Thus the acid gas remains undersaturated in water content. This approach requires that the acid gas does not cross the bubble point pressure upon pressure reduction in the liquid state. Cooling to a lower temperature in the liquid state before pressure reduction to that required for injection would increase the margin of safety for such a method of water content control.

12.7 Conclusions

The object of this paper was to evaluate the effectiveness of a choke valve placed after the final compression stage in order to artificially raise the injection pressure so that water content is sufficiently minimized in situations where the actual required injection pressure

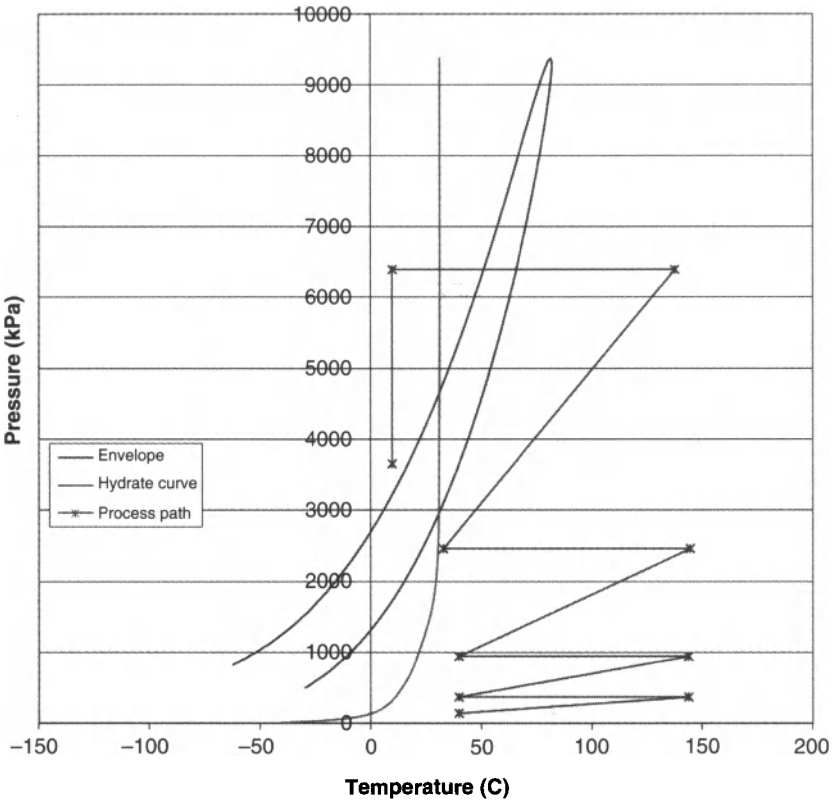

Figure 12.10 Phase diagram, hydrate and compression process path curves for 80% H_2S, 18% CO_2 and 2% C_1 with compression ratio of 2.6 and chilling of the discharge of the 4th stage compressor down to 10 C.

in itself was not high enough. This evaluation was completed via a number of simulation cases highlighting the effect of both the compression ratio and composition on the ability to dehydrate the stream to be injected. It was found that in some instances with high concentrations of H2S (> 60%) that indeed it was possible to dehydrate the injected stream with the use of a choke to raise the compression pressure though caution must be used and a detailed analysis must be conducted. The required injection pressure and the composition of the acid gas can affect the ability to be able to dehydrate with cooling and compression so the variation of these parameters over the life of the acid gas injection facility must be considered in the design of the facility.

13

The Kinetics of H_2S Oxidation by Trace O_2 and Prediction of Sulfur Deposition in Acid Gas Compression Systems

N. I. Dowling*, R. A. Marriott†, A. Primak, and S. Manley

Alberta Sulphur Research Ltd., Calgary, AB, Canada
**dowlingn@ucalgary.ca*
†rob.marriott@ucalgary.ca

Abstract

The appearance of elemental sulfur in systems handling acid gases, such as compression systems, can be linked to the ingress of oxygen. This can result in oxidation of H_2S to form elemental sulfur, which can appear as a solid, depending on the temperature and solubility of S_8 in the acid gas fluid. The formation of solid elemental sulfur in these types of systems can lead to problems due to deposition of S_8 within compressor components, resulting in operational as well as corrosion issues.

Investigation of the kinetics of H_2S oxidation by trace O_2 has been carried out in the laboratory over the temperature and pressure range from T = 50 to 140°C and p = 100 to 1000 psig using a Silcosteel reactor. The study was performed under pseudo-order reaction conditions, with H_2S in a concentration range of 2–5 mol% and O_2 levels from 1000–1600 ppmv by following the disappearance of O_2. Values for the pseudo-first order rate constant for H_2S oxidation in the range of $1–4 \cdot 10^{-4}$ min^{-1} were determined at 140°C over the pressure range from p = 100 to 1000 psig, along with the reaction orders with respect to H_2S and O_2. The ability of a bare steel surface to act as a catalyst for H_2S oxidation was also investigated, and was found to increase the reaction rate by as much as 3600 times.

These rate data can be used to compare the formation of elemental sulfur with the solubility of S_8 in sour mixtures, in order to examine the potential for S_8 deposition in sour systems due to trace O_2. The saturation solubility of elemental sulfur has been modeled using an infinite dilution virial model combined with the standard fugacities for elemental

Ying (Alice) Wu, John J. Carroll and Weiyao Zhu (eds.) Sour Gas and Related Technologies, (183–214)

sulfur [1] and the reduced Helmoltz energy equations-of-state from NIST REFPROP9. Both the solid and liquid sulfur formation conditions can be estimated using this model. By comparing the sulfur produced by oxidation at compression conditions, the potential for deposition was estimated for a hypothetical four-stage compression system containing a 50:50 H_2S/CO_2 acid gas mixture. The overall tolerance for oxygen ingress was found to be very small.

13.1 Introduction

Native elemental sulfur deposition has plagued sour gas producers for some time [2,3] since the severe pressure and temperature changes from the reservoir to the wellhead can drastically change the solubility within the producing fluid. More recently, some limited cases have been noted where sulfur has deposited within fluid interstage cooling of acid or sour gas fluids destined for injection. In both cases, elemental sulfur deposition is a concern due to flow assurance and corrosion tolerance.

Depositable elemental sulfur can form in a gas system by various mechanisms: (i) oxidation of H_2S, (ii) thermophilic bacterial sulfate reduction (BSR) (iii) thermal cracking of sulfides residing in kerogen or oils and (iv) thermal sulfate reduction (TSR). Of these four, the latter three are considered sources for native reservoir H_2S and TSR is an accepted mechanism for dissolved elemental sulfur in a lean sour gas reservoir [2]. For an acid gas injectate, assuming the gas has passed through an amine sweetening system, the most likely source of the elemental sulfur would be from the presence of oxygen, which produces elemental sulfur by oxidation of H_2S:

$$\tfrac{1}{2}\,O_2 + H_2S \rightarrow H_2O + \tfrac{1}{8}\,S_8 \qquad (13.1)$$

Thus sulfur deposition can be due to oxidation beyond the solubility capacity of the fluid. Potential sources of oxygen can include (i) the migration of oxygen across a dry gas seal on a centrifugal compressor (seal gas oxygen) or possibly (ii) the introduction of recovered vent gas in a reciprocating compressor system. In either possible case the kinetics of H_2S oxidation and elemental sulfur solubility need to be well understood over a wide range of temperature and pressure.

While the oxidation of H_2S has been studied at lower-pressures, the high-pressure kinetics in a compressor system are poorly understood. Several mechanisms for the oxidation of H_2S include (i) direct oxidation [4,5], (ii) formation of SO_2 followed by the Claus reaction [6] and (iii) the presence of a metal oxide followed by formation of a metal sulfide [6]. Although the un-catalysed reaction at atmospheric pressure is slow, the overall rate of Reaction (1) depends on temperature, O_2 partial pressure, H_2S partial pressure [7,8], phase (e.g., aqueous, hydrocarbon) and the presence of catalysts (metal oxide surfaces [6], metal sulfide surfaces, aqueous metal cations [9]). Also, the observation of autocatalysis under aqueous conditions suggests that the reaction may proceed through a hydropolysulfide intermediate in the aqueous phase [9]. Note that within a compression system the knock-out/suction scrubbers after each interstage cooling will contain water and the metal surfaces within the compressors will contain metal sulfides, e.g., surfaces within dry gas seals will sulfided.

Considering the various possible reaction mechanisms and lack of high-pressure information, this study aimed at defining the kinetics of H_2S oxidation in the gas phase under high-pressure conditions (with and without exposure to a bare metal surface) and the modelling of the sulfur carrying capacity (solubility) of an acid gas. Analysis of the experimental data revealed a surface active mechanism which is in a reaction controlled regime. The kinetics support a mechanism by which adsorbed H_2S reacts with O_2 in the gas phase. Using the kinetic and thermodynamic models, application is shown using a hypothetical 50:50 H_2S/CO_2 injectate fluid which is compressed in 4 stages. The tolerable O_2 ingress limits were found to be very low.

13.2 Experimental

Kinetic experiments were carried out in the experimental apparatus shown in Figure 13.1 using a standard Gas Chromatography (GC) oven to thermostat the reactor and Advanced Specialty Gas Equipment mass flow control system to deliver and blend the feed gases. Initial reaction mixtures were produced by blending pre-purchased gas mixtures of 10% H_2S in N_2 and 2000 ppmv O_2 in N_2 (Praxair) in the required proportions and using a Tescom back-pressure regulator to control the reactor pressure. Both passivated (Restek Silcosteel containing an inert silicon-based coating used to

passivate active metal surfaces) and bare steel (SS316) reactors were used consisting of coiled 12 foot lengths of ¼ o.d. tubing. Initial feed mixtures were charged by flowing the blended stream through the reactor at room temperature and an appropriate pressure so as to achieve the required p/T condition on raising the reactor temperature. This approach was based on preliminary experiments which showed no detectable reaction at 21°C over a 24 hour period. Due to the timescale of the kinetics, the experiments were performed in a batch mode as opposed to continuous flow by shutting in the reactor prior to raising the reactor temperature. Initial feed mixtures of 5% H_2S + 1000 ppmv O_2, 3.33% H_2S + 1330 ppmv O_2 and 2% H_2S + 1600 ppmv O_2 were examined in the study over a temperature and pressure range of 90–140°C and 100–1000 psig.

The concentrations of O_2 and H_2S in the feed were measured by GC using a direct transfer line for the O_2 measurements and syringe sampling for the H_2S. Samples of the feed mixture were obtained during setup from the gas flow behind the back pressure regulator and samples of the reaction products were similarly obtained during depressurization of the reactor, following cooling, at the end of the experiment. The latter step was performed in discrete block and bleed stages in order to maximize the gas usage for analysis. Analysis of O_2 was performed using a Varian 3400 gas chromatograph equipped with a TCD and Rt-molesieve 5Å column and H_2S was analyzed on a Varian 3800 GC equipped with a TCD and Poraplot U column. Following depressurization of the reactor and analysis of the reaction products, the reactor was opened and rinsed with CS_2 to recover and quantify the amount of elemental sulfur formed. This analysis was performed by the GC-TPP (triphenylphosphine) method [10], which is specific for elemental sulfur, using a Varian 3800 GC equipped with a PFPD detector operating in phosphorous mode.

13.3 Experimental Results and Calculation Methods

13.3.1 Determination of the Kinetics of H_2S Oxidation

The results of the kinetic experiments performed with feed mixtures of 5% H_2S + 1000 ppmv O_2, 3.33% H_2S + 1330 ppmv O_2 and 2% H_2S + 1600 ppmv O_2 are shown in Tables 13.1–13.3. These

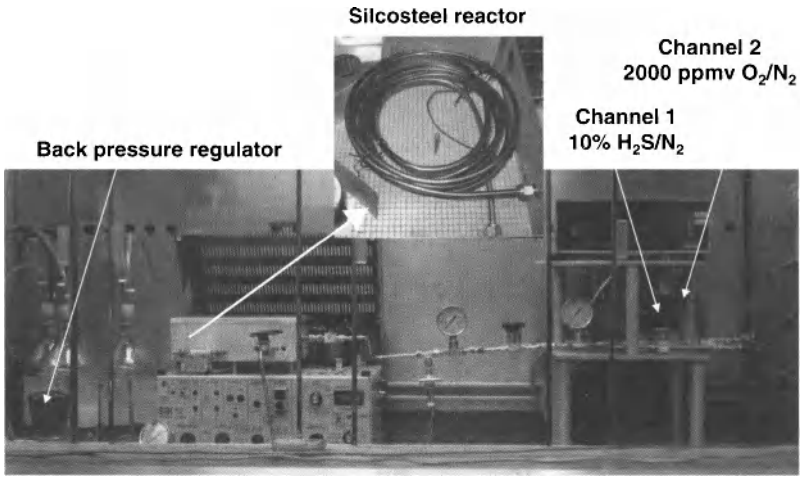

Figure 13.1 Experimental apparatus.

tables provide the temperature and pressure conditions and reaction time for each experiment as well as the % O_2 conversion and % S_8 formation calculated by O_2 GC and GC-TPP analyses. The majority of the experiments were performed at 140°C using reaction times on the order of 8 hours to 144 hours in order to acquire suitable kinetic data. Initial experiments performed at lower temperatures of 21°C and 50°C over a 24 hour period showed no reaction within the margin of error for the GC analyses. These results represent the basis for performing the kinetic experiments by the method described in the Experimental section of charging the reactor at room temperature (21°C) prior to setting the reaction temperature.

The stoichiometry of the H_2S oxidation reaction under the conditions of the study was established by comparing the experimental % O_2 conversion with the % S_8 formation in Tables 13.1–13.3. This comparison is shown by the correlation plot in Figure 13.2, which provided a slope of 0.99 for all of the experimental data. The extent of scatter indicated by a correlation coefficient (R^2) of 0.89 for this plot reflects the relatively small quantities of elemental sulfur, from sub-milligram to 10–15 mg, being worked with under the selected conditions. This correlation demonstrates that the overall reaction for H_2S oxidation under the conditions of the study can be written as shown in Reaction 1. Going to form sulfur and water as the principal products. This overall stoichiometry is also supported by the absence of SO_2 as a reaction

Table 13.1 Experimental results for the 5% H_2S/1000 ppmv O_2 feed in a Silcosteel reactor.

5% H_2S/1000 ppmv O_2			
Time (hrs)	**Temperature (°C)**	**Pressure (psig)**	**% Conversion of O_2 [a]/ % Formation of S_8**
95.2	90	100	3.3 / 2.3
95.8	120	100	11.6 / 4.4
8.2	140	102	2.2 / 4.2
24.2	140	102	8.7 / 11.5
48.0	140	107	16.6 / 11.4
71.2	140	104	25.9 / 13.5
94.2	140	107	35.7 / 35.7
123.0	140	102	39.8 / -
23.8	140	500	12.0 / 17.9
97.2	140	500	56.3 / 35.5
143.9	140	500	64.2 / 68.0
23.9	140	1000	20.4 / 19.2
50.3	140	1000	30.5 / 40.4
93.6	140	1000	54.4 / 55.0
143.8	140	1000	70.9 / 79.1

[a] O_2 GC analysis: $(\{[O_2]_{init}-[O_2]_{final}\} / [O_2]_{init}) \times 100$. [b] S_8 TPP analysis: (S_8 yield / theo. yield of S_8) × 100.

product, which was established by separate GC analyses using a GC-PFPD system.

The general form of the rate expression for oxidation of H_2S in the presence of trace O_2 based on the stoichiometry in equation (13.1) can be written as:

$$\frac{-d[H_2S]}{dt} = \frac{-2d[O_2]}{dt} = k[H_2S]^a[O_2]^b \qquad (13.2)$$

Table 13.2 Experimental results for the 3.33% H_2S/1330 ppmv O_2 feed in a Silcosteel reactor.

3.33% H_2S/1330 ppmv O_2			
Time (hrs)	**Temperature (°C)**	**Pressure (psig)**	**% Conversion of O_2 [a]/ % Formation of S_8**
24.1	140	107	7.9 / 8.2
47.7	140	107	13.9 / 5.8
95.5	140	107	26.5 / 24.7
22.7	140	500	12.7 / -
48.5	140	500	23.5 / 33.4
142.0	140	500	68.2 / 75.7
20.8	140	1000	17.8 / 31.4
46.3	140	1000	49.9 / 31.7
93.9	140	1000	74.9 / 76.3

[a] O_2 GC analysis: $(\{[O_2]_{init}-[O_2]_{final}\} / [O_2]_{init}) \times 100$. [b] S_8 TPP analysis: (S_8 yield / theo. yield of S_8) × 100.

Table 13.3 Experimental results for the 2% H_2S/1600 ppmv O_2 feed in a Silcosteel reactor.

2% H_2S/1600 ppmv O_2			
Time (hrs)	**Temperature (°C)**	**Pressure (psig)**	**% Conversion of O_2 [a]/ % Formation of S_8**
23.8	140	107	5.6 / 5.1
46.0	140	107	10.3 / 9.4
95.6	140	106	22.4 / 13.3
22.7	140	500	20.4 / -
48.5	140	500	29.2 / -
24.2	140	1000	21.6 / 19.0
46.5	140	1000	28.8 / -
96.1	140	1000	63.9 / 68.1

[a] O_2 GC analysis: $(\{[O_2]_{init}-[O_2]_{final}\} / [O_2]_{init}) \times 100$. [b] S_8 TPP analysis: (S_8 yield / theo. yield of S_8) × 100.

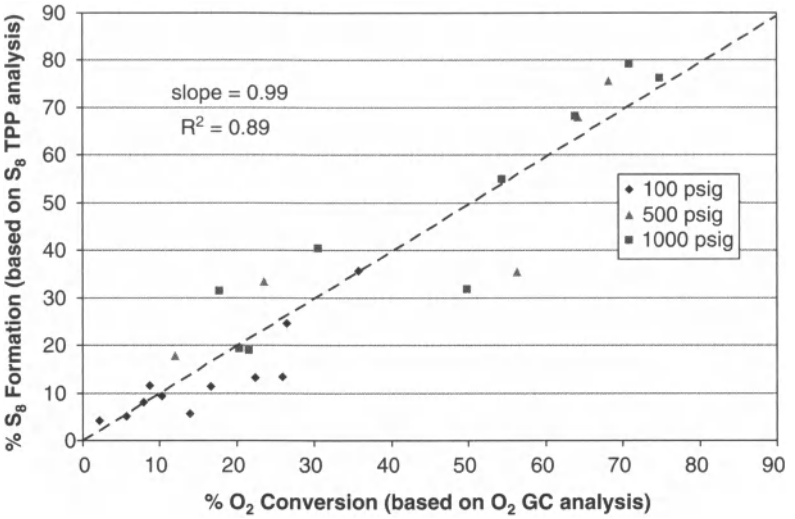

Figure 13.2 Correlation plot of O_2 conversion versus S8 formation for H2S oxidation.

The conditions selected for the study of percent concentrations of H_2S (2–5%) and ppmv levels of O_2 means that the system is setup, from a kinetics standpoint, as a pseudo-order condition with respect to the large excess of H_2S. This allowed the kinetics to be studied as an overall pseudo-order reaction by following the conversion of O_2.

The order with respect to $[O_2]$ for H_2S oxidation in the passivated Silcosteel reactor was determined by standard kinetic analysis by plotting the O_2 conversion data according to the integrated form of the rate expression for zero, first and second order reactions ($b = 0,1$ or 2). For the case representing an overall first order reaction in O_2 and pseudo-order with respect to H_2S, Equation (13.2) yields the following expression:

$$\ln\frac{[O_2]}{[O_2]_o} = \ln(1-conv) = \frac{-k't}{2}, \qquad (13.3)$$

where k', the pseudo-first order rate constant, $k' = k[H_2S]^a$. These plots are presented in Figures 13.3–13.5, as ln(1–*conv*) versus t,

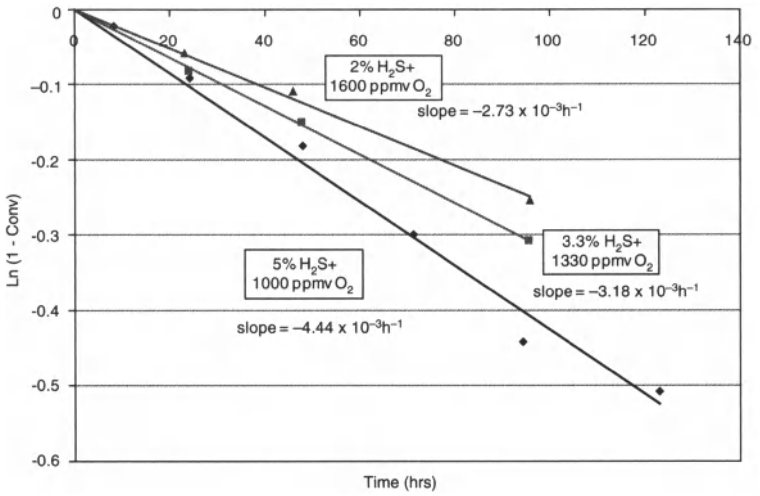

Figure 13.3 First order kinetic plots for O_2 conversion at 140°C and 100 psig for the passivated reactor.

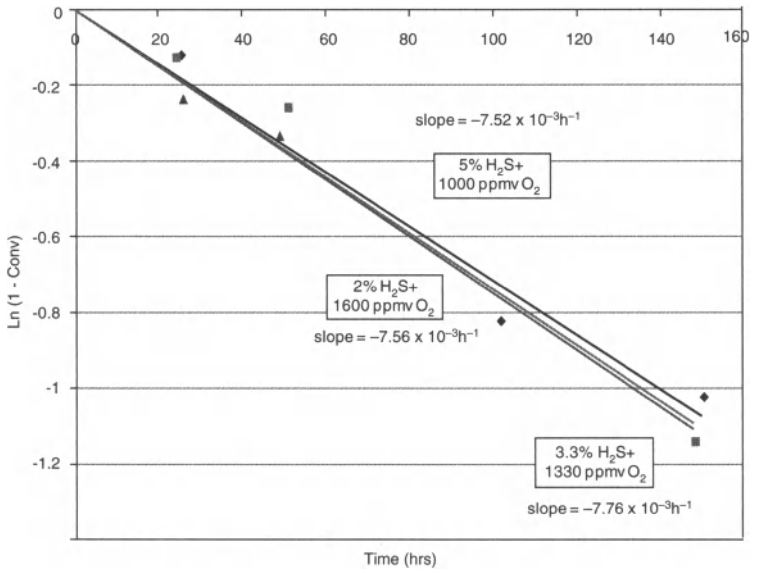

Figure 13.4 First order kinetic plots for O_2 conversion at 140°C and 500 psig for the passivated reactor.

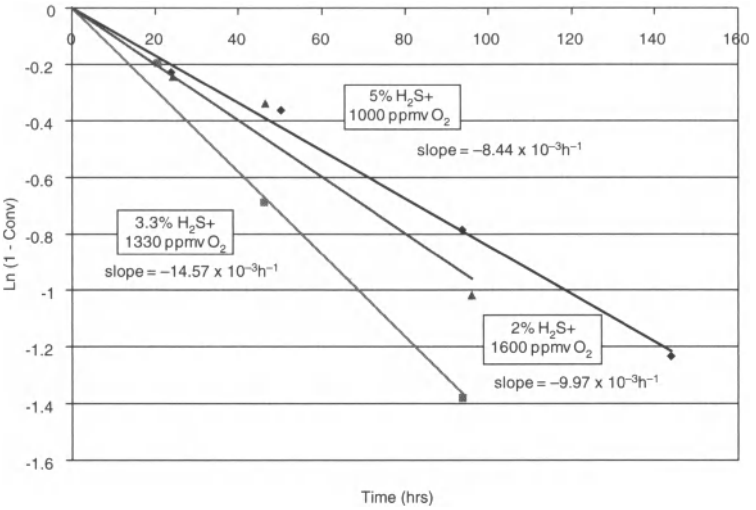

Figure 13.5 First order kinetic plots for O_2 conversion at 140°C and 1000 psig for the passivated reactor.

at the three pressures of 100, 500 and 1000 psig yielding values for the pseudo-first order rate constant from the slope (= $-k'/2$). These values are listed in Table 13.4 for all of the conditions examined in Tables 13.1–13.3.

The corresponding rate constants at 90°C and 120°C were obtained by using the fractional-life ($t_{1/x}$) approach or relationship between the fractional-life and conversion for a first order reaction [11]. This relationship can be expressed as:

$$t_{1/x} = \frac{\ln(x/(x-1))}{ak'} = \frac{\ln(1/(1-conv))}{ak'} \qquad (13.4)$$

where $t_{1/x}$ is the fractional-life or reaction time, x is 1/(fractional conversion) and a is the stoichiometric factor for O_2; $a = 1/2$, for the balanced reaction in Equation (13.1).

The corresponding order with respect to $[H_2S]$ for the oxidation reaction in the passivated Silcosteel reactor was examined by plotting $\ln k'$ versus $\ln[H_2S]$,

Table 13.4 Pseudo-first order rate constants (min^{-1}) for H_2S oxidation in a passivated reactor.

T (°C)	100 psig	500 psig	1000 psig
5% H_2S / 1000 ppmv O_2			
90	$1.16 \cdot 10^{-5}$	-	-
120	$4.30 \cdot 10^{-5}$	-	-
140	$1.48 \cdot 10^{-4}$	$2.51 \cdot 10^{-4}$	$2.78 \cdot 10^{-4}$
3.33% H_2S / 1330 ppmv O_2			
140	$1.06 \cdot 10^{-4}$	$2.59 \cdot 10^{-4}$	$4.87 \cdot 10^{-4}$
2% H_2S / 1600 ppmv O_2			
140	$9.10 \cdot 10^{-5}$	$2.55 \cdot 10^{-4}$	$3.32 \cdot 10^{-4}$

$$\ln k' = \ln k + a \ln[H_2S], \qquad (13.5)$$

for the individual feed mixtures at all three pressures. The concentration of H_2S in these plots is expressed in mole % terms in order to have all three plots appear at the same region on the x-axis. Thus, equation (13.5) can be re-written as

$$\ln k' = \ln k + a \ln \frac{p_{tot}}{100RT} + a \ln(\text{mole\%}H_2S), \qquad (13.6)$$

where the second term reduces to a constant for a given pressure. These plots are presented in Figure 13.6 with a slope and corresponding order with respect to H_2S of ~0.5 for the 100 psig case and a value of around zero for both the 500 and 1000 psig conditions.

The zero order behaviour with respect to H_2S at higher pressure was directly confirmed by performing a series of kinetic experiments with O_2 in large excess (18.54%) relative to H_2S (1.17%) and looking

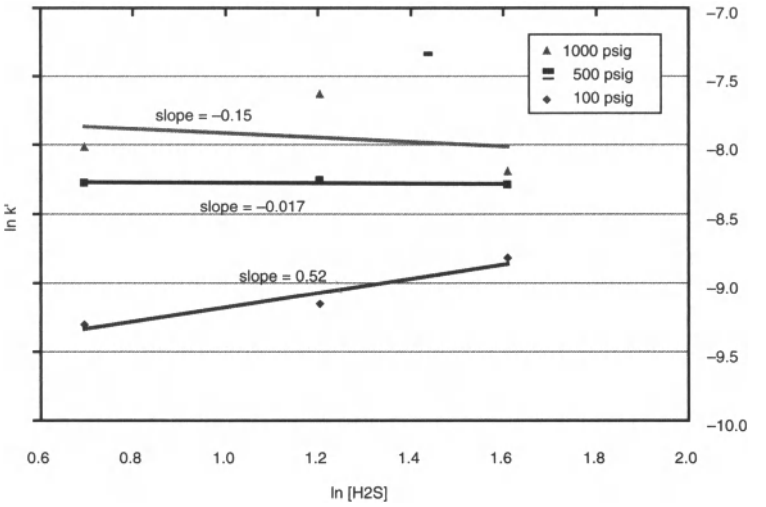

Figure 13.6 Kinetic order with respect to H_2S for reaction at p = 100, 500 and 1000 psig.

at the disappearance of H_2S instead. These conditions were achieved by switching the 2000 ppmv O_2 in N_2 mixture for air and using the same 10% H_2S in N_2 mixture. The experiments were performed in the same Silcosteel reactor used for the trace O_2 runs at a similar pressure of 1000 psig and temperature of 140°C. The results of these experiments are shown in Figure 13.7 as the standard kinetic analysis for a zero order reaction, of H_2S concentration versus time. This plot shows the expected linearity for a zero order reaction with intercept equal to $[H_2S]_o$, supporting the corresponding results for the order with respect to H_2S obtained from the trace O_2 experiments by plotting ln k' versus ln$[H_2S]$ in Figure 13.6.

This rate behaviour for H_2S oxidation leading to a non-zero order in H_2S at low pressure and zero order at higher pressure, with 1st order in O_2, can be explained by a bimolecular surface reaction occurring *via* the Eley-Rideal mechanism [12]. The overall mechanism of the surface mediated H_2S oxidation in the presence of trace O_2 within a passivated Silcosteel reactor can then be represented as:

$$H_2S(g) + S^* \leftrightarrow H_2S(ads)—S^* \qquad (13.7)$$

$$H_2S(ads)—S^* + 1/2O_2(g) \xrightarrow{rds} 1/8S_8 + H_2O + S^* \qquad (13.8)$$

involving reaction of gas phase O_2 with adsorbed H_2S. The general rate expression for this mechanism after substitution for the

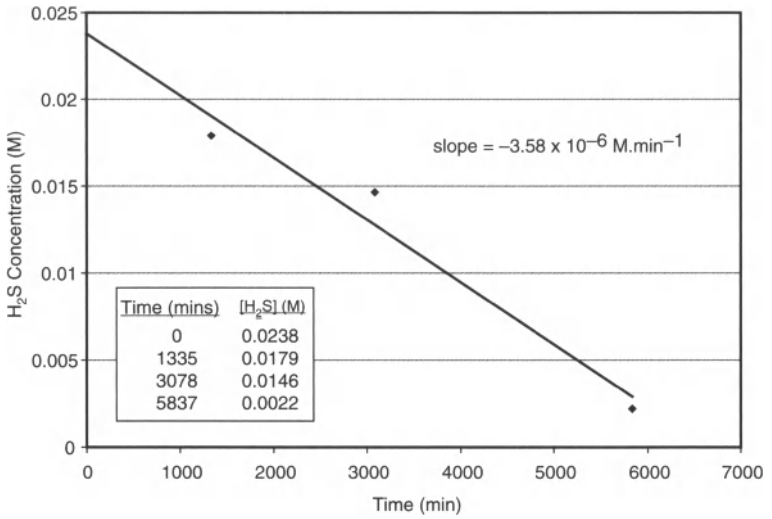

Figure 13.7 Zero order kinetic plot for H_2S conversion at 140°C and 1000 psig for the passivated reactor.

surface coverage of H_2S, $\theta_{H_2S} = (K_{H_2S}p_{H_2S})/(1+K_{H_2S}p_{H_2S})$ derived from the Langmuir isotherm, is given by

$$\frac{-d[H_2S]}{dt} = k\frac{K_{H_2S}p_{H_2S}p_{O_2}}{1+K_{H_2S}p_{H_2S}}, \tag{13.9}$$

where K_{H_2S} is the adsorption equilibrium constant and p_{H_2S} and p_{O_2} are the partial pressures of H_2S and O_2. This equation represents a shifting-order rate expression that simplifies to first order in H_2S and O_2 at low pressures and zero order with respect to H_2S at higher pressures.

Alternative rate expressions for the Eley-Rideal (Eqn 13.10) and Langmuir-Hinshelwood (Eqn 13.11) mechanisms involving dissociative adsorption of O_2 are given by

$$\frac{-d[H_2S]}{dt} = k\frac{K_{O_2}^{1/2}p_{H_2S}p_{O_2}^{1/2}}{1+K_{O_2}^{1/2}p_{O_2}^{1/2}} \tag{13.10}$$

and

$$\frac{-d[H_2S]}{dt} = k\frac{K_{H_2S}K_{O_2}^{1/2}p_{H_2S}p_{O_2}^{1/2}}{\left(1+K_{H_2S}p_{H_2S}+K_{O_2}^{1/2}p_{O_2}^{1/2}\right)^2}, \tag{13.11}$$

but these mechanisms correspond to a 1/2 order in O_2 instead [13]. The Eley-Rideal mechanism with either dissociative (Eqn 13.10) or molecular (Eqn 13.12) adsorption of O_2, instead of H_2S,

$$\frac{-d[H_2S]}{dt} = k\frac{K_{O_2}p_{H_2S}p_{O_2}}{1+K_{O_2}p_{O_2}} \tag{13.12}$$

also does not fit with the experimentally observed kinetic orders with respect to H_2S and O_2.

The expected rate behaviour based on gas phase O_2 reaction with adsorbed H_2S is further exemplified by plotting the pseudo-first order rate constants at 140°C in Table 13.4 as a function of H_2S partial pressure. This plot is shown in Figure 13.8 for all of the 140°C data for all three feed mixtures and pressures of 100–1000 psig. The curve was obtained by best fitting using non-linear regression to a form

$$1/y = a_0 + a_1/x \tag{13.13}$$

consistent with the plateau in k' at higher pressures. This particular form for the plot corresponds to the shifting-order rate behaviour observed experimentally, where $k' = k[H_2S]^a$, which for $a = 0$ at high partial pressures of H_2S becomes, $k' = k$ for $[H_2S]^a = 1$, or independent of pressure.

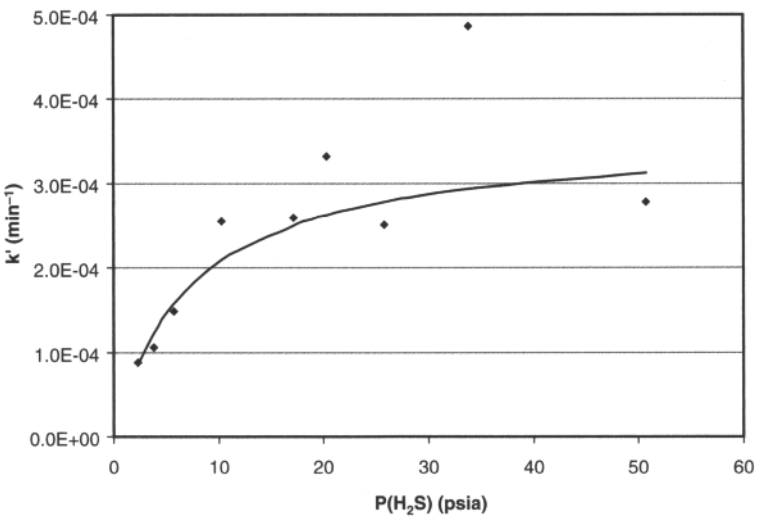

Figure 13.8 Plot of pseudo-first order rate constant for H_2S oxidation at 140°C against H_2S partial pressure.

Table 13.5 Experimental results for H_2S oxidation in a bare stainless steel reactor.

5% H_2S/1000 ppmv O_2			
Time (hrs)	**Temperature (°C)**	**Pressure (psig)**	**% Conversion of O_2 [a] / % Formation of S_8**
95.4	20	350	79.7
45.1	140	1000	> 99[b]

[a] O_2 GC analysis: $(\{[O_2]_{init}-[O_2]_{final}\} / [O_2]_{init}) \times 100$. [b] Corresponding % O_2 conversion for the Silcosteel reactor of ~30%.

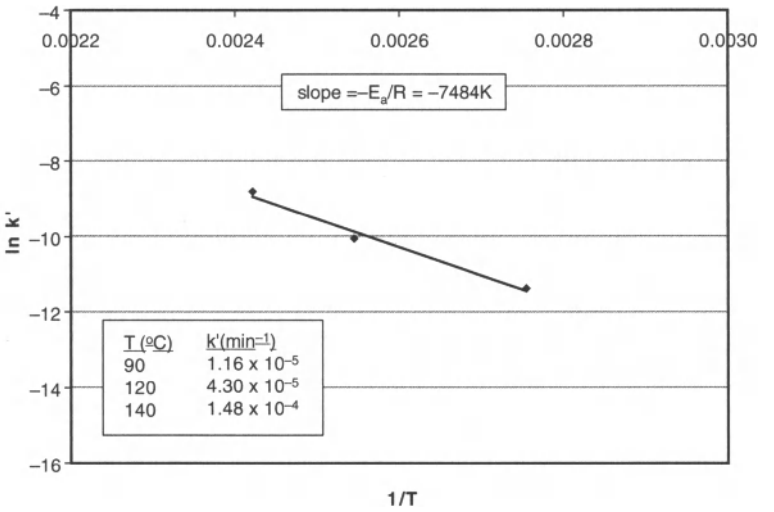

Figure 13.9 Arrhenius plot for H_2S oxidation in the passivated reactor at 100 psig.

The activation energy for H_2S oxidation can be determined from the pseudo-first order rate constants at 90, 120 and 140°C at a pressure of 100 psig for the 5% H_2S + 1000 ppmv O_2 feed in Table 13.4. The Arrhenius plot for the surface assisted H_2S oxidation in the passivated Silcosteel reactor is presented in Figure 13.9. This plot gives a slope = $-E_a/R = -7484$ K, providing a value of 62.2 kJ/mol for the activation energy. This value for E_a falls within the typical range of >30–50 kJ/mol for surface-reaction controlled catalytic processes involving adsorption or reaction of adsorbed species in the rate determining step [12].

Several experiments were also performed in a non-Silcosteel reactor to examine the effect of a bare steel surface on the rate of H_2S oxidation. These runs were performed with an uncoated 316 stainless steel reactor at select conditions only of 140°C/1000 psig and 20°C/350 psig using the same 5% H_2S + 1000 ppmv O_2 feed for comparison to the Silco-coated reactor. The results of these experiments are shown in Table 13.5 demonstrating that the rate of H_2S oxidation is faster at both 140°C and 20°C in the presence of the bare steel surface, compared to the passivated reactor, with the accelerated rate leading to significant reaction even at 20°C.

13.3.2 Thermodynamic Model for Sulfur Solubility

In order to utilize the above kinetic information to examine the potiential for sulfur deposition in an acid gas compression system, the equilibrium conditions for sulfur saturation in an acid gas must be known. Due to the conditions of an injection system, the accurate modelling of elemental sulfur solubility must extend over a wide temperature range of 0 to 150°C and high-pressures. Within this large temperature range, sulfur may be liquid, α-solid or β-solid; the acid gas fluids may be gaseous or dense phase. Adding to the modelling challenges is sulfur's ability to disproptionate to sulfur species other than S_8 and reversibly react with H_2S to form polysulfanes. For example, both Heideman *et al.* [14]. and Cézac *et al.* [15]. have incorporated the chemical equilibria containing polysulfanes into their respective models. Another approach is to empirically interpolate a spline fit of the experimental data [16] and avoid problematic modelling; however, with this method extrapolations to typical suction scrubber temperatures from experimental data are not possible. Here we describe the most recent update of a model which has been used by ASRL to address both production and injection fluids.

The current available experiment data have been reviewed and a model is presented which is based on the volume explicit virial equation for infinite dilution fugacity and the dimensionless Helmholtz energy equations compiled by the NIST [17]. The success of the model demonstrates that (1) a truncated and simplified virial equation can be successfully used at high pressures, provided that the volumetric properties are augmented by accurate calculations

using a different equation of state, and (2) the speciation or chemical formation of polysulfane in the non-sulfur-rich phase can be neglected below 200°C.

There are ten available data sets for elemental sulfur solubility in sour/acid gases [16,18-26]. Of these ten data sets, three were not included in the calibration of the model. The equilibrium time and sampling techniques of Kennedy and Weiland [22] have been suspected to be inadequate for good solubility measurements. [19,27] The inaccuracy is unfortunate given the extensive sour and sweet gas compositions investigated. The S_8-H_2S(g) data of Migdisov *et al.* [26]. has been neglected as the elemental sulfur solubility in the gas region increases with decreasing temperature and has an apparently constant pressure dependence. A possible reason for the errors within these data may be the presence of oxygen in the experimental vessel or sampling containers. This would cause the oxidation of H_2S to elemental sulfur which, in turn, may be incorrectly observed as gaseous sulfur dissolution/transportation. The reported solubilities in 100 % H_2S measured by Swift *et al.* [20]. have been smoothed and the original data appear to have a large variance. While the smoothed data was not used for calibration, it was used for a comparison at pressures beyond the calibration set. All mixtures included for calibration of this model have been summarized in Table 13.6.

Many authors have derived models which utilize various equations of state and/or include the chemical equilibria of polysulfane formation in the non-sulfur rich phase [14,23,27]. This model uses the dimensionless Helmholtz equations of state within the REFPROP9 [17] program supplied by NIST for all components except elemental sulfur. These equations of state are very accurate over large pressure and temperature ranges; therefore, they can be applied in the high pressure region which includes dense sour gas phases. The model is derived assuming that the H_2S_x in the non-sulfur rich phase is negligible below T = 200°C. Note that the disproportionation of elemental sulfur in the vapour phase is small at these low temperatures and also is less favourable at higher pressure. It is also likely that the final fitted virial coefficients for S_8 compensate for a portion of the chemical equilibrium.

The notation for species involved in the equilibria described here is as follows: S_8,1; H_2S,2; balance gases are 3, 4, 5, etc. The solubility

Table 13.6 The elemental sulfur solubility data used to calibrate the current model.

Reference	S_8-phase	$x(H_2S)$	$x(CO_2)$	$x(CH_4)$	$x(N_2)$	n	T range/°C	p range/MPa
Brunner and Woll (1980) [21]	(l)	1.00				37	100–160	10.0–60.0
Brunner and Woll (1980) [21]	(s)&(l)	0.20	0.10	0.66	0.04	19	100–160	10.0–60.0
Brunner and Woll (1980) [21]	(s)&(l)	0.07	0.20	0.65	0.08	24	100–160	10.0–60.0
Brunner and Woll (1980) [21]	(s)&(l)	0.06	0.09	0.81	0.04	28	100–160	10.0–60.0
Brunner and Woll (1980) [21]	(s)&(l)	0.01	0.14	0.81	0.04	22	100–160	10.0–60.0
Brunner *et al.* (1988) [24]	(l)	0.09	0.05	0.86		9	212	7.50–76.0
[a]Brunner *et al.* (1988) [24]	(l)	0.298	0.060	0.407	0.043	9	115–135	7.00–43.0
Brunner *et al.* (1988) [24]	(l)	0.35	0.08	0.57		11	125–185	6.70–134.2
[b]Brunner *et al.* (1988) [24]	(l)	0.35	0.08	0.45		8	125	7.00–43.0
[c]Brunner *et al.* (1988) [24]	(l)	0.35	0.08	0.45		8	125	7.00–43.5
Brunner *et al.* (1988) [24]	(l)	0.42	0.02	0.56		9	200	8.00–155.0
Brunner *et al.* (1988) [24]	(l)	0.84	0.09	0.07		10	125	12.85–48.8
Davis *et al.* (1993 [16]	(s)&(l)	0.40	0.10	0.50		21	60–150	12.20–54.68
Davis *et al.* (1993) [16]	(s)&(l)	0.60	0.10	0.30		27	60–150	12.13–56.12
Davis *et al.* (1993) [16]	(s)&(l)	0.80	0.10	0.10		33	60–150	11.31–54.33
Davis *et al.* (1993) [16]	(s)&(l)	0.90	0.05	0.05		35	60–150	5.31–53.85

Gu *et al.* (1993)[23]	(s)		1.000			12	90–110	12.07–38.62
Gu *et al.* (1993)[23]	(s)			1.000		4	110	20.52–50.17
Gu *et al.* (1993)[23]	(s)	1.000				6	90	11.83–36.21
[d]Gu *et al.* (1993)[23]	(s)	0.4411	0.0072	0.4797	0.0068	6	90	18.38–34.71
[e]Gu *et al.* (1993)[23]	(s)	0.9509	0.0372	0.0103	0.0001	6	90	11.47–32.78
Roof (1971)[19]	(s)&(l)	1.000				21	43.1–110.0	7.03–31.16
[f]Smith, et al. (1970)[18]	(s)	100				10	-78-80	0.0376–6.38
Sun and Chen (2003)[25]	(s)	0.0495	0.0740	0.8765		8	30.0–90.0	30–45
Sun and Chen (2003)[25]	(s)	0.0993	0.0716	0.8291		8	30.0–90.0	30–45
Sun and Chen (2003)[25]	(s)	0.1000	0.0086	0.8914		8	30.0–90.0	30–45
Sun and Chen (2003)[25]	(s)	0.1003	0.1039	0.7958		8	30.0–90.0	30–45
Sun and Chen (2003)[25]	(s)	0.1498	0.0731	0.7771		8	30.0–90.0	30–45
Sun and Chen (2003)[25]	(s)	0.1771	0.0681	0.7548		9	30.0–90.0	20–45
Sun and Chen (2003)[25]	(s)	0.2662	0.0700	0.6638		8	30.0–90.0	30–45

n = the number of experimental points in the data set. [a]The balance of the components are $x(C_2H_6)$= 0.107, $x(C_3H_8)$ = 0.037, $x(i\text{-}C_4H_{10})$ = 0.007, $x(n\text{-}C_4H_{10})$ = 0.013, $x(i\text{-}C_5H_{12})$ = 0.002, $x(n\text{-}C_5H_{12})$ = 0.004 and $x(n\text{-}C_6H_{14})$ = 0.022. [b]The balance of the mixture is $x(C_2H_6)$ = 0.12. [c]The balance of the mixture is $x(n\text{-}C_4H_{10})$ = 0.12. [d]The balance of the components are $x(C_2H_6)$= 0.0409, $x(C_3H_8)$ = 0.0191, $x(i\text{-}C_4H_{10})$ = 0.0028 and $x(n\text{-}C_4H_{10})$ = 0.0024. [e]The balance of the components are $x(C_2H_6)$= 0.0009, $x(C_3H_8)$ = 0.0004, $x(i\text{-}C_4H_{10})$ = 0.0001 and $x(n\text{-}C_4H_{10})$ = 0.0001. [f]Measurements were completed at the saturation pressure for H_2S. Pressures were recalculated here using REFPROP9.[17]

for a condensed phase, species 1, in a gas can be calculated using Equation (13.14) [28],

$$y_1 = \frac{p_1^{sat}}{p}\frac{\varphi_1^{sat}}{\varphi_1} e^{\int_{p_2^{sat}}^{p} \frac{V_2^{sat}}{RT} dp}, \qquad (13.14)$$

If Equation (13.14) is applied to elemental sulfur in a sour gas, y_1 is the mole fraction of S_8, p_1^{sat} is the saturation vapour pressure of pure S_8, p is the total pressure, φ_1^{sat} is the fugacity coefficient for a pure sulfur vapour at saturation, φ_1 is the fugacity coefficient for sulfur in a sour gas (with components 2, 3, 4, etc.), v_1^{sat} is the dense phase molar volume of sulfur at saturation, R is the ideal gas constant and T is the absolute temperature. The exponential term in Equation (13.14) is often referred to as an enhancement factor and is required to describe equilibrium at higher pressures.

Several authors have used equations similar to Equation (13.14) to describe solid solubility in sour gases including a previous model by Roberts and Hyne [29]. There are several challenges with how one treats or derives the values within Equation (13.14), including the choice of the equation of state used for the high pressure and temperature fugacity coefficients. Another significant challenge for elemental sulfur is that there are three dense phase transitions ($\alpha \rightarrow \beta$, $\alpha \rightarrow$liquid, and $\beta \rightarrow$liquid) within the conditions of interest (*ca.* 0–200°C and up to 100 MPa). Thus for elemental sulfur in sour gas, a more rigorous treatment using a complete thermodynamic pathway is necessary.

To begin, it is more convenient to write Equation (13.14) as an equilibrium expression,

$$y_1 p \varphi_1 = f_1^{g}(T,p) = f_1^{\alpha,\beta \text{ or } l}(T,p) = p_1^{sat}\varphi_1^{sat} e^{\int_{p_2^{sat}}^{p} \frac{V_2^{sat}}{RT} dp}, \qquad (13.15)$$

where the dense phase can be either α, β or liquid sulfur.

13.3.2.1 Pure Sulfur Phases

The phase behavior of pure elemental sulfur recently was reviewed by Ferreira and Lobo [30]. These authors chose to use volumetric and calorimetric data to calculate the phase change conditions using an integrated Clapeyron equation. Because our model requires fugacities at conditions well away from the pure sulfur phase transitions, we use a slightly different approach; however, where possible, we

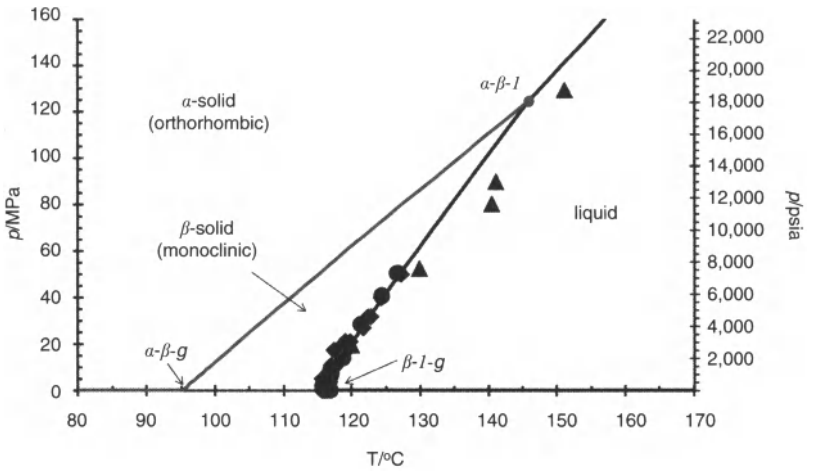

Figure 13.10 The phase diagram for pure elemental sulfur as calculated using Marriott and Wan [1]. ▲, experimental melting points of Tammann [31]; ◆ and ●, experimental melting points of Woll [32] under CH_4 and CO_2 pressure respectively.

utilized the Clapeyron equations of Ferreira and Lobo [30]. The overall equations have been described by Marriott and Wan [1]. Figure 13.10 shows a good agreement between the calculated melting point and the experimental measurements of Tammann [31] and Woll [32].

13.3.2.2 Liquid Sulfur Under Sour Gas Pressure

An equation for the Henry's law solubility of total H_2S in elemental sulfur has been reported by Marriott *et al.* [33]. At the melting point, nearly all dissolved H_2S is observed as free H_2S rather than H_2S_x. Other gases are nearly insoluble in elemental sulfur. Woll [32] has measured the melting point for liquid sulfur under various partial pressures of H_2S, CH_4 and CO_2. The later data were used to parameterize an activity relationship for the liquid sulfur, where,

$$f_1^l(T,p) = f_1^{l,o}(T,p)\gamma_1^l(1-x_2)\,. \qquad (13.16)$$

Recall that according to the notation here, x_2 is the dissolved mole fraction of H_2S (assuming no disproportionation of S_8), γ_1^l is the activity coefficient for the liquid sulfur and $f_1^{l,o}$ is the pure liquid sulfur fugacity. For Equation (13.16), the mole ratio of dissolved total H_2S, x_2, is given by Equation (13.3) of Marriott *et al.* [33]. multiplied

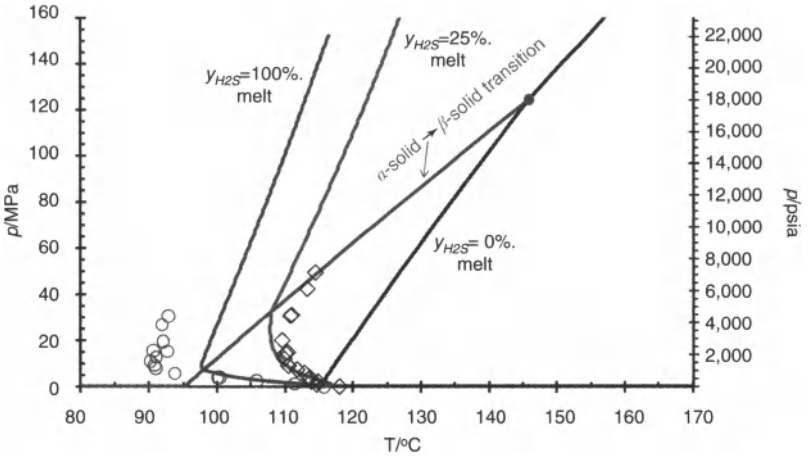

Figure 13.11 A melting point diagram for elemental sulfur under 0, 25 and 100% H_2S pressure [1]. ◇ and ○, experimental melting points of Woll [32].

by the fugacity coefficient for H_2S, φ_2 [17]. The activity coefficient has been optimized using a two parameter Margules equation,

$$\ln \gamma_1^l = [A_{12} + 2(A_{21} - A_{12})(1 - x_2)]x_2 . \qquad (13.17)$$

Using Equation (13.17), Figure 13.11 shows the calculated and experimental [32] melting point depression data corresponding to 100% H_2S and 25% H_2S overpressure. Although the activity model could be improved using a more complex activity equation, an adequate agreement with the experimental data was chosen for computation time and simplicity. The melting points are within 3°C for < 25% H_2S and the disagreement increases to 6°C at 100% H_2S.

13.3.2.3 Fugacity of S_8 in a Sour Gas or Acid Gas Phase

The fugacity coefficient for S_8 in a sour fluid has been estimated using the fugacity coefficient at the infinite dilution limit,

$$f_1^g = y_1 p \varphi_1^\infty \qquad (13.18)$$

These fugacities were calculated using the volume explicit virial equation,

$$\ln Z\varphi_1 = \rho 2\sum_i y_i B_{1i} + \frac{3}{2}\rho^2 \sum_i \sum_j y_i y_j C_{1ij} + \ldots , \qquad (13.19)$$

For Equation (13.19), ρ is the molar density of the sour fluid phase and Z is the compressibility factor for the sour fluid phase. B_{1i} and C_{1ii} are the second and third virial coefficients, respectively.

The interaction between sulfur and all components except H_2S are considered similar, thus Equation (13.19) has been expanded using only three components (1 = S_8, 2 = H_2S and 3 = N_2 + CH_4 + C_2H_6 + ...) and truncated at the third virial coefficient:

$$\ln Z\varphi_1 = 2\left[y_1B_{11} + y_2B_{12} + y_3B_{13}\right]\rho + \frac{3}{2}\left[y_1^2C_{111} + 2y_1y_2C_{112} + 2y_1y_3C_{113} + y_2^2C_{122} + 2y_2y_3C_{123} + y_3^2C_{123}\right]\rho^2 \tag{13.20}$$

Because the amount of elemental sulfur in the sour fluid phase is very small, Equation (13.20) can be simplified further by assuming all components with terms of y_1 are insignificant (i.e., fugacity coefficient is calculated at the infinite dilution limit, y_1 0),

$$\ln \varphi_1^{\infty} = 2\left[y_2B_{12} + y_3B_{13}\right]\rho + \frac{3}{2}\left[y_2^2C_{122} + 2y_2y_3C_{123} + y_3^2C_{123}\right]\rho^2 - \ln Z \tag{13.21}$$

This latter simplification has been described by Quiram *et al.* [34]. for the solubility of solids in compressed gas phases. As noted by Quiram *et al.* [34]. and many others, the truncated virial equation is not rigorous at high pressures or in high density regions. To overcome this limitation, this model uses the high accuracy equations of state from NIST (REFPROP 9) to calculate the densities and compressibility factors for the high pressure hydrocarbon mixtures. The correlation is improved considerably by using the high accuracy densities and the method is self consistent with the fugacities used to establish the liquid sulfur activities.

Substituting Equation (13.21) into Equation (13.15), provides the equilibrium condition for calibration of the virial coefficients with the sulfur solubility data in Table 13.6,

$$f_1^{\alpha,\beta \text{ or } l}(T,p) = y_1 p \exp\left\{2\left[y_2B_{12} + y_3B_{13}\right]\rho + \frac{3}{2}\left[y_2^2C_{122} + 2y_2y_3C_{123} + y_3^2C_{123}\right]\rho^2 - \ln Z\right\} \tag{13.22}$$

Table 13.7 Virial coefficient parameters for sulfur in a sour or acid gas fluid (Equation (13.22)).

Coefficient	Value	95% error
a_{12} / $m^3\ mol^{-1}$	0.00022583	0.00004888
a_{13}/ $m^3\ mol^{-1}$	0.00021732	0.00008394
b_{12} / $m^3\ mol^{-1}\ K$	–0.33077	0.02014
b_{13} / $m^3\ mol^{-1}\ K$	–0.22429	0.03265
a_{122} / $m^6\ mol^{-2}$	$9.6759 \cdot 10^{-9}$	$2.3712 \cdot 10^{-9}$
a_{123} / $m^6\ mol^{-2}$	$-1.2591 \cdot 10^{-8}$	$7.9937 \cdot 10^{-9}$
a_{133} / $m^6\ mol^{-2}$	$3.3820 \cdot 10^{-8}$	$8.6458 \cdot 10^{-9}$
b_{122} / / $m^6\ mol^{-2}\ K$	$5.1830 \cdot 10^{-6}$	$9.4203 \cdot 10^{-7}$
b_{123} / / $m^6\ mol^{-2}\ K$	$1.2734 \cdot 10^{-5}$	$3.0051 \cdot 10^{-6}$
b_{133} / / $m^6\ mol^{-2}\ K$	$-6.6857 \cdot 10^{-6}$	$3.3151 \cdot 10^{-6}$

Virial coefficients were found to be reasonably represented by the temperature dependent functions of

$$B_{1i} = a_{1i} + \frac{b_{1i}}{T} \tag{13.23}$$

and

$$C_{1ij} = a_{1ij} + \frac{b_{1ij}}{T} \tag{13.24}$$

The fitted coefficients and their respective 95% errors are reported in Table 13.7. The correlation plot with the experimental sulfur contents are shown in Figure 13.12.

For an example of how sulfur solubility changes with increasing pressure, the sulfur solubility in H_2S, CH_4 and CO_2 at $T = 100°C$ has been shown in Figure 13.13 along with the experimental data of Brunner and Woll [21], Roof [19] and Gu *et al.* [23]. The solubility trend shown in Figure 13.13 is very much like another system commonly studied in reference to acid gas injection, i.e., H_2O in acid gas fluid. The solubility decreases with increasing pressure at lower-pressures (Raoult's law) and then increases when the solvent

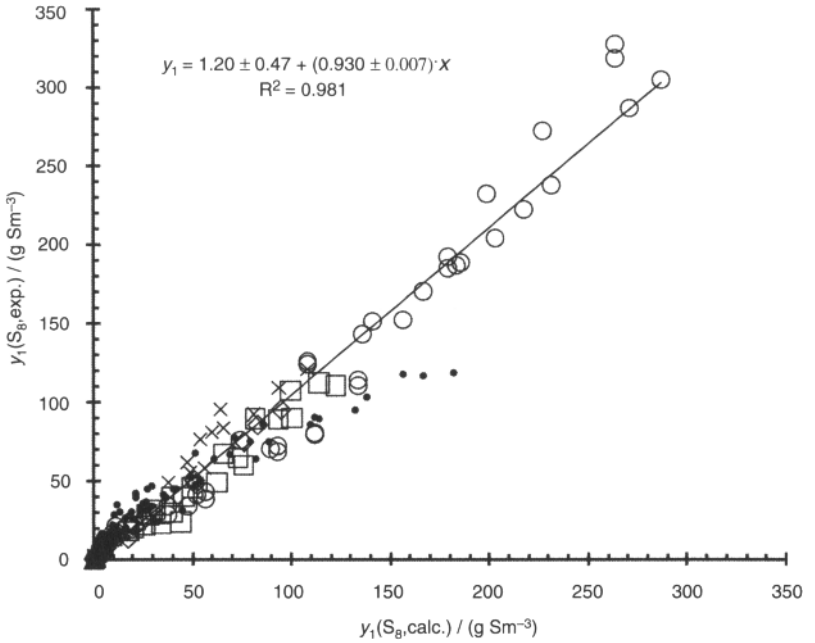

Figure 13.12 The correlation plot for sulfur saturation calculation in sour and acid gas fluids (Equation 22). ○, Brunner and Woll [21]; ◇, Brunner, Place and Woll [24]; □, Roof [19]; ●, Davis *et al.* [16]; × Gu *et al.* [23]; + Smith *et al.* [18]; △, Sun and Chen [25].

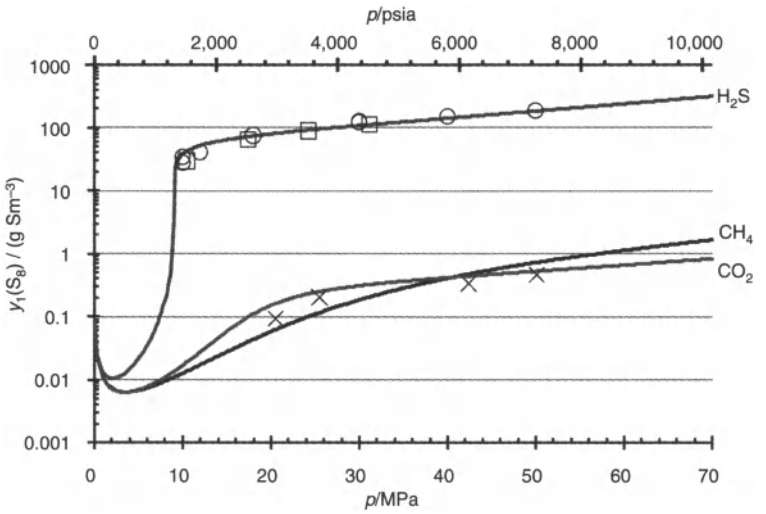

Figure 13.13 The solubility of elemental sulfur in H_2S, CH_4 and CO_2 at T = 100°C. ——, calculated using Equation (22). ○, Brunner and Woll [21] (H_2S, T = 100°C); □, Roof [19] (H_2S, T = 101.7°C); × Gu *et al.* [23] (CH_4, T = 110°C).

becomes more dense. In the example shown in Figure 13.13, dense phase H_2S (supercritical and near liquid) shows a much higher carrying capacity for elemental sulfur. In addition, each fluid shows a minimum carrying capacity for elemental sulfur.

Another note about the calculation shown in Figure 13.13 is that there is a continuous transition for solubility despite the phase changes for the elemental sulfur involved in the equilibria. For example, the sulfur which is dissolved in CO_2 and CH_4 follows β-solid$\rightarrow S_8$(sln) at low pressure and α-solid$\rightarrow S_8$(sln) at high pressure, $p > 12.05$ MPa (1750 psia). For the H_2S system, there is an intermediate pressure where the dense phase sulfur is liquid. The continuity of the fugacity between solid and liquid elemental sulfur is a thermodynamic necessity; however, it should be noted that the vapour pressures for elemental liquid were forced to match at the melt [1]. The discontinuity in the current experimental vapour pressures for sulfur would not allow for a continuous equilibrium model.

13.4 Discussion and Demonstration of Utility

We have combined the previous kinetic and thermodynamic work with a hypothetical injectate fluid (50:50 H_2S/CO_2). The hypothetical compression begins with the fluid at $p = 0.14$ MPa (20 psia) and $T = 40°C$. To simplify the system we have considered all compression stage inlets to be at $T = 40°C$ and all discharge pressures at $T = 140°C$. The outlet pressures are 0.43 MPa (62 psia), 1.3 MPa (190 psia), 3.9 MPa (570 psia) and 10 MPa (1500 psia) for stages 1, 2, 3 and 4 respectively.

The hypothetical compression conditions are shown in Figure 13.14 with selected sulfur saturation lines and the acid gas phase pocket. The bold grey lines show the calculated sulfur saturation using Equation (13.22) for 0.0001 to 1 g Sm^{-3}. For example, a fluid containing 1 g Sm^{-3} of elemental sulfur will deposit dense phase sulfur at temperatures below the 1 g Sm^{-3} saturation line. The dashed black near-vertical line is the sulfur melting point line. At temperatures less than this line, sulfur will deposit as a solid, i.e., sulfur would deposit as a liquid at the discharge temperatures. The solid black line shows the calculated sulfur-free acid gas phase pocket (VMGSim). Finally, the broken black line shows the compression and injection conditions for the hypothetical injectate fluid.

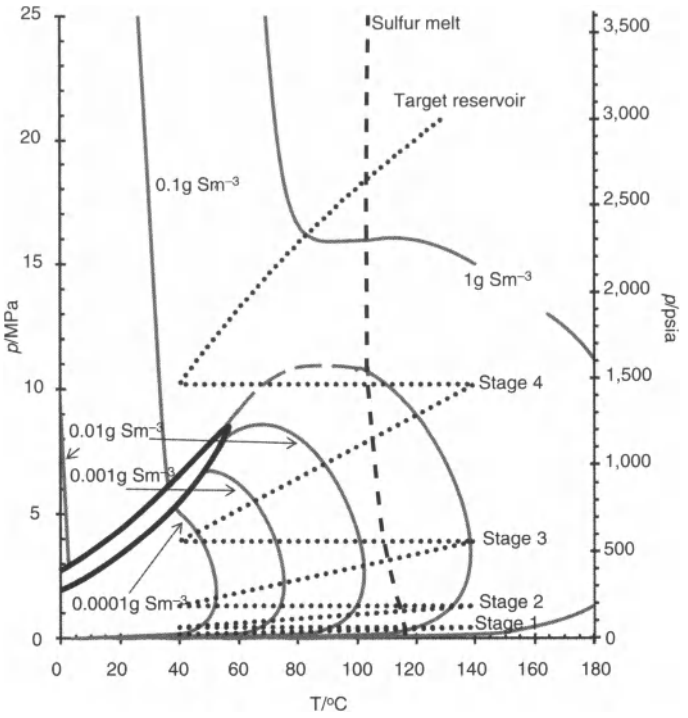

Figure 13.14 The phase diagram for elemental sulfur and a 50:50 H_2S/CO_2 mixture with hypothetical conditions of a four stage compression and injection. ,(grey) calculated sulfur saturation lines using Equation (22). ——,(solid black) calculated sulfur free acid gas phase pocket (VMGSim). ----------,(dashed black) calculated sulfur melting point line · · · · · ·,(dotted black) compression and injection conditions.

Two scenarios were conceptually investigated: (1) the fluid arrives at the first suction scrubber with no excess O_2 but saturated with elemental sulfur and (2) the fluid arrives at the suction scrubber with small quantities of O_2 (>1 ppm). This first scenario could occur with native sulfur which proceeds through the separation and with the acid gas stream; however, sulfur is not likely to pass through an amine stripping system. Because water is present in the first suction scrubber, saturation may occur due to the fast reaction catalysed in the aqueous phase. Thus all oxygen would be consumed before compression. In this case the 50:50 H_2S/CO_2 fluid would enter the first compression stage with 0.0001 g Sm^{-3} elemental sulfur; however, the solubility is reduced to 0.00005 g Sm^{-3} at the inlet to the second stage and 0.00003 g Sm^{-3} at the inlet to the third stage. The fluid would be undersaturated for the inlet to the fourth stage and downstream

of the compression. We note that this is very similar to the removal of water during acid gas compression; however, in this case sulfur would deposit as a solid. For an injection rate of $10{\cdot}10^3$ m^3 d^{-1}, this would result in 0.8 g d^{-1} of sulfur during the first interstage cooling and 0.2 g d^{-1} during the second interstage cooling. These small deposition rates may be tolerable in a compression system, as they may be moved or dissolved by other fluids in the system. To avoid deposition all together the ingress of O_2 would need to be less than 0.1 ppm.

In the second scenario we considered that the 50:50 H_2S/CO_2 fluid contains oxygen due to vent gas recovery, seal gas recovery or mixing within a dry gas seal. Based on thermodynamic saturation at each inlet condition (suction scrubber conditions), the stoichiometry of Reaction (1) and complete reaction, it would require less than 0.1 ppm O_2 to saturate the fluid with sulfur in each suction scrubber, i.e., infinite time for complete reaction. Alternatively, it would require much more oxygen (>50 ppm) to saturate the fluid after compression (wellhead). However, both the kinetic measurements with the passivated reactor and the known requirement for direct

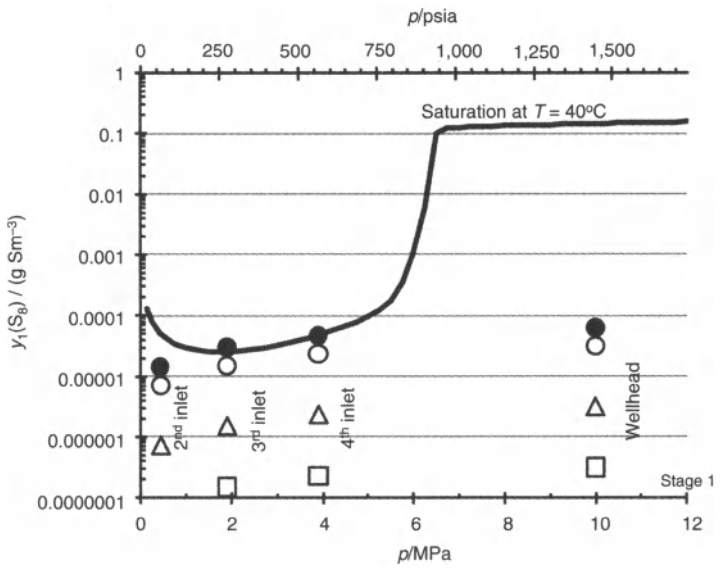

Figure 13.15 The increase in sulfur concentration due to passivated reaction rate at T = 140°C (discharge temperature) compared to the saturation concentration at inlet temperature (T= 40 °C) for a four stage compression of a 50:50 H_2S/CO_2 fluid. □, t = 0.1 s at T = 140°C for each stage; △, t = 1 s at T = 140°C for each stage; ○, t = 10 s at T = 140°C for each stage; ●, t = 20 s at T = 140°C for each stage.

oxidation catalysts suggests that not all incoming oxygen will react during the compression. In addition, the time the fluid remains at the high temperature will differ depending on the volumes within the interstage cooling equipment.

Based on the experimental rate studies for the passivated reactor, we have calculated the amount of sulfur which would build-up from oxidation at T = 140°C for a given time at each compression stage. For an example of this calculation, Figure 13.15 shows the sulfur concentration for 100 ppm O_2 ingress and various high-temperature resident times. For example, the t = 0.1 s points correspond to 0.1 seconds at T = 140°C for each stage of compression. The sulfur concentration increases at each stage according to passivated (minimally catalysed) reaction rates. In addition, the saturation curve for elemental sulfur at the inlet temperature of T = 40°C also is shown in Figure 13.15. By comparing the increasing sulfur concentration with the saturation line one can see that it would take 20 seconds at each stage to reach a point where the system would be saturated with elemental sulfur and deposition could occur. Because the reaction rate is first order with respect to oxygen, the example case also can be used for other oxygen concentrations by using the same ratio of oxygen concentration versus saturation time. For 1 ppm O_2 it would take 2000 seconds at each stage and for 10 ppm it would take 200 seconds at each stage before saturation. In all cases the system becomes saturated at the 3rd and 4th inlet conditions nearly simultaneously. Thus, if the system were sized such that the residence times were known, the O_2 tolerance could be estimated.

In the previous example, the rates are underestimated because they refer to a passivated reactor system; whereas, the experiments showed that bare stainless steel surfaces would catalyse the reaction. By comparing the conversion for the SS316 reactor (Table 13.5) at T = 20°C and the calculated rate at T = 20°C for the passivated reactor, the SS316 catalysed reaction rate is 3600 times faster. By applying this rate increase to the previous example, we see that the 10 ppm O_2 would require 0.06 seconds at each stage to saturate the compression system at the 3rd and 4th inlet conditions. Given that a 1000 rpm compressor system will replenish a fluid at a minimum of every 0.06 seconds, 10 ppm would cause saturation and potentially damaging deposition issues regardless of the size of the cooling equipment.

A note should be made regarding centrifugal compressors and dry gas seals. Process gas and seal gas will mix at the interface

within these seals and, due to a zero pressure difference across the gas interface, residence time could be very long. Thus, versus comparing the residence time with the oxygen ingress, we have used the SS316 (catalysed) reaction kinetics to calculate the build-up of elemental sulfur after saturation. The results show 2 g Sm^{-3} d^{-1}. Given the precise and small tolerance for these seals, it would seem reasonable to suggest that no oxygen should be permitted to enter the dry seal on a centrifugal compressor.

13.5 Conclusions

Investigation of the kinetics of H_2S oxidation by trace O_2 has been reported from T = 50 to 140°C and p = 100 to 1000 psig using a Silcosteel reactor (passivated). The study was performed under pseudo-order reaction conditions with H_2S in a concentration range of 2–5 mol% and O_2 levels from 1000–1600 ppmv by following the disappearance of O_2. Values for the pseudo-first order rate constant for H_2S oxidation in the range of $1–4 \cdot 10^{-4}$ min^{-1} were determined at 140°C over the pressure range from p = 100 to 1000 psig along with the reaction orders with respect to H_2S and O_2. The data support a mechanism involving the reaction of adsorbed H_2S with gaseous O_2. It was found that a bare steel surface acts as a catalyst for H_2S oxidation under similar conditions where the reaction rate is 3600 times faster than the passivated case.

A thermodynamic sulfur saturation model was calibrated for comparison to the increase in sulfur due to oxidation. The model utilizes a Virial equation at infinite dilution. The success of the model demonstrates that a truncated and simplified virial equation can be successfully used at high pressures, provided that the volumetric properties are augmented by accurate calculations using a different equation of state.

To demonstrate the utility of the rate information, a short case study was performed with a hypothetical four-stage compression of a 50:50 H_2S/CO_2 system. The slower (passivated) reaction rates showed that for a 100 ppm O_2 ingress concentration, a time at discharge temperature beyond 20 seconds would results in solid sulfur deposition within the interstage cooling. The SS316 catalysed rates corresponded to a faster build-up of elemental sulfur where 10 ppm O_2 showed potential for deposition at 0.06 seconds. Finally, if the reaction rate due to other *in situ* catalysts were faster than the

SS316 catalysed system, the tolerance for O_2 ingress was shown to be less than 0.1 ppm O_2.

References

1. R.A. Marriott and H.H. Wan, *J. Chem. Thermodyn.* **43**, 1224-1228 (2011).
2. R.A. Marriott, P.M. Davis, and P.D. Clark, "Estimation of sulfur deposition during the production of lean sour gas," SOGAT III, Abu Dhabi, United Arab Emirates (2007).
3. J.B. Hyne, *Oil Gas J.* **68**, (1968) 107–113.
4. D. Ramshaw and B. Ginger (1992), *Hydrocarbon Engineering* **6**, iss. 12, 33 (2001).
5. A.K. Kalai, A. Majumdar, and E.L. Tollefson, *Studies in surface science catalysis* **73**, 367 (1992).
6. M.A. Shields and P.D. Clark, *Ind. Eng. Chem. Res.* **47**, 2248 (2008).
7. J. Vollertsen, A.H. Nielsen, H.S. Jensen, T. Wium-Andersen, and T. Hvitved-Jocobsen, *Sci. Environ.* **394**, 162 (2008).
8. W. Bruckoff, O. Gier, K. Hofbauer, G. Schmitt, and D. Steinmetz, *Corrosion 85*, paper 389 (1985).
9. H.K. Abdel-Aal and M.A. Shalabi, *Ind. Eng. Chem. Res.* **35**, 1785 (1996).
10. P.D. Clark and K.L. Lesage, *Journal of Chromatographic Science* **27**, 259 (1989).
11. F. Basolo, W.R. Matoush and R.G. Pearson, *J. Am. Chem. Soc.* **78**, 4883 (1956).
12. C.H. Bartholomew and R.J. Farrauto, *Fundamentals of Industrial Catalytic Processes*, 2nd ed., New Jersey, John Wiley & Sons, Inc. (2006).
13. P.A. Deshpande, S. Polisetti, and G. Madras, *AIChE Journal*, WileyOnline 22 April, 2011 / DOI 10.1002/aic. 12636.
14. R.A. Heidemann, A.V. Pheonix, K. Karan, and L.A. Behie, *Ind. Eng. Chem. Res.* **40**, 2160–2167 (2001).
15. P. Cézac, J.P. Serin, J.-M. Reneaume, J. Mercadier, and G. Mouton, *J. Supercritical Fluids* **44**, 115–122 (2008).
16. P.M. Davis, C.S.C. Lau, and J.B. Hyne, *ASRL QB* **XXIX, No. 2,3 &4**, 1–22 (1993).
17. Eric W. Lemmon, Mark O. McLinden, and Marcia L. Huber, REFPROP 9.0, NIST, Bolder Co. (2010).
18. J.J. Smith, D. Jensen, and B. Meyer, *J. Chem. Eng. Data* **15**, 144–146 (1970).
19. J.R. Roof, *Soc. Pet. Eng J.* **272**, 272–276 (1971).
20. S.C. Swift, F.S. Manning, and R.E. Thompson, *Soc. Pet. Eng. J.* **16**, 57–64 (1976).
21. E. Brunner and W. Woll, *Soc. Pet. Eng. J.* **20**, 377—384 (1980).
22. H.T. Kennedy and D.R. Wieland, *Pet. Trans.* **219**, 166–169 (1960).
23. M.-X. Gu, Q. Li, S.-Y. Zhou, W.-D. Chen, and T.-M. Guo, *Fluid Phase Equilibria* **82**, 173-182 (1993).
24. E. Brunner, M.C. Place, Jr., and W.H. Woll, *J. Pet. Tech.* **40**, 1587–1592 (1988).
25. C.-Y. Sun and G.-J. Chen, *Fluid Phase Equilibria* **214**, 187–195 (2003).
26. A.A. Migdisov, O.M. Suleimenov, and Y.V. Alekhin, *Geochim. Cosmochim. Acta* **62**, 2627–2635 (1998).
27. K. Karan, R.A. Heidemann, and L.A. Behie, *Ind. Eng. Chem. Res.* **37**, 1679–1684 (1998).

28. J.M. Prausnitz, R.N. Lichtenthaler, and E.G. de Azevedo, *Molecular Thermodynamics of Fluid-Phase Equilibria*, 3rd Ed., Prentice Hall, NJ (1999).
29. B.E. Roberts and J.B. Hyne, *ASRL QB* **XXI, No. 2,3,** 53-59 (1985).
30. A.G.M. Ferreira and L.Q. Lobo, *J. Chem. Thermodyn.* **4**, 95–104 (2011).
31. G. Tammann, Kistallisieren, and Schmelzen, Leipzig, (1903) [W.N. Tuller, *The Sulphur Data Book*, McGraw Hill, New York, 1954].
32. W. Woll, *Erdoel Z.* **99 No. 9**, 297–300 (1983).
33. R.A. Marriott, E. Fitzpatrick, and K.L. Lesage, *Fluid Phase Equilibria* **269**, 69–72 (2008).
34. D.J. Quiram, J.P. O'Connell, and H.D. Cochran, *J. Supercritical Fluids* **7**, 159–164 (1994).

14

Blowout Calculations for Acid Gas Well with High Water Cut

Shouxi Wang[1], and John J. Carroll[2]

[1]Xi'an Shiyou University, Xi'an, China
[2]Gas Liquids Engineering, Calgary, Canada

Abstract

The blowout of an acid gas injection well would be a very dangerous event. There are many scenarios of such an event, but this paper will focus on a blowout with a large amount of water present.

Modeling of the blowout is done using the *GLEWPro* software [2]. Although the software was designed for the calculation of injection flow, it is suitable for flow in either direction. The surface pressure is set to atmospheric, and, given the reservoir pressure (or at least the pressure at the sandface), the flow rate is calculated. In the modeling, it is assumed that water is pure water, and not brine. Pure water has a lower density and viscosity than brine.

It is shown that under certain situations, the well will be self-killing. That is, there will be no flow from the well, even though there is no restriction to the flow at the surface. This occurs when the hydrostatic head of the fluid is greater than the reservoir pressure. Under other circumstances, the fluid will remain a single-phase for most of the flow, but the gas will come out of solution at the surface. Other scenarios are also possible.

Note, this is an engineering exercise and not for health, safety, and environment (HSE) purposes. For HSE, you must follow the regulations in your local jurisdiction.

14.1 Introduction

Figure 14.1 shows the schematic of an injection well. In reality injection wells are completed much like producing well. In normal operation the injected fluid flows down the tubing to the formation

Ying (Alice) Wu, John J. Carroll and Weiyao Zhu (eds.) Sour Gas and Related Technologies, (215–226)

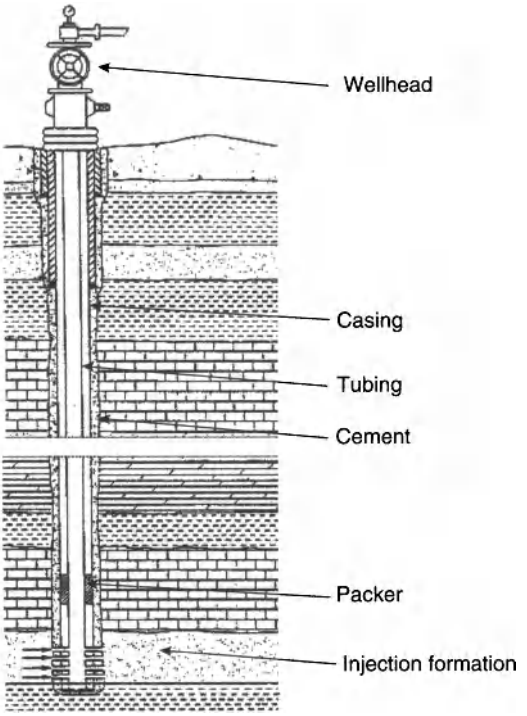

Figure 14.1 Schematic diagram of an injection well.

for disposal. The tubing is isolated from the casing with a downhole packer. The casing pressure can be monitored at the surface to detect any leakage from the tubing.

A well blowout is a catastrophic accident where the well head has been sufficiently damage that the well is free to flow to the surface essentially unimpeded. The back pressure at the surface is merely the atmospheric pressure. Depending upon the flow rate of the fluid there is resistance to the flow due to fluid friction.

There are many scenarios that can occur in the blowout of an acid gas injection well. These include the following:

1. *Acid gas only*: In this case only acid gas enters the well bore and flows to the surface. There may or may not be a phase change (liquid to gas), but this is an acid gas change. Typically this is the assumption well performing calculations for emergency planning purposes [3].

Table 14.1 Common tubing sizes used in this study.

Nominal	OD (mm)	ID (in)	ID (mm)	t (in)	t (mm)
2⅜ inch	60.325	1.975	50.165	0.190	4.826
2⅞ inch	73.025	2.441	62.001	0.217	5.512
3½ inch	88.900	2.992	75.997	0.254	6.452

OD – outside diameter ID – inside diameter t – wall thickness

2. *Mixed flow* (acid gas + water): Here the flow is at least two-phase throughout the well. However, this can be an extremely complex flow because the acid gas may undergo a phase change and thus three phases occur.
   a. Single acid gas phase (aqueous liquid + acid gas)
   b. Three phase flow (aqueous liquid + liquefied acid gas + gas)
3. *High water-cut*: The flow is predominantly water in this scenario. There may be a phase change (gas coming out of solution) but through most of the well bore the fluid is an aqueous liquid.
   a. Single aqueous phase
   b. Gas breakout (two-phase, but only a small amount of gas)

The high-water cut scenario is the subject of this paper; both the single phase and break-out cases will be examined.

For the purposes of this work, it is assumed that small diameter tubing is used to complete the well. This is common for the injection wells in Western Canada. Table 14.1 summarizes the dimensions of typical tubing.

14.2 Water

The first cases will assume that the blowout is pure water. In this case it is relatively easy to estimate whether or not there will be flow. Assuming water is incompressible (constant density), then if the hydrostatic head of the column of water, given by Equation (14.1):

$$P_{head} = \rho_{water}\, g\, h \tag{14.1}$$

is greater than the reservoir pressure, then there will be no flow from the well. If the reservoir pressure is greater than the head, then the flow rate can be calculated using well flow software such as *GLEWPro*.

14.2.1 Case Study 1

The first case is a simple configuration and it is assumed that the fluid is pure water. The other conditions are summarized in Table 14.2.

Typical of the province of Alberta in Canada, it is assumed that the ambient pressure is 97.5 kPa (0.975 MPa, 14.14 psia). However, this value should be adjusted to local conditions.

Assuming the density of water is approximately 1000 kg/m^3, then the head of the column of water is equivalent to 24.5 MPa (3553 psia). Therefore, in this case we would anticipate flow during a blowout, the actual rate is calculated in the next subsection.

14.2.1.1 Isothermal

The isothermal case assumes that the temperature is constant, in this case 75°C. Using *GLEWPro*, the estimated flow rate is 4.51 kg/s (9.95 lb/sec).

14.2.1.2 Linear Temperature

As an alternative scenario, it is assumed that the temperature varies from the reservoir temperature to the ground temperature (10°C) in a linear fashion. For this case, the flow rate has decreased to approximately 3.32 kg/s (7.31 lb/sec).

There are two reasons for the difference in the flow rate. The first is that at the lower temperatures the density of water increases.

Table 14.2 Conditions for blowout calculations used in this study.

Reservoir Pressure	25 MPa	3626 psia
Reservoir Temperature:	75°C	167°F
Surface (Ground) Temperature	10°C	50°F
Depth	2500 m	8200 ft
Tubing:	2 7/8 inch	

At 75°C, it is about 980 kg/m^3 (with some variation with the pressure), whereas at 10°C the density is closer to 1000 kg/m^3. Second, the warm water is significantly less viscous than the cold water. These two factors contribute to the reduction in the flow rate as follows:

1. The higher density increases the hydrostatic head
2. The higher viscosity increases the pressure drop due to fluid friction

14.2.1.3 Actual Temperature Profiles

The above two cases represent two extremes of the flow. The isothermal flow happens when the flow is extreme fast and the linear temperature means no flow exists and the temperature profile matches exactly to the formation temperature profile.

In reality, there is always heat exchanged between the fluid flowing in the tubing and formation. *GLEWPro* has the capability to calculate the heat transfer given the overall heat transfer coefficient (U). For the conditions given in Table 14.1 several heat transfer scenarios were calculated and these are summarized in Fig. 14.2 and Table 14.3.

The various temperature profiles lies between the two extremes (isothermal and linear), as shown in Fig. 14.2. The overall heat transfer coefficient has a great impact on the actual flow temperature profile. Even the adiabatic flow case (U = 0 W/m^2·K) has a temperature drop of 0.9°C. Table 14.3 shows that both flow

Table 14.3 Flow and wellhead temperature at different thermal conditions.

	Isothermal	**Overall Heat Transfer Coefficient (W/m^2·K)**				**Linear T**
		U = 0	**U = 1.5**	**U = 10**	**U = 20**	
Flow rate (kg/s)	4.51	4.49	4.47	4.37	4.26	3.32
Wellhead Flowing Temp. (°C)	75	74.1	72.7	65	57.3	10

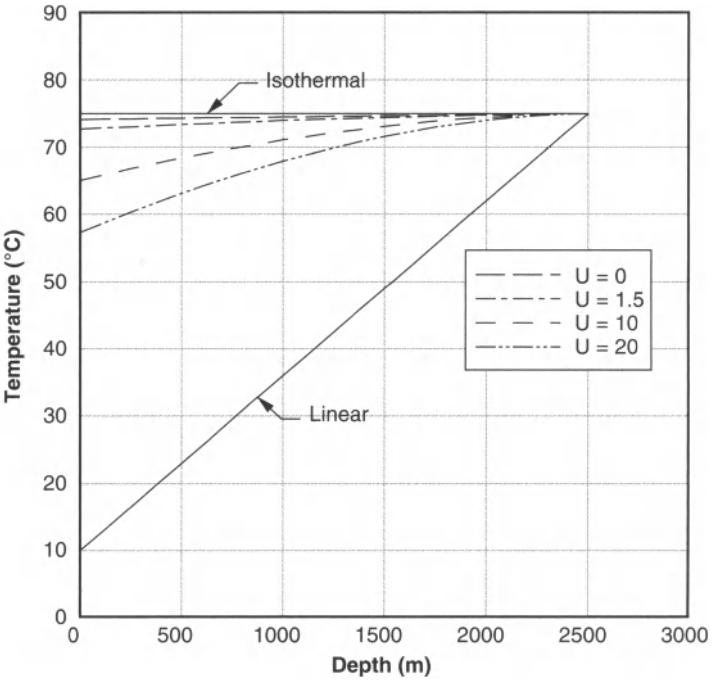

Figure 14.2 Temperature profiles along the wellbore for various heat transfer scenarios.

rate and wellhead temperature are bounded (limited) by the two extremes.

14.2.1.4 Reservoir Pressure

Not that we can change the reservoir pressure, but it is an interesting exercise to examine the effect of the reservoir pressure. For this case, all of the variables remain the same, except for the reservoir pressure, and the linear temperature model is used. The results of a series of calculations are summarized in Fig. 14.3.

As was noted earlier, for pressures less than about 24.5 MPa there is no flow. At pressures slightly greater than 24.5 MPa, there is a dramatic increase in the flow with small changes in the pressure. Therefore, for this well configuration, if the reservoir pressure is less than 24.5 MPa then the well is self-killing – it will not blowout.

Although the values given are for this well configuration similar calculations can be performed for others.

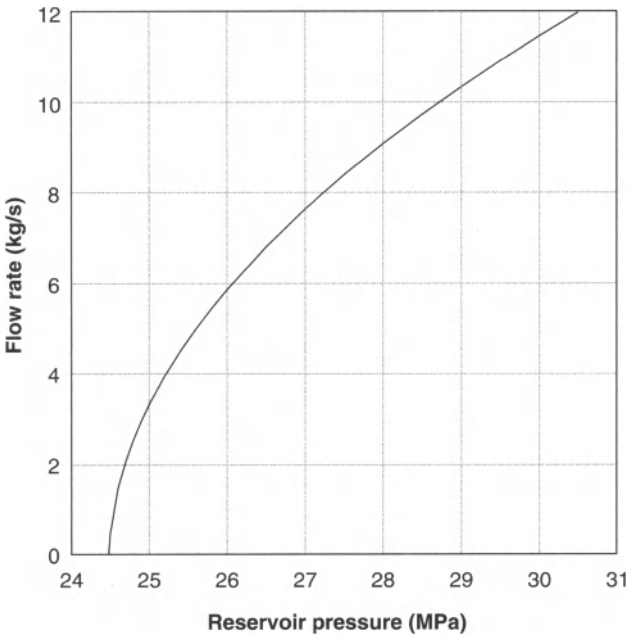

Figure 14.3 The effect of reservoir pressure on the blowout flow rate for the pure water case (other reservoir parameters in Table 14.2).

14.2.2 Effect of Tubing Diameter

Repeating the calculation using 2⅜ and 3½ inch diameter tubing, the estimated flow rates are about 1.94 and 5.69 kg/s (4.29 and 12.55 lb/sec) respectively. The difference between the three cases is the amount of fluid friction.

The reservoir pressure for zero-flow remains the same regardless of the tubing diameter. Since there is no flow, there is no pressure drop due to fluid friction.

14.3 Trace Amount of Gas

The next scenario involves the flow of an aqueous solution containing a small amount of dissolved acid gas. In this case the amount of gas is so small that it remains dissolved in the water right to the surface.

Table 14.4 Flow and wellhead temperature at different thermal conditions.

	Isothermal	Overall Heat Transfer Coefficient (W/m²·K)				Linear T
		U = 0	U = 1.5	U = 10	U = 20	
Flow Rate (kg/s)	4.87	4.85	4.83	4.68	4.49	3.32
Wellhead Flowing Temp. (°C)	75	73.7	72.4	65.4	57.8	10
Wellhead Water Mass%	99.87	99.87	99.88	99.92	99.96	100
Wellhead Vapor Mass%	0.13	0.13	0.12	0.08	0.04	0

14.3.1 Case Study 2

For this case study the well conditions are the same, however there is a trace amount of either H_2S or CO_2 or both.

For the first example, consider a mixture that is 99.9% water and 0.1% hydrogen sulfide. For the linear temperature case, the well flow is predicted to be single phase and the rate is 3.33 kg/s (7.33 lb/sec). This is a very slight, insignificant difference with the pure water case.

14.4 Break-Out Gas

In this scenario there is a little more gas in the fluid. At the bottom hole conditions the gas is completely dissolved in the water, largely because of the pressure. However as the fluid flows up the well the gas comes out of solution and the flow is two-phase.

14.4.1 Case Study 3

For this case study the well conditions are the same as those in Case 1. At low H_2S concentrations the fluid remains single phase.

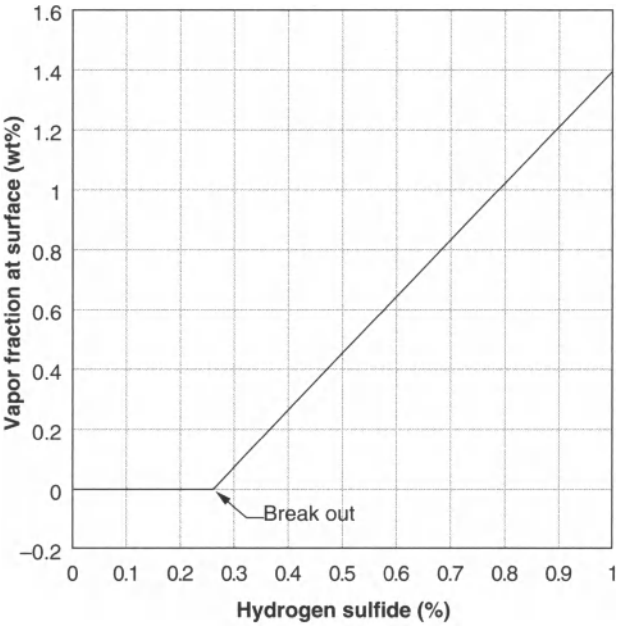

Figure 14.4 Fraction gas phase from a blowout well with a small amount of H_2S.

However at approximately 0.265% H_2S gas begins to break out. This is shown graphically in Fig. 14.4. After the gas comes out of solution, the amount of the gas phase tends to increase linearly as the amount of H_2S in the stream increases. It is worth noting that these values represent the total H_2S concentration in the stream.

The flow rate is also affected by the amount of H_2S present in the stream as shown in Fig. 14.5. Before the gas breaks out, the flow rate of the fluid is roughly constant at 3.33 kg/s. After break out the flow rate initially increases but reaches a maximum and then decreases. This maximum occurs at roughly 0.45% H_2S. With the initial gas break out the bulk density is reduced as a result the flow increases. However as the volume of gas increases so does the velocity. This increase in velocity results in higher pressure drop due to fluid friction.

A similar scenario occurs with CO_2, but for carbon dioxide the break out composition is 0.094%. The maximum flow rate occurs at approximately 0.25% CO_2. This is shown in Figs. 14.6 and 14. 7. The difference in the break-out is based on the solubility; H_2S is significantly more soluble than CO_2.

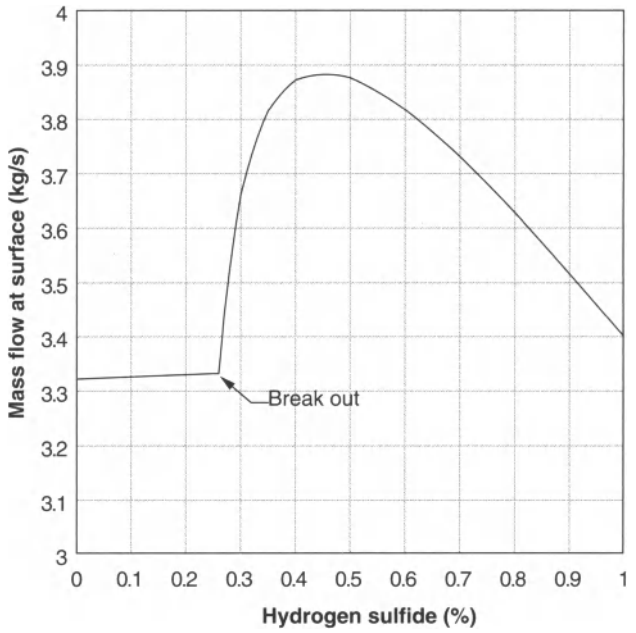

Figure 14.5 Flow rate from the blowout well with a small amount of H_2S.

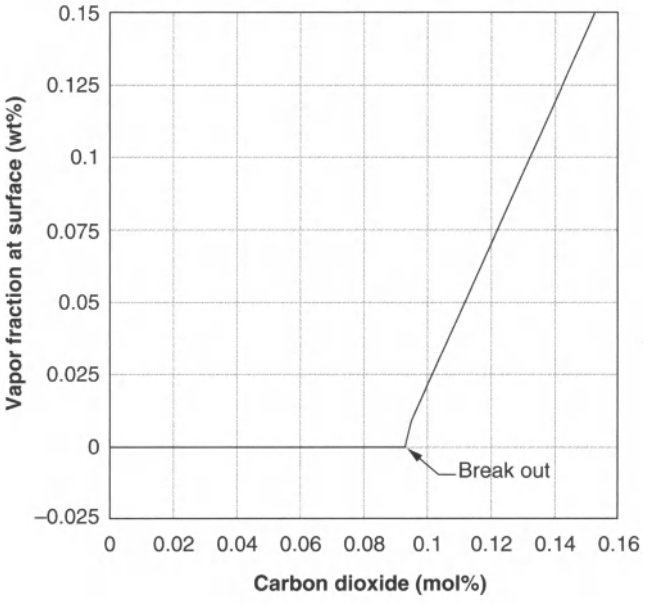

Figure 14.6 Fraction gas phase from a blowout well with a small amount of CO_2.

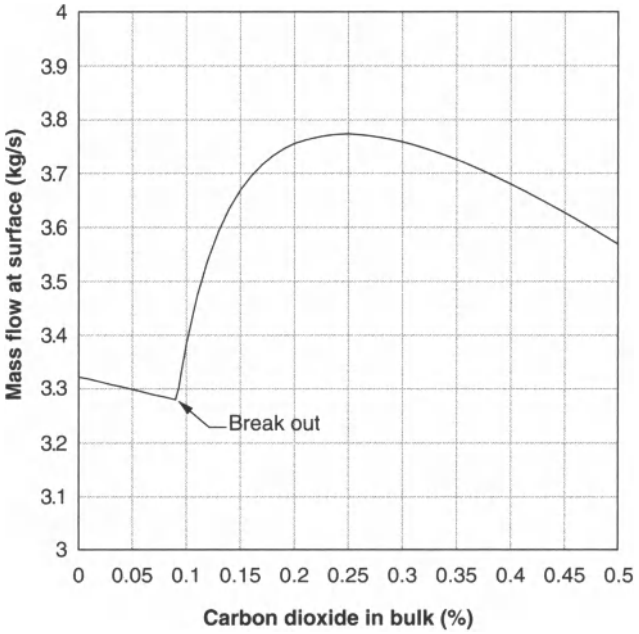

Figure 14.7 Flow rate from the blowout well with a small amount of CO_2.

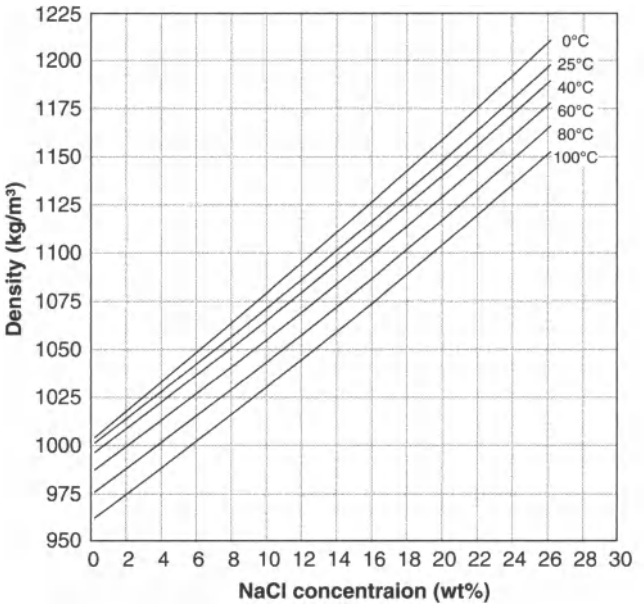

Figure 14.8 Density of sodium chloride brine as a function of temperature and concentration.

14.5 Brine vs. Water

One of the major assumptions made in this analysis is that the formation water is pure water whereas in reality it will be brine. And typical formation water is a complex mixture composed mostly of sodium chloride (NaCl) with significant amounts of other cations and anions including K^+, Ca^{2+}, Mg^{2+}, Br^-, HCO_3^-, and others.

Brine is more dense than pure water. Fig. 14.8 shows the density of sodium chloride solutions as a function of the composition and the temperature [1].

Finally, acid gas and hydrocarbons are less soluble in brine than in pure water – the so-called "salting-out effect."

14.6 Discussion

The blowout from an acid gas injection well is a complicated flow scenario. Even for the somewhat restrictive case studied here, the high water-cut, some interesting behavior is predicted.

In the extreme case, if the head of fluid in the tubing is greater than the reservoir pressure, there will be no blowout. This is true for both pure water cases and for the case when a small amount of acid gas is dissolved in the water.

However for other cases the dissolved acid gas will come out of solution due to the reduction in the pressure as the stream flows up the well. The dissolution of the gas has a significant effect on the flow rate for the blow out.

References

1. Green, D.W., and Perry, R.H. (eds.), *Perry's Chemical Engineers' Handbook*, 8th ed., McGraw-Hill, New York, p. 2–110, (2008).
2. Wang, S., and Carroll, J.J., "Model Calculates Acid-Gas Injection Profiles," *Oil & Gas Journal*, **104 (33)**, 61–69, (2006).
3. Wilson, T., Kaceli, I., Smith, T., Featherstone, R., Carroll, J.J., and Dunn, D., "H_2S Release Rate Assessment Guidelines and Audit Forms," Canadian Association of Petroleum Producers (CAPP), Calgary, AB, March (2012).

PART 4
SUBSURFACE

Ying (Alice) Wu, John J. Carroll and Weiyao Zhu (eds.) Sour Gas and Related Technologies, (3–20)

15

Influence of Sulfur Deposition on Gas Reservoir Development

Weiyao Zhu, Xiaohe Huang, Yunqian Long, and Jia Deng

Civil & Environment Engineering School,
University of Science & Technology Beijing
Beijing 10083, China

Abstract

One of the problems with high sour gas reservoirs is the presence of dissolved elemental sulfur. During the exploitation process of such reservoirs, the reservoir pressure decreases, and the elemental sulfur separates out from the gas. As the gas becomes oversaturated, the sulfur deposits in the pores or throats, which leads to the plugging of the percolation channels and causes changes to the pore throat structure, resulting in a decrease in the porosity and permeability. A model is constructed that includes the precipitation of elemental sulfur in the reservoir. This model provides a theoretical foundation for studying the behavior of the reservoir and predicting the production. The simulation results show that, as the pressure declines, elemental sulfur would deposit, and the zone of sulfur deposition is the nearby wellbore. In the early stages of sulfur deposition, sulfur saturation changes slowly, but then increases rapidly after a critical time. As the gas production increases, it is easier for the percolation channels to be plugged, thus shortening the gas producing time.

15.1 Introduction

There are many problems associated with the exploitation of high sour reservoirs. These include high corrosivity of the wet gas, high toxicity of H_2S, and in some cases the deposition of elemental sulfur in the reservoir, the wells, and the flow lines. The focus of this paper is the deposition of elemental sulfur in the reservoir and how

Ying (Alice) Wu, John J. Carroll and Weiyao Zhu (eds.) Sour Gas and Related Technologies, (229–246)

this effects the reservoir characteristics and ultimate the production of the gas from said reservoir. As the reservoir pressure and temperature decreases change during production and this can result in elemental sulfur particles separating from the gas. Sulfur deposition tends to block the pore throats and thus decrease the gas flow. In addition, the hydrogen sulfide ionizes in water and can react with rocks and minerals, turning them into insoluble sulfides that can also deposit on the pore surfaces.

The phase changes of gas with sulfur are complicated and many phases coexist such as: gas-solid, gas-liquid-solid and gas-liquid depending upon the temperature and pressure. In addition, the elemental sulfur can exist as gas, liquid and solid. The phase changes may lead to sulfur deposition on the surface of the porous media will contribute to pore changes in the dimensions of the pore and ultimately destroying the reservoir. Gas, liquid and solid distribution in the micro-space will affect the gas flow. Additionally, phase changes might result in alteration of the temperature field as well as the interstitial fluid pressure changes, thus influence the characteristics and courses of gas penetration. Meanwhile, due to the high speed of the flow near wells, the fluid movement is in accordance with the generalized Darcy's law. In order to study the gas-liquid-solid multiphase flow with sulfur deposition more accurately, a mathematical model of multiphase complex flow with phase change is presented in this paper.

15.2 Mathematical Models of Flow Mechanisms

15.2.1 Mathematical Model of Sulfur Deposition

The sulfur deposition mechanisms include molecular diffusion, shear diffusion, Brownian diffusion, gravity subsidence, etc., among which molecular diffusion and shear diffusion are considered to be major types of sulfur deposition according to some research. So the sulfur deposition model is:

$$\frac{dW}{dt} = \frac{dW_d}{dt} + \frac{dW_s}{dt} \tag{15.1}$$

In this equation, W is the total deposition amount, W_d is the molecular diffusion deposition amount, and W_s is the shear diffusion deposition amount.

1. Sulfur molecular diffusion deposition model. According to the Fick diffusion law, the molecular diffusion deposition speed of sulfur can be expressed as:

$$\frac{dW_d}{dt} = C_d C_1 \frac{\rho_s A}{\mu} \left| \frac{dC}{dT} \right| \left| \frac{dT}{dr} \right| \tag{15.2}$$

In the above formula, dW_d/dt is the mass of dissolved sulfur deposit from molecular diffusion in unit time, C_d is the deposit constant (generally 1500), C_1 is the liquid phase concentration, A is the surface area for sulfur deposition, μ is the liquid viscosity, C is the volume fraction of sulfur to the crude oil, dC/dt is the volume fraction gradient of sulfur in the liquid, and dT/dr is the radial thermal gradient.

2. Sulfur shear diffusion deposition model. Sulfur particles behave two ways of horizontal migration, i.e. Brownian movement and shear diffusion, but the influence of Brownian movement is relatively small. Because of the porous flow speed-gradient field, the sulfur particles suspended in the oil flow will rotate in an angular velocity, contributing to their horizontal movement and shear diffusion. The sulfur shear deposition gradient caused by speed gradient with laminar flows can be expressed as the following:

$$\frac{dW_s}{dt} = C_d k^* C^* \gamma A \tag{15.3}$$

In the equation, dW_s/dt is the mass of dissolved sulfur deposition from shear diffusion in unit time, k^* is the shear deposition rate constant, C^* is the volume fraction of sulfur particles on the surface and γ is the shear velocity.

15.2.2 Thermodynamics Model of Three-phase Equilibrium

1. Fugacity equilibrium equations.

$$f_i^v = f_i^l = f_i^s \tag{15.4}$$

$$f_i^v = x_i^v \phi_i^v p \tag{15.5}$$

$$f_i^l = x_i^l \phi_i^l p \tag{15.6}$$

$$f_i^s = a_i^s f_i^{os} = x_i^s r_i^s f_i^{os} \tag{15.7}$$

In these three equations, f_i is the fugacity of component i in the gas, liquid and solid phase (as indicated by the superscript v, l, and s respectively), ϕ_i is the fugacity coefficients for component i in the gas and liquid phases (as indicated by the superscript v and l), x_i is the mole fraction of component i in the gas, liquid and solid phase (as indicated by the superscript v, l, and s respectively), a_i^s and r_i^s are the activity and the activity coefficient of the component i in the solid phase, f_i^{os} is the fugacity of the component i in the solid phase and p is the pressure.

2. Equilibrium constant equations. The gas-liquid equilibrium is given by:

$$K_i^{vl} = \frac{x_i^v}{x_i^l} = \frac{\phi_i^l}{\phi_i^v} \tag{15.8}$$

and the solid-liquid equilibrium by:

$$K_i^{sl} = \frac{x_i^s}{x_i^l} = \frac{\phi_i^l p}{r_i^s f_i^{os}} \tag{15.9}$$

3. Solid phase parameter. Fugacity of the solid standard state f_i^{os}:

$$f_i^{os} = f_i^{ol} \exp\left\{-\frac{\Delta H_i^f}{RT}\left(1-\frac{T}{T_i^f}\right)+\frac{b_1 M_i}{R}\left(\frac{T_i^f}{T}-1-\ln\frac{T_i^f}{T}\right)+\frac{b_2 M_i}{2R}\left[\frac{\left(T_i^f\right)^2}{T}+T-2T_i^f\right]\right\} \tag{15.10}$$

The solid activity coefficient is given by:

$$\ln r_i^s = \frac{V_i^s\left(\delta_m^s-\delta_i^s\right)^2}{RT} \tag{15.11}$$

In the equations above, H_i^f stands for the dissolution enthalpy of the component i, T_i^f is the solution temperature of the component i, M_i is the relative molecular weight of the component i, R represents the universal gas constant, b_1 and b_2 are the equation coefficients, δ_m^s is the solubility parameter of the solid phase mixture, δ_m^s is the solid solubility parameter of the component i, V_i^s is the solid substance volume of the component i, K_i^{vl} and K_i^{sl} are gas-liquid and liquid-solid equilibrium constants and r_i^s is the solid activity coefficient.

4. Material balance equations of gas-liquid-solid three phases

$$V + L + S = 1 \tag{15.12}$$

$$Vx_i^v + Lx_i^l + Sx_i^s = Z_i \tag{15.13}$$

$$\sum x_i^v + \sum x_i^l + \sum x_i^s = \sum Z_i = 1 \tag{15.14}$$

5. Flash vaporization equations of gas-liquid-solid three phases. According to the material conservation principle for gas-liquid-solid phase equilibrium as well as the definition of the equilibrium constant, the three-phase flash vaporization equations are derived as follows:

$$\sum \frac{Z_i}{V(K_i^{vl} - 1) + S(K_i^{sl} - 1) + 1} = 1 \tag{15.15}$$

$$\sum \frac{Z_i K_i^{vl}}{V(K_i^{vl} - 1) + S(K_i^{sl} - 1) + 1} = 1 \tag{15.16}$$

$$\sum \frac{Z_i K_i^{sl}}{V(K_i^{vl} - 1) + S(K_i^{sl} - 1) + 1} = 1 \tag{15.17}$$

In the equations, V, L, and S represent the fractions to amount of substance of gaseous, liquid and solid phases in equilibrium, and Z is the total amounts of substance of all components.

The Newton-Simpson method is used to solve the set of equations and to get the fractions of gaseous, liquid and solid phases in equilibrium as well as the compositions of the three phases.

15.2.3 Equation of State

The Peng-Robinson state equation is selected to express the state equations of the system:

$$p = \frac{RT}{V-b} - \frac{a\,\alpha(T)}{V(V+b)+b(V-b)} \tag{15.18}$$

$$a_i = 0.45724 \times \frac{R^2 T_{ci}^2}{p_{ci}} \tag{15.19}$$

$$b_i = 0.07780 \times \frac{R^2 T_{ci}^2}{p_{ci}} \tag{15.20}$$

where, R is the universal gas constant, T is the system temperature, p is the system pressure, T_c is the critical temperature, and p_c is the critical pressure.

15.2.4 Solubility Calculation Model

The main factor influencing sulfur to deposition is the solubility of sulfur in natural gas, and with the increasing of the solubility of sulfur, it becomes difficult for simple substance sulfur to separate and deposition. Therefore, it is essential to set up the solubility prediction model of simple substance sulfur in the natural gas. According to thermodynamics and experiment results, the relationship among solubility of sulfur, pressure and temperature in the acid natural gas is as the following:

$$C = [M_a r_g / (ZRT)]\exp(-4666/T - 4571)P^4 \tag{15.21}$$

In the formula above: C is the solubility of the natural gas, g/m^3; P is the pressure, MPa; T is the temperature, K; M_a is 2897, the relative molecular quality of dry air; R_g is the density of the natural gas; Z is the deviation factor of the natural gas; R is the gas constant.

15.2.5 Influence Mathematical Model of Sulfur Deposition Migration to Reservoir Characteristics

Sulfur deposition migration and porous medium sorption to sulfur particles might influence on porous medium characteristics, such as porosity and permeability. The original porosity of the reservoir is ϕ_0, then the porosity change caused by sulfur deposition is:

$$\phi = \phi_0 - \varepsilon_s / \rho_s \tag{15.22}$$

In the formula, ρ_s is the solid particle (sulfur) density and ε_s is the particle mass increment in pores of per unit rock volume.

During the flow process of solid particles, some deposited solid particles may be released and entered the fluid again because of the surface deposition and the shearing force. Thus deposition speed minus release speed is the net deposition speed. According to the dynamics equations, the deposition speed can be expressed as:

$$\frac{\partial \varepsilon_s}{\partial t} = R_r - R_e \tag{15.23}$$

The deposition rate R_r with the particle mass contained in the fluid per unit rock volume and the flow rate is in direct proportion.

$$R_r = \frac{dW}{dt}\left[1 + a_r (u_j - u_{jc})^{\beta_r}\right] \tag{15.24}$$

The re-entering speed R_e of particles mainly depends on the hydrodynamic conditions.

when $\left(-\frac{\partial p}{\partial x}\right) > \left(-\frac{\partial p}{\partial x}\right)_{cr}$, it can be expressed as:

$$R_e = k_2 \varepsilon_s \left[\left(-\frac{\partial p}{\partial x}\right) - \left(-\frac{\partial p}{\partial x}\right)_{cr}\right] \tag{15.25}$$

and when $\left(-\frac{\partial p}{\partial x}\right) \le \left(-\frac{\partial p}{\partial x}\right)_{cr}$

$$R_e = 0 \tag{15.26}$$

This means that in order to make the deposited particles re-enter the fluid, the hydrodynamic pressure gradient $(-\partial p / \partial r)$ must be greater than the critical pressure gradient $(-\partial p / \partial p)_{cr}$.

The permeability reduction is in close relationship with the porosity changes. They are in direct proportion, and the higher the fluid velocity is, the more sulfur deposits and the more permeability drops. Release and migration of solid particles in porous medium flow course will obviously alter the primitive porosity and permeability, aggravate the heterogeneity of porous media and reduce the permeability. Therefore, permeability reducing formula can be expressed as:

$$\frac{K}{K_0} = \left(\frac{\phi}{\phi_0}\right)^m \left(1 - \frac{u_{lg} - u_c}{u_c}\right) \tag{15.27}$$

In the formula, K is the permeability after sulfur deposition, K_0 is the initial penetration, ϕ is the porosity after sulfur deposition, ϕ_0 is the original porosity, u_{lg} is the gas-liquid mixture flow rate, u_c is the critical flow rate of gas-liquid mixture when sulfur released, and m is the equation exponent.

15.3 The Mathematical Model of Multiphase Complex Flow

15.3.1 Basic Supposition

In a gas pool, fluids and rocks meet the following conditions: the water and gas in the reservoir both accord with the non-Darcy flow; the rocks can be compressed a little; there are N fixed hydrocarbon quasi-components in the oil-gas system, which can more precisely reflect the interphase mass transfer among oil-gas fluids and can meet the petrochemical engineering and gas pool exploitation requirements; the flow course is regarded as isothermal; solid sulfur is considered to be incompressible; sulfur is absorbed on porous media, but some moves with gas/liquid, and sulfur deposition is determined by phase equilibrium and deposition laws; chemical actions do not occur during the phase change and flow course, so matter characteristics (such as the density, heat capacity and the heat-conduction coefficient) remain constant.

15.3.2 The Mathematical Model of Gas-liquid-solid Complex Flow in Porous Media

15.3.2.1 Flow Differential Equations

1. Quality conservation equations
Gaseous phase:

$$\phi \frac{\partial\left[\rho_{Lg} R S_L + (1-y_c-z_c)\rho_g S_g\right]}{\partial t} = -\nabla\left[\rho_{Lg} R \mathrm{v}_L + (1-y_c-z_c)\rho_g \mathrm{v}_g\right] \quad (15.28)$$

Liquid phase:

$$\phi \frac{\partial\left[\rho_L S_L + y_c \rho_g S_g\right]}{\partial t} = -\nabla\left[\rho_L \mathrm{v}_L + y_c \rho_g \mathrm{v}_g\right] \quad (15.29)$$

Mixture:

$$\phi \frac{\partial\left[\rho_L S_L + \rho_{Lg} R_s S_L + \rho_g S_g + \rho_s S_s\right]}{\partial t} = -\nabla\left[\rho_L \mathrm{v}_L + \rho_{Lg} R_S \mathrm{v}_L + \rho_g \mathrm{v}_g + \rho_s \mathrm{v}_s\right] \quad (15.30)$$

In the formula, ϕ stands for the porosity, ρ_g, ρ_{og} and ρ_L are density of gas phase, density of gas dissolved in oil phases and density of liquid under normal conditions respectively, R_s is the dissolved GOR, S_o is the oil saturation, S_g is the gaseous phase saturation, v_g is the gaseous phase velocity, v_L stands for the liquid phase velocity, v_s is the solid phase velocity, y_c and Z_c are the liquid and solid sulfur components in the gaseous phase respectively, while t stands for the time.

2. Momentum equations. The speed of gas and liquid flow in porous media, especially near the well casing, is very high. So the fluid movement is in accordance with the generalized Darcy's law. The gas and liquid plane radial flows can be expressed as:

Gaseous phase:

$$\nu_g = \frac{KK_{rg}}{\mu_g}\nabla p = \frac{KK_{rg}}{\mu_g}\frac{\partial p}{\partial r} \tag{15.31}$$

Liquid phase:

$$\nu_L = \frac{KK_{rL}}{\mu_L}\nabla p = \frac{KK_{rL}}{\mu_L}\frac{\partial p}{\partial r} \tag{15.32}$$

Solid phase: Sulfur flows with gas to the direction in which pressure decreases, whose speed relates to the shear velocity and gas speed when sulfur particles start to move, moreover the sulfur flow course is with the suspended motion and the bed load movement:

$$\nu_s = a_s(\nu_g - \nu_{gc}) \tag{15.33}$$

$$\nu_{gc} \propto P_c \tag{15.34}$$

Here, v_{gc} is the particle commencement shear velocity, K is the absolute permeability, K_{rg} and K_{rL} are gas and liquid relative permeability respectively, P_c is the capillary pressure, p is the pressure, r is the radial distance, μ_g and μ_g are the viscosity of gaseous and liquid phases respectively and a_s is the equation coefficient.

15.3.2.2 *Unstable Differential Equations of Gas-liquid-solid Complex Flow*

Substitute Equations (4), (5), (6) for Equation (3), then the following equation can be obtained:

$$\begin{aligned}&\frac{1}{r}\frac{\partial}{\partial r}\left\{rK\left[\frac{K_{rL}}{\mu_L B_L}(\rho_L + \rho_{Lg}R_s) + \frac{K_{rg}}{\mu_g B_g}(\rho_g + \rho_s a_s)\right]\right\} \\ &= \frac{\partial}{\partial t}\left\{\phi\left[\frac{\rho_L S_L + \rho_{Lg}R_s S_L}{B_L} + \frac{\rho_g S_g}{B_g} + \rho_s S_s)\right]\right\}\end{aligned} \tag{15.35}$$

Here, B_g and B_L are the volume coefficients of the gas and liquid phases.

From Equation (8) it is easy to know that all parameters relate to the pressure and the equation is non-linear. A virtual pressure coefficient $\psi(p)$ is introduced to make the equation easy to use:

$$\psi(p)=\int_{pb}^{p}\left\{\left[\frac{K_{rL}}{\mu_L B_L}(\rho_L+\rho_{Lg}R_s)+\frac{K_{rg}}{\mu_g B_g}(\rho_g+\rho_s a_s)\right]\right\}dp \tag{15.36}$$

Based on the average law, Equation (8) can be changed to:

$$\frac{1}{r}\frac{\partial}{\partial r}\left\{r\frac{\partial\psi}{\partial r}\right\}=\frac{1}{D_h}\frac{\partial\psi}{\partial t} \tag{15.37}$$

$$D_h=\frac{K}{\phi}\frac{\left[\frac{K_{rL}}{\mu_L B_L}(\rho_L+\rho_{Lg}R_s)+\frac{K_{rg}}{\mu_g B_g}(\rho_g+\rho_s a_s)\right]}{S_L\frac{\rho_L+\rho_{Lg}R_s}{B_L}+\frac{\rho_g(1-S_L-S_s)}{B_g}+\rho_s S_s} \tag{15.38}$$

Here, p_b is the saturation pressure and D_h is the defined intermediate variable.

15.3.2.3 *Relationship between Saturation and Pressure of Liquid Phase*

$$R_Z=\frac{\left[\frac{K_{rL}}{\mu_L B_L}\rho_{Lg}R_s+\frac{K_{rg}}{\mu_g B_g}\rho_g(1-y_c-z_c)\right]}{\left[\frac{K_{rL}}{\mu_L B_L}\rho_{Ls}+\frac{K_{rg}}{\mu_g B_g}\rho_g y_c\right]} \tag{15.39}$$

Since $\nabla p|_{r=r_e}=0$, then the saturation equation is:

$$\frac{dS_o}{dp}\frac{\left[\frac{\rho_{og}R_s}{B_o}\right]+S_g\left[\frac{\rho_g(1-y_c-z_c)}{B_g}\right]-R_z\left\{S_g\left[\frac{\rho_g y_c}{B_g}\right]+S_o\left(\frac{\rho_o}{B_o}\right)\right\}}{R_Z\left(\frac{\rho_o}{B_o}-\frac{\rho_g y_c}{B_g}\right)+\frac{\rho_g(1-y_c-z_c)}{B_g}-\frac{\rho_{og}R_s}{B_o}} \tag{15.40}$$

In the equation, R_Z is the defined intermediate variable.

15.3.2.4 *Auxiliary Equations*

Capillary force and relative permeability equations:

$$K_{ro} = K_{ro}(S_g, N_c, \sigma_{og}) \tag{15.41}$$

$$K_{rg} = K_{rg}(S_g, N_c, \sigma_{og}) \tag{15.42}$$

$$p_g = p_o + p_{cog}(S_g, N_c, \sigma_{og}) \tag{15.43}$$

In the equations above, N_c is the capillary number, σ_{og} is the interfacial tension between gas and oil, p_o is the oil phase pressure, p_g is the gaseous phase pressure, and p_{cog} is the gas-oil capillary force.

Constraint condition:

$$S_g + S_1 + S_s = 1 \tag{15.44}$$

Here, S_1 is the liquid phase saturation.

15.3.2.5 *Definite Conditions*

1. Gas pool original state

$$P_o\Big|_{\Omega+T}^{t=0} = p_{o\Omega+T}^0, \quad T\Big|_{\Omega+T}^{t=0} = T_{\Omega+T^o}^0,$$

2. Boundary state
   The closed outer boundary $\overline{\nabla}\Phi|_{\Gamma_{outer}} = 0$, the constant pressure outer boundary $p|_{\Gamma_{outer}} = p_o$, the constant bottomhole flow pressure $p|_{\Gamma_{inner}} = const$ and the bottomhole constant $f\left[\frac{\partial p}{\partial n}\right]\Big|_{\Gamma_{inner}} = const.$

Here, Ω is the study domain, T is the temperature, $\overline{\nabla}\Phi$ is the potential gradient function, Γ_{outer} is the outer boundary, and Γ_{inner} is the inner boundary.

15.4 Solution of the Mathematical Model Equations

15.4.1 Definite Output Solutions

$$\frac{1}{r}\frac{\partial}{\partial r}\left\{r\frac{\partial \psi}{\partial r}\right\} = \frac{1}{D_h}\frac{\partial \psi}{\partial t} \tag{15.45}$$

$$\psi(r,0)=\psi_i \tag{15.46}$$

$$\frac{1}{r}\frac{\partial\psi}{\partial r}\Big|_{r=r_w}=\frac{m_t}{2\pi Kh} \tag{15.47}$$

$$\frac{\partial\psi}{\partial r}\Big|_{r=r_e}=0 \tag{15.48}$$

As to the initial stage of the unstable flow, the gas-liquid flow pressure drop is:

$$\psi_i-\psi(r,t)=\frac{m_t}{4\pi Kh}\ln\frac{2.25D_ht}{r^2} \tag{15.49}$$

The bottomhole pressure drop is:

$$\psi_i-\psi(r_w,t)=\frac{m_t}{2\pi Kh}\left(\ln\frac{2.25D_ht}{r_w}+2S\right) \tag{15.50}$$

Here, r_w is the shaft radius, m_t is the total flow mass of the gas well, h is the effective thickness of the reservoir, ψ_i is the original reservoir quasi-pressure, r is the radial flow distance and t is the production time.

For the quasi-steady stage, the quasi-drop of pressure is:

$$\psi_i-\psi(r,t)=\frac{m_t}{4\pi Kh}\left(\frac{2D_ht}{r_e^2}+\ln\frac{r_e}{r}-\frac{3}{4}+\frac{r^2}{2r_e^2}\right) \tag{15.51}$$

The bottomhole pressure drop is:

$$\psi_i-\psi(r_w,t)=\frac{m_t}{2\pi Kh}\left(\frac{2D_ht}{r_e^2}+\ln\frac{r_e}{r_w}-\frac{3}{4}+S_H\right) \tag{15.52}$$

Here, S_H is the well skin coefficient, $\psi(r_w, t)$ is the bottomhole quasi-pressure at the production time t, $\psi(r, t)$ is the quasi-pressure at r away from the well at the production time t.

15.4.2 Productivity Equation

According to the model equations and the solutions, the quasi-steady capability equation can be obtained:

$$m_t = 2\pi Kh \frac{\overline{\psi} - \psi(r_w, t)}{\ln \frac{r_e}{r_w} - \frac{3}{4} + S_H} \tag{15.53}$$

In the equation, $\overline{\psi}$ is the average pressure of the reservoir.

15.5 Example

The multiphase complex flow mathematical model above was utilized for a well and the PR state equation was selected in the simulation. The gas pool thickness is 23.8 m, the primitive stratum pressure is 44.5 MPa, the stratum temperature is 102.5°C, the porosity is 9.3% and the reservoir effective permeability is 21.26×10^{-3} μm^2 and these simulation compositions of gas-oil are shown in Table 15.1.

The relationship between production time and sulfur saturation is showed in Figure 15.1. This indicates that sulfur saturation increases with production time. In the early stages of sulfur deposition, sulfur saturation changes slowly, and increases rapidly after a critical time. Pore space was quickly occupied, and seepage channel was blocked in a very short period of time.

The relationship between radial distance and sulfur saturation at different time is showed in Figure 15.2. This indicates that on the pressure decline, the sulfur would deposit, and the zone of sulfur deposition is the formation that is nearby from wellbore.

The relationship between production time and sulfur saturation under different prouction is showed in Figure 15.3. This indicates that when gas production is less than critical production, that Is Solid sulfur deposited in the layer, the more gas production was, the easier the percolation channels to be plugged, the shorter gas producing time is.

The relationship between production time and sulfur saturation under different prouction is showed in Figure 15.4. This indicates that when gas production is less than critical production, that Is Solid sulfur deposited in the layer, the more gas production was, the easier the percolation channels to be plugged, the shorter gas producing time is.

Table 15.1 Fluid compositions in gas pool.

Relative density	Volume fraction (%)							H_2S mass concentration (g/m^3)
	CH_4	C_2H_6	C_3H_8	CO_2	H_2S	N_2	H_2	
0.699	80.66	0.08	0.03	6.54	12.83	0.43	0.016	183.48

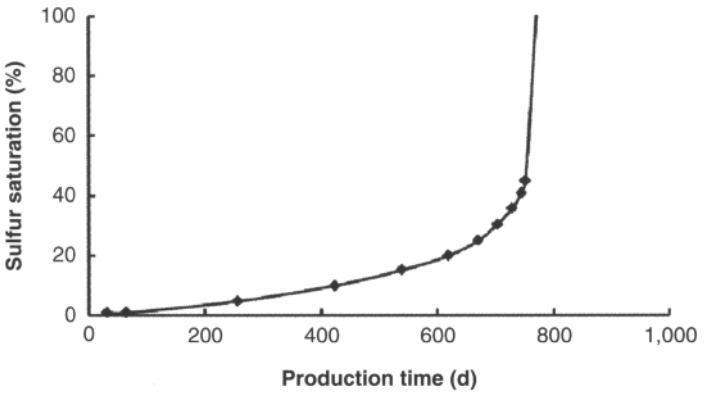

Figure 15.1 The relationship between production time and sulfur saturation ($q = 20*10^4 m^3/d$).

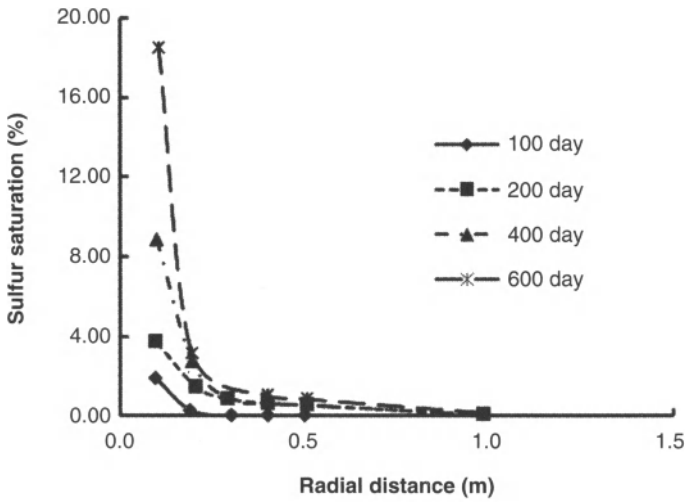

Figure 15.2 The relationship between radial distance and sulfur saturation at different time ($q = 20*10^4 m^3/d$).

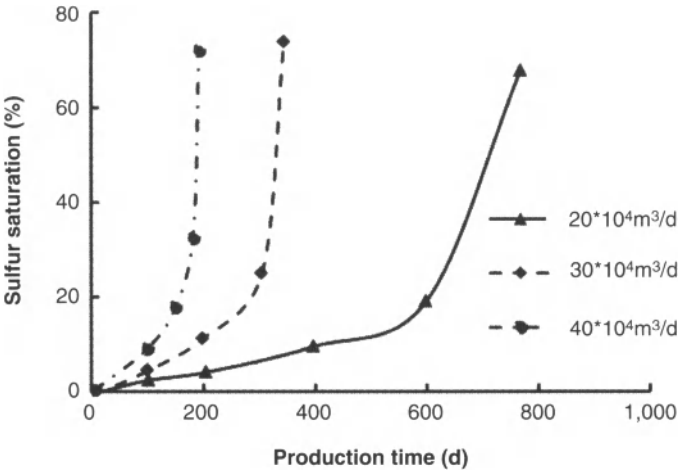

Figure 15.3 The relationship between production time and sulfur saturation under different prouction (Solid sulfur deposited in the layer).

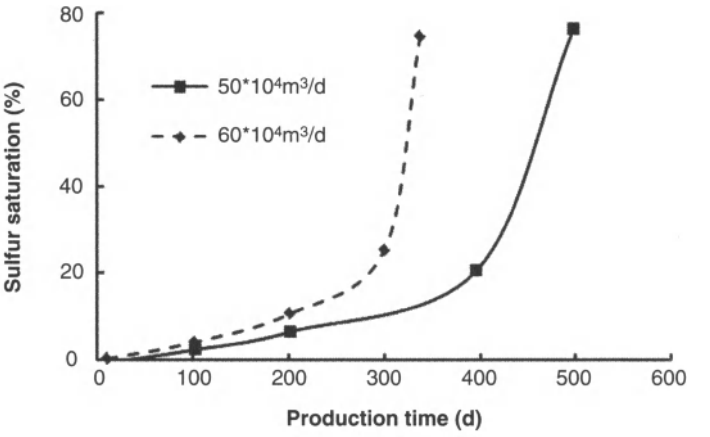

Figure 15.4 The relationship between production time and sulfur saturation under different prouction (Solid sulfur suspension in radial distance 0.2cm to wellhead).

15.6 Conclusions

1. Based researched on the gas-liquid-solid flow physical simulation and phase changes, established the mathematical model of multiphase flow with gas-liquid-solid

phase changes accompanied by sulfur deposition. The flow changes and the complex flow features caused by sulfur deposition were analyzed, and gas-liquid-solid complex flow characteristics and courses could be described accurately.

2. Studied on the multiphase flow theory of gas-liquid-solid phase changes with sulfur deposition and established the mathematical model of multiphase fluid-solid coupling seepage. The model showed the characteristic of multiphase flow with gas-liquid-solid phase changes while the liquid and sulfur released. This model could serve as theoretical foundation for future research on dynamic exploitation predicting, numerical simulating and field engineering.
3. On the pressure decline, the sulfur would deposit, and the zone of sulfur deposition is the formation that is nearby from wellbore. In the early stages of sulfur deposition, sulfur saturation changes slowly, and increases rapidly after a critical time. The more gas production was, the easier the percolation channels to be plugged, the shorter gas producing time is.

References

1. Roberts, B.E. "The effect of sulfur deposition on gas well in flow performance," SPE 36707[R].
2. Shedid A. Shedid and Abdulrazag Y. Zekri. "Formation damage due to sulfur deposition in porous media," SPE 73721[R].
3. Zhu Weiyao, Liu Xuewei, and Luo Kai. "Dynamic Model of Gas-Liquid-Solid Porous Flow with Phase Change of Condensate Reservoirs." *Natural Gas Geoscience*. 2005, (16) 3, 363.
4. Zhu Weiyao. "Theoretical Studies on the Gas-Liquid Two-phase Flow (Including a Phase Change)Through Porous Media." *Acta Petrolei Sinica*. 1990, (9)1, 15.
5. Zhang Dihong, Wang Li, and Zhang Yi. "Phase Behavior Experiments of Luojiazhai Gas Reservior with High Sulfur Content." *Natural Gas Industry*, 2005, 25, S1.

16

Modeling and Evaluation of Oilfield Fluid Processing Schemes

Jie Zhang[1], Ayodeji A. Jeje[2], Gang Chen[1], Haiying Cheng[3], Yuan You[4], and Shugang Li[5]

[1]Xi'an Shiyou University
Xi'an, People's Republic of China
[2]University of Calgary
Calgary, Canada
[3]Dagang Oilfield Company, PetroChina
Tianjing, People's Republic of China
[4]Changqing Oilfield Company, PetroChina
Xi'an, People's Republic of China
[5]CNOOC Energy Technology & Services Ltd.,
Tianjing, People's Republic of China

Abstract

Oilfield fluids, that is, produced water, water-based mud, and gas cut mud, were processed in a continuous-flow, closed-loop test facility, with controlled addition of chemicals. Chemicals were added to treat the liquid and suspension streams before discharge into ambient, or before re-circulation in drilling operations. The facility was designed and constructed to evaluate the effect of varying chemical dosages and mixing schemes. The system was also analyzed to identify important operating parameters for effective treatment of the streams. Since chemical reactions occur from the point of injection of chemicals, both the kinetics of reaction and the flow rates determine optimal relations between the flow patterns in process units and the compositions of the oilfield fluids at discharge or re-circulation points. Prescriptions for the type of chemical additives, and the process conditions for their application, are suggested to optimize the system performance. Continuous processing removes reliance on periodic laboratory tests of samples of oilfield fluids to determine how to adjust the

Ying (Alice) Wu, John J. Carroll and Weiyao Zhu (eds.) Sour Gas and Related Technologies, (247–260)

operating conditions in treating the streams. The risk of secondary pollution is reduced by controlled application of chemicals of the proper type, and at optimal dosages.

Keywords: Dynamic simulation, oilfield chemicals, evaluation method, oilfield fluids treatment, continuous flow operations

16.1 Introduction

More environmentally conscious production techniques are being promoted all over the world for the recovery of crude oils and natural gas. Pollution results, not only from the extensive commercial and industrial uses of the hydrocarbons, and deliberate or accidental discharge of fluids extracted from reservoir formations into the environment through spills and flaring – the primary pollution, but from the many chemicals in use that are associated with reservoir preparation, drilling and production. Chemicals, such as acids, are frequently injected to dissolve rocks to increase the porosity and permeability of formations for enhanced fluid flow through the porous media. The mud used for drilling is often contaminated with compounds associated with reservoir formations and these need to be removed before the mud can be re-circulated. Water produced with hydrocarbons also contains dissolved compounds that require removal through chemical treatment. It is desirable to reduce, or even avoid, the use of chemical additives that results in secondary pollution in the oilfields.

Treatment of water produced with hydrocarbons has primarily been by batch operations. Continuous processes that involve automated control are expected to be more economical. To predict performance characteristics and establish operating parameters for continuous flow systems, proposed schemes should be modeled. Physical models or pilot units can suggest the type of water treatment agent to be applied and optimal dosages, and establish other operation parameters for the system.

Mud, with cuttings from drilling operations, is re-conditioned before re-injection. The operation involves adding chemicals to the flow stream to coagulate particles or react with compounds. Relationships between extent of reactions and the flow patterns in equipment units are little understood and have not been much studied experimentally or theoretically.

Monitoring and controlling the effect of chemicals added to produced-water and to drilling mud in field operations are becoming increasingly important. Results of experimental studies and calculations are reported in this paper. Test facilities used model both continuous and batch oilfield unit operation processes. Effects of chemicals added to produced-water, water-based mud and gas-cut mud were determined through concentration measurements. The additives were screened for type, appropriate dosages were determined, and process parameters were established under different hydrodynamics conditions.

16.2 Treatment of Produced Water

16.2.1 Experiments

A schematic of the test equipment for treatment of produced water is shown in Figure 16.1. Water that has compositions similar to produced-water is passed through a flow meter. A coagulant, discharged by a constant flow pump, is mixed into the water rapidly in a stirred tank. The effluent from the tank is passed into a laminar current, clap-board flocculating tank. Particles in the precipitate that is formed grow up by means of collision, coagulation and

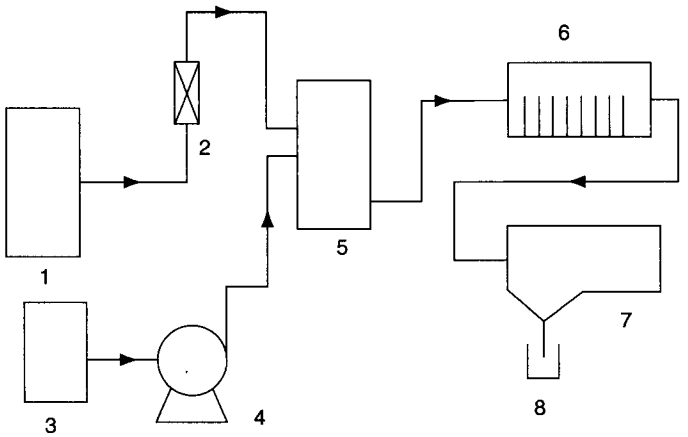

Figure 16.1 A flowchart of the equipment for treating produced water.
1 water storage, 2 Glass flow meter, 3 Dosing cans, 4 Constant flow rate pump (Dosing pump), 5 Stirred tank, 6 Laminar current & clapboard flocculating tank, 7 Settling tank, 8 Water receiver.

adsorption, and are recovered at the bottom of the settling tank. The supernatant in the settler flows over a weir into a collecting tank. The turbidity of the supernatant was measured.

16.2.2 Test Methods

Water for the foregoing test was prepared to be similar in composition to water typically produced at an oil field. The turbidity of the "produced water" was 136 FTU (Formazin Turbidity Units). Volumetric flow rates, into and out of the mixing tank, were steady and equal. Retention times for mixing in the tank, in the flocculation and in the sedimentation units were determined as follows. A fixed amount of salt (NaCl), used as tracer, was poured into the mixing tank at once. From this instant, the pulse signal of tracer (salt concentration) was measured at the outlet of the mixing tank at fixed time intervals. Residence time distribution functions and the extent of back-mixing were estimated from the data illustrated with the example in Table 16.1.

Tracer concentrations c(t) were determined by measuring by the electrical conductivities (K) of the flow stream out of the mixing tank and calibrating the results with the conductivities of standard solutions of NaCl prepared with distilled water. E(t) is the residence time distribution function (calculated from effluent volume rate (Q) multiplied by c(t) and divided by the total amount of salt

Table 16.1 Estimation of retention time distribution functions in mixing tank.

Sampling Time t/min	Electrical Conductivity K μS/cm	Effluent salt concentration $c(t)$ mol/L	$E(t) = Qc(t)/M$ min^{-1}
0	4950	0.05395	0.35969
2	2600	0.02483	0.16554
5	1020	0.00810	0.05403
9	397	0.00180	0.01200
14	233	0.00044	0.00296
19	195	0.00015	0.00103

added, M). Mean residence time (τ) and the variance (σ) are estimated from:

$$\tau = \frac{\int_0^\infty tE(t)dt}{\int_0^\infty E(t)dt} = \int_0^\infty tE(t)dt; \quad \sigma_t^2 = \int_0^\infty (t-\tau)^2 E(t)dt$$

Mechanical parameters such as mixing, coagulation and sedimentation times were chosen to be in the same range as for conventional batch processes (mixing time of 1 ~ 3 min, flocculation time of 10 ~ 20 min, and settling time of 20–30 min). Four coagulants, aluminum sulphate (Al_2SO_3), poly-aluminum chloride (PAC), polyferric sulphate (PFS) and hydrolyzed polyacrylamide (HPAM), were tested and the optimal dosage for each was determined. The results for both laboratory-scale batch experiments and the continuous-flow test facility were compared.

16.2.3 Results

For both the batch (bench-scale) laboratory tests and the continuous-flow unit, the trends for activity of coagulants on produced water were similar. However, the level of reduction of the turbidity of the produced water was less for the continuous-flow facility than for batch experiments, for the same amount of coagulant used in similar volumes of water. The turbidity reduction rate for the continuous-flow system was 80% of the batch tests. Optimal amounts of coagulant for the continuous-flow system were also determined to be 1.5 to 2 times larger than for batch tests.

A particular difference between batch and continuous flow methods is that mixing is less effective for the flow system compared to the batch operation. The probability of particles collisions is higher in a stirred beaker than in a flow loop over a fixed time interval. Parts of the flow system, such as in the flocculation tank, have short-circuit flows and dead ends and thus the probability of particles colliding with and sticking to each other is reduced. When flocculation does not occur sufficiently in the flow system, the water will not be cleaned. Data shows that dispersion is higher at lower flow velocities and this is consistent with the suggestion that smaller particles are involved more in back-mixing. With less flocculation, the particles in the continuous-flow system were smaller than observed

for the batch tests in the settling tanks. Thus settling required much longer times than for the batch experiments. The configuration of the mixing system and the hydrodynamic conditions are also different for the two kinds of tests. These factors explain the difference in performance, not that the operating procedures have not been standardized, as has been suggested by previous investigators.

In summary, batch tests for coagulation give ideal process limits. Conditions for continuous-flow tests are very much like those for industrial water treatment processes. Data from batch tests are useful for designing continuous flow systems and for choosing operating parameters.

16.3 Treatment of Re-circulating Mud

16.3.1 Test Facility

A schematic diagram of the test loop for chemical treatment of drilling mud is shown in Figure 16.2.

Mud, with a coagulating agent added, is pumped through a flow meter into the wellbore. The suspension returns in the annular space between drill pipe and wall of the bore hole. After exiting

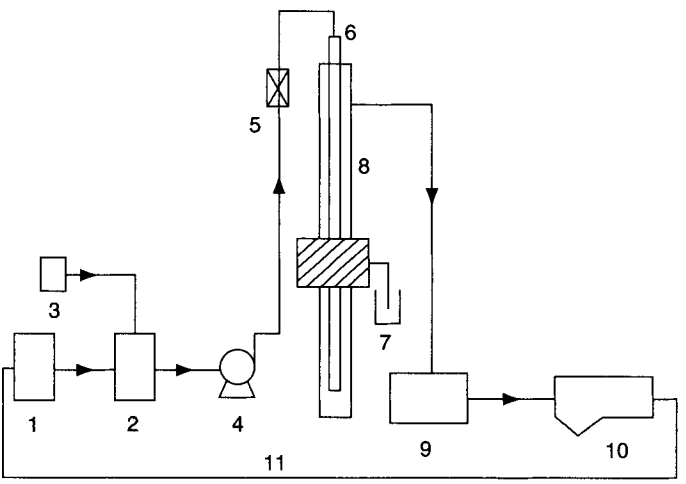

Figure 16.2 Flow diagram for test loop with mud re-circulation.
1 Mud storage tank, 2 Mixing vessels, 3 Coagulating agent dosing cans, 4 Mud pump, 5 Flow meter, 6 Drill pipe, 7 Filtrate receiver, 8 Wellbore hole, 9 The de-sander and de-silter, 10 Settlement pool, 11 Pipeline.

the annulus, gravel and precipitate are removed from the mud in the de-sander/de-silter and in the sedimentation tanks. The mud recovered from the sedimentation tank is re-circulated.

16.3.2 Test Methods

The fluids tested in the system were water, water + bentonite suspension (polymer-free, low solids) and water + PAM suspensions (dispersed). Cuttings carrying capacities of the three fluids were determined in different wall to pipeline diameter ratios. Parameters recorded are as follows: weight of suspended solid m (g), volume of wellbore annular space V_1 (ml), and volume of drill pipe V_2 (ml), time t (s), flow rate of mud pump Q (m^3/h), suspension height of solids h (cm).

16.3.3 Analysis of Test Results

Table 16.2 shows the test results for mud. For the three fluids, at low injection velocities (<0.69 cm/s), as the flow rate of mud (Q) is increased, the height to which solids can be lifted (h) increased. Water was less effective than bentonite suspension, and bentonite is less effective than polyacrylamide. When the flow velocity of mud is high (over 0.93 cm/s), the height to which solids can be suspended in water decreased as the flow rate was increased, indicating that the cuttings carrying ability has been reduced greatly. This is reflected in an observation termed the "Flip sink", a phenomenon in which suspended solid particles flow downwards within the annular space, is observed through transparent wall with water as the carrying medium. For water + bentonite and water + PAM, the cutting carrying capacity continue to increase, but at a progressively reduced rate, indicating that the cuttings carrying ability were degraded. Cuttings carrying ability of water + bentonite was much weak than that of water + PAM. "Flip sink" was seldom observed for water + PAM.

The facility test results are similar to actual oilfield results. Cuttings carrying ability of polymer mud is greater than any other mud in the test flow rate range. Flip sink phenomenon becomes weaker as the annular space between drill pipe and wall is decreased. This observation would seem to confirm good performance of slim hole drilling.

Table 16.2 Results of simulation test for mud circulation.

V_2	m	Test parameters	Water				Water + bentonite				Water + PAM			
			1	2	1	2	3	4	3	4	1	2	3	4
		V_1	2000				1000				1000			
		t	27	23.5	23.5	13.5	19	7.4	5.6	4.8	15.6	10.4	7.5	6.8
		h	3.3	6.7	6.7	13.6	0	6.1	12.5	15.8	3.3	9.9	16.5	19.8
1000	50	Q	0.267	0.306	0.306	0.533	0.190	0.486	0.643	0.750	0.231	0.346	0.480	0.529
		V_1	2000				1000				1000			
		t	55.4	33.6	33.6	24.5	26.2	14.4	9.4	5.6	23	12.1	9.2	7.8
		h	0	5.1	5.1	10	0	8.7	13.5	18.3	0	7.5	12.5	34.8
500	25	Q	0.130	0.214	0.214	0.294	0.137	0.250	0.383	0.643	0.157	0.298	0.391	0.461
		V_1	1000		2000		500		1000		500	1000		
		t	58.4	21.5	21.5	24.5	23.6	9	8.6	7	21.5	24.4	18.5	8.6
		h	0	3.5	3.5	8.4	0	10.3	16.5	20.3	0	6.3	10.5	28.1
250	13	Q	0.062	0.167	0.167	0.294	0.076	0.200	0.419	0.514	0.084	0.148	0.195	0.419
		V_1	1000				500		1000		500		1000	
		t	49	27.5	27.5	25.2	27.7	14.1	12.8	8.4	103.2	29.7	26.1	17
		h	3.6	7.2	7.2	12.4	0	7.3	10.7	14.1	0	3.4	11.9	24.6
100	6	Q	0.073	0.131	0.131	0.143	0.065	0.128	0.141	0.429	0.017	0.061	0.138	0.212

16.4 Test on Gas-cut, Water-based Mud

16.4.1 Test Facility

A flow chart of test facility for when hydrogen sulfide gas invades the water-based mud circulated in drilling is shown in Figure 16.3. Hydrogen sulphide is injected into the mud within the wellbore. The gas is carried into a gas-liquid separator and recovered in a multi-stage absorber. The mud, with chemicals added, is passed through the wellbore, a separator and a sedimentation tank before being re-cycled.

16.4.2 Test Method

To 80 litres of mud, chemicals that react with hydrogen sulfide are added. The fluid was circulated through the test loop. Properties of a sample of the mud, such as its rheology, rates of liquid removal

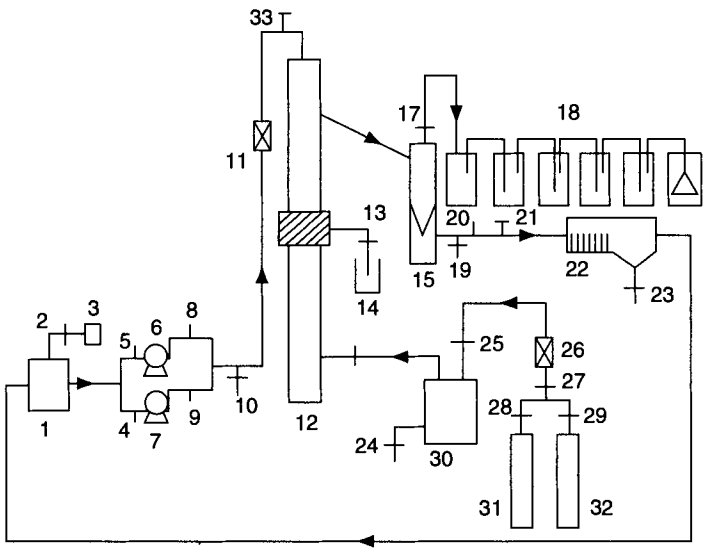

Figure 16.3 Flow chart of test facility for hydrogen sulfide gas cut water-based mud. 1 Pool of mud, 3 Coagulant dosing cans, 6, 7 mud pumps, 11 flow meter, 12 Wellbore hole, 14 Filtrate receiver, 15 Gas-liquid separation device, 18 Tail gas treatment unit, 22 Solid-liquid separation unit, 26 Gas flow meter, 30 Buffer tank, 31 Hydrogen sulphide gas cylinders, 32 Nitrogen cylinder, 2, 4, 5, 8, 9, 10, 13, 16, 17, 19, 20, 21, 23, 24, 25, 27, 28, 29, 33 valves.

during filtration (fluid loss), conductivity and pH, were measured after the system had been operated for 30 mins. Hydrogen sulfide gas was then admitted into the system at an average rate of 500 standard cm^3/min. Samples (350 mL each) were taken from the borehole exit (sample point 1), liquid outlet of gas-liquid separator (sampling point 2) and mud settling tank (sampling point 3) every 5min. The rheology, fluid loss, conductance, pH, ion content of sulfur of the samples were tested. After the system had been operated for 50 to 60 minutes, saturated sodium hydroxide solution was injected into the loop from a dosing can and the circulation was continued for another 10 ~ 15 mins. Then the system was cleaned out.

The drilling fluid formulation used were:

1#: Base mud (water +0.5%+4% anhydrous sodium bentonite);
2#: Base mud +0.2% KJ-1;
3#: Base mud +0.4% PCC;
4#: Base mud +0.4% PCC +0.4% +0.1% NaOH basic zinc carbonate solution (keep the pH values of the mud greater than 11).

16.4.3 Test Results

The results for mud invaded with hydrogen sulfide are presented in Table 16.3.

From Table 16.3, it is observed that as the pH values of mud decreased, the conductivity increased. The sulfur ion content also increased gradually as the time elapsed of hydrogen sulfide gas injection into the mud increased. The pH values and the electrical conductivities of the samples withdrawn at different sampling ports, at the same time, were similar; but the sulfur ion content of mud decreased from sampling points 1 to 4. When the pH value of mud is less than 11, the hydrogen sulfide gas in mud exist mainly in the molecular form H_2S and as HS^- ions. The passage of the mud from the outlet of the separator into the settling tank caused the sulfur ion content to decrease because of the escape of hydrogen gas.

Table 16.3 Test results for gas cut mud (test temperature: 24 ~ 26°).

Number of mud		1#			2#			3#			4#		
Sampling time/min	Sampling point	pH	Λ/ $\times 10^4$ (μs/cm)	C_{S2-}/ (mg/L)	pH	Λ/ $\times 10^4$ (μs/cm)	C_{S2-}/ (mg/L)	pH	Λ / $\times 10^4$ (μs/cm)	C_{S2-}/ (mg/L)	pH	Λ/ $\times 10^4$ (μs/cm)	C_{S2-}/ (mg/L)
5	1	11.02	0.42	20.43	10.03	0.38	326.07	10.03	0.38	425.07	11.98	0.56	525.07
	2	11.01	0.41	20.38	9.92	0.38	278.18	9.92	0.38	388.28	11.96	0.56	488.28
	3	11.02	0.42	20.36	9.95	0.37	234.02	9.95	0.37	314.71	11.98	0.56	414.71
10	1	10.98	0.43	142.58	9.40	0.38	749.36	9.40	0.38	819.35	10.96	0.54	919.35
	2	10.97	0.43	140.31	9.41	0.39	665.73	9.41	0.39	745.78	10.90	0.55	845.78
	3	10.97	0.42	138.03	9.38	0.39	596.28	9.38	0.39	672.21	10.92	0.54	772.21
15	1	10.84	0.44	241.14	7.48	0.40	1234.93	7.48	0.40	1334.33	10.13	0.53	1534.33
	2	10.79	0.43	236.34	7.52	0.41	1197.64	7.52	0.41	1297.54	10.10	0.53	1497.54
	3	10.80	0.43	222.18	7.42	0.41	913.83	7.42	0.41	1113.63	10.06	0.53	1313.63
20	1	9.46	0.45	598.62	7.34	0.43	1367.90	7.34	0.43	1507.90	9.04	0.50	1707.90
	2	9.40	0.43	584.21	7.32	0.42	1389.24	7.32	0.42	1549.24	9.00	0.51	1749.24
	3	9.38	0.44	562.03	7.32	0.42	1399.03	7.32	0.42	1549.24	8.99	0.51	1749.24
25	1	8.43	0.47	948.42	6.88	0.44	1673.23	6.88	0.44	2070.03	8.56	0.48	2370.03
	2	8.48	0.46	903.80	6.87	0.43	1594.34	6.87	0.43	1992.04	8.57	0.49	2292.04
	3	8.40	0.46	776.43	6.85	0.43	1546.62	6.85	0.43	1945.62	8.53	0.48	2245.62

(Continued)

Table 16.3 (Cont.) Test results for gas cut mud (test temperature: 24 ~ 26°).

Number of mud		1#			2#			3#			4#		
Sampling time/min	Sampling point	pH	Λ/ $\times 10^4$ (μs/cm)	C_{S2-}/ (mg/L)	pH	Λ/ $\times 10^4$ (μs/cm)	C_{S2-}/ (mg/L)	pH	Λ / $\times 10^4$ (μs/cm)	C_{S2-}/ (mg/L)	pH	Λ/ $\times 10^4$ (μs/cm)	C_{S2-}/ (mg/L)
30	1	7.96	0.49	1368.24	6.64	0.44	1947.10	6.64	0.44	2217.17	8.10	0.49	2617.17
	2	7.90	0.49	1301.00	6.62	0.43	1876.48	6.62	0.43	2146.28	8.06	0.49	2546.28
	3	7.91	0.48	1286.62	6.58	0.43	1800.03	6.58	0.43	2070.03	8.02	0.50	2470.03
35	1	7.43	0.51	1549.92	6.46	0.45	2295.02	6.46	0.45	2785.02	7.64	0.49	3085.02
	2	7.40	0.51	1500.83	6.43	0.45	2232.78	6.43	0.45	2742.68	7.63	0.48	3042.68
	3	7.39	0.50	1463.48	6.48	0.45	2198.40	6.48	0.45	2698.43	7.63	0.48	2998.43
40	1	7.18	0.52	1632.21	6.39	0.45	2517.98	6.39	0.45	2816.08	7.23	0.46	3216.08
	2	7.12	0.51	1598.43	6.40	0.46	2582.82	6.40	0.46	2792.12	7.26	0.47	3192.12
	3	7.10	0.51	1586.32	6.42	0.46	2560.02	6.42	0.46	2767.32	7.30	0.46	3167.32
45	1	6.98	0.52	1698.41	6.32	0.47	2793.42	6.32	0.47	3163.22	6.84	0.48	3363.22
	2	6.94	0.52	1682.04	6.28	0.46	2784.53	6.28	0.46	3104.83	6.88	0.49	3304.83
	3	6.95	0.51	1643.58	6.30	0.46	2774.10	6.30	0.46	3074.10	6.70	0.47	3274.10
50	1	6.73	0.53	1710.43	6.27	0.47	2872.32	6.27	0.47	3172.32	6.80	0.48	3372.32
	2	6.74	0.53	1689.76	6.24	0.47	2821.31	6.24	0.47	3121.31	6.80	0.48	3321.31
	3	6.70	0.52	1653.43	6.26	0.47	2884.35	6.26	0.47	3084.35	6.90	0.47	3284.35

Note: Λ, Conductivity; C_{S2-}, Sulfur ion content.

16.5 Conclusion

1. Dosages of chemicals for treating produced water are higher for continuous flow systems than for batch operations. Mixing and flocculation occur readily in batch processes, and the settlement of particles is not affected by hydrodynamic conditions. The continuous operation involves a mixing unit in which fluid back-mixing exists and it approximates a constant continuous stirred reactor (CSTR). The mixing patterns in the flocculation and sedimentation tanks are between CSTR and plug flow reactors.
2. The polymer solid-free mud has outstanding ability to carry cuttings, mainly because it can effectively overcome solids Flip sink.
3. The reduction of wellbore hole size, which helps to overcome solids Flip sink, will increase effective drilling rate.
4. The mud with formula water +4% bentonite +0.5% anhydrous sodium carbonate +0.2% KJ^{-1} and water +4% bentonite +0.5% anhydrous sodium carbonate +0.4% PCC are ideal absorbers for injected hydrogen sulfide gas. The absorption rate of the two formulations mud reached 80% and 90%, when the average hydrogen sulfide injection rate was 500s cm^3/min and the cumulative injected amount was between 40 ~ 280 g.
5. Three test schemes were used to model continuous-flow processing of oilfield engineering fluids – water-based mud, gas cut water-based mud and oilfield produced-water. Prescriptions for the type of chemical additives and the process conditions for their application are suggested to optimize the system performance. Continuous processing removes reliance on periodic laboratory tests of samples of oilfield fluids to determine how to adjust the operating conditions in treating the streams. The risk of secondary pollution is reduced by controlled application of chemicals of the proper type and at optimal dosages.

References

1. Quiqley, M.S. and Sifferman, T.R. "Unit provides dynamic evaluation of drilling fluid properties." *[J].World Oil*, 1990, 210(1): 43–48.
2. Zhang Shao-huai and Zhang Jie. "Drilling Technology in the 21st Century Development and Innovation." *[J].ACTA PETROLEI SINICA*, 2001, 22(6): 63–68.
3. Ma Xiao-ou, Kang Si-qi, and Yi Geng-ming. "Chemical Oxidation-coagulation Process for Papermaking Dynamic Experiment." *[J]. Environmental Engineering*, 2001, 19(2): 17–19.
4. Cheng Hai-ying. *Create a new dynamic evaluation method of industrial wastewater treatment*, [D], Xi'an Shiyou University, May 18, 2003.
5. You Yuan. *Development and Application of a Device for Experimental Simulation of Drilling Fluids*, [D], Xi'an Shiyou University, May 15, 2006.
6. Hu Qi. *The Water-base Drilling Fluid Architectural Study of Assimilating Hydrogen Sulfide——The Evaluation Studies of Assimilating Effect*, [D], Xi'an Shiyou University, May 20, 2008.
7. Li Shu-gang. *The Study on FieldTechnology of H_2S Gas Absorption in Drilling Fluid in The Borehole*, [D], Xi'an Shiyou University, May 20, 2009.
8. Guo Gang. *Study on Changqing Oilfield Universal Water-based Working Fluid of Fracturing and Drilling*, [D], Xi'an Shiyou University, May 20, 2010.

17

Optimization of the Selection of Oil-Soluble Surfactant for Enhancing CO_2 Displacement Efficiency

Ping Guo[1], Songjie Jiao[2], Fu Chen[2], and Jie He[2]

[1]*State Key Laboratory of Enhanced Oil Recovery*
Southwest Petroleum University, Chengdu, People's Republic of China
[2]*State Key Laboratory of Oil and Gas Reservoir Geology and Exploitation*
Southwest Petroleum University, Chengdu, People's Republic of China

Abstract

Currently, the main international trend of gas injection is the applications in low permeability reservoirs, especially through CO_2 miscible flooding. In China, most low permeability reservoirs are subaerial deposition, which usually have large reserves and serious heterogeneity. It is not easy to reach CO_2 miscible because of the quality of the heavy oil and high viscosity. In some extra low permeability reservoirs, it is difficult to inject water, and thus, gas injection is a good way to realize additional production. However, due to non-miscible flooding, coupled with the influence of heterogeneity, gas injection breaks through quickly, and the resultant recovery is very poor. Generally, miscible flooding will not break through until achieving 1PV. The key problems to developing CO_2 injection in China are enhancing oil displacement efficiency with lower costs, and reducing miscible pressure.

This paper discusses a new kind of surfactant that is insoluble in water, but is soluble in both supercritical CO_2 and crude oil. As with all surfactants, this one reduces the interfacial tension. The reduction in the interfacial tension between CO_2 and crude oil achieves the purpose of enhanced oil recovery. Through the effort of development and preparation, as well as the evaluation experiments of solubility and viscosity reduction, we have found two kinds of surfactants, i.e., CAE and CAF, both of which have good results of viscosity reduction. When the concentration of surfactant added in crude oil amounts to 1.0%, the result of viscosity

Ying (Alice) Wu, John J. Carroll and Weiyao Zhu (eds.) Sour Gas and Related Technologies, (261–272)

reduction reaches a maximum. The surfactant CAE's viscosity reduction rate can reach 37.8%, and the CAF's is 27.3%. Under the same conditions, we have measured the solubility of CAE and CAF in supercritical CO_2. Experiment results show that both of them can be dissolved in CO_2 to some extent, but the surfactant CAE's solubility is better. CAE has a solubility of 1.405×10^{-2} g/mL under 22.64 MPa, compared with the solubility of CAF of 1.16×10^{-3} g/mL. Using actual crude oil in a high temperature and pressure formation, based on displacement efficiency through slim tube test, confirms that the displacement efficiency of CAE is higher than CAF by 8% under the same conditions. We can determine the preferred surfactant as CAE. Slug displacement experiments, with different concentrations considering multiple factors, such as the increasing amount of displacement efficiency and costs, have determined a more economical concentration of 0.2%. Under the same usage, we have made an oil displacement comparison between plug flooding and the flooding of dissolving solvent in CO_2. Experiments show that, compared with pure CO_2 flooding, both of the displacement methods can enhance displacement efficiency to some extent, and slug flooding makes a more pronounced increase. Under the formation conditions (85°C, 22.64 MPa), the slug flooding with concentrations of 0.3% can improve the displacement efficiency by about 10%. According to a series of studies, this article provides an efficient way to reduce miscible pressure and enhance oil displacement efficiency in low permeability reservoirs of China.

17.1 Introduction

For low permeability reservoir, the research on enhancing oil recovery through gas injection is a sustained and highly exploratory issue. Since the 1950s, gas injection studies have been launched in succession. The United States, Canada and other countries have continually conducted field test of gas injection flooding and achieved good stimulate result. However, because the vast majority of China's oil reservoirs have high crude oil viscosity, it's quite hard to realize miscible and gas injection cannot enhance the oil recovery effectively. Whereas the oil-soluble surfactant flooding technology combines the surfactant's advantages of reducing interfacial tension and enhancing the ability of CO_2 miscible flooding, which ensures the reservoirs that cannot reach miscible achieving miscible flooding conditions, thus acquiring a better improvement of displacement efficiency.

17.2 Experiment Preparation and Experimental Conditions

17.2.1 Experiment Preparation

1. The synthesis of surfactant and its physical parameters

   Through literature review and preliminary screening experiments, we found that ordinary commercial thinning agent was almost insoluble in supercritical CO_2. Analyzing the structural features of surfactants that can dissolve in supercritical CO_2 as well as heavy oil viscosity reducer, we synthesized two kinds of liquid surfactant CAE and CAF, both of which were characterized with oil-soluble, CO_2-soluble and with viscosity reduction properties. The basic physical parameters are shown in Table 17.1.
2. Fluid sample preparation of slime-tube displacement test

   In this experiment, degassing oil samples were obtained from crude oil of the F48 block in Daqing (25L, 2 barrel). Based on gas composition, gas samples were determined in accordance with industry standard SY/T 5542–2000 "Analytical method for reservoir crude oil physical properties". The single degassing oil ratio, volume factor, viscosity and bubble-point pressure of prepared oil sample were required to be basically consistent with the determined representation fluid.

Table 17.1 The basic physical parameters of CAE and CAF

Surfactant Measurement items	Density (25°C) (g/mL)	Viscosity (25°C) (mPa•s)	Remarks
CAE	0.8710	2.0	Viscosity was measured by NDJ-79 rotary viscometer (×1 rotor)
CAF	0.8574	3.0~4.0	

Table 17.2 Basic parameters of experiment fluid.

Formation Temperature: 85° Formation pressure: 22.64 MPa

Bubble point (MPa)	Degassing oil density (g/L)	Crude oil viscosity (mPa·s)	volume factor	gas/oil ratio (m^3/t)
5.2	0.8881	10.3 (85°C)	1.088	22

17.2.2 Experimental Conditions

1. The basic parameters of slim-tube used in experiment.
2. The experimental temperature and conditions

   The experiment temperature was 85°C, i.e, the reservoir temperature; the screening tests of different surfactants were conducted under the formation pressure 22.64 MPa; but the optimization tests of surfactant concentration were conducted under a lower pressure 18 MPa.

17.3 Experiment Contents and Methods

1. Screening of Oil-soluble surfactants.
2. For optimized surfactants, investigating oil displacement efficiency through different injection methods.
3. Optimizing the injection concentration for optimized surfactants.
4. The studies on oil-soluble surfactant displacement efficiency were conducted in accordance with industry standard SY/T 6576–2003 "Slim-tube experimental determination of minimum miscibility pressure".

Table 17.3 Slim-tube parameters.

Length (cm)	diameter (cm)	Pore volume (cm^3)	Porosity (%)	Permeability ($10^{-3}\mu m^2$)
2000	0.44	95.228	31.31	7058

17.4 Optimization of Surfactants

17.4.1 Oil-soluble Determination of Surfactant CAE

Mix 0.3g CAE with 5mL n-decane and water respectively. Shake fully and then rest for 5min. Experiment results indicate that, CAE can be dissolved in n-decane and can stratify with water with apparent interface (as shown in figure 17.1).

Through figure 17.1, we can infer that surfactant CAE has well oil-soluble.

17.4.2 The solubility Evaluation of CAE and CAF in Supercritical CO_2

Drawing on the experience of single degassing method, we can measure the solubility of CAE and CAF in supercritical CO_2. Pump full amount of surfactant and CO_2 into high pressure and high temperature sample prepared container by precision pump, then stir for 4 hours. Open the valve of sample prepared container in the case of maintaining a constant pressure. Measure the amount of precipitated surfactant under a certain volume of CO_2. Thereby calculate the surfactant's solubility in CO_2 under that pressure.

Table 17.4 shows that CAE has a good solubility in CO_2 under the pressure of 22.64 MPa (formation pressure conditions).
Solubility evaluation conclude that in the condition of 22.64 MPa and 85°C, CAF only has a solubility of 1.16×10^{-3} g/mL in CO_2, which is an order of magnitude lower when compared with the solubility of CAE under the same condition.

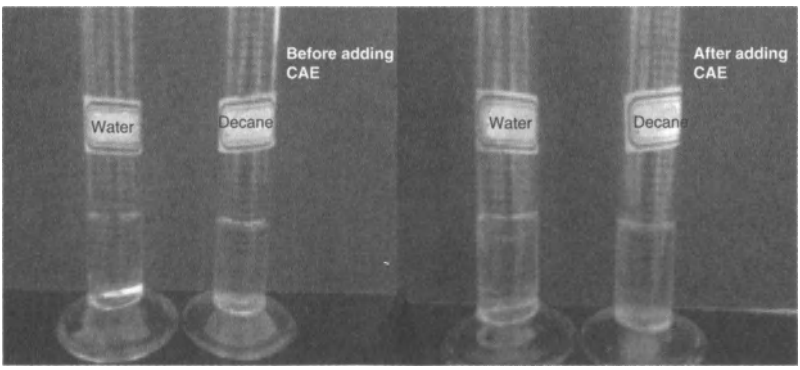

Figure 17.1 Comparison chart before and after adding CAE to water and decane.

Table 17.4 The solubility of CAE in CO_2 under different pressure.

Temperature: 85°C

Measuring pressure (MPa)	**22.64**	**15**	**10**	**7**
Solubility (g/mL)	1.405×10^{-2}	1.225×10^{-2}	4.285×10^{-4}	1.35×10^{-4}

17.4.3 The Viscosity Reduction Evaluation of CAE and CAF

According to the oil industry standard "SY/T 0520–2008", we evaluated the heavy oil viscosity reduction effect of CAE and CAF at 50°C. The results are shown in table 17.5 and table 17.6 respectively.

Through table 17.5 and table 17.6, we can find that when the concentration of surfactant added in crude oil amounts to 1.0%, the result of reducing viscosity reaches the highest. The viscosity reduction rate of CAE can reach 37.8%, and CAF is 27.3%.

17.4.4 The Displacement Efficiency Contrast of CAE and CAF

The formation crude is prepared with practical crude. Determine the oil displacement efficiency in accordance with industry standard SY/T 6576–2003 "Slim-tube experimental determination of minimum miscibility pressure."

Table 17.5 The evaluation of heavy oil viscosity reduction of CAE.

Amount of added surfactant (g)	0.00	0.05	0.10	0.15	0.2	0.25
viscosity (mPa•s)	37	35	27	24	23	25

Note: the amount of crude oil in the experiment is always 20 g.

Table 17.6 The evaluation of heavy oil viscosity reduction of CAF.

Amount of added surfactant (g)	0.00	0.05	0.10	0.15	0.20	0.25
viscosity (mPa•s)	37	37	33	29	27	27

Note: the amount of crude oil in the experiment is always 20 g.

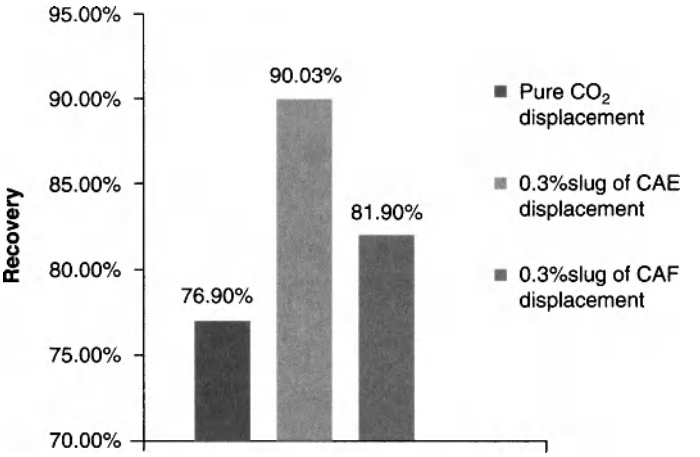

Figure 17.2 The displacement efficiency contrast of volume vs. surfactant under the same concentration.

In the condition of 85°C and 22.64 MPa, pure CO_2 flooding test, slug flooding test with 0.3% CAE and slug flooding test with 0.3% CAF were conducted respectively in order to acquire the displacement efficiency of different flooding methods. The results are shown in figure 17.2 and figure 17.3.

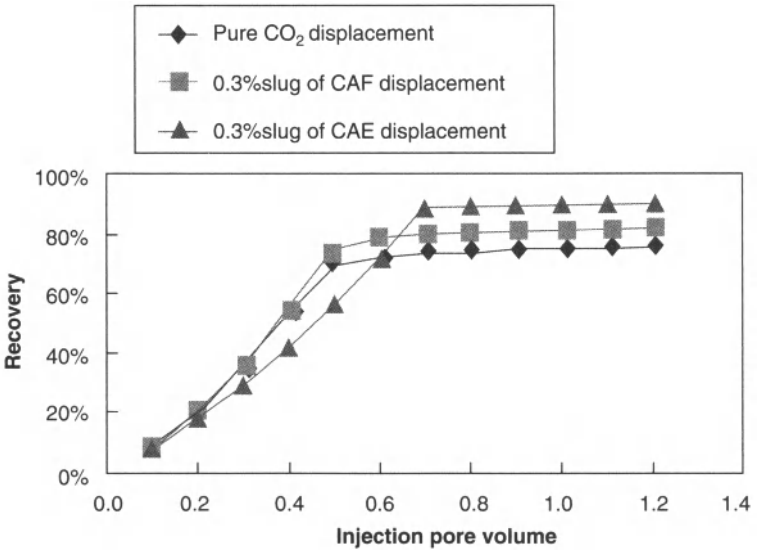

Figure 17.3 The contrast curve of slug injection displacement efficiency under the same concentration.

As is shown in figure 17.2 and figure 17.3, under the same experimental conditions, the slug flooding test with 0.3% CAE enhance the oil recovery from 76.90% to 90.03% when compared with pure CO_2 flooding. The total recovery increment is 13.13%. Whereas, the test with 0.3% CAF enhances the oil recovery from 76.90% to 81.90% when compared with pure CO_2 flooding. The recovery increment is 5.30%. Thus, it's apparent to see oil-soluble surfactant CAE has better displacement efficiency than CAF.

17.5 The Displacement Efficiency Research on Oil-soluble Surfactant Optimization

17.5.1 The Optimization of Surfactant Flooding Pattern

Under the temperature of 85°C and the pressure of 22.64 MPa, the flooding tests with different injection pattern (0.1% dissolved concentration, 0.3% dissolved concentration and 0.3% slug) were conducted for surfactant CAE. And then made a comparison with the displacement efficiency of pure CO_2 flooding.

Figure 17.4 and figure 17.5 shows that compared with pure CO_2 flooding, the oil recovery of CAE surfactant flooding tests with 0.1% dissolved concentration, 0.3% dissolved concentration and 0.3% slug can be increased from 76.90% to 79.70%, 80.30% and 90.03% respectively. The recovery increments are 2.80%, 3.40% and 13.13%. Therefore, the oil displacement experiment indicates

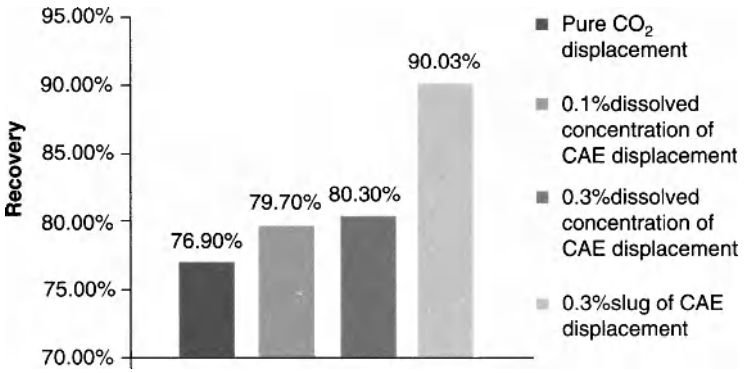

Figure 17.4 The displacement efficiency contrast of CAE under different injection pattern.

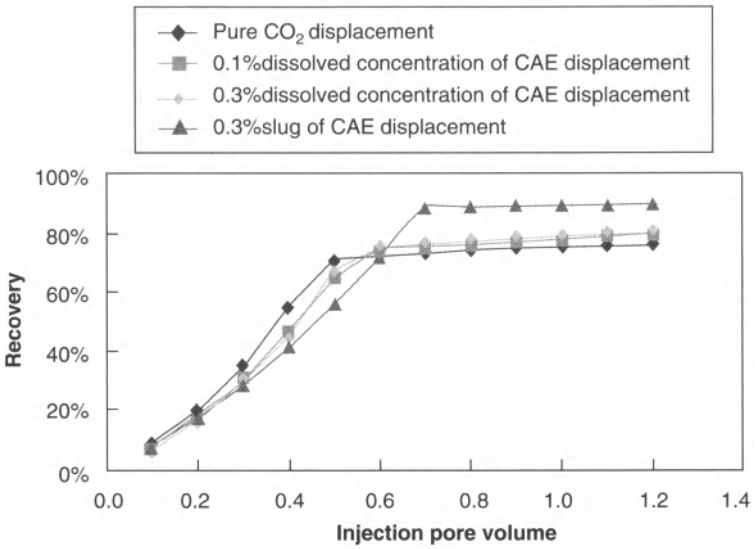

Figure 17.5 The CAE's contrast curve of injection volume vs. displacement efficiency under different injection pattern.

that dissolving CAE in the CO_2 cannot improve oil recovery obviously, however slug flooding is better.

17.5.2 The Slug Flooding Optimization of Different Surfactant Concentration

Under the temperature of 85°C and the pressure of 22.64 MPa, the flooding tests with different concentration slug (0.1% slug, 0.2% slug and 0.3% slug) were conducted for surfactant CAE, and then made a comparison with the displacement efficiency of pure CO_2 flooding.

As is shown in figure 17.6 and figure 17.7, we have conducted pure CO_2 flooding as well as slug flooding with the concentration of 0.1%, 0.2% and 0.3% respectively under 18 MPa. It can be seen from the contrast of displacement efficiency that CAE surfactant flooding with 0.1% slug doesn't have obvious stimulation result when compared with the pure CO_2 flooding. But the slug displacement with the concentration of 0.2% and 0.3% can improve the oil recovery by 3.82% and 5.05% respectively. Consider the costs and economic benefits, CAE slug with 0.2% concentration can be selected as the best slug concentration.

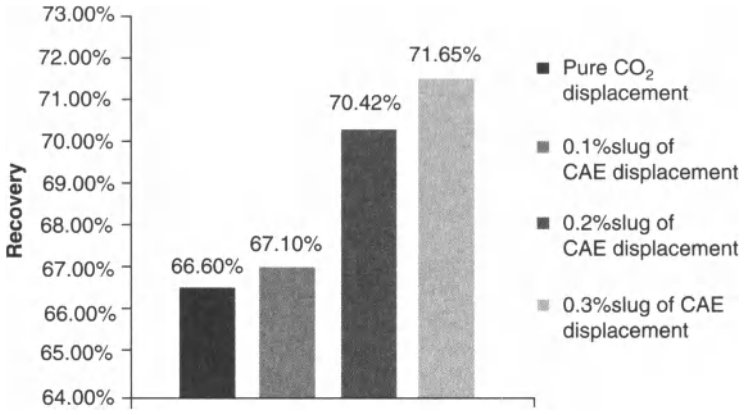

Figure 17.6 The displacement efficiency contrast of CAE with different concentration slug.

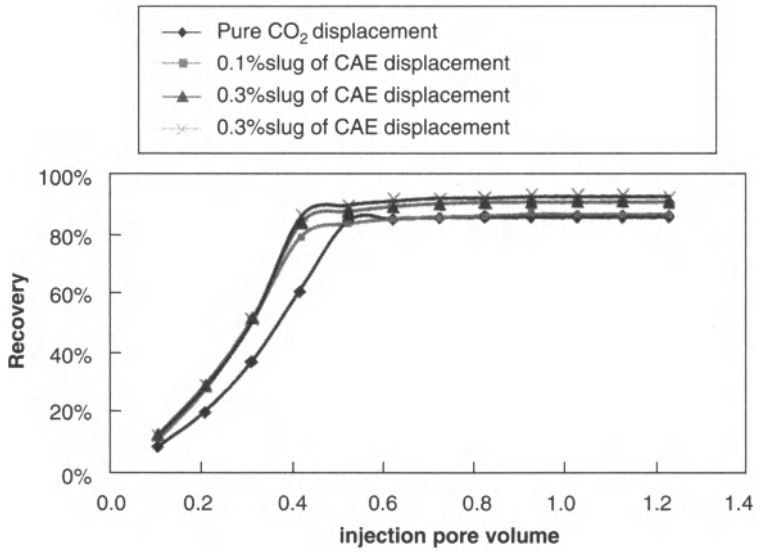

Figure 17.7 The CAE's contrast curve of injection volume vs. displacement efficiency with different concentration slug.

17.6 Conclusions and Recommendations

1. All of the synthetic oil-soluble surfactant can enhance oil recovery to a certain extent.
2. Through the study of displacement efficiency, we can find that the slug flooding of optimized oil-soluble

sufactant CAE has better stimulation effect than the flooding of dissolving CAE in CO_2.

3. Based on the study of displacement efficiency, it's easy to see the optimized surfactant CAE has a more economical concentration of 0.2% for slug displacement.
4. The research of oil-soluble surfactant can improve the efficiency of CO_2 flooding, which is a new exploration and attempt in the area of EOR study. Therefore, further exploration and research are needed to focus on this new method.

17.7 Acknowledgement

This paper is funded by the "State Key Laboratory of Enhanced Oil Recovery", the open fund key project "The Study of Reducing Miscible Pressure of CO_2 Oil Displacement", the state oil and gas key project "The Energy Supplementary Method by Gas Injection in Low Permeability Reservoir and The Auxiliary Technology Research (2008ZX05013- 02-02)".

References

1. Guo, P., Yuan, Z., and Liao, G., "Status and enlightenment of international gas injection EOR technology." [J]. *Natural Gas Industry*, 2009. (29)8: 92–96.
2. Guo, P., Li, S., and Du, Z., "Evaluation on IOR by Gas Injection in Low Permeability Oil Reservoir," [J]. *Journal of Southwest Petroleum Institute*, 2002, (05).
3. Li, S., *Gas Injection for Enhanced Oil Recovery*, [M]. Chengdu: Sichuan Science and Technology Press, 2001.
4. Zhang, F., Li, J., and Zhu, L., "Advances in oil-soluble viscosity reducers for viscous crude oil," [J]. *Special Oil & Gas Reservoirs*, 2006.
5. Guo, P., Zhang, S., Wu, R., Li, S., and Sun, L., "The Minimum Miscible Pressure of CO_2 Flooding in Dagang Oilfield," *Journal of Southwest Petroleum Institute*, 1999, (03).
6. Guo, P., Liu, J., Li, S., and Sun, L., "Evaluation System of Gas Injection Experiment for EOR," *Xinjiang Petroleum Geology*, 2002, (05).
7. Reid B. Grigg, "Improving CO_2 Efficiency for Recovering Oil in Heterogeneous Reservoirs," [C] 1698-NETL, 2010.
8. Min Li, M., Guo, P., and Li, S., "Modeling Technique of Asphaltene Precipitation," [C]. SPE 70048, 2001.
9. Reid B. Grigg, and David S. Schechter, "Improved Efficiency of Miscible CO_2 Floods and Enhanced Prospects For CO_2 Flooding Hetrogeous Reservoirs," [C]. 284- NETL, 2010.

10. Bernard, George C., Union Oil Co. of California; Holm, L.W., Union Oil Co. of California; Harvey, Craig P., Union Oil Co. of California, "Use of Surfactant to Reduce CO_2 Mobility in Oil Displacement," [C]. SPE 8370-PA, 1980.
11. Cao, X., Guo, P., Yang, X., and Li, S., "An Analysis of Prospect of EOR by Gas Injection in Low-Permeability Oil Reservoir," [J]. *Natural Gas Industry*, 2006.
12. Ma, T., "Progress in Research on Surfactants Used as Oil Displacement Agents," [J]. *Speciality Petrochemicals*, 2008.

Index

Ying (Alice) Wu, John J. Carroll and Weiyao Zhu (eds.) Sour Gas and Related Technologies, (3–20) © 2012 Scrivener Publishing LLC

Also of Interest

Check out these forthcoming related titles coming soon from Scrivener Publishing

Now Available from the Same Author:

Acid Gas Injection and Carbon Dioxide Sequestration, by John J. Carroll, ISBN 9780470625934. Provides a complete overview and guide on the hot topics of acid gas injection and CO_2 sequestration.

Carbon Dioxide Thermodynamic Properties Handbook, by Sara Anwar and John J. Carroll, ISBN 9781118012987. The most comprehensive collection of carbon dioxide (CO_2) data ever compiled.

Advances in Natural Gas Engineering Series, Volumes 1 and 2:

Carbon Dioxide Sequestration and Related Technologies, by Ying Wu and John J. Carroll, ISBN 9780470938768. Volume two focuses on one of the hottest topics in any field of engineering, carbon dioxide sequestration. *NOW AVAILABLE!*

Carbon Dioxide Sequestration and Related Technologies, by Ying Wu and John J. Carroll, ISBN 9780470938768. Volume two focuses on one of the hottest topics in any field of engineering, carbon dioxide sequestration. *NOW AVAILABLE!*

Other books in Energy and Chemical Engineering:

Zero-Waste Engineering, by Rafiqul Islam, February 2011, ISBN 9780470626047. In this controvercial new volume, the author explores the question of zero-waste engineering and how it can be done, efficiently and profitably.

Ying (Alice) Wu, John J. Carroll and Weiyao Zhu (eds.) Sour Gas and Related Technologies, (3–20) © 2012 Scrivener Publishing LLC

Advanced Petroleum Reservoir Simulation, by M.R. Islam, S.H. Mousavizadegan, Shabbir Mustafiz, and Jamal H. Abou-Kassem, ISBN 9780470625811. The state of the art in petroleum reservoir simulation. *NOW AVAILABLE!*

Energy Storage: A New Approach, by Ralph Zito, ISBN 9780470625910. Exploring the potential of reversible concentrations cells, the author of this groundbreaking volume reveals new technologies to solve the global crisis of energy storage. *NOW AVAILABLE!*

Ethics in Engineering, by James Speight and Russell Foote, December 2010, ISBN 9780470626023. Covers the most thought-provoking ethical questions in engineering.